Liquefaction-Induced Downdrag on Drilled Shafts

WA-RD 865.1

Balasingam Muhunthan
Noel V. Vijayathasan
Babak Abbasi

April 2017

Washington State Department of Transportation
Office of Research & Library Services

WSDOT Research Report

17-07-0293

Research Report

Agreement T4120, Task 26

WA-RD 865.1

LIQUEFACTION-INDUCED DOWNDRAG ON DRILLED SHAFTS

by

Balasingam Muhunthan, Principal Investigator
Noel V. Vijayathasan
Babak Abbasi

Department of Civil and Environmental Engineering
Washington State University
Pullman, WA 99164-2910

Washington State Department of Transportation
Technical Monitor
Tony Allen
State Geotechnical Engineer

Prepared for

The State of Washington
Department of Transportation
Roger Millar, Secretary

April 2017

1. REPORT NO.	2. GOVERNMENT ACCESSION NO.	3. RECIPIENTS CATALOG NO
WA-RD 865.1		

4. TITLE AND SUBTILLE	5. REPORT DATE
Liquefaction-Induced Downdrag on Drilled Shafts	April 2017
	6. PERFORMING ORGANIZATION CODE

7. AUTHOR(S)	8. PERFORMING ORGANIZATION REPORT NO.
Balasingam Muhunthan, Noel V. Vijayathasan and Babak Abbasi	

9. PERFORMING ORGANIZATION NAME AND ADDRESS	10. WORK UNIT NO.
Washington State University Civil and Environmental Engineering Pullman, WA 99164-2910	11. CONTRACT OR GRANT NO. Agreement T4120, Task 26

12. SPONSORING AGENCY NAME AND ADDRESS	13. TYPE OF REPORT AND PERIOD COVERED
Washington State Department of Transportation Olympia Washington 98504-7370 Lu Saechao, Project Manager, 360-705-7260	Final Research Report
	14. SPONSORING AGENCY CODE

15. SUPPLEMENTARY NOTES

This study was conducted in cooperation with the U.S. Department of Transportation, Federal Highway Administration.

16. ABSTRACT

Sandy soil layers reduce in volume during and following liquefaction. The downward relative movement of the overlying soil layers around drilled shafts induces shear stress along the shaft and changes the axial load distribution. Depending on the site conditions, the change in the axial responses that result from liquefaction-induced settlement and the drag load can have a significant impact on the performance of drilled shafts in seismic regions.

This study presents an analytical method to quantify the effects of liquefaction-induced downdrag on drilled shafts. The analytical method is based on the neutral plane method originally developed for clays but modified to account for liquefaction-induced effects. The neutral plane method is a simplification of soil-shaft interactions and is more representative of actual conditions compared to other methods. In this study, the neutral plane method was applied to an observed case of downdrag during the 8.8 magnitude earthquake in Maule, Chile and was able to predict the liquefaction-induced settlement that was the major cause of failure of the structure. The developed procedure is illustrated for two field cases of drilled shafts in liquefiable soils in Washington State.

17. KEY WORDS	18. DISTRIBUTION STATEMENT
Axial loads, liquefaction-induced settlement, sand, seismic analysis, side resistance, soil liquefaction, soil settlement, drilled shafts	No restrictions. This document is available to the public through the National Technical Information Service, Springfield, VA 22616

19. SECURITY CLASSIF. (of this report)	20. SECURITY CLASSIF. (of this page)	21. NO. OF PAGES	22. PRICE
None	None		

Disclaimer

The contents of this report reflect the views of the authors, who are responsible for the facts and the accuracy of the data presented herein. The contents do not necessarily reflect the official views or policies of the Washington State Department of Transportation. This report does not constitute a standard, specification, or regulation.

TABLE OF CONTENTS

FIGURES

TABLES

CHAPTER 1: INTRODUCTION

1.1 OVERVIEW

Drilled shafts often are used to transfer the structural loads to deeper firm strata. Load transfer from shaft to soil or vice versa is accomplished by relative movement between shaft and soil, which mobilizes shaft and tip resistances. The direction of side resistance depends on the direction of the shaft movement. By definition, when the pile moves downward the resulting shear stress along the shaft is in the upward direction, which is known as positive direction. The downward relative movement of the soil around the shaft also induces shear stress along the shaft, which is referred to as negative side resistance.

Sandy soil layers can reduce soil volume during and following liquefaction (Tokimatsu and Seed 1987, Ishihara and Yoshimine 1992). The downward relative movement of the soil around the shaft induces shear stress along the shaft commonly called negative side resistance. The accumulated negative side resistance will affect the pile load and add axial force to the shaft, called "drag force".

Movement of the soil affects the load distribution along a drilled shaft. Depending on the site conditions, the change in the axial responses that result from liquefaction-induced settlement can have a significant impact on the performance of drilled shafts in seismic regions. In extreme circumstances, the drag force may exceed the structural axial strength of the shaft. Other than for very long piles (aspect ratio larger than about 100), the soil settlement around the pile will tend to move the pile downward, i.e., add downdrag that may affect the serviceability of the structure. Incidences of liquefaction-induced downdrag on piers and shafts that varied from near zero to excessive amounts occurred February 27, 2010 during the 8.8 magnitude earthquake off the Maule coast in central Chile (Yen et al. 2011).

Methods that often are employed to account for the effects of liquefaction on deep foundations are addressed in terms of drag load development in design manuals, including the American Association of State Highway and Transportation Officials (AASHTO) 2014 guidelines and the Washington State Department of Transportation (WSDOT) 2015 guidelines. The AASHTO (2014) specifications recommend adding the factored drag load from the soil layers above the liquefiable zone to the factored loads from the superstructure. The AASHTO (2014) specifications also contain simplified techniques to compute the drag load and recommend the use of non-liquefied shaft resistance in the layers within and above the liquefied zone as well as shaft resistance as low as the residual strength within the soil layers that do liquefy in order to estimate the drag load for an extreme event limit state.

The development of drag load in piles and drilled shafts that have been constructed in consolidating soils (i.e., under static loading) has been researched extensively for geotechnical design. Different researchers have proposed several solutions to determine the magnitude and distribution of drag loads that may act on piles in settling soils (e.g., Poulos and Davis 1990, Matyas and Santamarina 1994, and Fellenius 1984, 2004). These studies present procedures to estimate the forces and the location of the neutral plane (NP), which is the location along the pile where sustained forces are in equilibrium with resisting forces (i.e., positive side resistance below the NP and mobilized tip resistance).

Similarly, several researchers have proposed a number of numerical methods to account for many of the features associated with drag load development (Lee and Ng 2004, Jeong et al. 2004, Hanna and Sharif 2006, Yan et al. 2012). These studies address the drag load that is caused by a surcharge or consolidation of the surrounding soil. Wang and Brandenberg (2013) proposed a method to estimate the pile response that is due to consolidation by applying a beam on a nonlinear Winkler foundation using t-z elements to model the soil-pile interactions, with the pile

as the beam-column element. These researchers carried out their analysis using the finite element code OpenSees (Open System for Earthquake Engineering Simulation) (2012) and provided an estimate of the drag load by assuming that the relative velocity between the pile and the soil at the NP is zero.

Unlike the number of studies of drag development in consolidating soils, only a few analytical studies have addressed drag load and downdrag in cases where the soil settlement is caused by seismic liquefaction (e.g., Boulanger and Brandenburg 2004, Rollins and Strand 2006, Fellenius and Siegel 2008). For example, Boulanger and Brandenberg (2004) related the shaft resistance in a reconsolidating liquefied zone to the dissipation of excess pore pressure over time and then estimated the resulting drag load. In their study, downdrag was correlated incrementally over time in parallel with the pore pressure dissipation. Also, Fellenius and Siegel (2008) applied the concepts of 'unified method' (Fellenius 1984, 2004, 2014) to study the effects of seismic liquefaction on downdrag. The unified method is based on the interaction between pile resistance and soil settlement, notably the interaction between the pile tip resistance and pile tip penetration. The method adopted by Fellenius and Siegel (2008) involves repositioning the NP based on the location of a single liquefiable zone with respect to the original location, i.e., with the liquefiable zone located above or below the NP. The validity of this approach has been demonstrated at a site in northern California (Knutson and Siegel 2006) and in field tests by Rollins and Strand (2006) and Strand (2008).

1.2 RESEARCH OBJECTIVES

The primary objective of this research is to develop an analytical method that can account for liquefaction-induced downdrag (settlement) in deep foundations. The study includes a critical examination of the existing analytical and numerical methods for downdrag analysis of piles and

drilled shafts. In this study, the NP method has been modified further to account for multiple layers of liquefaction and applied to a case study of the 2010 earthquake off the Maule coast in Chile. The analysis also identified the need to account for soil-structure interactions to better quantify the effects of liquefaction-induced downdrag. Numerical simulations were performed using OpenSees finite element software, which is widely used in earthquake engineering simulations (OpenSees 2014). The specific objectives of the study are to:

(i) Develop an analytical method to account for liquefaction-induced downdrag with regard to piles and drilled shafts.

(ii) Verify the key assumptions made in (i) using OpenSees.

(iii) Evaluate the performance of selected drilled shafts in the State of Washington that are vulnerable to liquefaction-induced downdrag during earthquakes.

1.3 OUTLINE OF REPORT

Chapter 1 provides an introduction to the concept of downdrag as it applies to deep foundations and introduces the ideas used for the research conducted in this study. Chapter 2 presents a literature review of the current methods that pertain to liquefaction-induced downdrag. Chapter 3 includes a review of the NP method and improvements and modifications to the method for its application to liquefaction-induced downdrag. Also in Chapter 3, the modified NP method is applied to study the observed settlement responses of piers along the Juan Pablo II Bridge during the 2010 Maule 8.8 magnitude earthquake in Chile. Appendix A presents the numerical analysis conducted using OpenSees to verify some of the key assumptions used in the analytical method. Chapter 4 illustrates the developed procedure used to calculate downdrag for two field cases in the State of Washington; these sites are potentially vulnerable to liquefaction. One of the field cases

is analyzed in detail, whereas the details relevant to the second case are presented in Appendix B to ensure brevity of Chapter 4. Chapter 5 summarizes the study with conclusions and recommendations for further advances in this research area.

CHAPTER 2: LITERATURE REVIEW

2.1 INTRODUCTION

When loose granular soils are saturated and subjected to strong ground shaking (repeated loading or cyclic loading) under undrained conditions, the contractant behavior (reduction in volume) of the soil layers causes pore pressure to accumulate, resulting simultaneously in the reduction of effective stress. This reduction in effective stress progressively transfers granular soils from a solid state to a liquefied state. In dense soils, such liquefaction leads to transient softening and increased cyclic shear strain, dilatant behavior (expansion in volume) during shear induces major strength loss and large ground deformations (Youd et al. 2001).

2.2 LIQUEFACTION-INDUCED DOWNDRAG

Sandy soil layers reduce the volume of the soil during and following liquefaction (Tokimatsu and Seed 1987, Ishihara and Yoshimine 1992). This volume reduction manifests as a downward movement, or settlement, of the overlying soil layers. Such movement may affect the load distribution on deep foundations. Depending on the site conditions, the change in the axial responses (i.e., drag load and downdrag) that result from liquefaction-induced settlement can have a significant impact on the performance of piles or drilled shafts in seismic regions.

The development of drag load on piles and drilled shafts that have been constructed in consolidating soils (i.e., under static loading) has been researched extensively for geotechnical design. Researchers have proposed several solutions to determine the magnitude and distribution of drag loads that may act on piles in settling soils (e.g., Poulos and Davis 1990, Matyas and Santamarina 1994, and Fellenius 1984, 2004). These studies have proposed procedures to estimate the forces and the location of the NP, i.e., the location along the pile where sustained forces are in

equilibrium with the resisting forces (i.e., positive side resistance below the NP and mobilized tip resistance).

2.3 ENDO ET AL. (1969)

Endo et al. (1969) presented a case history that involves the behavior of the negative side resistance on single piles installed in a clay medium. Measurements of side resistance for four kinds of steel pipe piles, i.e., friction and point-bearing piles and open-point and closed-end pipe piles, were taken for more than two years at a thick alluvial stratum where consolidation had been observed due to a decrease in pore pressure. As shown in Figure 2.1, the observed load distribution pattern indicates both positive side resistance and negative side resistance. Figure 2.2 presents the measured soil and pile settlements. Endo et al. (1969) noted the existence of a NP, where the axial stress in a pile is at a maximum level. The axial force due to the negative side resistance is transmitted to the tip of pile while it is being diminished by the positive side resistance acting on the pile below the neutral point.

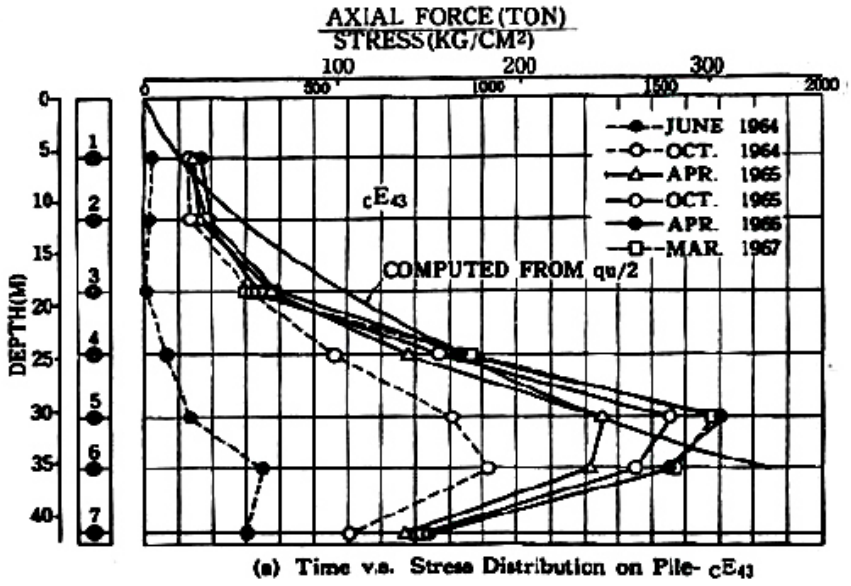

Figure 2.1. Stress distribution on a test pile (cE43) with time (Endo et al. 1969).

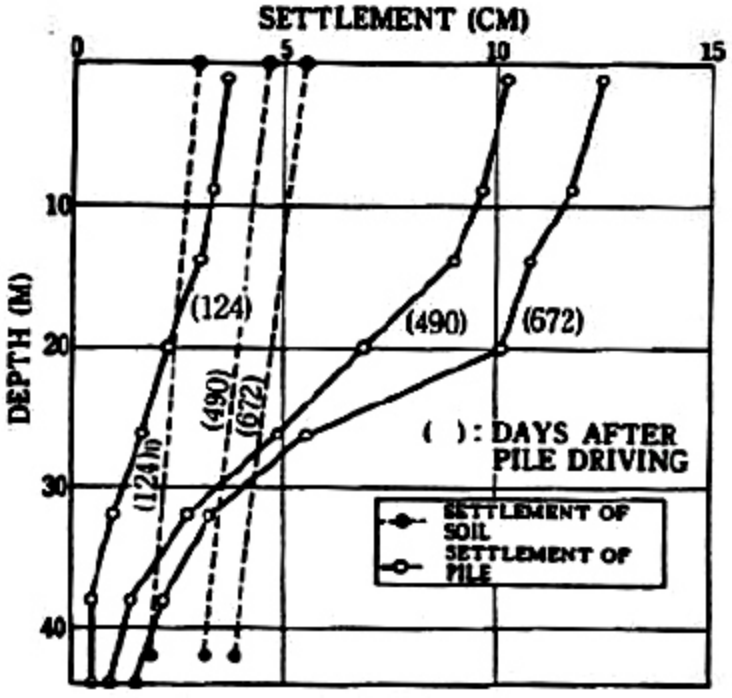

Figure 2.2. Comparison of soil and pile settlements for cE43 test pile with time (Endo et al. 1969).

2.4 BOULANGER AND BRANDENBERG (2004)

Fellenius (1972) developed the NP method to estimate drag load and downdrag for piles in clay. Boulanger and Brandenberg (2004) later modified the NP method for its application to liquefaction-induced downdrag on vertical piles. This modified method accounts for the variation in excess pore pressure (Δu) and ground settlement over time as a liquefied layer reconsolidates. Sand compressibility (m_v) and side resistance (f_s) are considered as functions of the excess pore pressure ratio. Drag load or side resistance in the consolidating soil will increase over time as the effective stress increases (pore pressure decreases) during consolidation.

Sand compressibility, which depends on the excess pore pressure ratio ($r_u = u/\sigma'_{vo}$), is used to calculate soil settlement and pile head settlement as the liquefied layer reconsolidates. A description of excess pore pressure isochrones over time and the relationship between m_v and r_u

are required to evaluate these settlements (Boulanger and Brandenberg 2004). Excess pore pressure distribution patterns (isochrones) depend on the boundary and drainage conditions. The isochrones may change according to the boundary conditions. The isochrones in the top liquefied layer satisfy the test conditions whereas the bottom three liquefiable layers may not. The layers right above and below the liquefied layer affect the distribution pattern. Figure 2.3 (a) shows typical excess pore pressure isochrones within a liquefied layer at different times ($t_0 - t_3$) during reconsolidation. Here, t_0 is the time immediately after r_u = 100 percent, and t_3 is the time that corresponds to when Δu has fully dissipated. That is, the effective stress is almost zero at time t_0 and is expected to reach a value at the end of primary consolidation. Florin and Ivanov (1961) also observed a trapezoidal distribution of isochrones during their tests when the bottom soil layer and the top layer are impermeable and permeable, respectively.

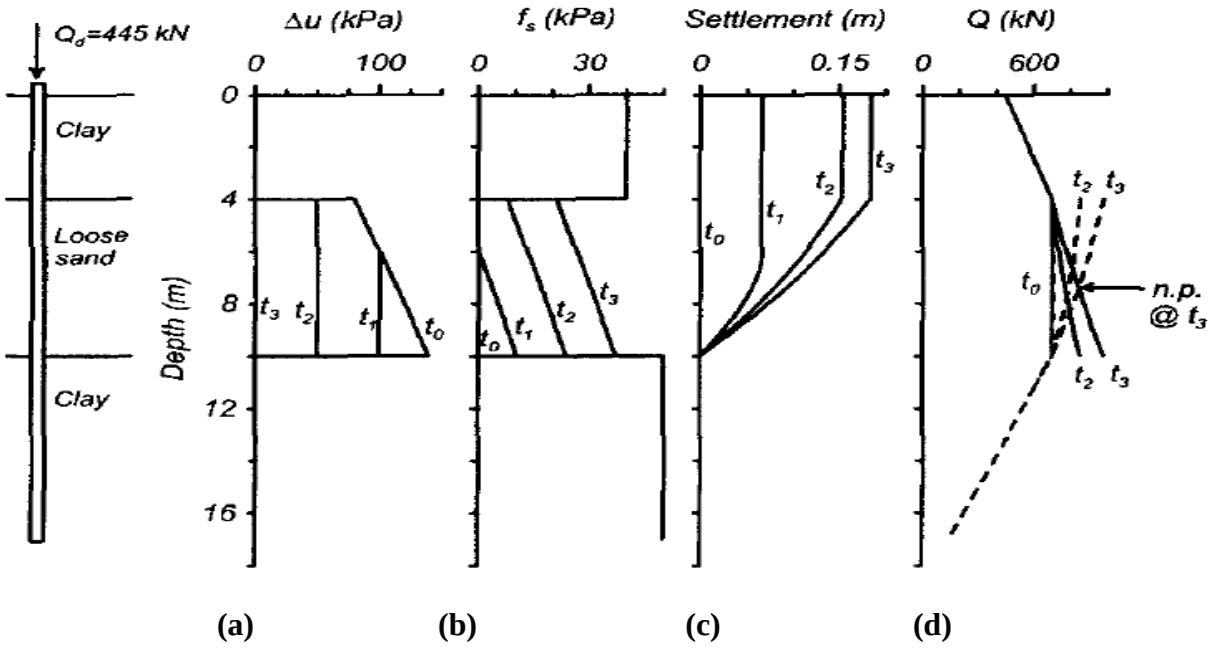

Figure 2.3. Variations within a liquefied layer: (a) excess pore pressure patterns (isochrones), (b) side resistance, (c) soil settlement, and (d) changing neutral plane location (Boulanger and Brandenberg 2004).

The side resistance within liquefied sand is modeled as being proportional to the effective stress in the sand, as expressed as Equation 2.1:

$$f_s = \sigma'_{vo} K_o \tan(\delta)(1 - r_u), \qquad [2.1]$$

where σ_{vo}' is the vertical effective consolidation stress, K_o is the coefficient of lateral earth pressure at rest, and δ is the interface friction angle during liquefaction and reconsolidation. Variations in K_o and δ over time are likely to have only a small effect on side resistance compared to the contribution from changes in r_u (Boulanger and Brandenberg 2004). Thus, these parameters are kept constant in the absence of data in the analysis.

Lee and Albeisa (1974) determined the volumetric strains that are due to the reconsolidation of samples subjected to increases in excess hydrostatic pore pressure caused by cyclic loading or static loading. Seed et al. (1975) developed an analytical expression for the increase in compressibility using the pore pressure ratio and relative density, as shown in Equations 2.2 (a) through (c):

$$\frac{m_v}{m_{vo}} = \frac{e^{AX^B}}{1+AX^B+\frac{1}{2}A^2X^{2B}} \qquad [2.2a]$$

$$A = 5(1.5 - D_r) \qquad [2.2b]$$

$$B = 3(2)^{-2D_r}\,, \qquad [2.2c]$$

where X (= r_u) is the excess pore pressure ratio, D_r is the relative density, and m_{vo} is the sand compressibility at low pore pressure. The soil settlement is calculated by integrating the vertical strain (ϵ_v) in the soil profile as the liquefiable layers reconsolidate. The vertical strains are calculated by Equation 2.3:

$$\epsilon_v = \Delta\sigma'_{vo}.\, m_v\,, \qquad [2.3]$$

where $\Delta\sigma_{vo}'$ is the change in the effective stress and m_v is sand compressibility. It should be noted that changes in side resistance and soil settlement will occur as a result of the dissipation of excess pore pressure, as shown in Figure 2.4. The loads are summed downwards from the pile head (Q_{down}) and upwards from the pile tip (Q_{up}). The NP location is found at the depth where Q_{down} equals Q_{up}. These changes alter the load distribution patterns for the pile.

The pile settlement equals the soil settlement at the NP location at the end of consolidation (Fellenius 1972). Here, the NP location varies with time as the side resistance in the liquefied sand increases during consolidation. So, the downdrag is estimated incrementally, as illustrated in

Figure 2.4. For example, between times t_2 and t_3, the NP location moves upwards. The increment of the pile settlement (ΔS_{pile}) equals the increment of the soil settlement (ΔS_{soil}) at the NP location at the end of this time step t_3. Then, the total pile settlement is evaluated by numerically integrating the increments of the pile settlement over the time for reconsolidation. This approach predicts substantially smaller pile settlements for the end of the consolidation stage than the traditional NP method.

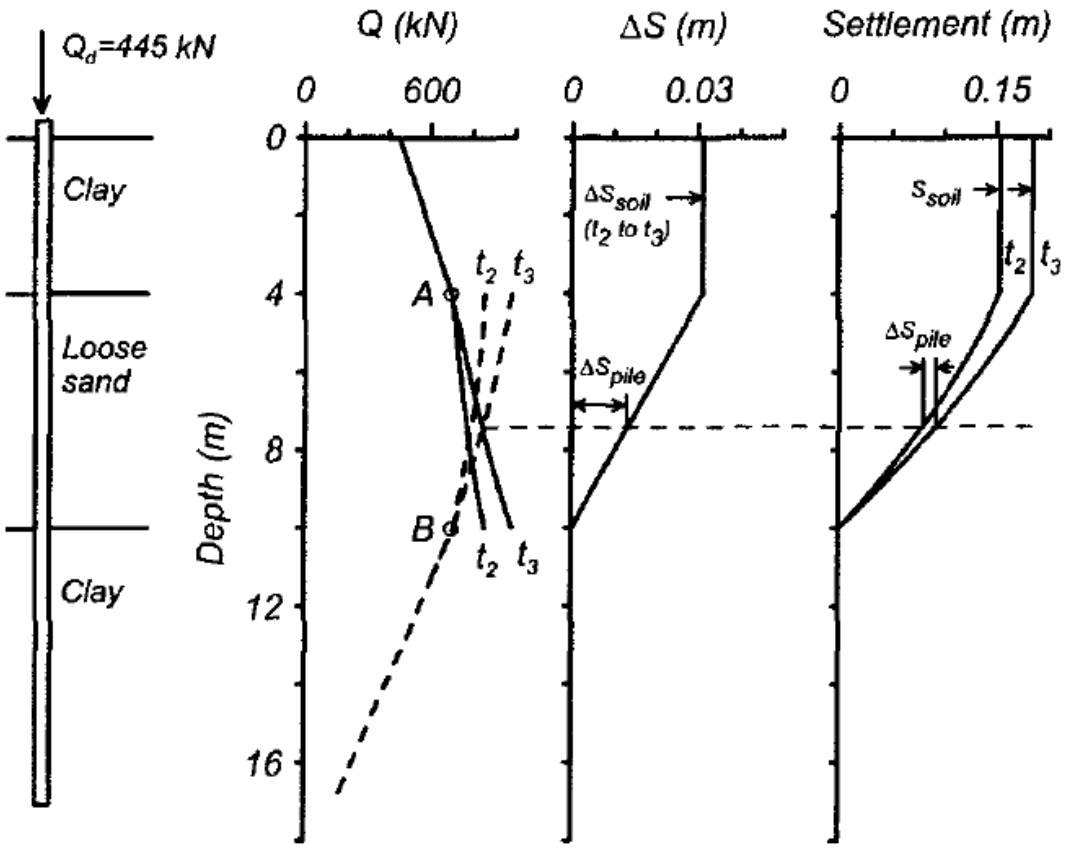

Figure 2.4. Incremental liquefaction-induced downdrag (Boulanger and Brandenberg 2004).

2.5 ROLLINS AND STRAND (2006)

Rollins and Strand performed instrumented full-scale testing to investigate the loss of side resistance, the development of negative side resistance, and the axial load distribution after blast-

induced liquefaction at a site near Vancouver, Canada. They measured these parameters before and after the liquefaction event. The test pile was a 324-mm outside diameter steel pipe pile with a 19-mm wall thickness that was driven close-ended to a depth of 21.3 m, as shown in Figure 2.5. The soil profile consisted of clean sand, silty clay, and silty sand. A total of 16 explosive charges at depths of 6.4 m and 8.5 m below the ground surface and equally spaced in a 10-m diameter circle around the test pile were detonated sequentially with a one-second delay between detonations to induce liquefaction. Figure 2.6 presents the recorded pore pressure measurements. The settlement of the soil profile also was measured along with the pore pressure dissipation. Figure 2.7 displays the axial load distribution on the pile immediately before and immediately after blast-induced liquefaction and after the pore pressure had completely dissipated to zero. Figure 2.7 shows that the side resistance essentially reduced to zero around the liquefied zone as the excess pore pressure ratio approached unity. As this layer settled due to the dissipation of the excess pore pressure, negative side resistance developed with a unit value that was approximately half of the positive side resistance prior to blasting. The soil settlement was about 270 mm. As a result of the loss of the side resistance and then the downdrag load in the liquefied layer, the applied load was transferred to the denser soil below the liquefied zone. The required displacement needed to mobilize this additional side resistance was less than 10 mm (Rollins and Strand 2006). To the author's knowledge, this Rollins and Strand 2006 work is the only field test that has been performed to date regarding liquefaction-induced downdrag and drag load.

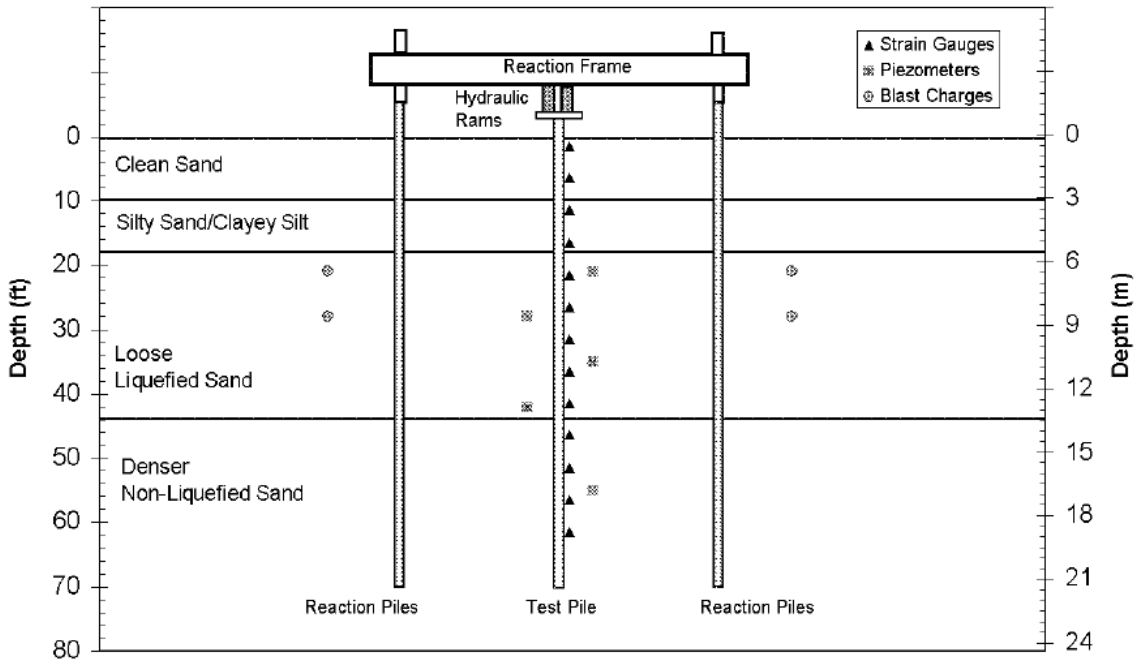

Figure 2.5. Layout of test pile, instrumentation, and blast charges relative to the soil profile at the Massey Tunnel test site south of Vancouver, Canada (Rollins and Strand 2006).

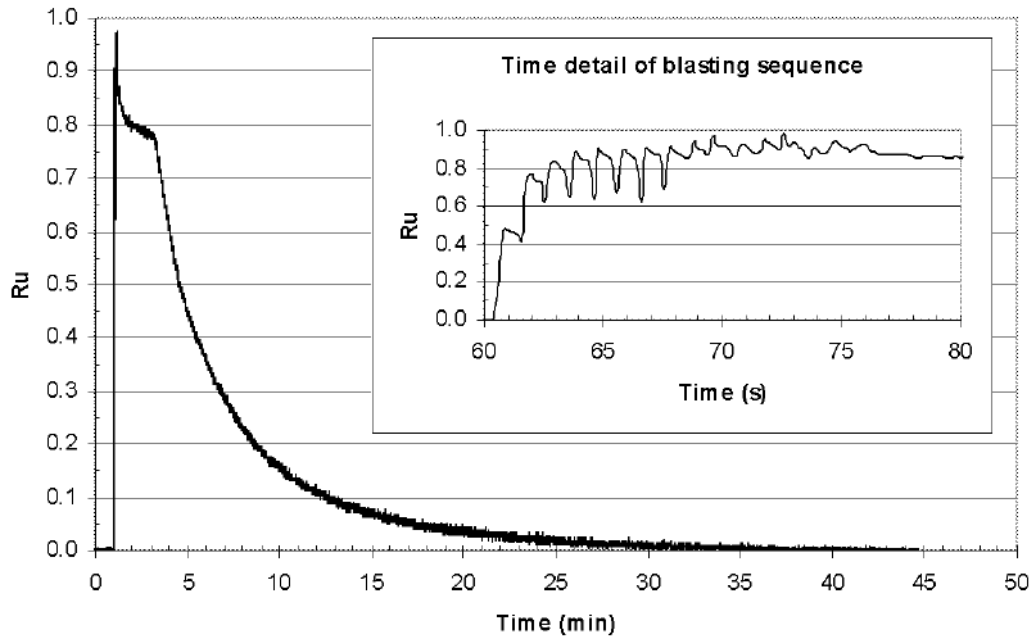

Figure 2.6. Build-up and dissipation of excess pore pressure ratio (*ru*) at a depth of 8.4 m below the ground surface after detonation of explosive charges (Rollins and Strand 2006).

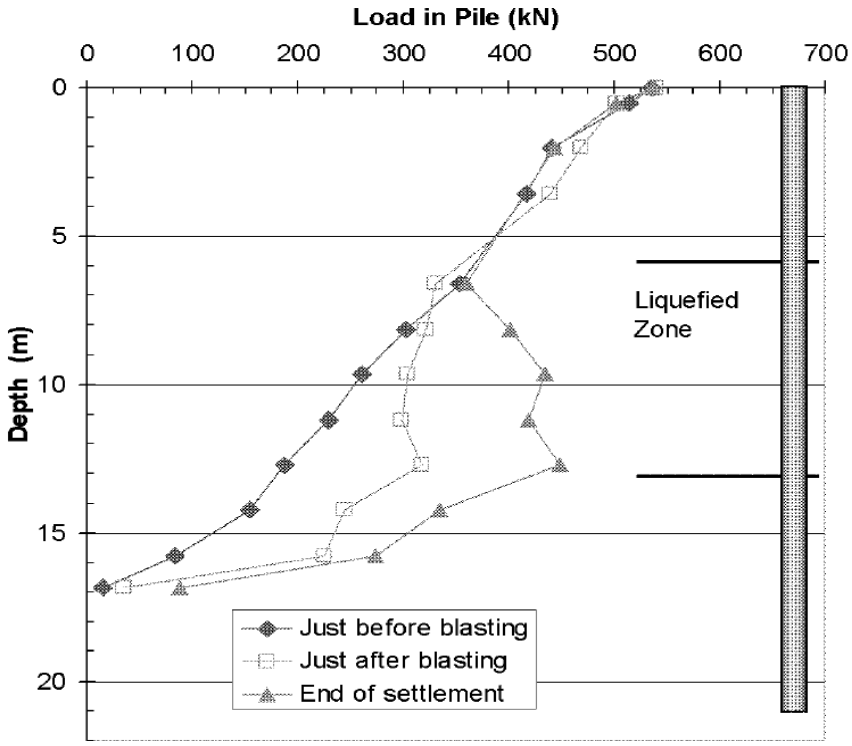

Figure 2.7. Load distribution at the pile immediately before and immediately after blast-induced liquefaction and when the pore pressure had dissipated to essentially zero (Rollins and Strand 2006).

2.6 FELLENIUS AND SIEGEL (2008)

Fellenius and Siegel (2008) applied the 'unified method' (Fellenius 1984, 2004, 2014) that is based on the interaction between pile resistance and soil settlement, notably the interaction between the pile toe resistance and pile toe penetration, to study the effects of seismic liquefaction. The unified method involves repositioning the NP based on the location of a single liquefiable zone with respect to the original location, i.e., with the liquefiable zone located above or below the NP. This approach was demonstrated at a site in northern California by Knutson and Siegel (2006) and in field tests by Rollins and Strand (2006) and Strand (2008). In general, however, several potentially liquefiable zones within an embedded pier length may exist, as was observed in the

case of the Maule, Chile earthquake. Such cases present the need to extend the recommendations by Fellenius and Siegel (2008) to include multiple liquefiable zones, which forms the subject of Chapter 3.

2.7 AASHTO METHOD

Methods that account for liquefaction effects on pile foundations are addressed in terms of drag load development in a few design manuals, such as the AASHTO (2014) and WSDOT (2013) specifications. The AASHTO (2014) specifications recommend adding the factored drag load from the soil layers above the liquefiable zone to the factored loads from the superstructure. The AASHTO (2014) specifications also contain simplified techniques to compute the drag load, recommending the use of the non-liquefied side resistance in the layers within and above the liquefied zone and a side resistance as low as the residual strength within the soil layers that do liquefy to estimate the drag load for an extreme event limit state.

AASHTO (2014) also recommends using the 'explicit method' to calculate downdrag instead of the NP method. Figure 2.8 describes the explicit method conceptually whereby the negative side resistance is assumed to develop when the relative downward movement of the soil is 0.4 inch or more. Hanningan et al. (2005) presented a step-by-step procedure for determining the downdrag load; this procedure is based on the assumption that at least a 0.4-inch settlement between the soil and the pile is needed to mobilize the negative side resistance. Along the shaft where the settlement of the soil is more than 0.4 inch is assumed to have negative side resistance. The drag load is applied as the top load after applying the appropriate load factor.

Siegal et al. (2014) compared the explicit and the NP analysis methods. The most important difference between these two methods is the exclusion of the drag load at the geotechnical limit

state in the NP method. Siegal et al. (2014) also state that the NP method is a simplification of soil-pile interaction and is more representative of actual pile conditions than the explicit method.

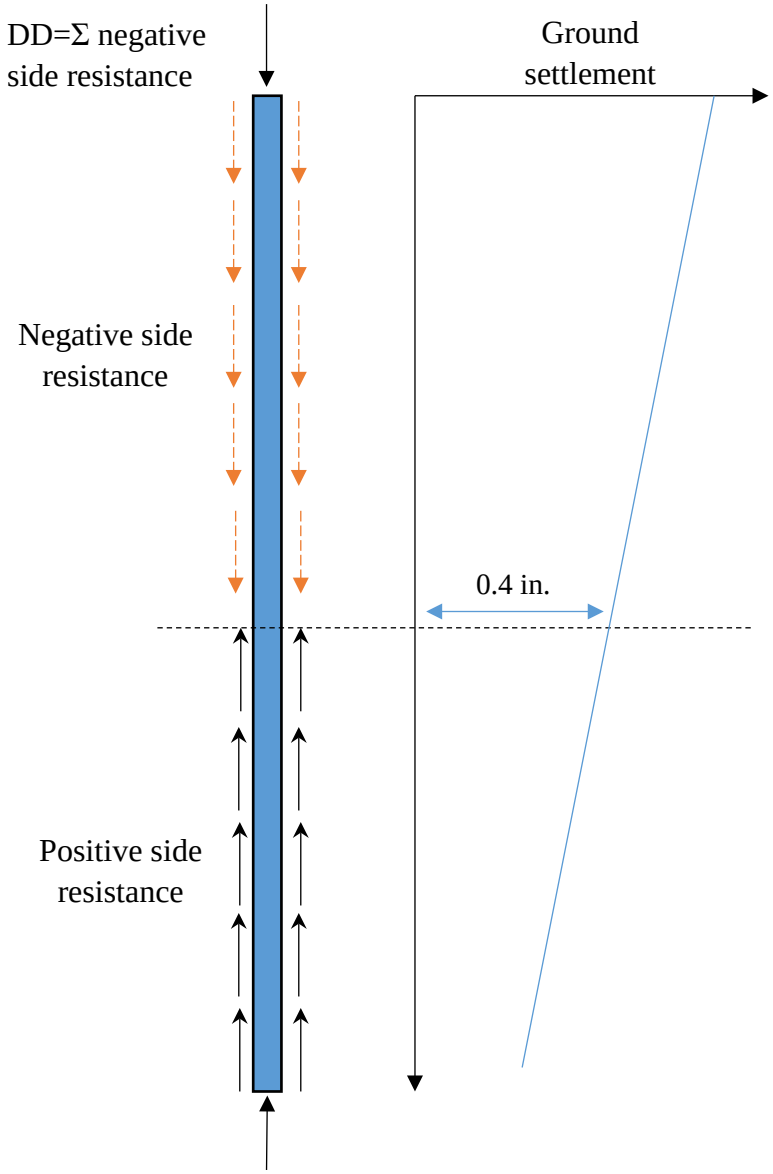

Figure 2.8. Conceptual illustration of explicit method (Siegel et al. 2014).

In summary, the experimental and field observation during the past decades urged the geotechnical engineers to develop methods of downdrag analyses. These methods mostly involve

the design at static loading conditions on piles in fine-grained soils (e.g. Boulanger and Brandenberg 2004, and Fellenius 1972). Recently these methods are modified and applied for liquefaction-induced downdrag analysis (e.g. Fellenius and Siegel 2008). Methods to account for liquefaction-effects on deep foundations are also addressed in terms of drag load development in a few design manuals, such as AASHTO (2014) and WSDOT (2015). In this study we further modified the unified method by Fellenius and Siegel (2008) to be used for drilled shafts by including their self-weight as well as the potential for the presence of multiple liquefiable layers. This method is capable of predicting the downdrag settlement, drag load, and the axial load distribution along the shaft, during and after the liquefaction, which gives a better understanding of loads on the deep foundations compared to explicit methods addressed in design manuals.

CHAPTER 3: MODIFIED UNIFIED METHOD FOR LIQUEFACTION-INDUCED DOWNDRAG: APPLICATION TO JUAN PABLO II BRIDGE

3.1 INTRODUCTION

Fellenius and Siegel (2008) modified the original unified method (Fellenius 1984, 2004, 2014) for pile analysis to account for seismic liquefaction effects. The unified method is based on the concept of the NP in piles and accounts for the interaction between pile resistance and soil settlement, notably the interaction between the tip resistance and tip penetration. Fellenius and Siegel's modification for seismic liquefaction involves repositioning the NP based on the location of a single liquefiable zone with respect to the original location, i.e., whether the liquefiable zone is located above or below the NP. The validity of the approach has been demonstrated for a site in northern California (Knutson and Siegel 2006) and in field tests by Rollins and Strand (2006) and Strand (2008).

In the current study, this NP method has been extended further to include drilled shafts and applied to the case of the pier performance at the Juan Pablo II Bridge during the Maule, Chile earthquake in 2010 to verify its potential. Also in this study, numerical analyses were conducted using OpenSees finite element software to examine some of the assumptions made in the study in order to reinforce the study's potential for applications to practice (see Appendix A).

3.2 THE MODIFIED UNIFIED ANALYSIS METHOD FOR PILES (FELLENIUS AND SIEGEL 2008)

Fellenius (1984, 1988, 2014) proposed the unified method to analyze the responses of deep foundations to load and soil movement. This method makes use of the NP that relies on force and settlement equilibria. The NP is located at the depth of the force equilibrium, i.e., where the load and resistance curves intersect. The NP is also the plane where the soil and the pile both move equally, i.e., the location of the settlement equilibrium.

Neutral Plane for Liquefied Soils

Figures 3.1 (a) and (b) show variations in the load and resistance curves and the pile and settlement curves, respectively, in terms of depth along a pile before liquefaction. The NP is at the intersection of the load and resistance curves.

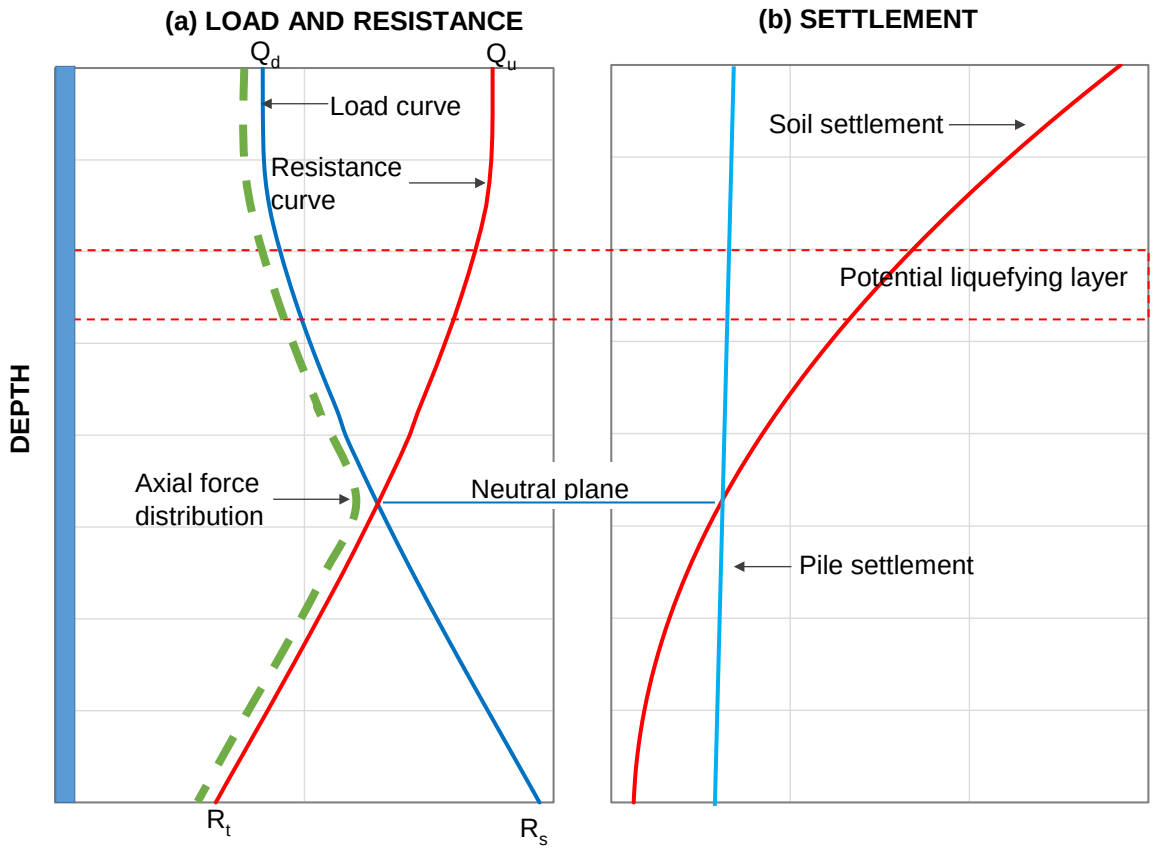

Figure 3.1. Schematic diagram of location of neutral plane before liquefaction: (a) load and resistance curves and (b) soil and pile settlement curves.

The underlying principle of the load distribution curve is common for all conditions, i.e., before, during, and after liquefaction. The curve begins with the dead load, Q_d, at the pile head and increases with depth, assuming fully mobilized negative side resistance along the pile, with the value R_s at the tip. The resistance curve initiates with the mobilized tip resistance, R_t, and increases

upward along the pile, thus corresponding to the fully mobilized positive side resistance and attaining the value Q_u. The load curve is not necessarily the actual load on the pile, but the potential maximum load per depth if all the side resistance is dragging on the foundation. The resistance curve is also the maximum available resistance distribution. The distribution of the axial force along the pile (dashed line in Figure 3.1 (a)) follows the load distribution curve above the NP and the resistance curve below the NP.

The liquefaction of a zone will result in (1) loss of effective stress, which indicates a corresponding loss of side resistance, and (2) loss of volume, which indicates that the zone will reduce in thickness and will potentially show up as settlement of the ground surface. Unless the liquefiable portion of the soil profile is significant, the loss of the side resistance will be negligible. The side resistance will be regained when the seismically imposed liquefaction effects have waned. However, the loss of soil volume, i.e., settlement, may have a significant effect on the pile, depending on whether or not the liquefiable zone is located above or below the NP, as explained as follows.

a) If the liquefiable zone is located above the NP (Figure 3.2), then due to the unloading of the pile, theoretically a small (hardly measurable) temporary elongation of the pile may potentially appear as heave at the pile head. The load distribution curve will translate downward, but the associated small unloading of the pile tip will show a similar upward translation of the resistance curve. The combined effect is that the location of the NP will not change appreciably.
b) When the liquefiable zone is located below the NP (Figure 3.3), the loss of volume in the liquefiable soil zone will increase the amount of settlement at the NP. Therefore, in the absence of supporting tip resistance, increased downdrag (settlement) on the pile by the amount of the reduction in the height of the liquefied soil zone will result. The increase in

the pile tip penetration will increase the tip resistance, which will lower the NP and offset some of the liquefaction settlement for the pile (Figure 3.3).

c) When the liquefiable zone is located below the pile tip, no change will occur with regard to the side resistance and tip resistance and the location of the NP relative to the pile. However, the loss of volume in the liquefied zone will result in a corresponding settlement of the soil around the pile and, therefore, also of the pile.

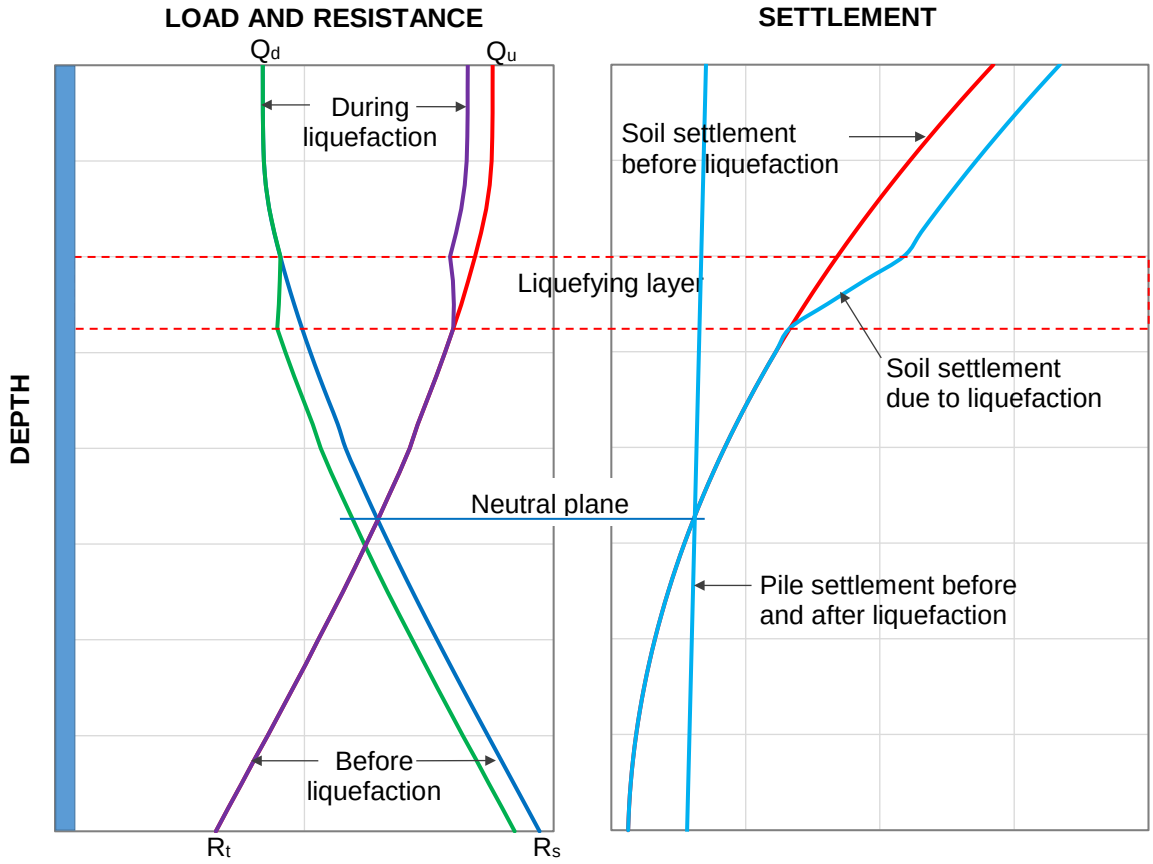

Figure 3.2. Schematic diagram of typical responses when the liquefying zone is located above the neutral plane.

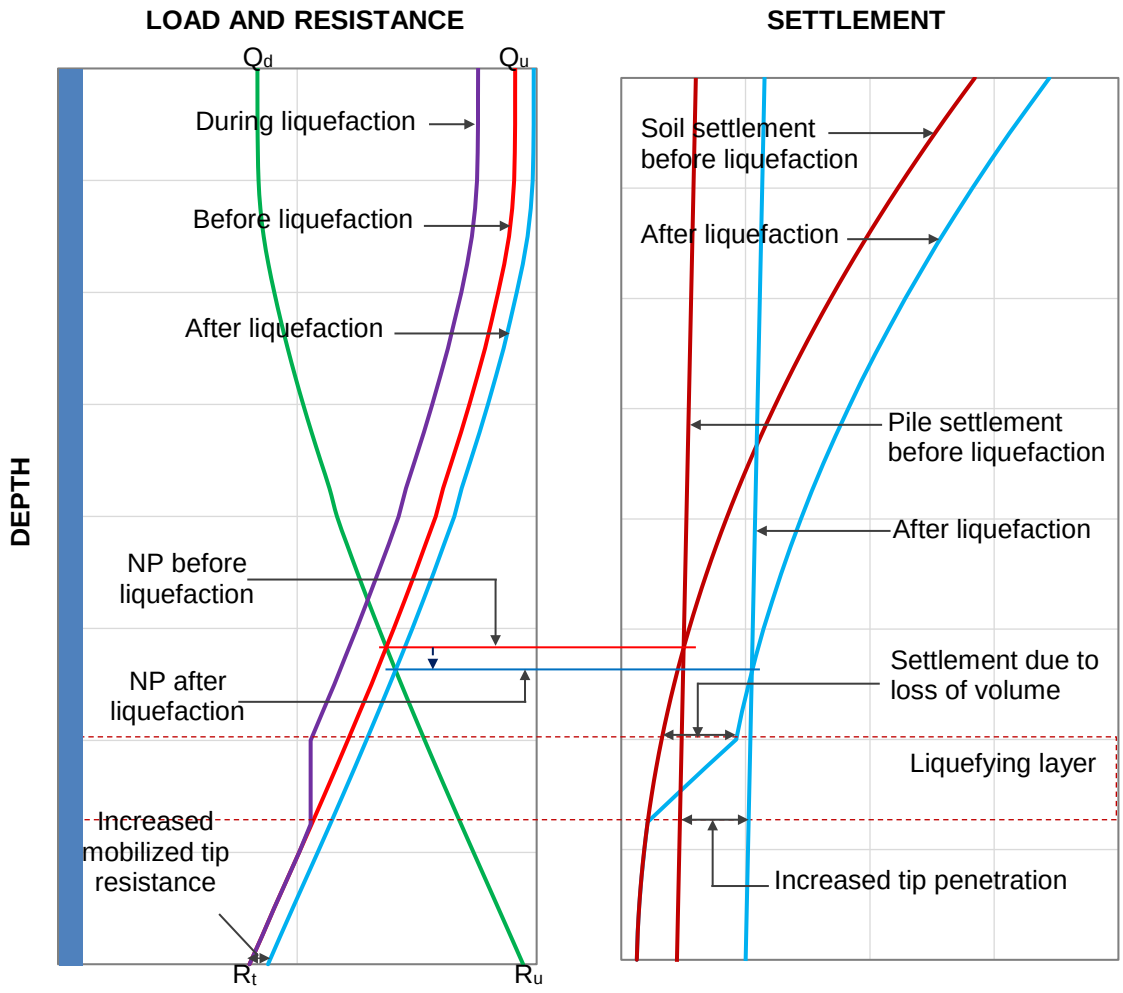

Figure 3.3. Schematic diagram of typical responses when the liquefying zone is located below the neutral plane.

3.3 THE MODIFIED UNIFIED METHOD FOR DRILLED SHAFTS

The unified method that was modified by Fellenius and Siegel (2008) and discussed in Section 3.2, needed to be modified further in order for it to be applied for drilled shafts by including their self-weight as well the potential for the presence of multiple liquefiable layers. In addition, consideration must be given to the two different schools of thought that relate to the development of negative side resistance before liquefaction. The first approach (Case I), which is preferred by AASHTO, assumes that negative side resistance is not present prior to liquefaction, especially in

sandy soils. The other school of thought (Case II), suggested by Fellenius (1984, 2004, 2014), assumes that due to creep and other phenomena, a drilled shaft will experience some downdrag settlement (typically 0.4 inch) before liquefaction.

The methodology that was used in this study to modify the unified method further is presented and developed in a step-by-step manner in Section 3.3.1.

3.3.1 STEP-BY-STEP ANALYSIS PROCEDURE FOR FURTHER MODIFICATION OF UNIFIED METHOD

Step 1: Prepare input data.

(i) Properties of the soil: The input data for the soil properties include layer thickness, saturated unit weight, groundwater location, and information about liquefaction characteristics. The available Standard Penetration Test (SPT) data (N or N_{60}) or any other similar test data can be used to evaluate the tip resistance and side resistance of the shaft.

(ii) Properties of the shaft: The input data for the shaft properties include the length (L), diameter (D), and dead load (DL).

Step 2: Estimate the shaft resistance and tip resistance and plot the load-resistance curves.

The primary method used to provide information about the distribution of the side resistance and tip response is to obtain results from a static loading test. The second best method is to obtain results from *in situ* cone penetrometer tests, and lastly, from SPT boreholes using N-values. Such SPT N-values are affected significantly by several variables, and therefore, using SPT N-values as inputs for calculations of any kind leads to a great variation in output. Nonetheless, in the absence of a more reliable method, the obtained N-values can be applied to pile response analysis.

With regard to shaft resistance, Kulhawy and Chen (2007) proposed using the basic soil parameter method by applying Equations 3.1a through 3.1d. Similarly, tip resistance can be

calculated using Equation 3.2. The β-method proposed by O'Neill and Reese (1999) thus was replaced by the approach presented by Kulhawy and Chen (2007) in AASHTO (2014) because the O'Neill and Reese approach did not account for the variation in N-values or effective stress in calculating the β coefficient. The shaft resistance can be calculated using Equations 3.1.a and b.

$$r_s = \beta \sigma'_v \qquad [3.1a]$$

in which

$$\beta = \left(1 - sin\varphi'_f\right)\left(\frac{\sigma'_p}{\sigma'_v}\right)^{\sin\varphi'_f} tan\varphi'_f \qquad [3.1b]$$

where

β = effective stress correlation coefficient (dimensionless),

φ'_f = soil friction angle (°),

σ'_p = effective vertical stress,

σ'_v = vertical effective stress at mid-depth of the soil layer.

According to Kulhawy and Chen (2007), the friction angle, φ'_f, can be calculated using corrected SPT N-values (values adjusted for effective overburden stress), $(N_1)_{60}$, using Equation 3.1c.

$$\varphi'_f = 27.5 + 9.2 \log[(N_1)_{60}] \qquad [3.1c]$$

The effective vertical stress, σ'_p, is calculated using Equation 3.1d:

$$\frac{\sigma'_p}{p_a} = 0.47\ (N_{60})^m \qquad [3.1d]$$

where

m = 0.6 for clean quartzitic sands and 0.8 for silty sand to sandy silt,

p_a = atmospheric pressure (same units as σ'_p: 2.12 ksf or 14.7 psi).

The 'target' shaft tip resistance (*ksf*) for drilled shafts in sandy soils (Brown et al. 2010) is calculated using Equation 3.2:

$$r_t = 1.2\ N_{60} \quad for\ N_{60} \leq 50 \qquad [3.2]$$

where

N_{60} = average SPT blow count (corrected only for hammer efficiency) in the design zone under consideration (blows/ft).

The target shaft tip resistance is based on measured base resistance values obtained from compression load tests of drilled shafts with clean bases at settlements equal to five percent of the base diameter. The shaft tip displacement response to the load is assumed to follow the variation shown in Figure 3.4 (O'Neill and Reese 1999).

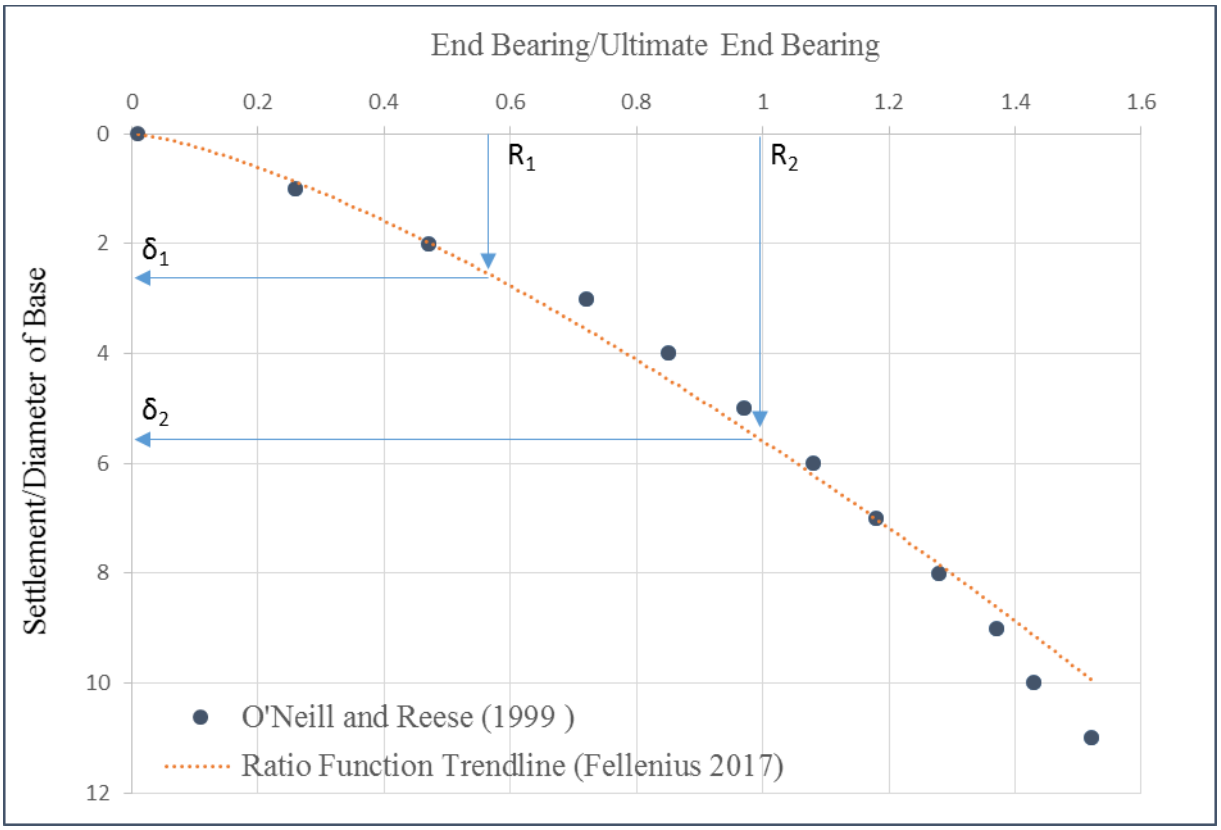

Figure 3.4. Toe displacement response to end bearing load. The data points are from the curve suggested by O'Neill and Reese (1999), and the dotted curve is fitted to the data using Ratio Function (Fellenius 2014).

The fit of the curve to the experimental measured data presented by O'Neill and Reese (1999) can be obtained using a ratio function, as expressed by Equation 3.3 (Fellenius 2014):

$$\frac{R_1}{R_2} = \left(\frac{\delta_1}{\delta_2}\right)^{\theta}, \qquad [3.3]$$

where

R_1 and R_2 = referenced tip resistance; one value usually is chosen to serve as the target value, e.g., the R_2 in Figure 3.4.

δ_1 and δ_2 = movement mobilized at R_1 and R_2, respectively.

θ = exponent potentially ranging from a small value through unity; typical shaft tip values for sand usually range from 0.5 through 0.8. Here, the fit was obtained by $\theta = 0.73$.

Note that, for side resistance, the ratio function is often not the most applicable function and that hyperbolic and other functions could be chosen (Fellenius 2014). Once suitable functions for the tip and side resistance are established, the full load-movement curve of the shaft can be calculated as fitted to the target load-movement value of the static loading test, back-analyzed or predicted, as the case may be. In the current approach, we assume that the tip resistance develops mainly after the side resistance is fully mobilized to its capacity.

At the elevation of the drilled shaft head, the load equals the dead load (DL) and then increases due to the accumulated negative side resistance. The load distribution along the shaft can be calculated using Equations 3.4a and 3.4b.

$$Load_{(z=z_0)} = DL \qquad [3.4a]$$

$$Load_{(z+dz)} = Load_{(z)} + \underbrace{\overbrace{d_z r_{s\left(z+\frac{dz}{2}\right)} P_s}^{side\ resistance\ term} + \overbrace{(w)dz}^{shaft\ unit\ weight\ term}}_{\Delta Load_z} \qquad [3.4b]$$

$$where \qquad r_{s\left(z+\frac{dz}{2}\right)} = \beta_{\left(z+\frac{dz}{2}\right)} \sigma'_{\left(z+\frac{dz}{2}\right)}.$$

P_s is the perimeter of the shaft, and w is the unit weight of the shaft per length.

In integral form, Equation 3.4 can be rewritten as Equation 3.5:

$$Load_{(z)} = DL + \int_{z_0}^{z} \left[r_{s_{(z)}} P_{s_{(z)}} + w_{(z)} \right] dz \qquad [3.5]$$

where z_0 is the elevation of the shaft head.

The resistance curves can be determined using Equations 3.6 through 3.9 for the two cases described in the following.

Case I: No negative side resistance develops before liquefaction.

In Case I, the location of the NP is at the head of the drilled shaft, and the resistance at the head of the shaft would equal the dead load, as expressed by Equation 3.6a:

$$Resistance_{(z@head)} = Dead\ Load. \quad [3.6a]$$

At depths below the head of the shaft, the resistance can be calculated by subtracting the incremental side resistance, as expressed by Equation 3.6b:

$$Resistance_{(z+dz)} = Resistance_{(z)} - \underbrace{d_z r_{s\left(z+\frac{dz}{2}\right)} P_s}_{\Delta Resistance_{(z)}} \geq 0 \quad [3.6b]$$

In integral form, Equation 3.6 can be rewritten as Equation 3.7:

$$Resistance_{(z)} = DL - \int_{z_0}^{z} r_{s(z)} P_{s(z)}\, dz \geq 0 \quad [3.7]$$

where z_0 is the elevation of shaft head.

Case II: Negative side resistance develops along the shaft, with allowance for 0.4-inch downdrag settlement before liquefaction.

In order to plot the resistance curve for Case II, we start with the tip where the resistance is equal to the mobilized tip resistance at an additional settlement of 0.4 inch with respect to short-term settlement. The short-term case is when no negative side resistance develops along the shaft (basically the same as Case I). The short-term tip resistance is the dead load subtracted from the shaft resistance, or zero if the shaft resistance is greater than the dead load (Equation 3.6b).

The ratio function (Figure 3.4) can be used to derive the tip resistance-movement curve. With the values of the tip response known, the movement can be obtained using $\frac{R_1}{R_2} = \left(\frac{\delta_1}{\delta_2}\right)^{\theta}$, where θ is assumed to be 0.73 for the present study of drilled shafts.

If the settlement δ_1 for a specific tip resistance value R_1 is known, then any settlement δ_2 can be estimated knowing the tip resistance R_2. AASHTO (2014) recommends using the O'Neill and Reese (1999) results for calculating settlements, which is similar to the ratio function used here. In sandy soils, the target tip resistance often is considered to be reached when the tip

movement is equal to approximately 5 percent of the shaft diameter; this percentage also is used here as the movement for the target load applied to the ratio function.

The short-term settlement then can be calculated for R_2 = [the target short-term tip resistance] using the ratio function. The 0.4-inch value is added to the short-term settlement and, using the ratio function, the mobilized tip resistance at this settlement can be calculated, as shown in Equation 3.8a:

$$Resistance_{(z=z_0+L)} = Mobilized\ \ toe\ resistance\ @\ additional\ 0.4\ inch\ tip\ settlement\ after\ short-term\ condition \qquad [3.8a]$$

The resistance at depths above the tip can be calculated by adding the shaft resistance, as shown in Equation 3.8b:

$$Resistance_{(z-dz)} = Resistance_{(z)} + \underbrace{d_z r_{s\left(z-\frac{dz}{2}\right)} P_s}_{\Delta Resistance_{(z)}} \qquad [3.8b]$$

In integral form, Equation 3.8 can be rewritten as Equation 3.9:

$$Resistance(Z) = Resistance_{(z_0+L)} + \int_Z^{z_0+L} r_s(z) P_s(z) dz \qquad [3.9]$$

The intersection of the load and resistance curves is the location of the NP. Figure 3.5 illustrates how Equations 3.4 through 3.9 are used to obtain the load and resistance curves. (Note, the intersection of the load and resistance curves is the location of the NP. However, in an actual case, the transfer from the load curve to the resistance curve is smooth rather than sudden).

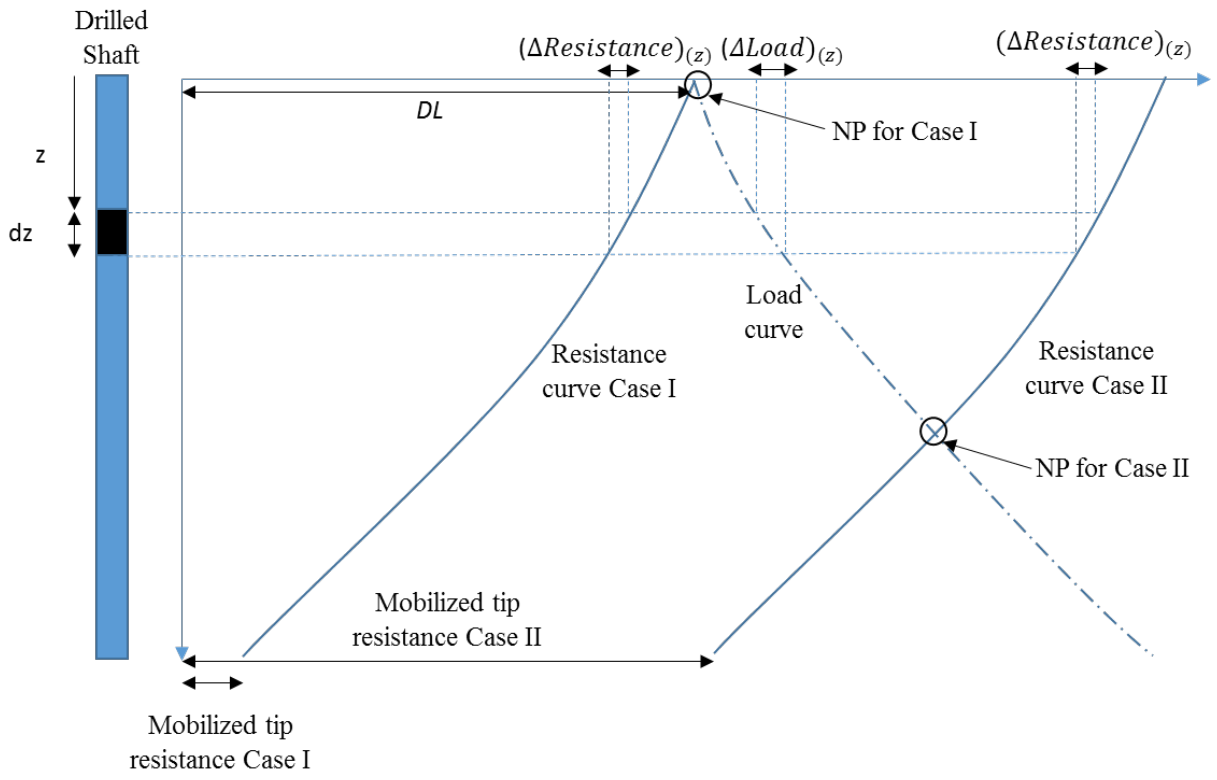

Figure 3.5. Load and resistance curves derived from Equations 3.4 through 3.9.

Step 3: Calculate liquefaction-induced drag load.

For liquefiable layers above the NP, the drag load on the drilled shafts is reduced during a liquefaction event, which theoretically results in a slight elongation of the shaft. On the other hand, if the layers below the NP liquefy, their side resistance during liquefaction is assumed to drop to zero momentarily, as the liquefied layers are assumed to provide no side resistance. (Residual strength is sometimes used in practice, however; see Appendix C.) As such, if only a single liquefiable layer below the NP exists, the load and resistance curves would coincide with the value that corresponds to the bottom of the liquefiable layer, as shown in Figure 3.6. This phenomenon is based on the assumption that soil moves downward with respect to the shaft and that negative side resistance develops all along the shaft above the liquefiable layer. Although the load curve will remain the same above the liquefiable layer, a slight change in the resistance curve will occur,

and the NP would shift accordingly to the lowest location of the liquefiable layer (Figure 3.6). The corresponding decrease in side resistance during liquefaction would be transferred to the tip, resulting in an increase in mobilized tip resistance. After liquefaction, with the increased tip resistance, the resistance curve will adjust accordingly, as shown in Figure 3.6. The drag load can be calculated using Equation 3.10:

$$(Drag\ Load) = \int_{z_0}^{z_{NP}} r_{s(z)} P_{s(z)} dz \qquad [3.10]$$

where z_{NP} indicates the depth of the NP. Equation 3.10 can be used to calculate the drag load before, during, and after liquefaction by substituting the appropriate z_{NP} for any of these cases.

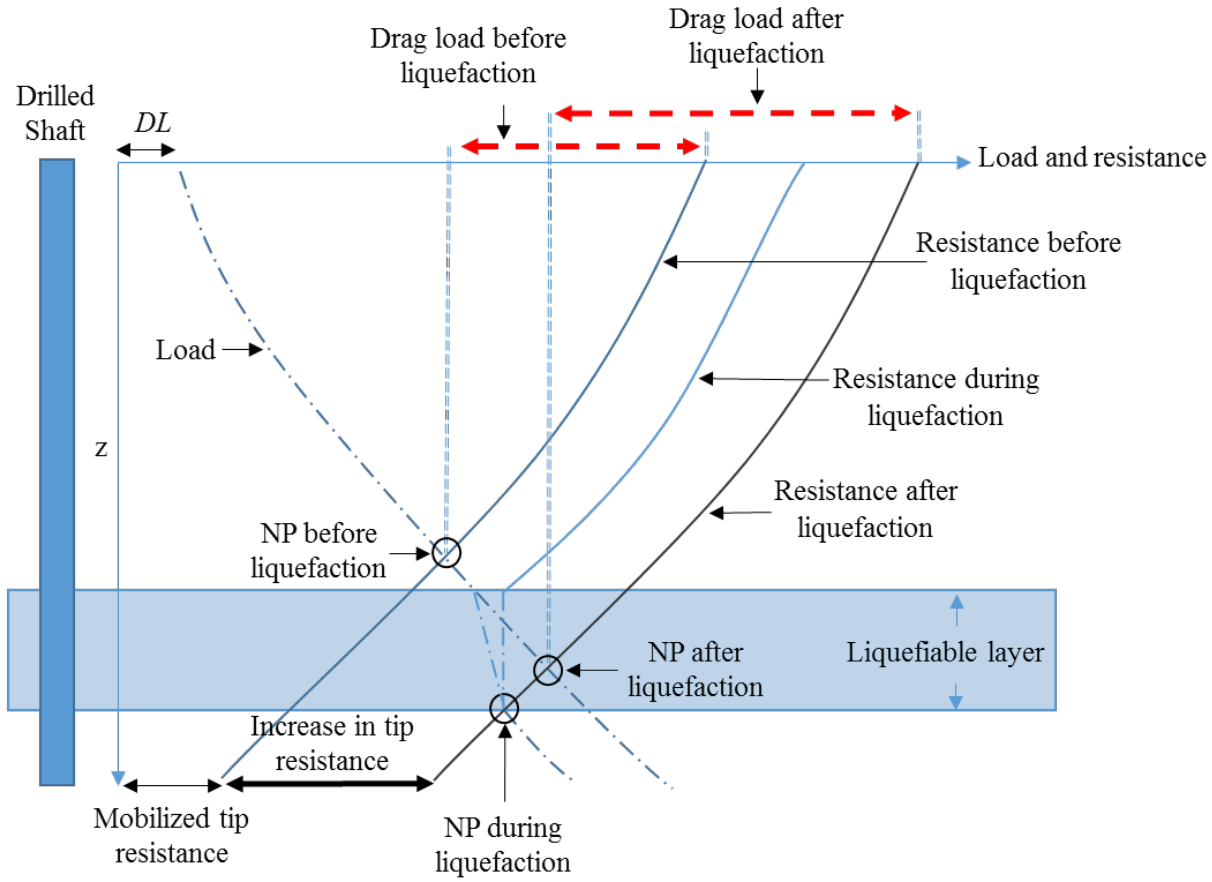

Figure 3.6. Calculation of drag load and increase in tip resistance after liquefaction.

Note that, in the liquefiable layer, the load curve during liquefaction would be an inclined line when considering only the weight of the shaft and making the side resistance equal to zero. If the weight of the drilled shaft is ignored, the load and resistance curves will coincide along the liquefiable layer.

The drag load, which is the summation of the negative side resistance along the shaft, should be distinguished from the increase in the mobilized tip resistance that is due to liquefaction. The drag load affects the structural design of the shaft, whereas the increase in the mobilized tip resistance due to liquefaction controls the geotechnical response of the shaft (i.e., settlement). In this step, the drag load and the mobilized tip resistance variations are calculated, and the corresponding settlement is calculated in the next step.

Step 4: Calculate liquefaction-induced downdrag.

The liquefaction-induced downdrag is calculated based on the increase in tip resistance. To estimate the amount of downdrag settlement, the relationship between the tip resistance and corresponding settlement should be known. In the absence of actual values from load test data, the load-movement (q-z) function (e.g., see Fellenius 2004) discussed in Step 2 can be used.

The settlement of the shaft can be calculated for three different cases based on the probable negative side resistance development:

- Short-term: No negative side resistance develops along the shaft.
- Probable long-term after liquefaction: The negative side resistance is assumed to be fully developed along the shaft above the NP after liquefaction. The resistance curve after liquefaction should be used to find the NP. Note that the resistance curve that matches the increased tip resistance due to liquefaction is used to find the NP.
- Ultimate case: The side resistance is negative all along the shaft.

When a load is applied to a drilled shaft, the side resistance and tip resistance mobilize based on the capacity of the shaft and the magnitude of the applied load. In the current approach, our assumption is that the tip resistance develops mainly after the side resistance is fully mobilized to its capacity. The short-term condition is when no negative side resistance exists and the load is assumed to transfer first to the side resistance of the shaft, and the remaining load, if any, transfers to the tip resistance of the shaft. (This is a simplified approach used in absence of load-settlement test, but provides a very good estimation in case of drilled shafts.)

Downdrag settlement before liquefaction can occur due to the lowering of the water table, the compression of materials on the top layers, placing fill after installing shafts, and/or previous earthquakes. In these cases, the negative side resistance is assumed to develop based after 0.4-inch settlement, and the resistance curve that matches the mobilized tip resistance is used for the before-liquefaction case. If no negative side resistance is probable prior to liquefaction, then the liquefaction-induced downdrag settlement can be calculated assuming the static NP to be at the top of the shaft (i.e., the liquefiable layers are all below the static NP).

3.4 THE JUAN PABLO II BRIDGE CASE STUDY

On February 7, 2010, an 8.8 magnitude earthquake struck in the Pacific Ocean just off the coast of Chile. The earthquake epicenter was located approximately 208 miles southwest of Santiago, 65 miles northeast of Concepción, and 71 miles west-southwest of Talca. The depth of the earthquake hypocenter was 22 miles. The earthquake was characterized by its long duration (>2 minutes) and strong ground motion. Recorded peak ground accelerations at Station Colegio San Pedro, Concepción in the directions of north-south, east-west, and vertical were 0.65 g, 0.61 g, and 0.58 g, respectively (Yen et al. 2011). The earthquake caused surface deformations, structural damage, and loss of life. The transportation network, including roads,

embankments, and bridges, were affected significantly. Geotechnical failures included landslides, uplifts, and widespread liquefaction, especially along the coastline and rivers. Nearly 200 bridges suffered varying degrees of damage to both their superstructures and foundations. Many of these bridges were designed after the mid-1950s in accordance with the AASHTO Standard Specifications for Highway Bridge Design (Yen et al. 2011).

The Juan Pablo II Bridge was opened to the public in 1974. It is the longest vehicular bridge in Chile, connecting the cities of Concepción and San Pedro de la Paz by traversing the Bío-Bío River in the northeast-southwest direction, as shown in Figure 3.7. The bridge is nearly 1.4 miles long, with more than 70 spans that are 72-ft wide and 108-ft long concrete decks, with each span having seven reinforced concrete girders. The span supports are reinforced concrete bents founded on two 8.2-ft diameter and approximately 52-ft long piers (Ledezma et al. 2012). The piers along this bridge settled appreciably at various locations after the earthquake, forcing the bridge to be closed to public access.

Figure 3.8. (a) Column settlement under approach and (b) back face of failure plane at northern end of Juan Pablo II Bridge (Yen et al. 2011).

Figure3.7. Google Earth view of Juan Pablo II Bridge location.

3.4.1 FIELD OBSERVATIONS

A team of researchers that toured the area immediately after the earthquake found evidence of soil liquefaction and lateral spreading at the northeast approach of the bridge. The team reported that the earthquake caused noticeable pier settlement and lateral displacement of the bridge decks, with column shear failure and significant displacements and rotations of the bridge bents (Figure 3.8). Several sand boils were observed near the structure on the north and south sides of the embankment as well as around the piers, as shown in Figure 3.9 (Bray and Frost 2010). The volume loss from such ejecta will have contributed to the soil and pier settlements.

Figure 3.9. Fine-grained material brought to the surface at Juan Pablo II Bridge (Bray and Frost 2010).

Information regarding 16 SPT boreholes (BHs), which were drilled to about a 40-m depth for the post-quake site investigation, showed that the soil profile consisted of sand, sandy silt, silty clay, and silty sand. The groundwater table was at the ground level; we assume that the pore pressure distribution was distributed hydrostatically, as would be the case for the pervious deposit at the site.

The report by the Geotechnical Extreme Events Reconnaissance (GEER) Association (2010) documented that the northeast approach (toward Concepción) of the bridge suffered more than the southwest approach (toward San Pedro). For the study reported herein, two piers, Nos. 1-

2 (BH 16) and 5-6 (BH 10) toward the southwest end of the bridge, and two piers, Nos. 117-118 (BH 3) and 119-120 (BH 7) toward the northeast, were selected.

Figure 3.10 presents a plan view of these support pier locations and closest boreholes. Verdugo and Peters (2010) reported a range of pier settlements along the Juan Pablo II Bridge after the earthquake. The observed settlements of Support Piers 1-2 and 5-6 at the approach toward Concepción and Support Piers 117-118 and 119-120 at the approach toward San Pedro were about 7.9, 15.7, 17.7, and 25.6 inches, respectively.

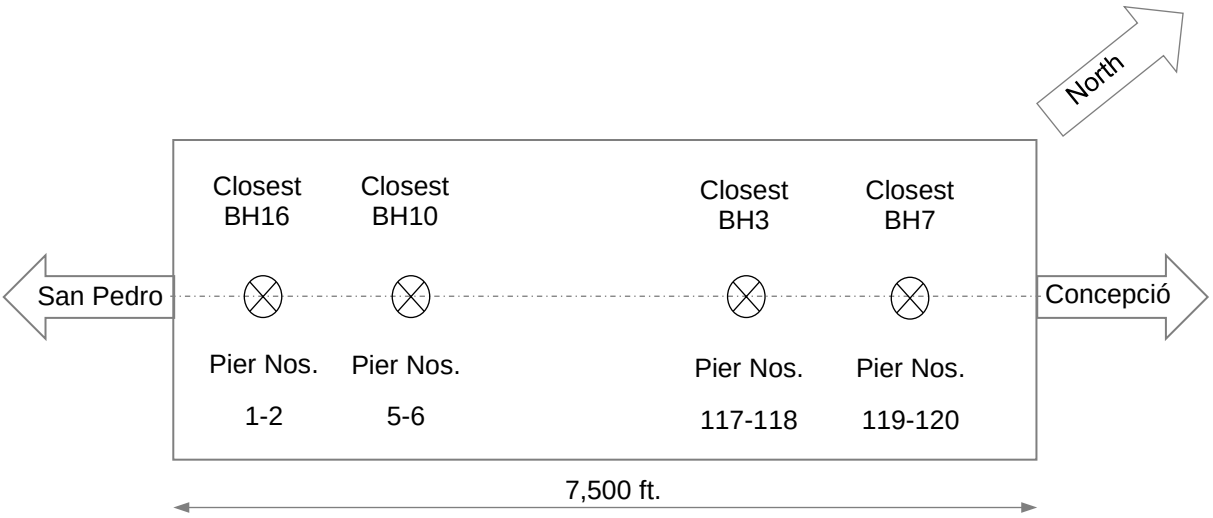

Figure 3.10: Schematic diagram of piers and nearby boreholes along Juan Pablo II Bridge.

Figure 3.11 through Figure 3.18 present the potentially liquefiable zones, as determined using the Youd et al. (2001) procedure. Three potentially liquefiable zones can be found along the lengths of the embedded piers. The first zone is at the ground surface and is about 10-ft thick. The second and third zones are 3-ft and 13-ft thick, respectively, and are located between the depths of 23 ft through 26 ft and 29 ft through 43 ft, respectively. At BH 3, an approximately 3-ft thick liquefiable zone can be identified right at the pile tip. Three additional zones, approximately 6-ft to 25-ft, thick, are present below the pile tip, starting at depths of about 80 ft, 105 ft, and 108 ft,

respectively. Variations in the thickness and location of the liquefiable zones are likely to exist between the boreholes.

SPT blow count correction factors, such as correction for the borehole diameter (C_B), sampler type (C_S), rod length (C_R), and hammer energy ratio (C_E), are assumed to be 1.05, 1.0, 0.85, and 0.85, respectively, and the maximum overburden correction factor (C_N) is 1.7. Fine content variation with depth and normalized SPT N-values, $(N_1)_{60}$, were applied to determine the liquefiable zone identified in Figures 3.11 through 3.18. Additional liquefaction susceptibility key parameters, such as the cyclic stress ratio, ratio of total stress to effective stress (σ_v/σ_v'), and stress reduction coefficient (r_d), are in the ranges of 0.4 to 0.9, 2.0 to 2.2, and 0.4 to 1.0, respectively. Values of $(N_1)_{60}$ below 30 blows/ft were considered representative of a liquefiable zone, as indicated in Figures 3-11 to 3.18. Although the method supposedly applies only to depths above 80 feet, it has been used to delineate the liquefiable zones below 80 feet also.

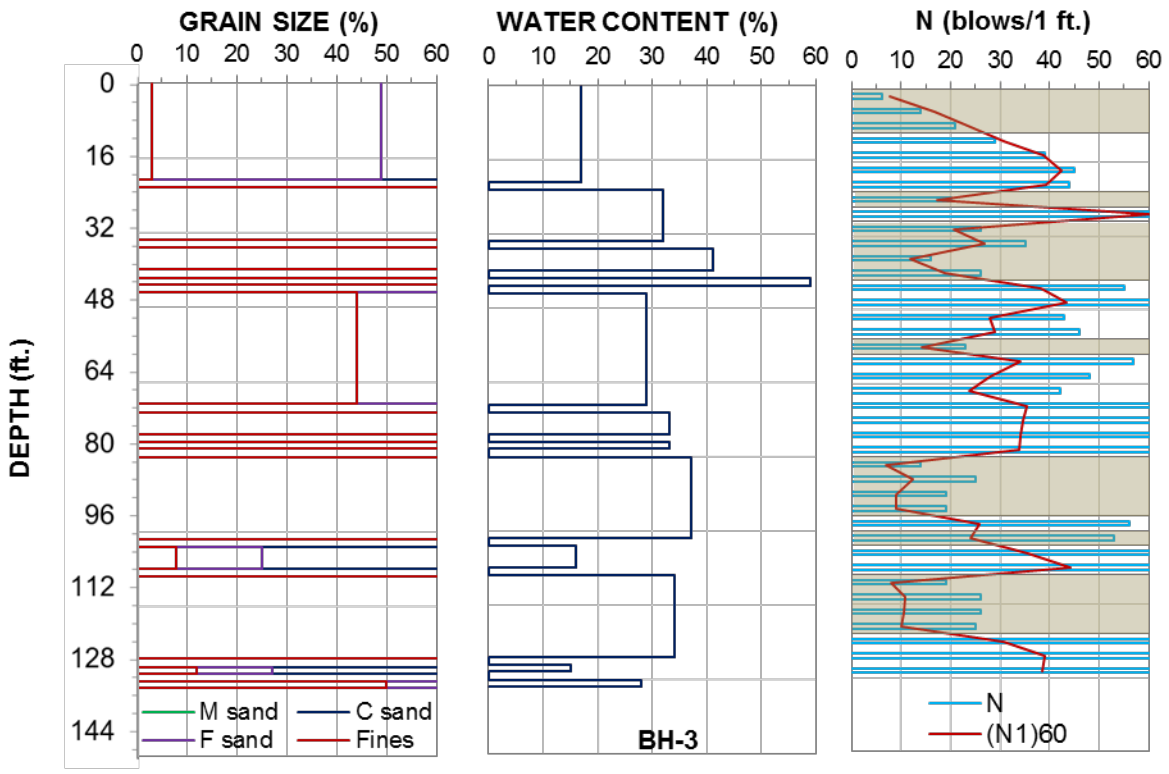

Figure 3.11. Borehole 3 grain size, water content, corrected SPT $(N1)_{60}$, and N-values with depth.

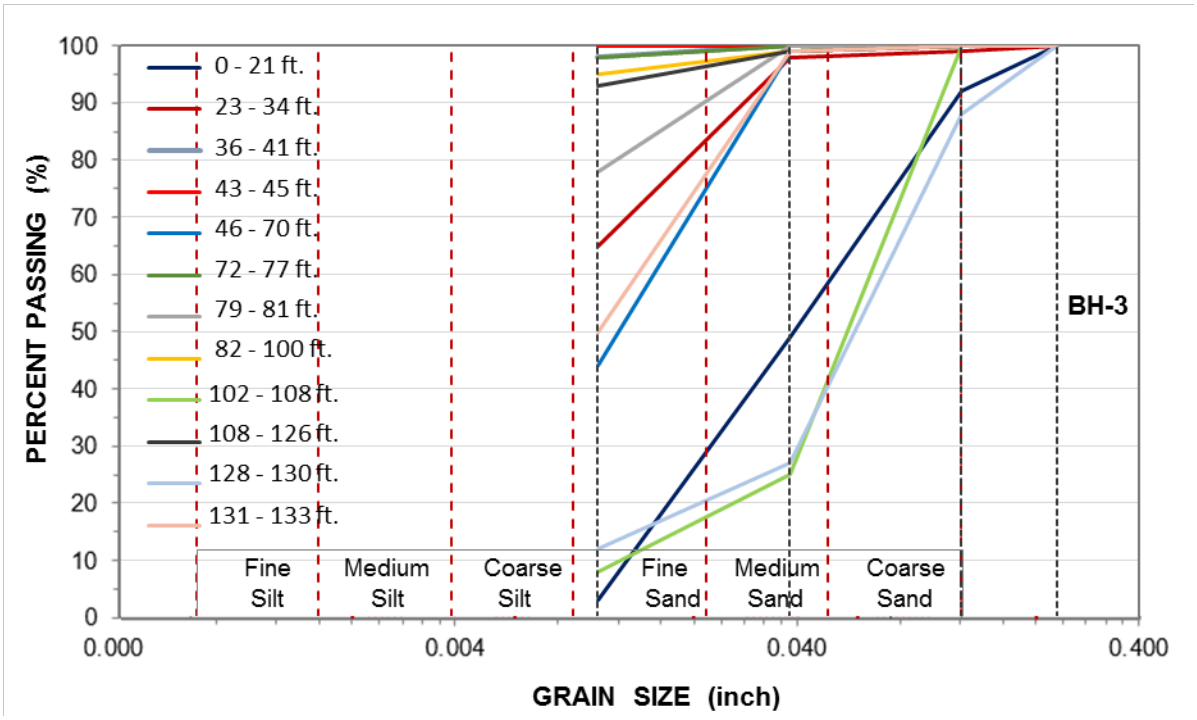

Figure 3.12. Borehole 3 grain size with percent passing #200 sieve.

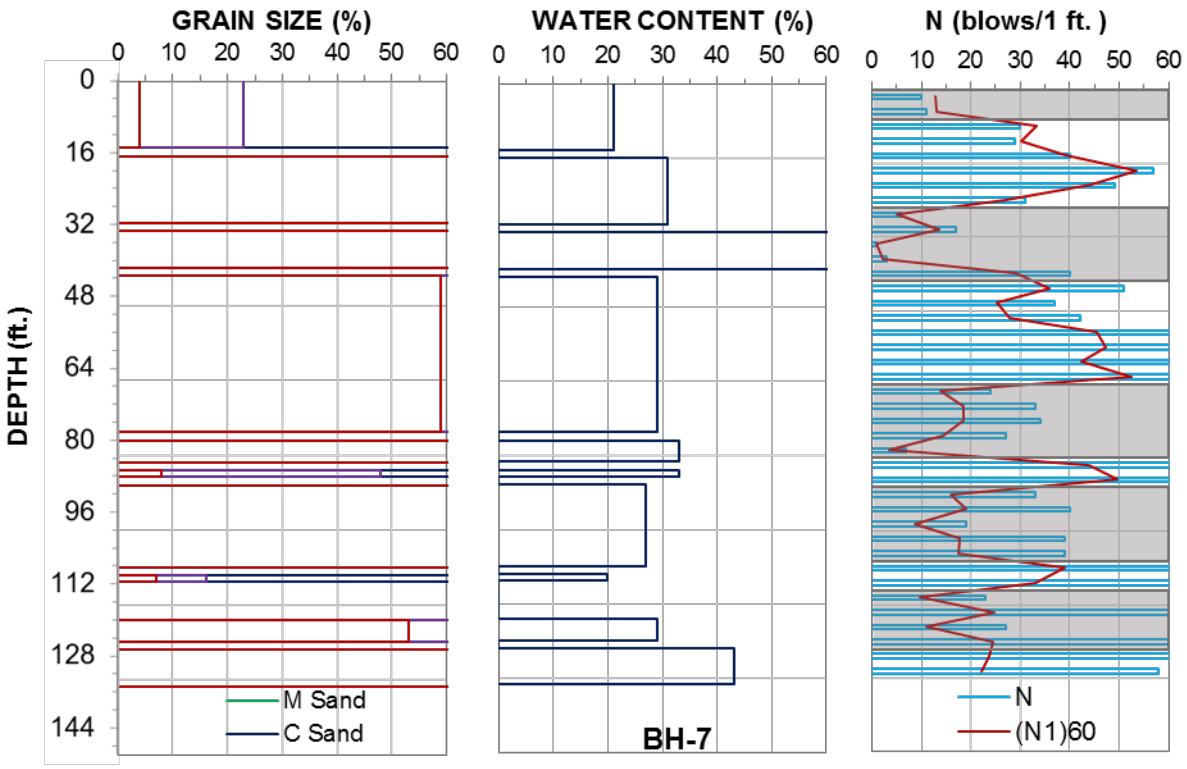

Figure 3.13. Borehole 7 grain size, water content, corrected SPT $(N1)_{60}$, and N-values.

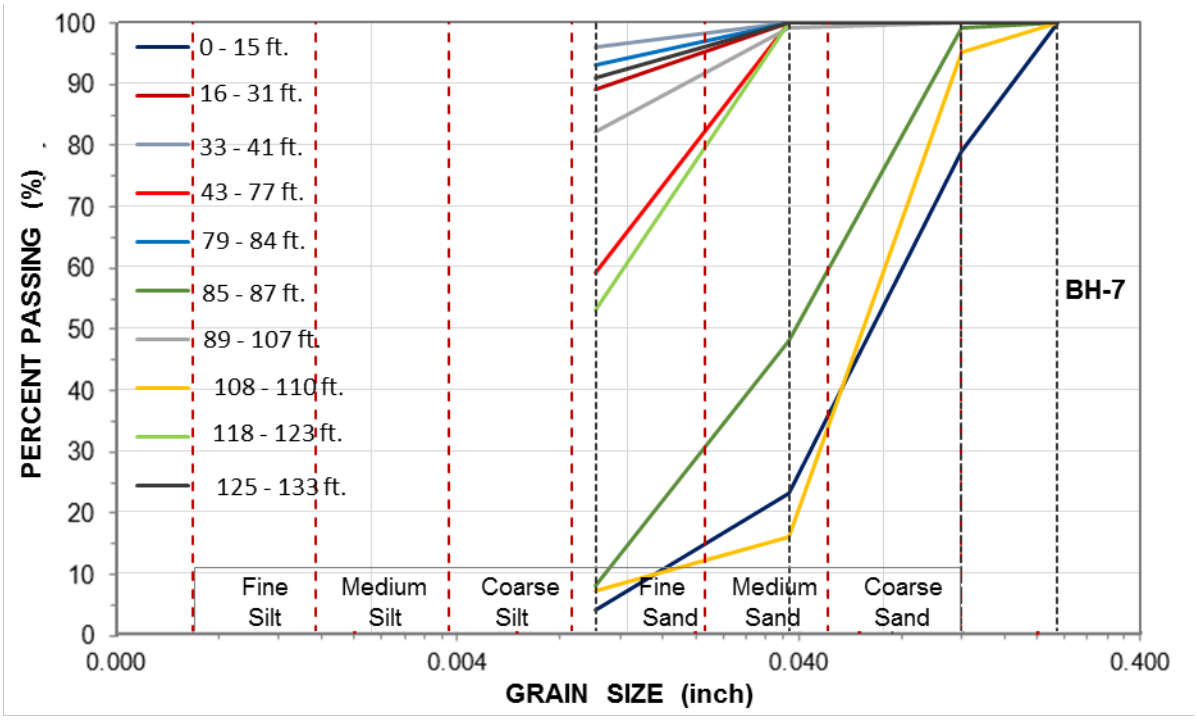

Figure 3.14. Borehole 7 grain size with percent passing #200 sieve.

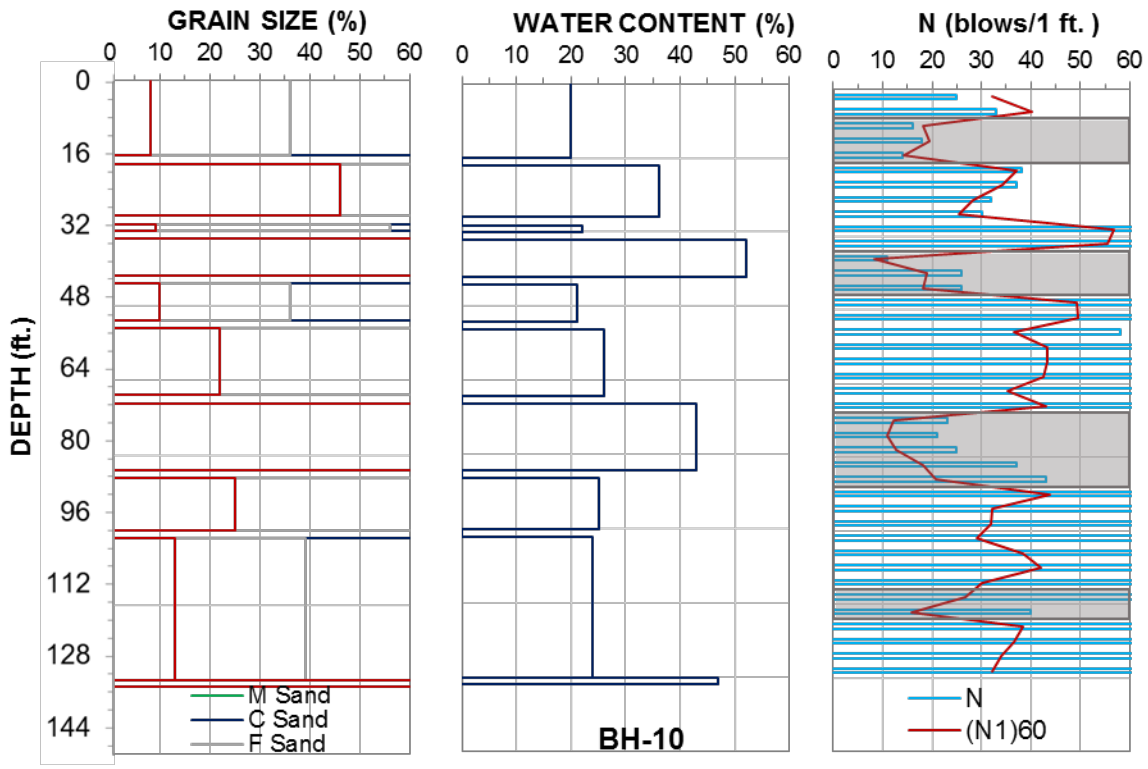

Figure 3.15. Borehole 10 grain size, water content, corrected SPT $(N1)_{60}$, and N-values.

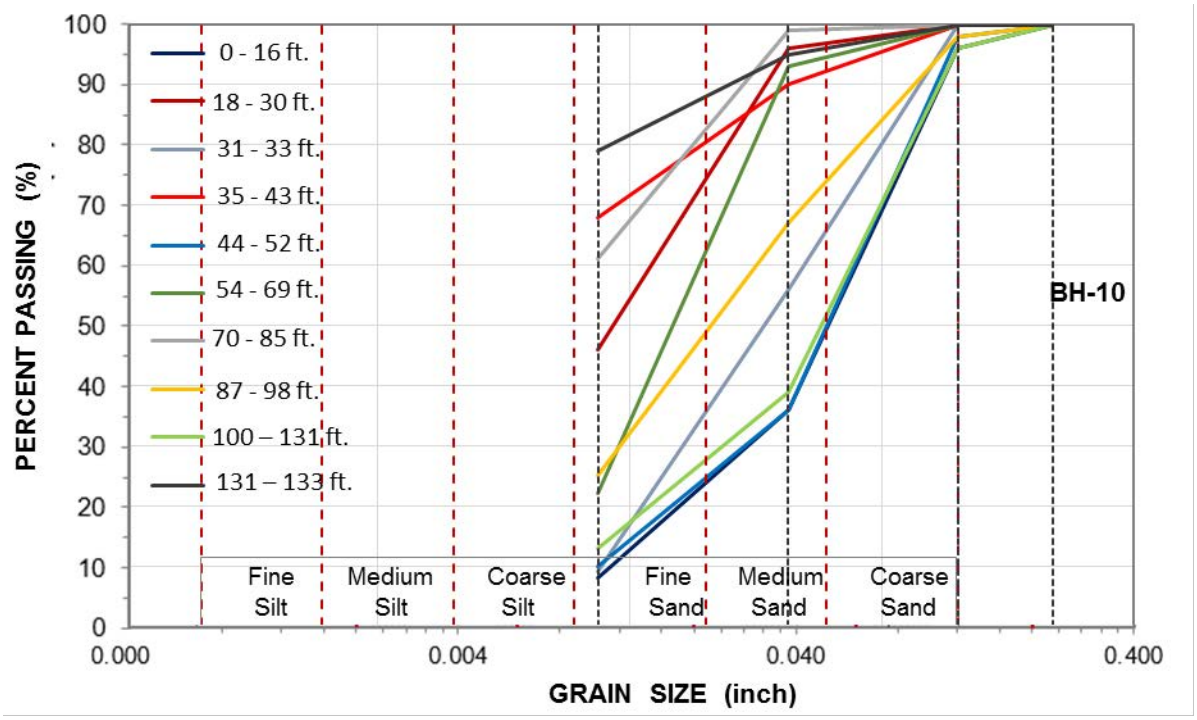

Figure 3.16. Borehole 10 grain size with percent passing #200 sieve.

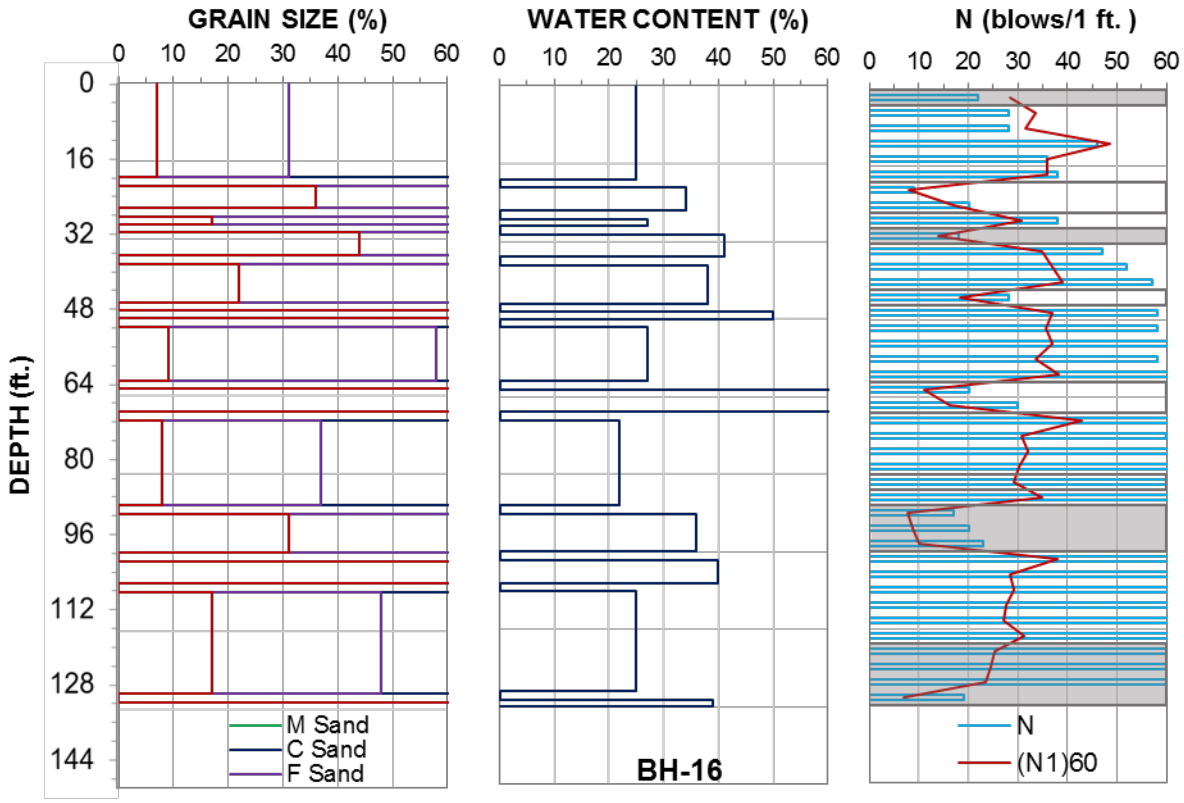

Figure 3.17. Borehole 16 grain size, water content, corrected SPT $(N1)_{60}$, and N-values.

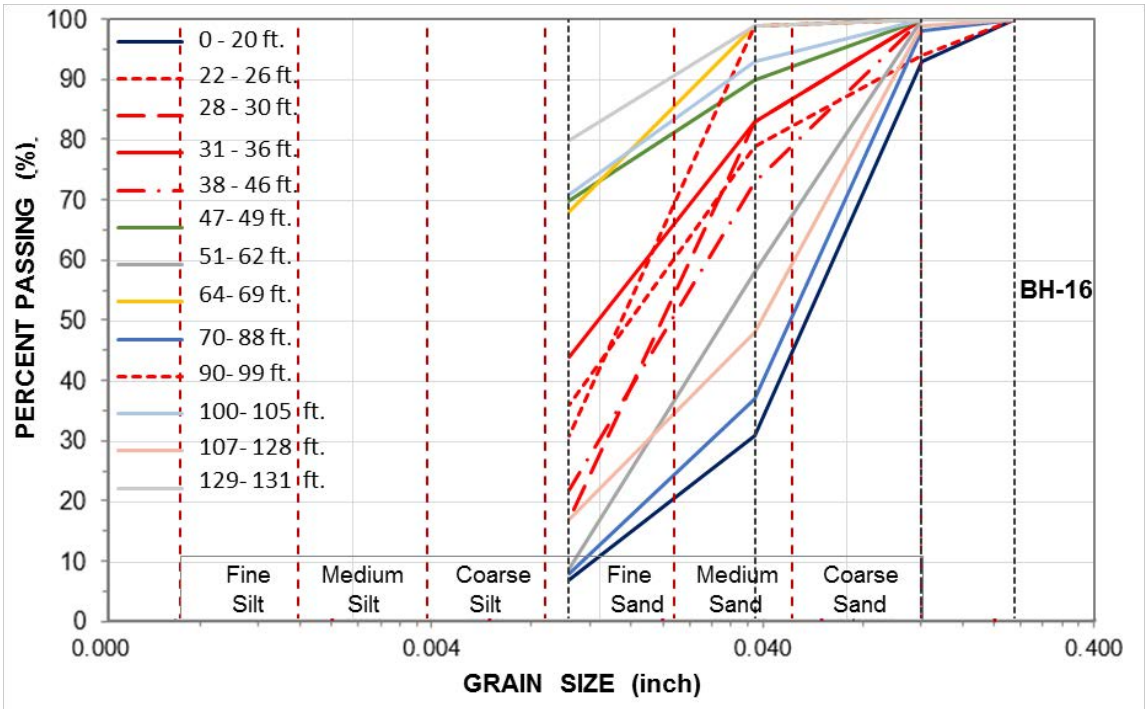

Figure 3.18. Borehole 16 grain size with percent passing #200 sieve.

As mentioned, the borehole records show that the Juan Pablo II Bridge site contained liquefiable zones within the pier embedment length and below the pier tip level. BH 7 includes two liquefiable zones, 6-ft and 16-ft thick, at the ground level and at depths of 26 ft through 42 ft, respectively. Three additional zones with varying thicknesses ranging from 13 ft to 16 ft were identified at depths of 65 ft, 89 ft, and 112 feet. BH 10 also comprises two liquefiable zones between the depths of 6 ft through 16 ft and 36 ft through 46 ft, respectively, within the pier depth. The other two zones were found at depths of 72 ft and 112 ft with thicknesses of 16 ft and 6 feet. BH 16 consists of four liquefiable zones within the pier embedment length; those thicknesses varied from 3 ft to 6 ft between the ground level and depths of 3 ft, 20 ft through 26 ft, 30 ft through 33 ft, and 43 ft through 46 feet, respectively. In addition, four more zones were identified at depths of 62 ft, 82 ft, 89 ft, and 118 ft with thicknesses of 6 ft, 3 ft, 10 ft, and 13 ft, respectively.

3.4.2 SOIL SETTLEMENT

The soil information presented in Figure 3.11 through Figure 3.18 shows the post-quake conditions and identifies potentially liquefiable zones. Tokimatsu and Seed (1987) proposed a correlation for post-liquefaction volumetric compressions of liquefiable zones. Their procedure estimates the volumetric strains from the correlation to $(N_1)_{60}$ and the cyclic stress ratio via a family of curves. The post-liquefaction settlement is calculated by integrating the volumetric strain over the thickness of each liquefiable zone.

For this study, each liquefiable zone was divided into sub-zones with constant SPT N-values. The cumulative post-liquefaction settlement was obtained by summing the settlements of the individual zones. Figure 3.19 shows the distribution of the post-liquefaction settlements calculated at the four borehole locations. It is interesting to note that major settlement occurred below the pier tip level.

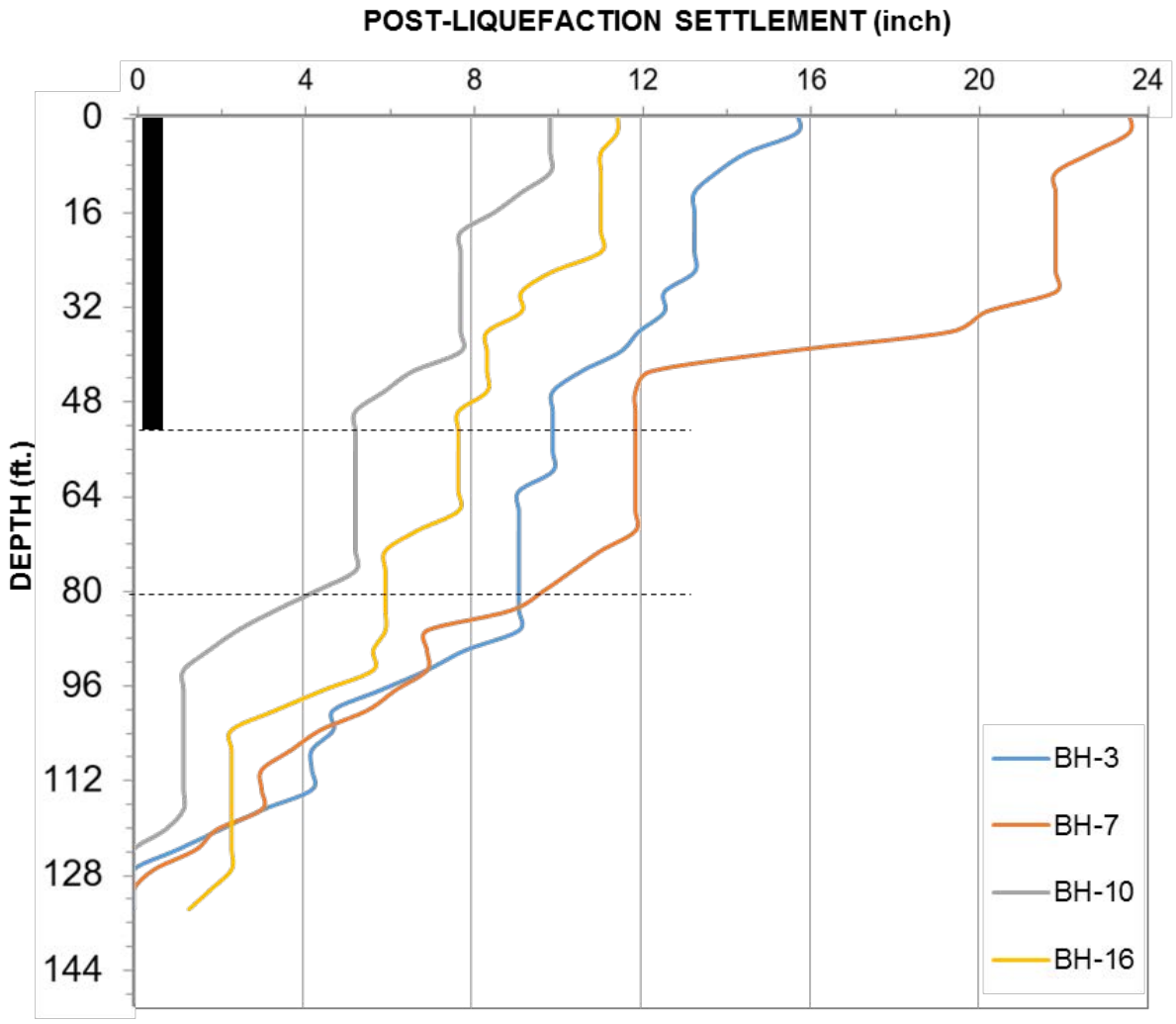

Figure 3.19. Post-liquefaction soil settlement profile near Boreholes 3, 7, 10, and 16 using the Tokimatsu and Seed (1987) procedure.

3.4.3 LIQUEFACTION-INDUCED DOWNDRAG ANALYSIS BASED ON THE MODIFIED UNIFIED ANALYSIS METHOD FOR DRILLED SHAFTS

The proposed method discussed in Section 3.3 was applied in this study to the liquefaction-induced downdrag analysis of the Juan Pablo II Bridge. Pier 117, which is close to BH 3, is analyzed in this section.

Step 1: Prepare input data

Section 3.4.2 presents the soil properties. The average load per pier was estimated to be 2,855 kips, which was calculated based on the weight of the bridge span, girder, wearing surface, and column. The unit weight of the concrete was assumed to be 150 pcf, and the unit weight of the steel was assumed to be 480 pcf. The length of the drill shaft was 52.5 ft and the diameter was 5.2 feet.

Step 2: Calculate the side resistance and tip resistance, and then plot the load and resistance curves.

Immediately after construction, which is a short-term condition, the load would have been supported by side resistance, R_s, acting along the full length of the pier, with the remaining being the mobilized tip resistance, R_t. The calculations were performed based on the groundwater table located at the ground surface, hydrostatic pore pressure distribution, and soil density of 125 pcf. The side resistance of the shaft was calculated using Equation 1, and the load and resistance curves were plotted as shown in Figure 3.20 for both Cases I and II. The NP location can be seen at the intersection of the load and resistance curves.

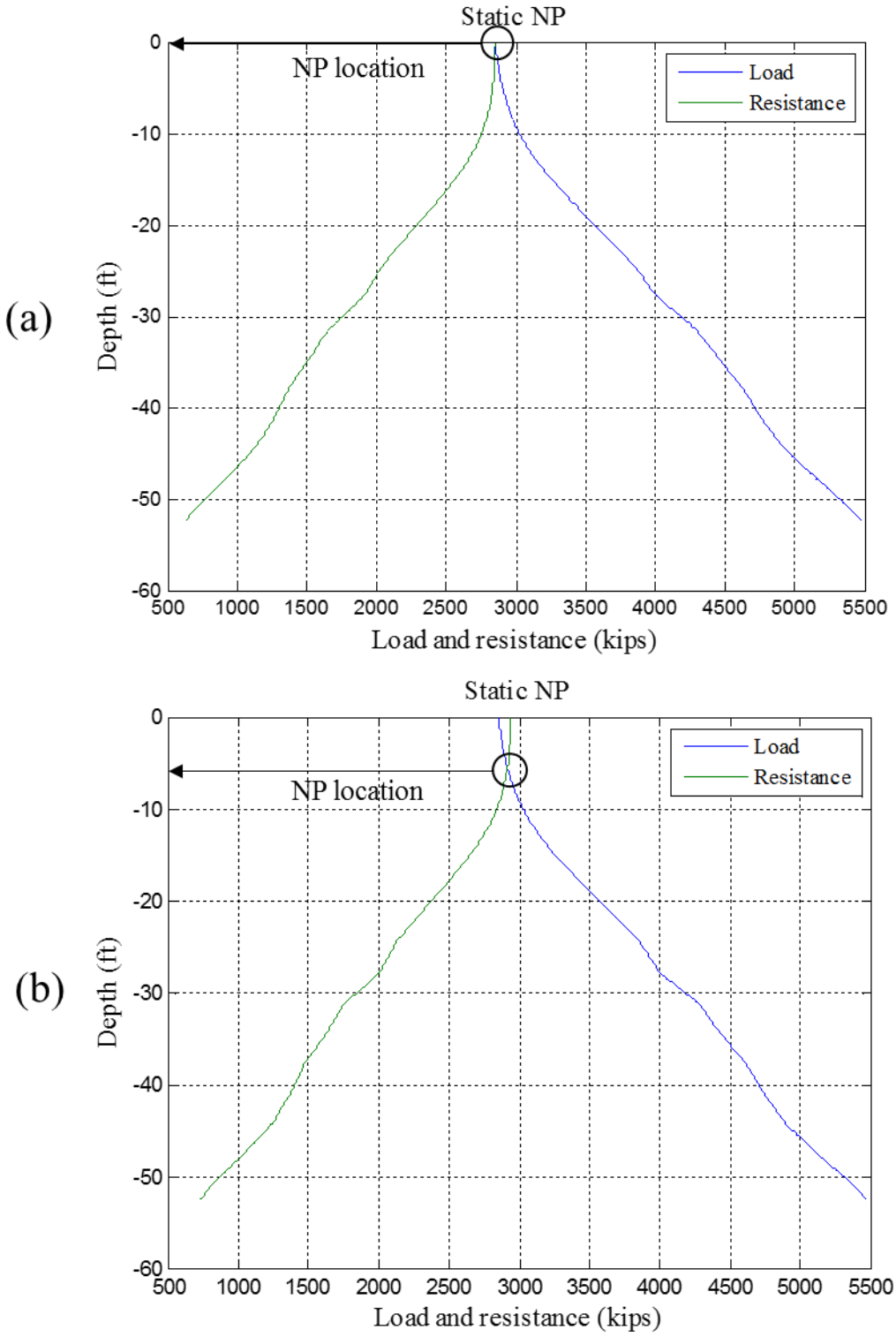

Figure 3.20. Load and resistance curves and neutral plane locations for drilled shafts before liquefaction for (a) Case I and (b) Case II analyses. The NP is located at the drilled shaft head for Case I analysis and at z = -5.4 ft for Case II analysis.

Step 3: Calculate the liquefaction-induced drag load.

Figure 3.21 shows the increase in the tip resistance after liquefaction for the Case I analysis. This figure also shows the location of the NP before, during, and after liquefaction. The drag load after liquefaction and the increase in tip resistance that is due to liquefaction can be calculated using the curves, as shown in the figure. Table 3.1 lists the ultimate drag loads and NP locations after liquefaction. No difference is evident in the calculated drag load between the Case I and Case II analyses.

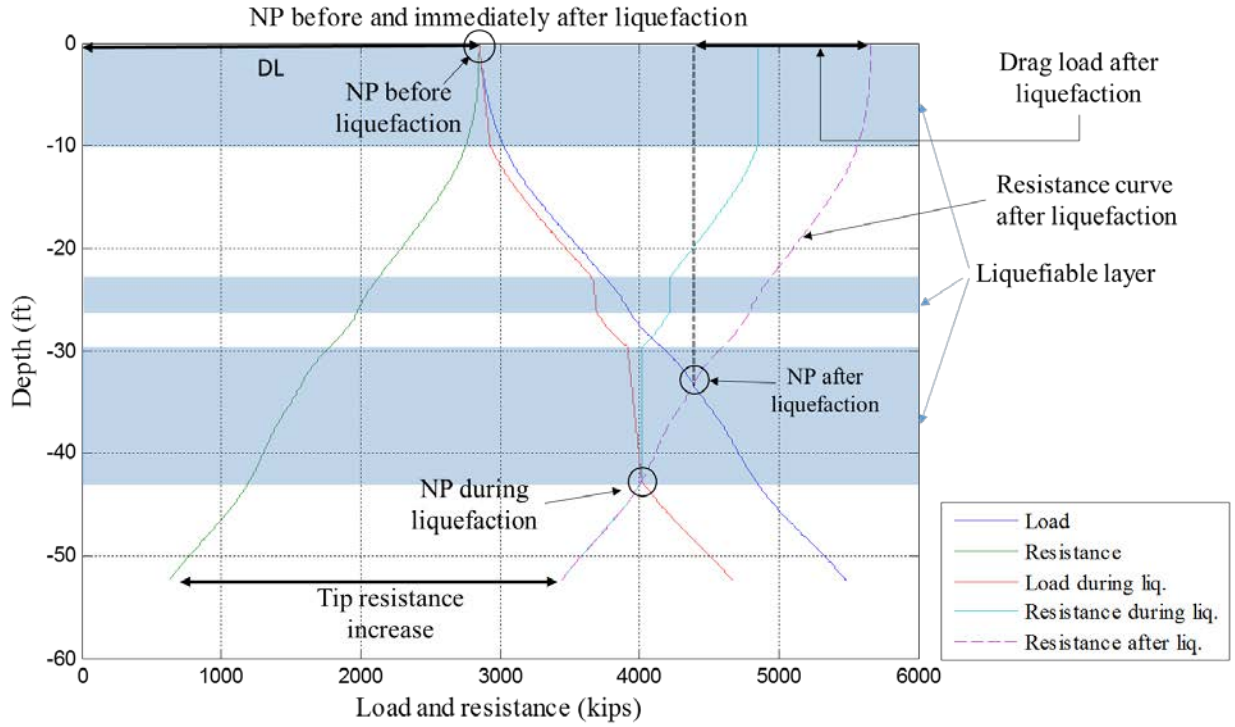

Figure 3.21. Load-resistance curves and neutral plane (NP) locations for different conditions: before, during, and after liquefaction. The load curve is the same before and after liquefaction. During liquefaction, the NP moves to the lowest point of the liquefiable layer. The drag load before liquefaction is zero because the NP is at the head of the shaft for Case I. Case II analysis would be similar; the only difference is the resistance curve before liquefaction, which is shown in Figure 3.20.

Table 3.1. Drag loads for pier 117 of Juan Pablo II Bridge

	Case I	Case II
Max drag load before liquefaction (% of ultimate drag load)	0.0 kips (0%)	24 kips (1%)
Max drag load after liquefaction (% of ultimate drag load)	1,271 kips (57%)	1,271 kips (57%)
Ultimate drag load	2,221 kips	2,221 kips
NP location before liquefaction (ft)	0	-5.4
NP location after liquefaction (ft)	-33.4	-33.4

Step 4: Calculate liquefaction-induced downdrag.

Figure 3.22 shows the load distribution for the Case I analysis where the NP for the short-term condition is at the shaft head. The figure shows a probable long-term condition after liquefaction distribution for a NP located at a depth of about 33 feet. This location corresponds to 3,443-kip tip resistance. The maximum total tip resistance for a NP located right at the tip thus equals 5,486 kips.

Figure 3.22 also includes the variation in tip penetration that was calculated according to Equation 3.3 with an exponent of $\theta = 0.7$. The curve indicates that the short-term and long-term conditions after liquefaction and the maximum long-term shaft tip movements are 0.9 in., 9.6 in., and 18.1 in., respectively. The maximum long-term distribution after liquefaction can occur if the soil around the shaft settles more than the shaft itself. This situation might be the case for the Juan Pablo II Bridge piers, as several liquefiable layers were located below the shaft tips. Moreover, if the sand below the tip, i.e., deeper than 52.5 ft, would have been unaffected by the quake, then the indicated 9.6 in. minus 0.9 in. = 8.5-in. tip movement is the maximum possible movement of the tip due to liquefaction and, therefore, the maximum possible movement also of the pier. No amount of liquefaction-caused soil settlement above the tip, even that due to the soil loss from ejecta (the geyser action and sand boils), would have induced any larger settlement of the piers than that shown in Figure 3.22 for the maximum long-term condition.

As the pier settlements are larger than the probable long-term post-liquefaction settlement, the liquefaction that affected the piers might have caused a final downdrag calculated as 18.1 ft minus 0.9 ft = 17.2 feet. The ultimate downdrag compares well with the pier settlement measured at the site for BH 3, which is 17.7 inches. Assuming that only the probable long-term post-liquefaction settlement (8.5 in.) was due to downdrag, the rest of the settlement (17.7 in. minus 8.5 in. = 9.2 in.) could be due to the effect of liquefaction below the pier tip level. The pier settlement that was the accumulation of volume loss in the various liquefiable zones at and below about 52.5 ft may have resulted in a mere 10-in. settlement (Figure 3.19). Either way, the downdrag settlement played a major role in the observed large pier settlement.

Over a 35-year long term, the sand around the piers will have settled a fraction of an inch, assumed to be 0.4 in., which will have resulted in negative side resistance along the upper part of a drilled shaft and increased the tip resistance. Figure 3.23 presents the Case II analysis results. Table 3.2 lists the downdrag settlements and shows that the Case I and Case II analysis results exhibit practically the same downdrag settlements.

Table 3.2. Downdrag settlements for pier 117 Close to BH 3

	Short-term settlement (inch)	**Long-term downdrag settlement before liquefaction (inch)**	**Long-term downdrag settlement after liquefaction (inch)**	**Ultimate downdrag settlement (inch)**
Case I	0.9	NA	9.6	18.1
Case II	0.9	1.4	9.6	18.1

Pier 1 near BH 16, Pier 5 near BH 10, and Pier 119 near BH 7 also were analyzed using the modified unified method. Table 3.3 provides a summary of the downdrag settlement of the piers, and Table 3.4 provides a summary of the drag loads.

Based on the discussion of the liquefaction-induced settlement for Pier 117, the minimum settlement expected is the downdrag after liquefaction, and the maximum settlement expected is

the ultimate downdrag plus the soil settlement from the layers below the shaft's tip. For Piers 1, 5, and 119, the settlement then is expected to be in the range of 7.5 to 20 in., 6.5 to 15.4 in., and 8.3 to 23.1 in., respectively. The settlement results obtained from the modified unified method are close to the lower bound for Pier 1 (7.9 in.) and close to the upper bounds for Pier 5 (15.7 in.) and Pier 119 (25.6 in.). For Pier 117, the expected settlement range is 8.5 in. to 28.2 in., with the observed settlement (17.7 in.) being in the middle of the expected settlement range.

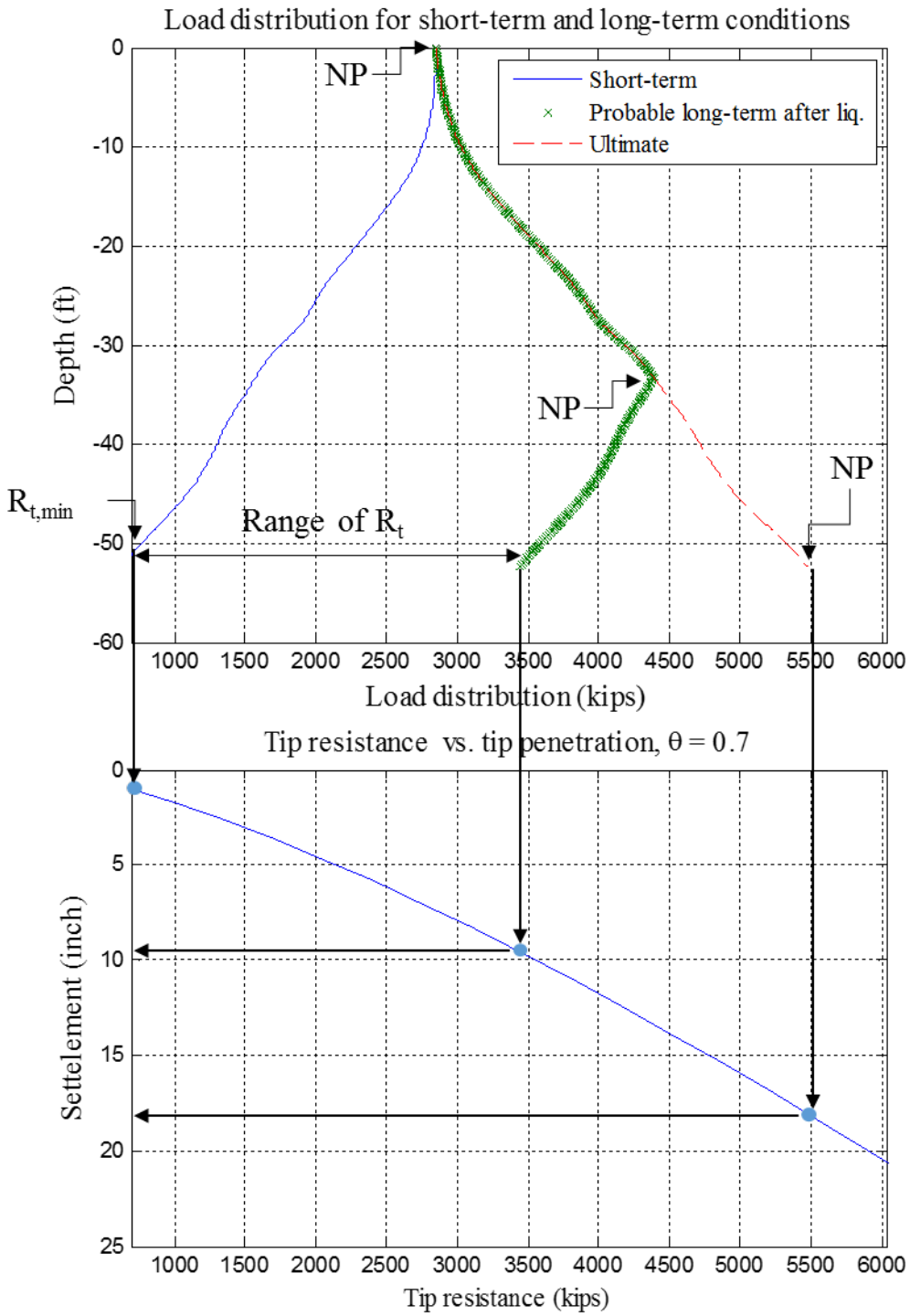

Figure 3.22. Load distribution for short-term and long-term conditions and corresponding pile tip penetration (Case I).

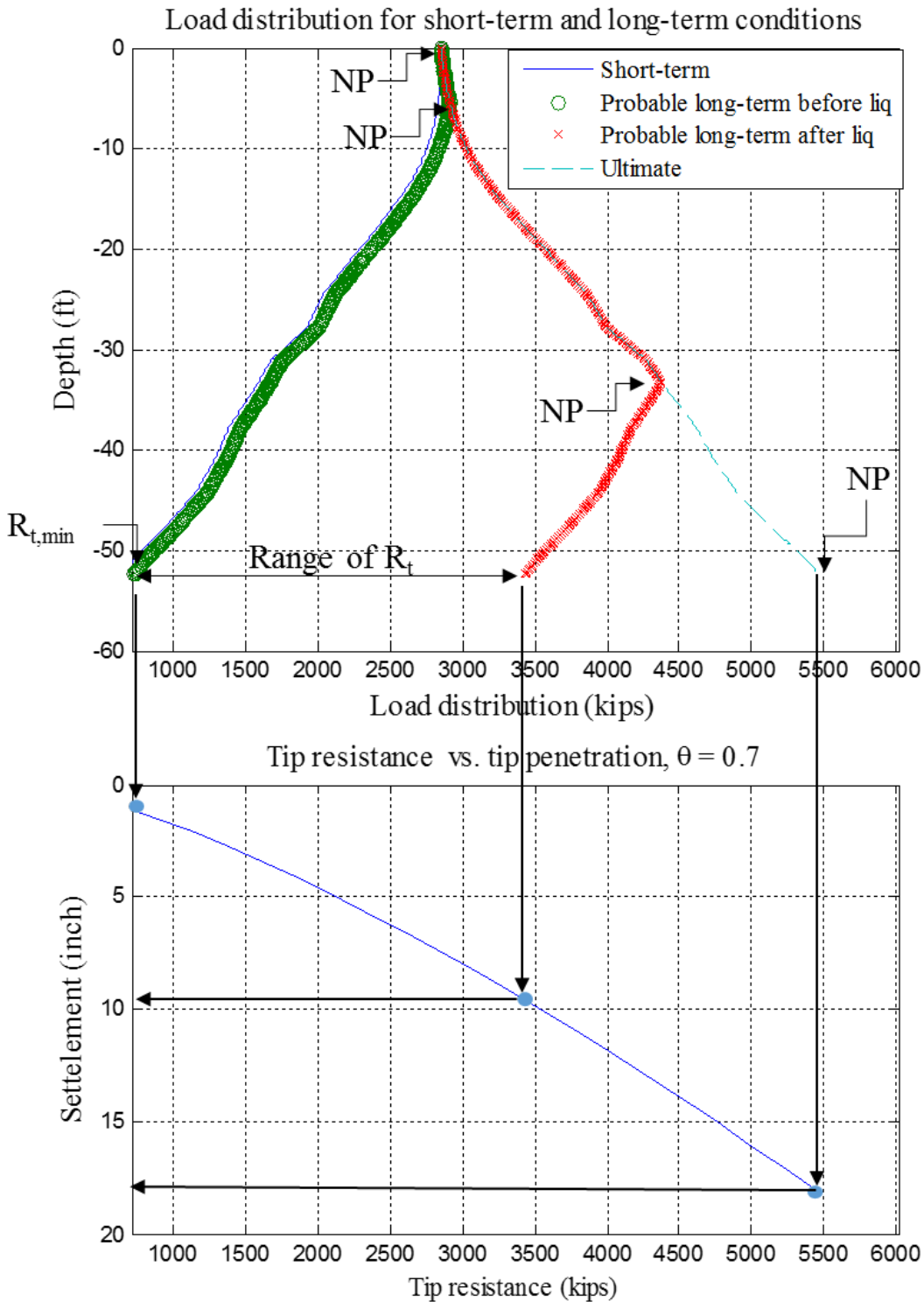

Figure 3.23. Load distribution for short-term and long-term conditions and corresponding pile tip penetration (Case II).

Table 3.3. Downdrag settlements for piers 1, 5, and 119

		Short-term settlement (in.)	Long-term downdrag settlement before liquefaction (in.)	Long-term downdrag settlement after liquefaction (in.)	Ultimate downdrag settlement (in.)
Pier 1	Case I	0.7	NA	8.2	12.0
	Case II	0.7	1.1	8.2	12.0
Pier 5	Case I	0.7	NA	7.2	11.4
	Case II	0.7	1.1	7.2	11.4
Pier 119	Case I	1.7	NA	10.0	17.3
	Case II	1.7	2.1	10.0	17.3

Table 3.4. Drag loads for piers 1, 5, and 119

		Max drag load before liquefaction (% of ultimate drag load)	Max drag load after liquefaction (% of ultimate drag load)	Ultimate drag load (kips)	NP location before liquefaction (ft)	NP location after liquefaction (ft)
Pier 1	Case I	0.0 kips (0%)	1572 kips (71%)	2203	0.0	-41.5
	Case II	55 kips (2.5%)	1572 kips (71%)	2203	-6.1	-41.5
Pier 5	Case I	0.0 kips (0%)	1453 kips (67%)	2176	0.0	-38.0
	Case II	68 kips (3%)	1453 kips (67%)	2176	-6.4	-38.0
Pier 119	Case I	0 kips (0%)	1116 kips (59%)	1897	0.0	-32.1
	Case II	24 kips (1%)	1116 kips (59%)	1897	-5.4	-32.1

CHAPTER 4: LIQUEFACTION-INDUCED DOWNDRAG ANALYSIS: APPLICATION TO DRILLED SHAFTS IN BRIDGES IN WASHINGTON STATE

4.1 INTRODUCTION

The methodology developed in Chapter 3 is illustrated in this chapter for two field site profiles in the State of Washington. The first site is at the interchange between Interstate 5 (I-5) and State Route (SR) 432. The second case involves a bridge site on NE 139th Street near the I-5/I-205 interchange. Both sites contain soils that are potentially liquefiable under seismic loading. The step-by-step application of the methodology is presented in this chapter for one of the piers considered in the original design at the interchange between I-5 and SR 432. For brevity of the main text, additional details of the analysis for all the piers at this site as well as for the piers for the second field case are presented in Appendix B. The analysis results, including downdrag settlements and drag loads, are summarized in this chapter for both case studies.

4.2 I-5/SR 432 TALLEY WAY INTERCHANGE

As part of the initial design considerations, WSDOT engineers originally considered the use of either 2.5-ft diameter closed-toe steel pipe driven piles or an 8-ft diameter drilled shaft to support the bridge structure at the I-5/SR 432 Talley Way interchange. However, given that the site profile consisted of several potentially liquefiable layers, the final foundation design called for shallow spread footings, which were supported on a raft of stone columns, with a buried strut between the piers. Nonetheless, the initial design that considered piles and drilled shafts presents a useful case for illustrating the liquefaction-induced downdrag analysis methodology developed in this study.

Tables 4.1 and 4.2 present the soil parameters along the depth of the profiles for Pier 1 and Pier 2, respectively. Figure 4.1 shows a cross-section of the ramp structure, along with the soil profile and location of the piers at the Talley Way interchange. Figure 4.2 presents the site map for the interchange, which shows the existing topography. The profile at the site consisted mainly of loose sand up to a depth of about 150 feet. To illustrate the steps involved in the application of the proposed method, the design with the 8-ft diameter drilled shaft is analyzed in detail.

Table 4-1. Soil profile under pier 1

Layer	Soil Type	Layer Thickness (ft)	$(N_1)_{60}$	Liquefaction Potential	Eff. Unit Weight (pcf)
1	Sand	11	31	No	56
2	Sand	5	21	No	56
3	Sand	5	2	Yes	48
4	Sand	5	1	Yes	48
5	Sand	12	3	Yes	48
6	Sand	23	3	Yes	48
7	Sand	35	3	Yes	48
8	Sand	10	2	Yes	63
9	Sand	45	3	Yes	53
10	Sand	10	19	No	63

Table 4-2. Soil profile under pier 2

Layer	Soil Type	Layer Thickness (ft)	$(N_1)_{60}$	Liquefaction Potential	Eff. Unit Weight (pcf)
1	Sand	10	10	No	58
2	Sand	5	32	No	58
3	Sand	7	2	Yes	48
4	Sand	10	3	Yes	48
5	Sand	10	2	Yes	48
6	Sand	40	1	Yes	48
7	Sand	30	5	Yes	48
8	Sand	32	3	Yes	48
9	Sand	8	15	No	48
10	Sand	12	19	No	73

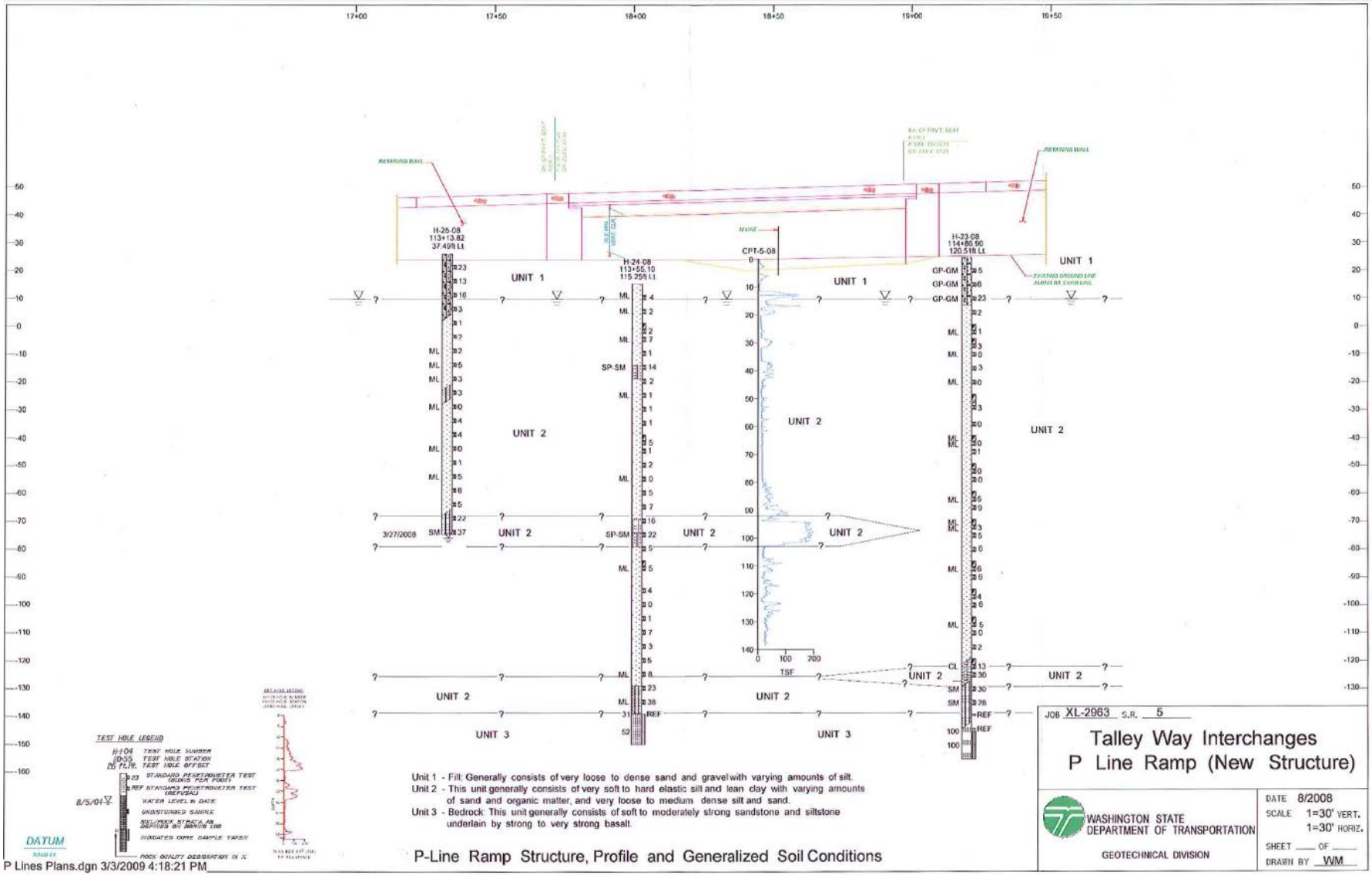

Figure 4-1. Cross-section of ramp structure, soil profile, and location of piers for Talley Way interchange.

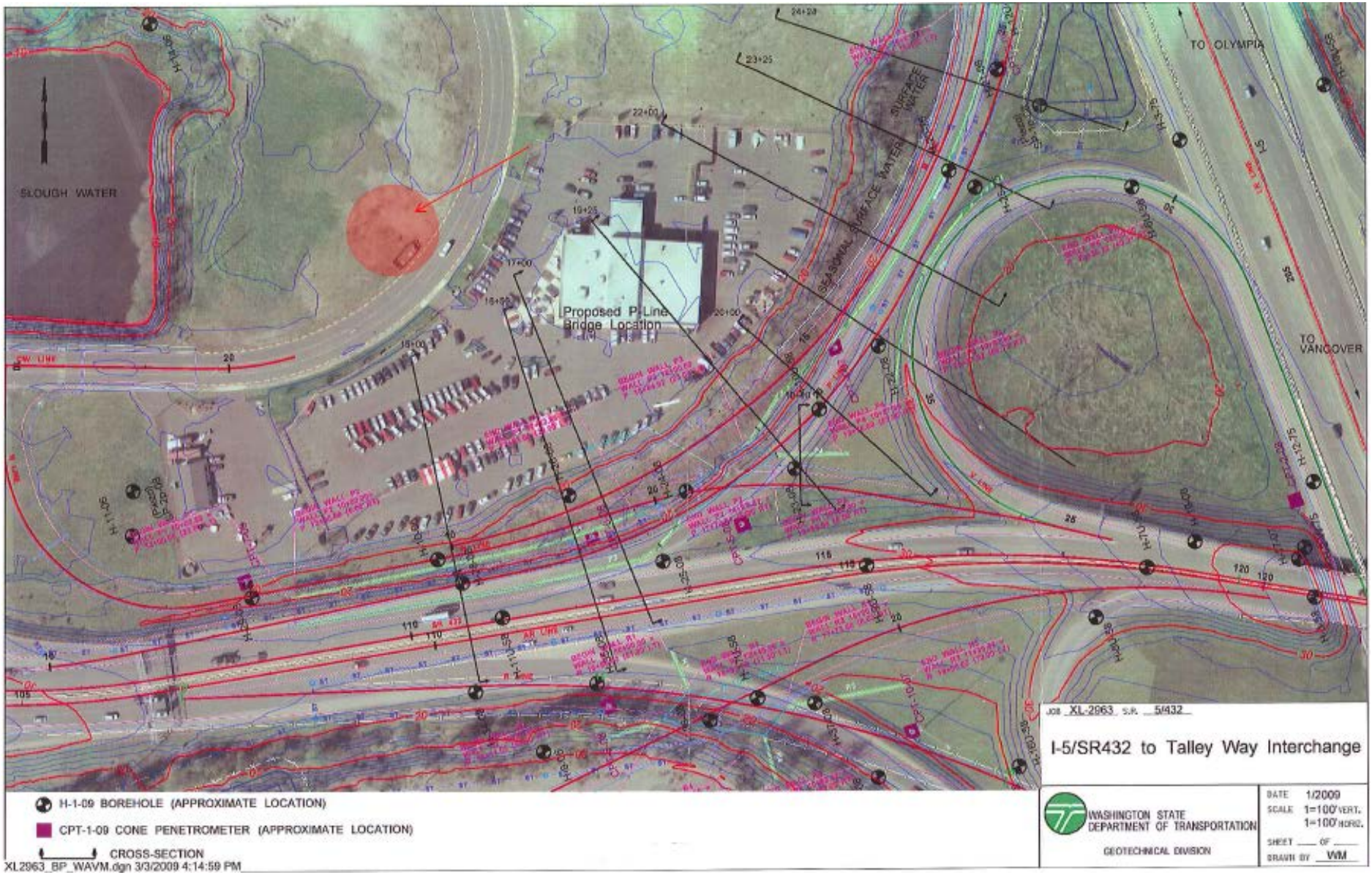

Figure 4.2. Site map for Talley Way interchange.

4.2.1 STEP-BY-STEP ANALYSIS PROCEDURE

The analysis discussed in this section assumes no initial downdrag on the drilled shafts in sandy soils (Case I in Section 3.3.1). For comparison purposes, however, Case II analysis, which allows for limited downdrag of 0.4 in., also was carried out. Appendix B presents the details.

Steps 1: Prepare input data

Table 1, and 2 present the soil parameters along the depth of the profiles for Pier 1 and Pier 2, respectively. The SPT N-values are used to calculate the side and tip resistance based on Equations 3.1, and 3.2 in section 3.3.1. The dead load on drilled shafts are 500 kips.

Step 2: Calculate the shaft resistance and tip resistance, and plot the load and resistance curves.

Figure 4.3 presents the load and resistance curves for the Pier 2 drilled shaft in the Talley Way interchange. The location of the NP is at the intersection of the two curves, which would always be at the head of the shaft for Case I.

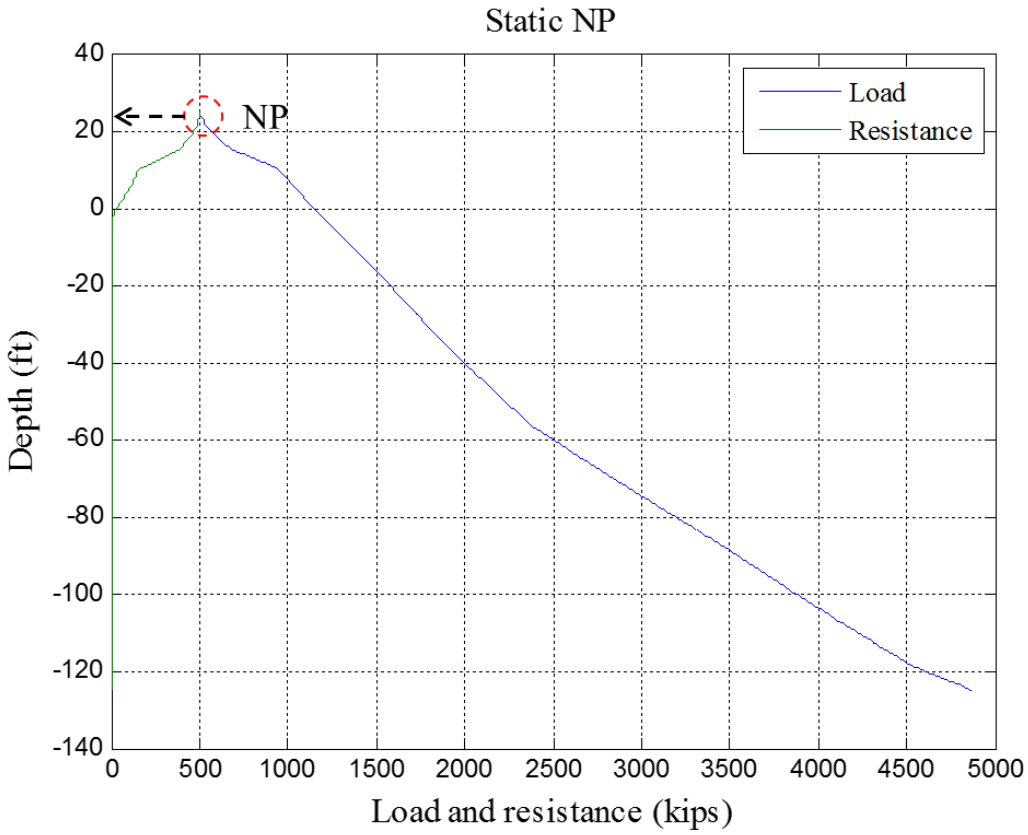

Figure 4.3. Load and resistance curves and neutral plane location for drilled shaft before liquefaction is assumed to occur at Pier 2 of the Talley Way interchange. The NP is located at the drilled shaft head before liquefaction.

Step 3: Calculate liquefaction-induced drag load.

Figure 4.4 presents the load and resistance curves and neutral plane locations for different conditions: before, during, and after liquefaction. The load curve is the same before and after liquefaction, and during liquefaction the neutral plane moves to the lowest point of the liquefiable layer. Table 4.3 presents the drag loads, and the NP locations for different conditions as shown in figure 4.4. The maximum drag load after liquefaction is roughly half of ultimate drag load.

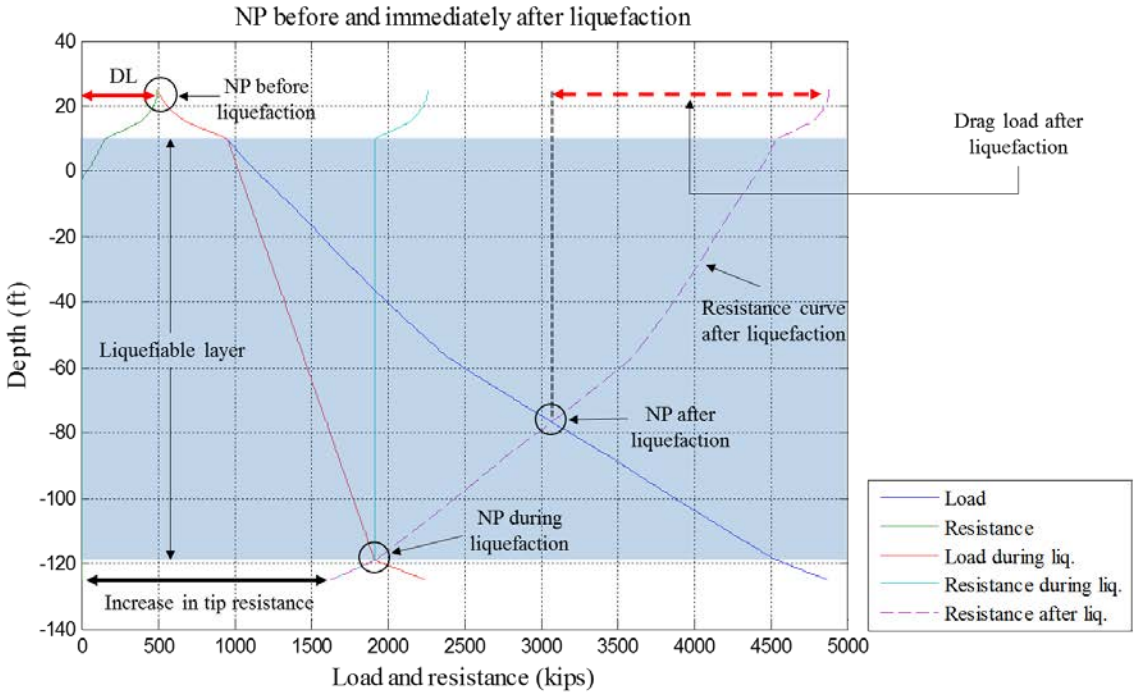

Figure 4.4. The resistance curve is shown by the dashed line. The drag load before liquefaction is zero because the neutral plane is at the head of the shaft.

Table 4.3. Drag loads for Talley Way interchange drilled shafts

	Pier 1		**Pier 2**	
	Case I	Case II	Case I	Case II
Max drag load before liquefaction (% of ultimate drag load)	0 kips (0%)	1515 kips (37%)	0 kips (0%)	1168 kips (36%)
Max drag load after liquefaction (% of ultimate drag load)	2218 kips (54%)	2223 kips (54%)	1811 kips (56%)	1812 kips (56%)
Ultimate drag load	4107 kips	4107 kips	3252 kips	3252 kips
NP location before liquefaction (ft)	25.0	-55.3	25.0	-49.5
NP location after liquefaction (ft)	-77.7	-77.7	-76.6	-76.6

Step 4: Calculate liquefaction-induced downdrag.

Figure 4.4 shows the increase in tip resistance after liquefaction for Pier 2 at the Talley Way interchange. It also shows the load distributions for the short-term, probable long-term after

liquefaction, and the ultimate conditions. The corresponding tip resistances are 0, 1633, and 4870 kips, respectively.

For the probable long-term resistance after liquefaction, the tip resistance becomes 1,633 kips (Figure 4.5). Using the ratio function, the corresponding settlement becomes 5.7 inches. The difference between this value and the short-term settlement before liquefaction, $\delta = 0$ in., is the liquefaction-induced downdrag settlement, which equals 5.7 inches. For the ultimate condition, the tip resistance becomes 4,870 kips and would result in a settlement of 25.3 inches.

Analysis also was carried out for the 8-ft diameter drilled shaft installed in Pier 1; Appendix B presents the details. Table 4.4 presents the downdrag settlements for both piers.

Table 4.4. Downdrag settlements for Talley Way interchange piers

		Short-term settlement (in.)	**Long-term downdrag settlement before liquefaction (in.)**	**Long-term downdrag settlement after liquefaction (in.)**	**Ultimate downdrag settlement (in.)**
Pier 1	Case I	0	NA	4.2	21.9
	Case II	0	0.4	4.2	21.9
Pier 2	Case I	0	NA	5.7	25.3
	Case II	0	0.4	5.7	25.3

The potential for large settlements for the liquefaction-induced downdrag shown in Table 4.4 for the ultimate case confirms that WSDOT was prudent to have improved the soil using stone columns, as was done in the final design.

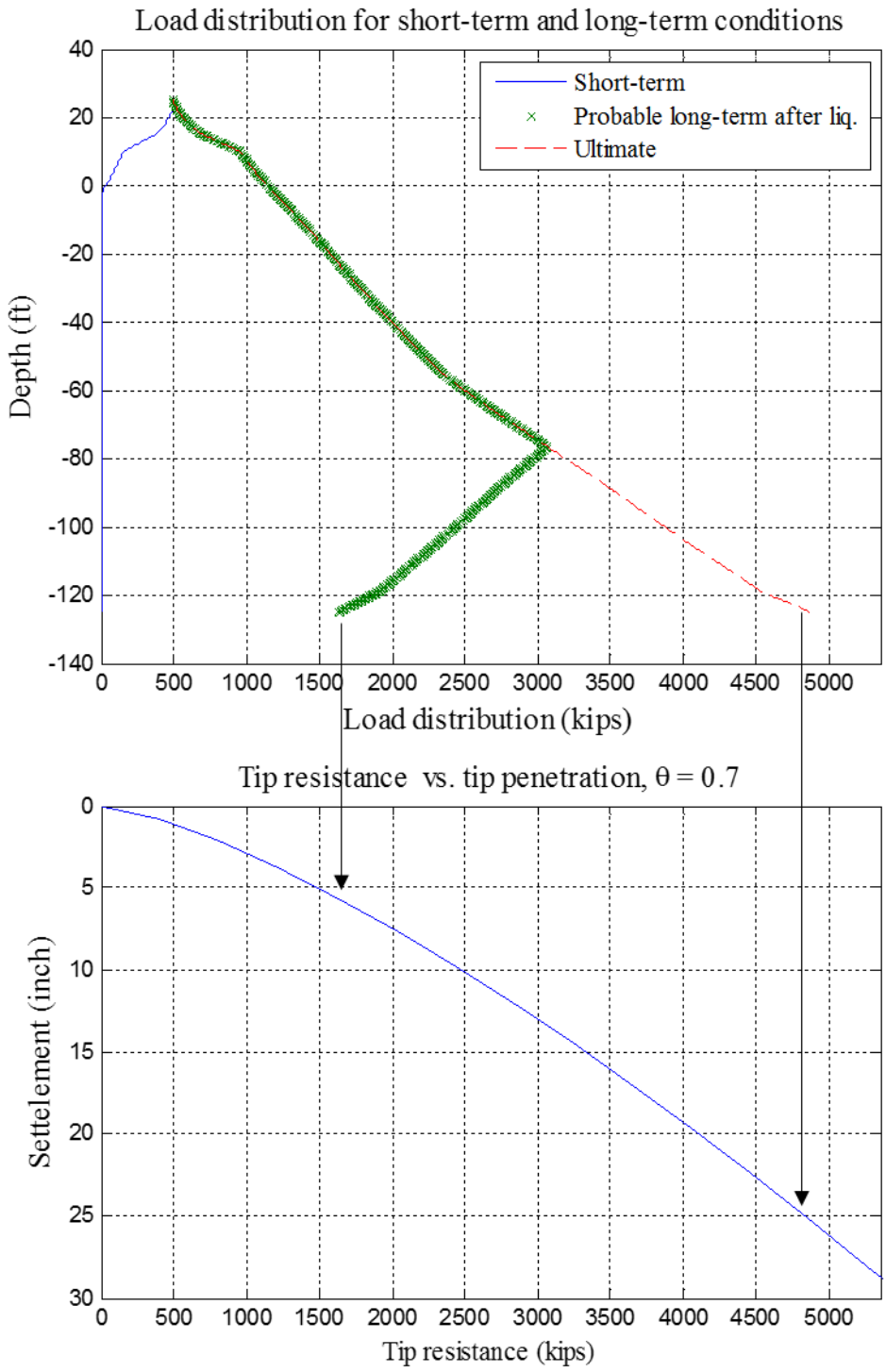

Figure 4.5. The load distribution (top) and downdrag settlements (bottom) for short-term, long-term after liquefaction, and ultimate conditions.

4.3 BRIDGE ON NE 139TH ST INTERCHANGE (I-5/I-205)

The bridge on NE 139th Street near the I-5/I-205 interchange has ten piers supported by drilled shafts. Borings and in situ test results confirmed the existence of potential liquefiable layers below the piers. Figure 4.6 shows the plan view and location of the bridge. Table 4.5 presents the diameter and length of the drilled shafts used as well as the corresponding dead loads at the top of the shafts for each of the ten piers. The site contains loose soil up to depths of 40 ft to 50 ft below the ground surface. All the drilled shafts for the NE 139th Street project were founded on sound bearing soil at the tip.

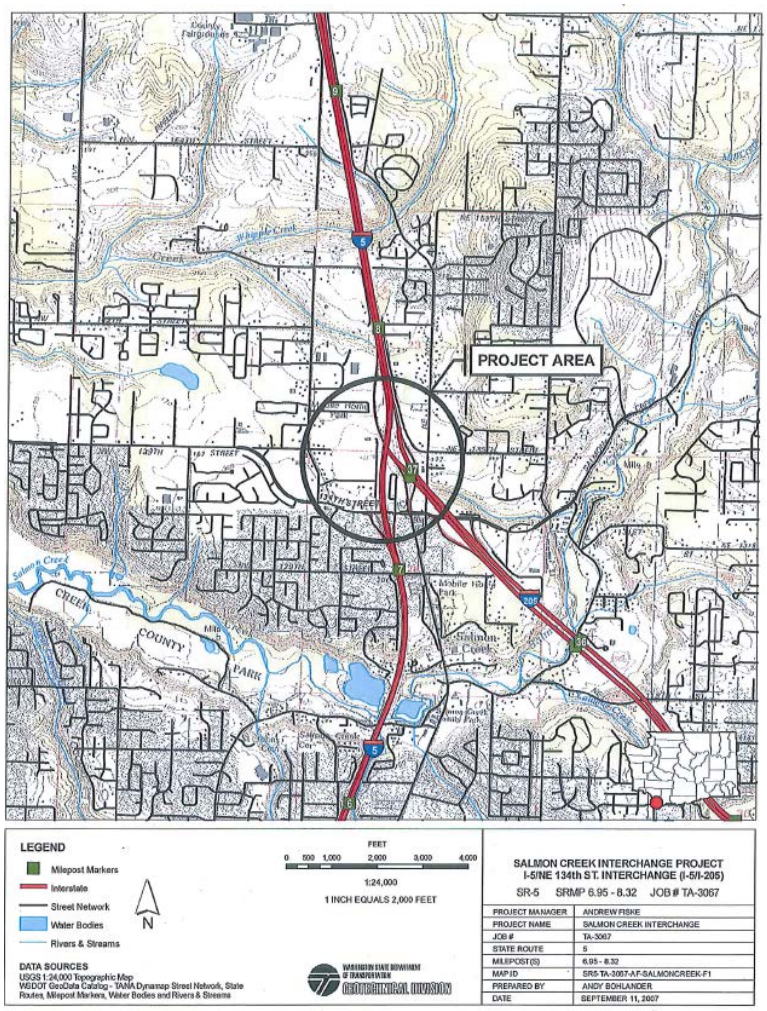

Figure 4.6. NE 139th Street interchange (I-5/I-205).

Table 4.5. Shaft diameters and lengths, and dead loads on top of shafts for NE 139th Street Bridge Piers

	Shaft Diameter (ft)	Shaft Length (ft)	Dead Load at Top of Shaft (kip)
Pier 1	6.0	75.0	836.0
Pier 2	9.0	90.0	1600.0
Pier 3	9.0	100.0	1570.0
Pier 4	9.0	95.0	1390.0
Pier 5	9.0	95.0	1005.0
Pier 6	9.0	114.0	1650.0
Pier 7	9.0	117.0	1700.0
Pier 8	9.0	105.0	1700.0
Pier 9	9.0	105.0	1650.0
Pier 10	6.0	75.0	580.0

Details of analysis for Pier 2 of the bridge structure for the NE 139th Street bridge project based on Case I analysis is presented in Figures 4.7 and 4.8. Following the same approach for the Talley Way interchange case study, we used the SPT N-values (Table 4.6) to plot the load and resistance curves. Figure 4.7 shows the load and resistance curves for short-term, during liquefaction, and after liquefaction conditions.

Table 4.6. Soil profiles under Pier 2 of bridge structure for NE 139th Street project

Layer	Soil Type	Layer Thickness (ft)	$(N_1)_{60}$	Liquefiable?	Eff. Unit Weight (pcf)
1	Sand	7	23	No	56
2	Sand	7	7	Yes	56
3	Clay	3	1	No	56
4	Sand	12	4	Yes	56
5	Sand	10	11	Yes	56
6	Sand	15	20	Yes	56
7	Sand	5	27	No	56
8	Sand	71	50	No	78

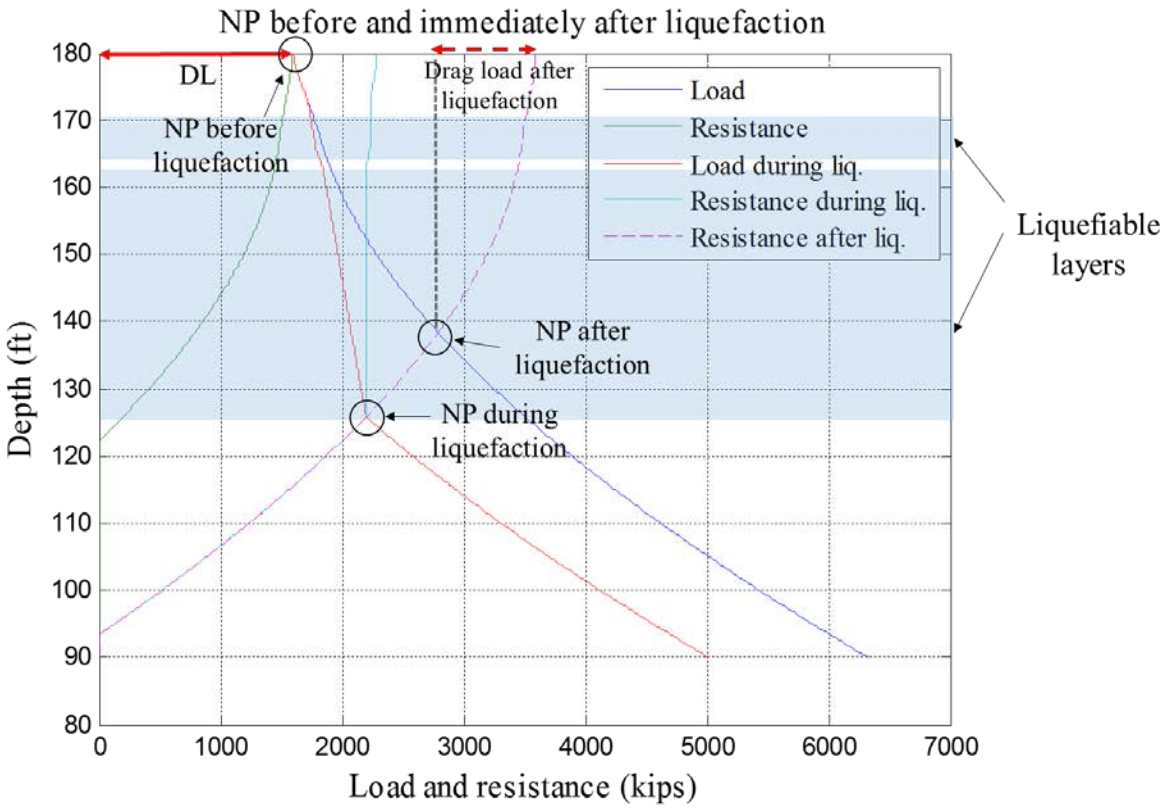

Figure 4.7. Load and resistance curves before, after, and during liquefaction for Pier 2 of NE 139th Street Bridge.

Figure 4.8 shows the downdrag settlements for the short-term, long-term after liquefaction, and ultimate conditions. The settlement for the short-term condition was estimated to be zero, and in the ultimate condition (with negative side resistance along the shaft), the downdrag settlement would be 12.2 inches. The drag load on the drilled shaft can increase up to 778 kips, which is 19 percent of the ultimate drag load and 49 percent of the dead load.

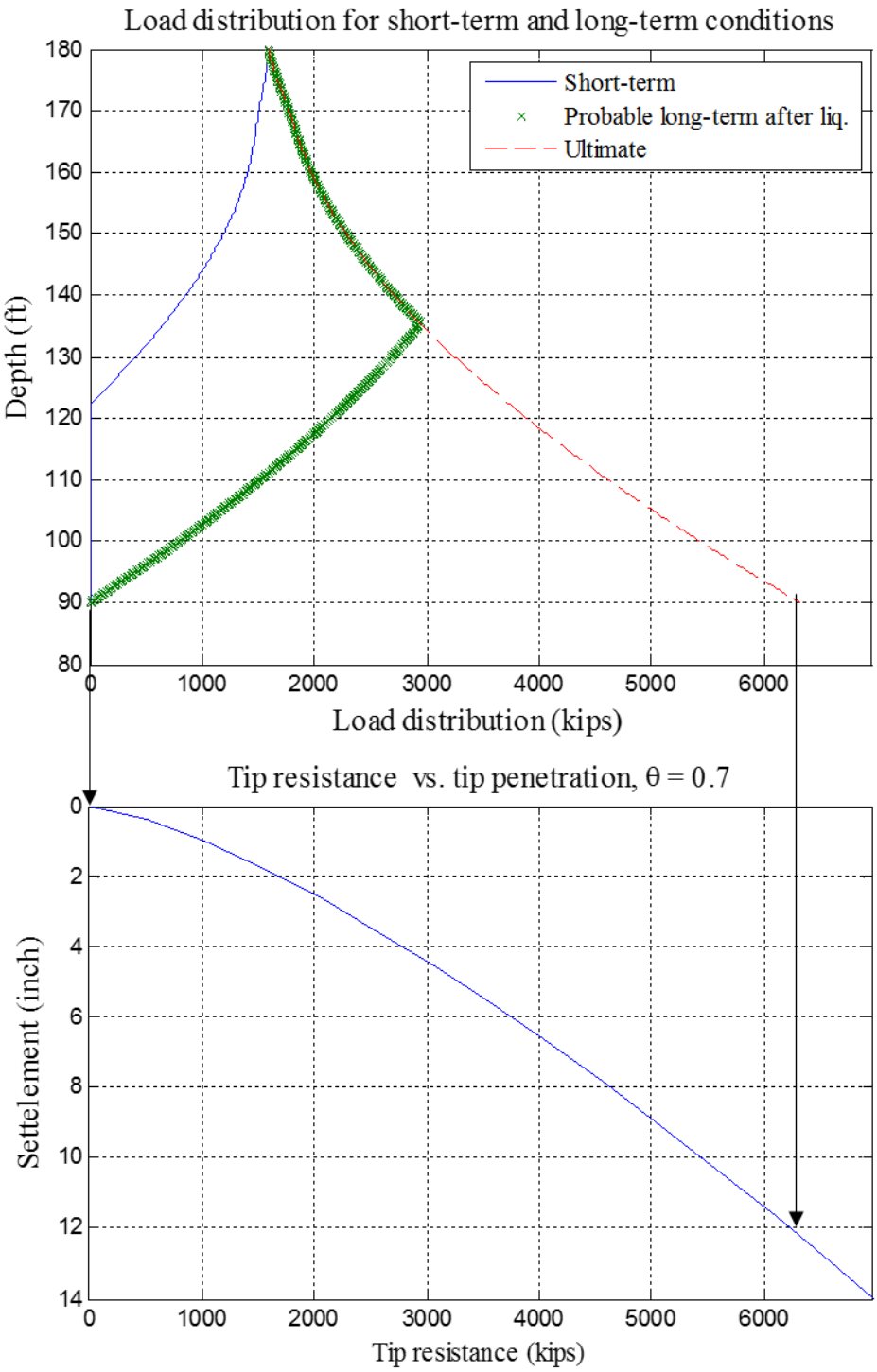

Figure 4.8. Load distribution and downdrag settlements for short-term, probable long-term after liquefaction, and ultimate conditions.

The proposed methodology was used to estimate the potential downdrag settlements and drag loads for all ten piers; Appendix B presents the details. Table 4.7 and Table 4.8 provide a summary of the settlements and the drag loads, respectively. Based on the method preferred by WSDOT (Case I), the liquefaction-induced downdrag settlement is zero for all the shafts. The reason for zero settlement is that the drilled shafts were long enough to resist the loads on them only by a portion of their side resistance; thus, even after liquefaction, the mobilized tip resistance remained close to zero. The drag load due to liquefaction was not sufficient to mobilize all of the side resistance, and so, the tip resistance did not increase in any of the shafts. Even if some negative side resistance developed along the shaft before liquefaction, thus mobilizing the tip resistance so that it would not be zero, no liquefaction-induced settlement would occur. Based on Case II analysis, we suggest that a fraction of downdrag settlement before liquefaction (assumed to be 0.4 in.) can be seen as heave after liquefaction for Piers 1, 2, and 10.

Table 4.7. Downdrag settlements for NE 139th Street project

		Short-term settlement (in.)	Long-term downdrag settlement before liquefaction (in.)	Long-term downdrag settlement after liquefaction (in.)	Ultimate downdrag settlement (in.)
Pier 1	Case I	0.0	NA	0.0	7.7
	Case II	0.0	0.4	0.0*	7.7
Pier 2	Case I	0.0	NA	0.0	12.2
	Case II	0.0	0.4	0.0*	12.2
Pier 3	Case I	0.0	NA	0.0	14.4
	Case II	0.0	0.4	0.4	14.4
Pier 4	Case I	0.0	NA	0.0	13.2
	Case II	0.0	0.4	0.4	13.2
Pier 5	Case I	0.0	NA	0.0	13.1
	Case II	0.0	0.4	0.4	13.1
Pier 6	Case I	0.0	NA	0.0	19.3
	Case II	0.0	0.4	0.4	19.3
Pier 7	Case I	0.0	NA	0.0	20.7
	Case II	0.0	0.4	0.4	20.7
Pier 8	Case I	0.0	NA	0.0	16.9
	Case II	0.0	0.4	0.4	16.9
Pier 9	Case I	0.0	NA	0.0	15.6
	Case II	0.0	0.4	0.4	15.6
Pier 10*	Case I	0.0	NA	0.0	6.8
	Case II	0.0	0.4	0.0*	6.8

* Liquefaction-induced heave can be a fraction of the settlement before liquefaction, which is assumed to be 0.4 inch.

Table 4.8. Drag loads for NE 139th Street project

		Max drag load before liquefaction (% of ultimate drag load)	Max drag load after liquefaction (% of ultimate drag load)	Ultimate drag load (kips)	NP location before liquefaction (ft)	NP location after liquefaction (ft)
Pier 1	Case I	1.0 kips (0%)	325 kips (20%)	1598	181.0	141.0
	Case II	444 kips (27%)	327 kips (20%)	1598	135.3	141.1
Pier 2	Case I	0.0 kips (0%)	778 kips (19%)	4108	180.0	138.6
	Case II	1272 kips (31%)	778 kips (19%)	4108	127.5	138.6
Pier 3	Case I	0 kips (0%)	427 kips (9%)	4733	180	150.4
	Case II	1551 kips (33%)	1551 kips (3 %)	4733	118.6	118.6
Pier 4	Case I	0.0 kips (0%)	631 kips (14%)	4521	180.0	141.2
	Case II	1546 kips (34%)	1546 kips (34%)	4521	121.6	121.6
Pier 5	Case I	0.0 kips (0%)	448 kips (9%)	4799	180.0	150.5
	Case II	1857 kips (39%)	1857 kips (39%)	4799	115.7	115.7
Pier 6	Case I	0.0 kips (0%)	521 kips (11%)	6257	177.0	144.6
	Case II	2514 kips (36%)	2514 kips (36%)	6257	111.0	111.0
Pier 7	Case I	0 kips (0%)	741 kips (11%)	6663	176.0	140.0
	Case II	2428 kips (37 %)	2428 kips (37%)	6663	109.0	109.0
Pier 8	Case I	0.0 kips (0%)	670 kips (12%)	5452	172.0	136.1
	Case II	1850 kips (34%)	1850 kips (34%)	5452	110.4	110.4
Pier 9	Case I	0 kips (0%)	778 kips (15%)	5059	185.0	146.0
	Case II	1666 kips (33 %)	1666 kips (33%)	5059	121.1	121.1
Pier 10	Case I	0 kips (0%)	397 kips (25%)	1603	188.0	152.7
	Case II	571 kips (36%)	397 kips (25%)	1603	141.0	152.7

4. 4. DISCUSSION OF THE NEED TO ACCOUNT FOR 0.4 IN. DOWNDRAG BEFORE LIQUEFACTION (CASE II)

For the Case II analysis, the resistance curve that matches the 0.4 inch mobilized tip resistance was used to find the NP before liquefaction. As a result, the probable long-term before liquefaction condition could be distinguished as the case where the negative side resistance is assumed to develop along the shaft above the NP prior to liquefaction. The procedure to find the resistance curve before liquefaction is given below for Pier 2 of the Talley Way interchange structure.

(1) Find the short-term settlement.

With the values of the tip resistance known, the corresponding settlements were calculated using the ratio function (Eq. 3.3). The base diameter of the shaft is 8 ft and the tip resistance was calculated as 3,817 kips (Eq. 3.2). The ratio function parameters would be:

δ_1 = 5% of base diameter = 4.8 in.

R_1 = [tip resistance] = 3,817 kips

θ = 0.7

Using the ratio function, the settlement can be calculated using Equation 4.1:

$$\delta_2 = \delta_1 \left(\frac{R_2}{R_1}\right)^{\frac{1}{\theta}} = 4.8 \left(\frac{R_2}{3{,}817 \text{ kips}}\right)^{\frac{1}{0.7}} in. \qquad (4.1)$$

If the tip resistance does not mobilize prior to liquefaction, then the settlement would be zero, as is the case here. If not, the short-term settlement can be calculated using Equation 4.1.

(2) Determine the long-term settlement and mobilized tip resistance of the shaft before liquefaction.

The settlement of the shaft before liquefaction is calculated using Equation 3.8a, and the mobilized tip resistance is calculated using the ratio function (Eq. 3.3). Figure 4.9 shows the load

distributions and settlement curves, assuming a long-term downdrag settlement of 0.4 in. before liquefaction. Note that the liquefaction-induced downdrag settlement and drag load remain the same as for Case I discussed in Section 4.2. If the liquefaction-induced downdrag settlement is more than 0.4 in., then Cases I and II would have the same results, as is the case for pier 2 of Talley Way interchange structure.

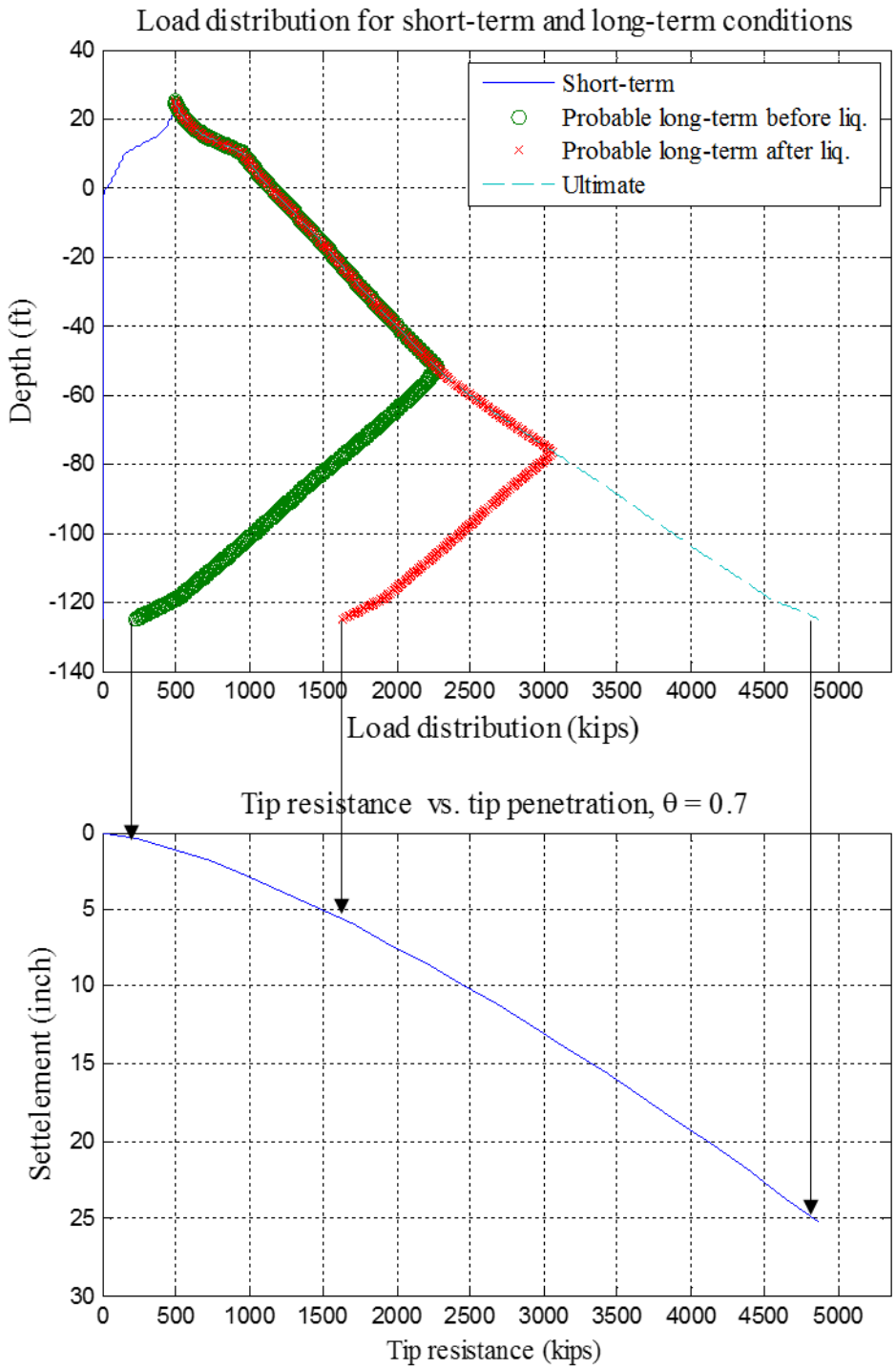

Figure 4.9. Downdrag settlements for short-term, long-term before and after liquefaction, and ultimate conditions for Pier 2 of the Talley Way interchange structure (Case II analysis).

4.4.3. Multiple liquefiable layer

For Case I, the same methodology discussed in Section 3.3.1 would apply, even if multiple liquefiable zones are present that cannot be combined into a single-layer zone approximation. However, for Case II, the procedure must be considered for the different cases, as described below.

All liquefiable layers located above the NP

If all the liquefiable layers are above the NP, the drag load and tip resistance would not change compared to the Case II analysis. Figure 4.10 shows the load and resistance curves before, during, and after liquefaction for Pier 9 of the NE 139th Street Bridge where all the liquefiable layers are located above the NP before liquefaction. The drag load also does not change compared to that before liquefaction. Note that the resistance curves before and after liquefaction are identical.

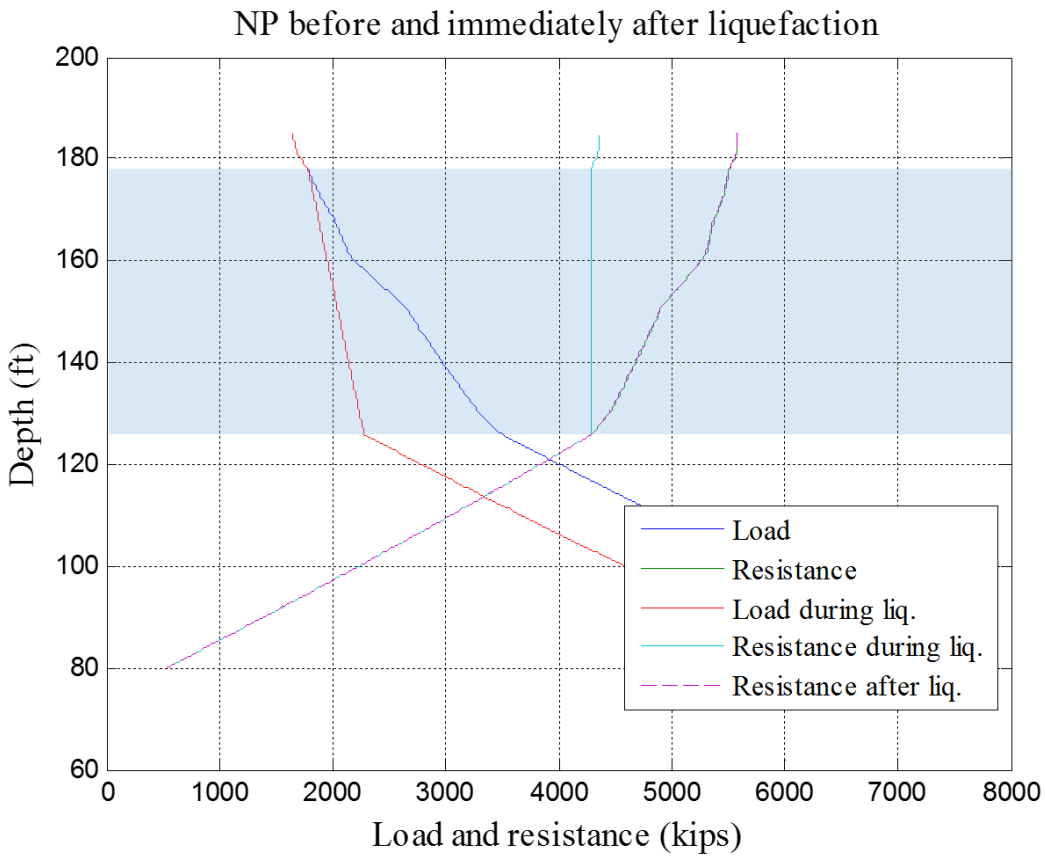

Figure 4.10. Load and resistance curves before, after, and during liquefaction for Pier 9 of NE 139th Street Bridge. All liquefiable layers are above the NP.

Some layers located above the NP and some layers located below the NP

Figure 4.11 (a) shows the load and resistance curves before, after, and during liquefaction for Pier 10 of the NE 139th Street Bridge where some liquefiable layers are located above the NP and some below, and where all layers are assumed to be liquefied. Figure 4.11 (b) shows the load and resistance curves, assuming that only the layers below the NP are liquefied. The location of the NP is lower in Figure 4.11 (b) compared to Figure 4.11 (a). The downdrag settlement for Case (b) is 1.0 in., whereas for Case (a) it is 0.0 inch. The drag load for Case (a) is 397 kips and for Case (b) it is 701 kips.

Therefore, if some layers are located above the NP and some layers are located below the NP, in order to have a conservative liquefaction-induced downdrag design, the liquefiable layers above the NP might not be considered liquefied. Both of the piers in the Talley Way interchange structure and Piers 1, 2, and 10 of the NE 139th Street Bridge have some liquefiable layers below the NP and some above the NP. Table 4.9 provides a comparison of the liquefaction-induced downdrag settlements and drag loads, assuming all layers to be liquefied, Case (a), and only layers below the NP to be liquefied, Case (b).

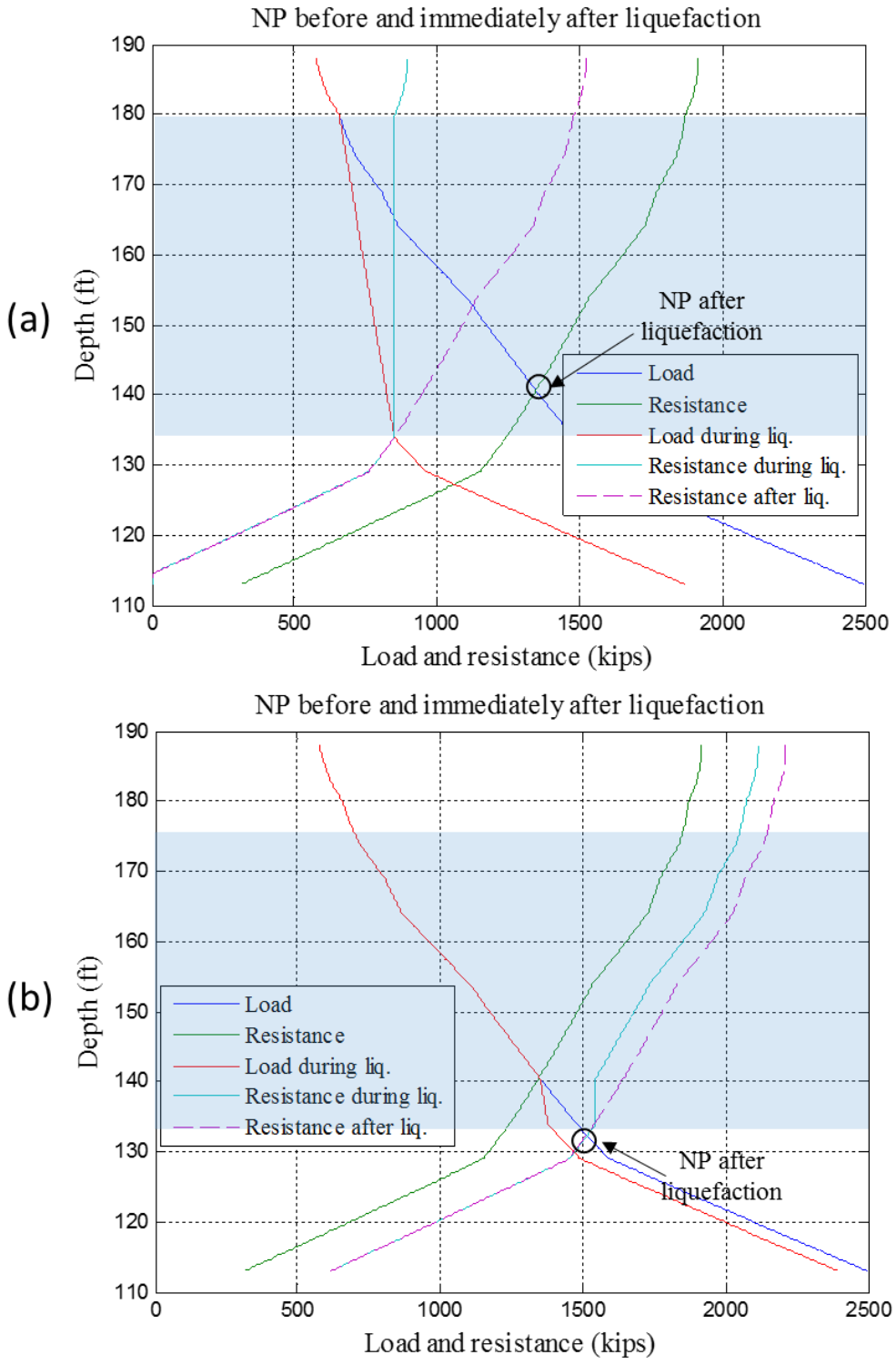

Figure 4.11. Load and resistance curves before, after, and during liquefaction for Pier 10 of NE 139th Street Bridge: (a) all liquefiable layers are considered to be liquefied and (b) the liquefiable layers above the neutral plane are not liquefied during an earthquake.

Table 4.9. Comparison of liquefaction-induced downdrag settlements and drag loads for case (a) and case (b) analyses (Figure 4.11)

		Drag Load (Case a)	Drag Load (Case b)	Downdrag (Case a)	Downdrag (Case b)
Talley Way interchange structure	Pier 1	2223 Kips	2934 kips	4.2 inch	10.0 inch
	Pier 2	1812 kips	2394 kips	5.6 inch	12.8 inch
NE 139th Street Bridge	Pier 1	327 kips	604 kips	0.0 inch	1.1 inch
	Pier 2	778 kips	1497 kips	0.0 inch	1.0 inch
	Pier 10	397 kips	701 kips	0.0 inch	1.0 inch

4. 5. COMPARISON OF DRAG LOAD DERIVED FROM THE MODIFIED UNIFIED METHOD AND FROM THE CURRENT APPROACH USED BY WSDOT

The WSDOT Geotechnical Design Manual indicates that engineering judgement is required to determine the magnitude of a drag load. The load should be somewhere between the extreme residual side friction and the nominal side friction. It is common practice at WSDOT to assume that the drag load is the average of the extreme residual resistance and the nominal side resistance. However, this recommendation does not work well when the variation of the residual side friction and nominal side friction is large. Table 4.10 shows that the modified unified method would lead to lower liquefaction-induced drag loads than the WSDOT manual recommendations. The results are based on the assumption of zero residual strength in the liquefiable layers.

Assume that the nominal side friction load is $Rs_{nominal}$ and the side friction load along the liquefiable layers is $Rs_{Liquefiable}$ .The extreme residual side friction then can be calculated using Equation 4.2:

$$Rs_{Ex\_residual} = Rs_{nominal} - \bar{x}Rs_{Liquefiable}, \quad (4.2)$$

where $\bar{x}$ is the average fraction of the side resistance in liquefiable layers, which is degraded during liquefaction. The WSDOT approach suggests Equations 4.3 and 4.4:

$$Drag\ \ Load = \frac{Rs_{nominal}+Rs_{Ex\_residual}}{2} = \frac{Rs_{nominal}+\left(Rs_{nominal}-\bar{x}Rs_{Liquefiable}\right)}{2}. \quad (4.3)$$

Substituting Equation (4.2) into (4.3) drag load is calculated as:

$$Drag\ \ Load = Rs_{nominal} - \frac{\bar{x}}{2}Rs_{Liquefiable}. \quad (4.4)$$

Equation 4.4 implies that all the side resistance becomes negative and then is recovered by half of the degraded side resistance in liquefiable layers. Higher values of $\bar{x}$ would result in lower drag loads. The ultimate drag load corresponds to the case of $\bar{x} = 0$, and $\bar{x} = 1$ is the assumption made in this study for analysis of the long-term after liquefaction cases. Appendix C justifies the assumption of $\bar{x} = 1$ for the unified method, showing that the unified method predicts the highest values for drag load and downdrag settlement in case of $\bar{x} = 1$. In the NP method, the liquefaction-induced effects are reflected in both of load and resistance curves and considering the residual strength would not lead to a more conservative analysis.

Table 4.10. Comparison of Liquefaction-Induced Drag Loads Obtained Using WSDOT Approach and Modified Unified Method

Case History	WSDOT Approach	Modified Unified Method
Juan Pablo II Bridge, Pier 1	1936 kips	1572 kips
Juan Pablo II Bridge, Pier 5	1852 kips	1453 kips
Juan Pablo II Bridge, Pier 117	1812 kips	1271 kips
Juan Pablo II Bridge, Pier 119	1730 kips	1116 kips
Talley Way Interchange Pier 1	2528 kips	1515-(2934)* kips
Talley Way Interchange Pier 2	1942 kips	1811-(2394)* kips
NE 139th St Bridge Pier 1	1309 kips	325-(604)* kips
NE 139th St Bridge Pier 2	3490 kips	778-(1497)* kips
NE 139th St Bridge Pier 3	4374 kips	424 kips
NE 139th St Bridge Pier 4	3951 kips	631 kips
NE 139th St Bridge Pier 5	4530 kips	448 kips
NE 139th St Bridge Pier 6	5827 kips	521 kips
NE 139th St Bridge Pier 7	6103 kips	741 kips
NE 139th St Bridge Pier 8	4940 kips	670 kips
NE 139th St Bridge Pier 9	4451 kips	778 kips
NE 139th St Bridge Pier 10	1289 kips	397-(701)* kips

*The values in parentheses are based on the discussion given in Section 4.4.

CHAPTER 5: CONCLUSIONS AND RECOMMENDATIONS

5.1. CONCLUSIONS

The downward relative movement of overlying soil layers around deep foundations induces shear stress along drilled shafts and changes the axial load distribution on them. Depending on the site conditions, the changes in the axial responses that result from liquefaction-induced settlement can have a significant impact on the performance of drilled shafts and piles in seismic regions. This study presents an analytical method to quantify the effects of liquefaction-induced downdrag on piles and drilled shafts.

The analytical method is based on the NP method that was developed originally for clays but has been modified to account for liquefaction-induced effects. This method assumes that the soil settlement equals the pile settlement at the NP location and that the load transfer during liquefaction within the liquefied layer during an earthquake is nearly zero. In this study, the NP method was applied to an observed case of downdrag during the 8.8 magnitude earthquake in Maule, Chile. The proposed unified method for drilled shafts was able to predict the downdrag settlement observed at the site. Numerical simulations of the liquefaction-induced downdrag were performed using OpenSees software to verify the key assumptions used in the analytical method. The developed procedure also is illustrated for two field cases of drilled shafts in liquefiable soils in Washington State.

Two different analysis methods are discussed in this report for comparative purposes (see Section 3.3.1):

- Case I: No negative side resistance develops before liquefaction. This method is preferred by AASHTO.

- Case II: Negative side resistance develops along the shaft. This study recommends 0.4 in. downdrag settlement before liquefaction.

This study reached the following conclusions.

- The analysis results for a pier supporting the Juan Pablo II Bridge (Section 3.4) and for both piers at the Talley Way interchange structure (Section 4.2) indicate that both Case I and Case II analyses would result in practically the same downdrag settlements and drag loads.
- The analysis results for the bridge piers at the NE 139th St. interchange (Section 4.3) indicate that downdrag settlement was not significant at this site. However, the drag load might be the controlling parameter in this case for liquefaction-induced downdrag analysis. All the drag loads calculated using Case II analysis are larger than those calculated using Case I analysis for this site. This finding indicates that Case II analysis is more conservative in terms of drag loads calculated for shafts than Case I analysis.
- When a liquefiable layer is located below the shaft tip, the pile and soil systems above this liquefiable layer will move together. In this case, the liquefaction-induced downdrag settlement should be added to the settlement caused by compression of the liquefiable zones below the shaft tip to find the total liquefaction-induced settlement. The drilled shafts discussed in Chapter 3 for the Juan Pablo II Bridge are likely to experience such settlement (see Section 3.4.3).
- Based on Case II analysis, the magnitude of the liquefaction-induced downdrag settlement depends on the location of the liquefiable layers (above the NP, below the NP, and below the pile tip).
    - If a liquefiable layer is located above the NP, liquefaction-induced downdrag settlements are negligible. In this case, however, very large drag loads could cause

structural failure of the shafts rather than settlement-induced failure of the structure. All Case II analysis results for the drilled shafts in the NE 139th St. interchange, except Piers 1, 2, and 10, are examples of this condition (see Appendix B).

- When a liquefiable layer is located below the NP, liquefaction-induced downdrag effects occur as a result of changes to the NP location. The side resistance value of the shaft during liquefaction will drop to zero momentarily throughout the liquefiable layers. The lost positive side resistance (from layers below the NP) transfers to the tip resistance, which causes downdrag settlement. After liquefaction, with time, the drag load increases along with the development of negative shaft resistance because of the relative settlement of the soil with respect to the drilled shaft. The NP location after liquefaction would be lower than the case before liquefaction that corresponds to higher values of negative side resistance or drag load. All of the Case II analysis results for the drilled shafts at the Juan Pablo II Bridge are examples of this condition (see Appendix B).
- If some layers are above the NP and some layers are below the NP, in order to have a conservative liquefaction-induced downdrag design, the liquefiable layers above the NP might not be considered liquefied during an earthquake (see Section 4.4).

- The need for using residual strength when pore pressure is not fully dissipated does not arise when using the NP analysis (see Appendix C).
- The calculated drag loads on drilled shafts that are based on the modified unified method are lower than the drag loads predicted using the current approach adopted by WSDOT (see Section 4.5).
- If downdrag settlement before liquefaction is unlikely to happen, Case I analysis can be performed with no further consideration. Although the results from the different case

studies reveal no significant difference in terms of downdrag settlement between Case I and Case II analyses, the predicted drag loads are higher when using Case II analysis compared to Case I analysis.

5.2. RECOMMENDATIONS

- This study focused on single piles, but most of the applications for pile foundations are for pile groups. Extending this liquefaction-induced analysis for pile groups therefore is recommended.
- This study's approach assumes that tip resistance develops mainly after the side resistance is fully mobilized to its capacity, and only the q-z function (tip resistance-vertical movement of the shaft) is utilized. This assumption represents a simplified approach, but it provides a very good estimation because the side resistance fully develops along the shaft when only 10 percent of the tip resistance is mobilized (O'Neill and Reese 1999). Using both the q-z and t-z functions (side resistance and vertical movement of the shaft) would be more realistic to capture the load distribution along the shaft.
- This study considered liquefaction-induced downdrag, which is associated with earthquake shaking. Pile movement involves not only vertical movement but also lateral movement. This study recommends that p-y relationships that account for lateral movement should be incorporated in future analysis. A complete model that accounts for vertical soil movement, lateral soil movement, and inertial loads would give more insights about pile performance.

ACKNOWLEDGEMENTS

The authors would like to thank the Washington State Department of Transportation (WSDOT) for its financial support of this research. We would also like to thank Dr. Bengt Fellenius for his valuable remarks and guidance. Also, Tony Allen of WSDOT provided valuable comments and input. Sincere thanks also are extended to Dr. Gonzalo Montalva at the University of Concepción, Chile and Dr. Christian Ledezma Araya of the Pontificia Universidad Católica de Chile for assisting in the collection and translation of relevant data.

REFERENCES

AASHTO (2014). *LRFD Bridge Design Specifications*. American Association of State Highway and Transportation Officials (4th ed.), Washington, DC.

Bjerrum, L. and I. J. Johannessen (1965). Measurements of the Compression of a Steel Pile to Rock Due to Settlement of the Surrounding Clay. *Proceedings of the 6th International Conference on Soil Mechanics and Foundation Engineering*, Montreal, Canada, September 8-15, University of Toronto Press, Vol. 2, 261-264.

Bjerrum, L., I. J. Johannessen, and O. Eide (1969). Reduction of Negative Skin Friction on Steel Piles to Rock. *Proceedings of the 7th International Conference on Soil Mechanics and Foundation Engineering*, Mexico City, Mexico, August 25-29, Mexico Geotechnical Society, Vol. 2, 27-34.

Boroschek, R. L., V. Contreras, D. Y. Kwak, and J. P. Stewart (2012). Strong Ground Motion Attributes of the 2010 M 8.8 Maule, Chile, Earthquake. *Earthquake Spectra*, S19-S38.

Boulanger, R. W. and S. J. Brandenberg (2004). *Neutral Plane Solution for Liquefaction-Induced Down-Drag on Vertical Pile*. (M. K. Yegian and E. Kavazanjian, eds.) Geotechnical Engineering for Transportation Projects, Proceedings of Geo-Trans 2004, Geotech, ASCE, Special Publication No. 126, 470-478.

Boulanger, R. W., B. L. Kutter, S. J. Brandenberg, et al. (2003). *Pile Foundations in Liquefied and Laterally Spreading Ground during Earthquakes: Centrifuge Experiments and Analyses*. Report No. UCD/CGM-03/01, Center for Geotechnical Modeling, Department of Civil Engineering, University of California, Davis, CA.

Bray, J. D. and J. D. Frost, eds. (2010). *Geo-Engineering Reconnaissance of the 2010 Maule, Chile Earthquake*. Report of the NSF-Sponsored GEER Association Team; primary authors: Arduino et al., <www.geerassociation.org>.

Canadian Geotechnical Society (1985). *Canadian Foundation Engineering Manual* (2nd ed.), Vancouver: BiTech Publishers,

Decourt, L. (1982). Prediction of Bearing Capacity of Piles Based Exclusively on N-values of the SPT. *Proceedings of the ESOPT II*, Amsterdam, 19-34.

Endo, M., A. Minou, T. Kawasaki, and T. Shibata (1969). Negative Skin Friction Acting on Steel Piles in Clay. *Proceedings of the 8th International Conference on Soil Mechanics and Foundation Engineering*, Mexico City, Mexico, August 25-29, Mexico Geotechnical Society, Vol. 2, 85-92.

Fellenius, B. H. and B. B. Broms (1969). Negative Skin Friction for Long Piles Driven in Clay. *Proceedings of the 7th International Conference of Soil Mechanics and Foundation Engineering*, Vol. 2, 93-98.

Fellenius, B. H. (1972). Downdrag on Long Piles in Clay Due to Negative Skin Friction. *Canadian Geotechnical Journal*, 9(4), 323-337.

Fellenius, B. H. (1984). Negative Skin Friction and Settlement of Piles. *Proceedings of the 2nd International Seminar, Pile Foundations*, Nanyang Technological Institute, Singapore,

Fellenius, B. H. (1988). Unified Design of Piles and Pile Groups *Transportation Research Board Record*, 1169, Transportation Research Board, Washington, DC, 75-82.

Fellenius, B. H. (1999). Bearing Capacity—A Delusion? *Proceedings of the Annual Meeting of the Deep Foundation Institute*, Hawthorne, NJ and Dearborn, MI, October 14-16,

Fellenius, B. H. (2004). *Unified Design of Piled Foundations with Emphasis on Settlement Analysis. Honoring George G. Goble—Current Practice and Future Trends in Deep Foundations*. Geo-Institute Geo TRANS Conference, Los Angeles, CA, July 27-30, 2004, edited by J. A. DiMaggio and M. H. Hussein. ASCE GSP 125, 253-275.

Fellenius, B. H. and T. C. Siegel (2008). Pile Design Consideration in a Liquefaction Event. *Journal of Geotechnical and Environmental Engineering*, ASCE, 132(9), 1412-1416.

Fellenius, B. H. (2014). *Basics of Foundation Design*. Electronic Ed., <www. Fellenius.net>.

Florin, V. A. and P. L. Ivanov (1961). Liquefaction of Saturated Sandy Soil. *Proceedings of the 5th International Conference on Soil Mechanics and Foundation Engineering*, Paris, France, 106.

Goudreault, P. A. and B. H. Fellenius. (2013). *UniPile Version 5, Users and Examples Manual*. UniSoft Geotechnical Solutions, Ltd. [www.UniSoftLtd.com],

Hanna, A. M. and A. Sharif (2006). Drag Force on Single Piles in Clay Subjected to Surcharge Loading. *International Journal of Geomechanics*, ASCE 6(2), 89-96.

Ishihara, K. and M. Yoshimine (1992). Evaluation of Settlements in Sand Deposits Following Liquefaction During Earthquakes. *Soil Mechanics and Foundation Engineering* 118(32), 173-188.

Jeong, S., J. Lee, and C. J. Lee. (2004). Slip Effect at the Pile-Soil Interface on Dragload. *Computers and Geotechnics*, 31, 115-126.

Johannessen, I. J. and L. Bjerrum (1965). Measurement of the Compression of a Steel Pile to Rock Due to Settlement of the Surrounding Clay. *Proceedings of the 6th International Conference of Soil Mechanics and Foundation Engineering*, Vol. 2, 261-264.

Knutson, L. and T. C. Siegel (2006). Consideration of Drilled Displacement Piles for Liquefaction Mitigation. *Proceedings of DFI Augered Cast-in-Place Pile Committee Specialty Seminar*, 129-132.

Kramer, S. L. (1996). *Geotechnical Earthquake Engineering*. Upper Saddle River, NJ: Prentice Hall.

Ledezma, C., T. Hutchinson, S. A. Ashford, et al. (2012). Effects of Ground Failure on Bridges, Roads, and Railroads. *Earthquake Spectra* 28(S1), S119-S143.

Lee, C. J. and W. W. Ng (2004). Development of Down-drag on Piles and Pile Groups in Consolidating Soil. *Journal of Geotechnical and Geoenvironmental Engineering*, ASCE, 130(9), 905-914.

Lee, K. L. and A. Albeisa (1974). Earthquake Induced Settlements in Saturated Sands. *Journal of the Soil Mechanics and Foundation Division*, ASCE, Vol. 100, No. GT4, April.

Lu, J., A. Elgamal, and Z. Yang (2011). *OpenSeesPL: 3D Lateral Pile-Ground Interaction. User Manual (Beta 1.0)*. University of California, San Diego, CA.

Lysmer, J. and A. M. Kuhlemeyer (1969). Finite Dynamic Model for Infinite Media. *Journal of the Engineering Mechanics Division*, ASCE, 95, 859-877.

Matyas, E. L. and J. C. Santamarina (1994). Negative Skin Friction and the Neutral Plane. *Canadian Geotechnical Journal* 31(3), 591-597.

Meyerhof, G. G. (1976). Bearing Capacity and Settlement of Pile Foundations. The Eleventh Terzaghi Lecture, November 5, 1975. *Journal of Geotechnical Engineering*, ASCE, 102(GT3) 195-228.

O'Neill, M. W. and L. C. Reese (1999). *Drilled Shafts. Construction Procedures and Design Methods*. Federal Highway Administration, Report No. FHWA-IF99-025, Transportation Research Board, Washington, DC.

OpenSees (2014). *Open System for Earthquake Engineering Simulation*. Pacific Earthquake Engineering Research Center (PEER), University of California, Berkeley, CA. http://opensees.berkeley.edu.

Parra, E. (1996). *Numerical Modeling of Liquefaction and Lateral Ground Deformation Including Cyclic Mobility and Dilation Response in Soil Systems*. Ph.D. dissertation, Rensselaer Polytechnictechnic Institute, New York, NY.

Poulos, H. and E. H. Davis (1990). *Pile Foundation Analysis and Design* (reprint ed.). Robert E. Krieger Publishing Company, FL.

Prevost, J. H. (1985). A Simple Plasticity Theory for Frictional Cohesionless Soils. *Soil Dynamics and Earthquake Engineering* 4(1), 9-17.

Rollins, K. M. and S. R. Strand (2006). Downdrag Forces Due to Liquefaction Surrounding a Pile. *Proceedings of the 8th U.S. National Conference on Earthquake Engineering*. Paper No. 1646, San Francisco, CA, April 18-22.

Seed, H. B. et al. (1975). *The Generation and Dissipation of Pore Water Pressures During Soil Liquefaction*. Report No. UCB/EERC-75/26, University of California, Berkeley, CA.

Siegel, T. C. et al. (2014). *Neutral Plane Method for Drag Force of Deep Foundations and the AASHTO LRFD Bridge Design Specifications*.

Strand, S. R. (2008). *Liquefaction Mitigation Using Vertical Composite Drains and Liquefaction-induced Downdrag on Piles: Implications for Deep Foundation Design*. Ph.D. thesis, Department of Civil and Environmental Engineering, Brigham Young University, Provo, UT.

Tokimatsu, K. and H. B. Seed (1987) Evaluation of Settlements in Sands Due to Earthquake Shaking. *Journal of Geotechnical Engineering*, ASCE, 113(8), 861-879.

United States Geological Survey (USGS) (2012). *USGS Earthquake Hazards Program, Chile Earthquake of 27 Feb 2010*. http://www.strongmotioncenter.org/cgi-bin/CESMD/iqr_dist_DM2.pl?IQRID=Chile_27Feb2010_us2010tfan&SFlag=0&Flag=2. (last accessed 17 March 2014).

Verdugo, R. and G. Peters (2010). Informe Geotécnico Fase Anteproyecto Infraestructura Puente. *Mecano Eje Chacabuco*, Rev7, August.

Wang, R. and S. J. Brandenberg (2013). Beam on Nonlinear Winkler Foundation and Modified Neutral Plane Solution for Calculating Downdrag Settlement. *Journal of Geotechnical and Geoenvironmental Engineering*, ASCE, doi:10.1061/(ASCE)GT.1943-5606.0000888.

Washington State Department of Transportation (WSDOT) (2013). *Geotechnical Design Manual M 46-03.09*. < http://www.wsdot.wa.gov/publications/manuals/m46-03.htm>.

Yan, W. M., T. K. Sun, and L. G. Tham (2012). Coupled-Consolidation Modeling of a Pile in Consolidating Ground. *Journal of Geotechnical and Geoenvironmental Engineering*, ASCE, 138(7) 789-798.

Yen, W. P., G. Chen, I. Buckle, et al. (2011). *Post-Earthquake Reconnaissance Report on Transportation Infrastructure: Impact of the February 27, 2010, Offshore Maule Earthquake in Chile*. Federal Highway Administration, Report No. FWWA-HRT-11-030, 214.

Yang, Z. (2000). *Numerical Modeling of Earthquake Site Response Including Dilation and Liquefaction*. Ph.D. dissertation, Columbia University, New York, NY.

Yang, Z. and A. Elgamal (2002). Influence of Permeability on Liquefaction-Induced Shear Deformation. *Journal of Engineering Mechanics*, ASCE, 128(7), 720-729.

Yang, Z., A. Elgamal, and J. Parra (2003). Computational Model for Cyclic Mobility and Associated Shear Deformation. *Journal of Geotechnical and Geoenvironmental Engineering*, ASCE, 129(12), 1119-1127.

Yang, Z. and A. Elgamal (2008). *OpenSees Soil Models and Solid-Fluid Fully Coupled Elements. User's Manual, 2008 (Version 1.0)*. University of California, San Diego, CA.

Youd, T. L., I. M. Idriss, R. D. Andrus, et al. (2001). Liquefaction Resistance of Soils: Summary Report from the 1996 NCEER and 1998 NCEER/NSF Workshop on Evaluation of Liquefaction Resistance of Soils. *Journal of Geotechnical and Geoenvironmental Engineering*, ASCE, 127(10), 817-833.

APPENDIX A: NUMERICAL ANALYSIS OF STRESS AND SETTLEMENT SOIL RESPONSES

A.1 INTRODUCTION

The neutral plane (NP) analysis presented in Chapter 3 makes the assumption that the pile settlement equals the soil settlement at the equilibrium location and that the load transfer during liquefaction within the liquefied layer is nearly zero. This assumption is in contrast with that of Wang and Brandenberg (2013) who assume that the relative velocity between the pile and the soil is zero at the NP location. In order to examine the validity of the assumptions for liquefaction, a numerical simulation of the downdrag problem was conducted for this study using finite element analysis.

OpenSees (Open System for Earthquake Engineering Simulation) is a widely used finite element software package in earthquake geotechnical engineering that has been made available as an open source for users. Many solution procedures and algorithms are available in OpenSees to solve linear and nonlinear structural and geotechnical problems under static or dynamic loading. OpenSees uses a fully programmable scripting language, tcl (tool command language), to define models, analysis steps, and output results (OpenSees 2014). OpenSees often is used by geotechnical engineers to predict ground surface motions in order to develop design response spectra, evaluate dynamic stresses and strains of liquefaction hazards, and determine earthquake-induced forces (Kramer 1996). However, this study focused on the use of numerical analysis to predict stress and settlement responses in order to verify the downdrag analysis method developed in Chapter 3. A soil profile was idealized using a two-dimensional single column in OpenSees, and then the profile was subjected to ground motion.

A.2 SOIL MODELING

In order to facilitate the numerical modeling procedure, the soil profile of the Juan Pablo II Bridge region (Chapter 3) was idealized into three subsoil layers, i.e., medium-dense sand, loose sand (potentially liquefiable), and dense sand, as shown in Figure A.1. The groundwater table is located at the ground surface. For purposes of finite element modeling, the entire profile is represented by a single column composed of the three layers, as shown on the left-hand side of Figure A.1.

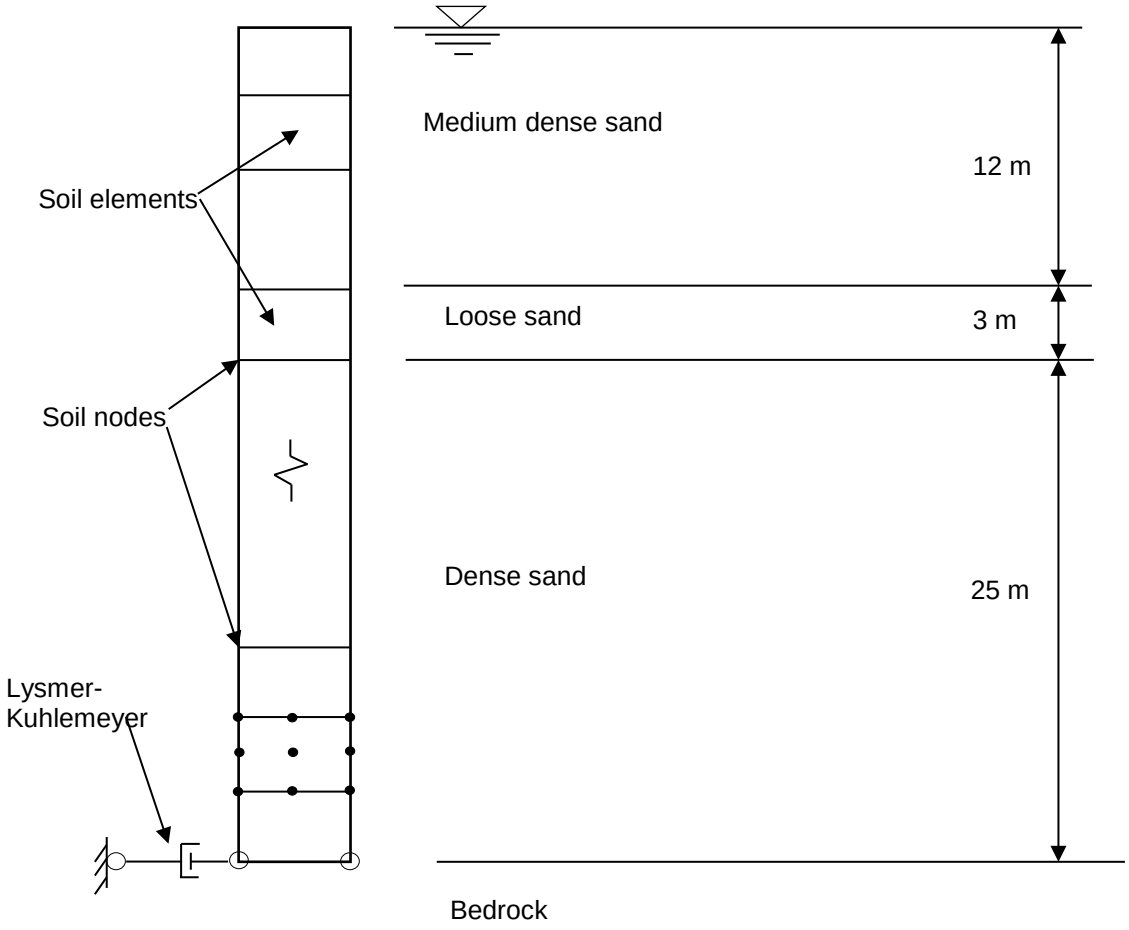

Figure A.1. Soil column modeling for stress and settlement analyses.

The soil domain was discretized using multiphase 9-node quadrilateral plane strain (Nine_Four_Node_QuadUP) elements, as shown in Figure A.2. The four corner nodes have three degrees-of-freedom (DOFs) each: DOFs 1 and 2 for solid displacements (u) and DOF 3 for fluid

pressure (p). The other five nodes have two DOFs each for solid displacements. This element is based on Biot's theory of a porous medium that captures the dynamic response of solid-fluid fully coupled material (Yang and Elgamal 2008). The soil profile was discretized into 0.2-m elements for a total of 200 elements.

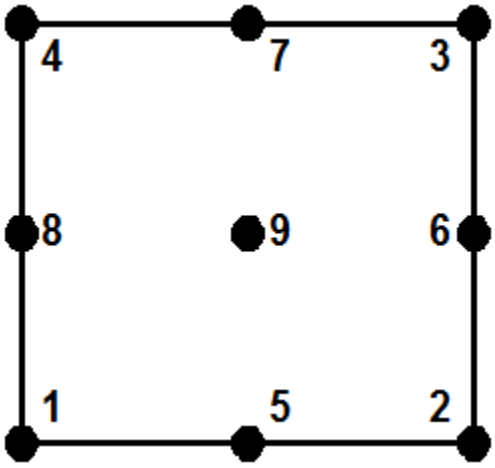

Figure A.2. Solid-fluid fully coupled (u-p) plane strain 9-4 node element.

The soil elements were considered to be elasto-plastic and were input to a model developed by Elgamal and his colleagues (i.e., Yang and Elgamal 2008). This model employed the multi-yield surface (nested surfaces) concept proposed by Iwan (1964) (Figure A.3) with a Drucker–Prager type yield surface to account for pressure dependency (PressureDependMultiYield02, or PDMY02). This model has been shown to be effective in simulating the essential response characteristics of pressure-sensitive soil materials under general loading conditions (Yang and Elgamal 2008). Sands or silts typically exhibit dilatancy (shear-induced volume contraction or dilation) and non-flow liquefaction (cyclic mobility) under monotonic or cyclic loading. In this model, emphasis is placed on controlling the magnitude of cycle-by-cycle permanent shear strain accumulation in clean medium-to-dense sands (Figure A.4). A non-associative flow rule was adopted to reproduce the observed dilation (Lu et al. 2011). Solid-fluid fully coupled elements

with low permeability values can be used to simulate the soil behavior under fully undrained conditions. Note that OpenSees also has a PressureIndependMultiYield (PIMY) material (J2 type) in which plasticity exhibits only in the deviatoric stress-strain response. The latter model is useful for clays and thus is not used here. The model parameters for the PDMY02 material are given in Table A.1, and their descriptions are provided in Section A.3.

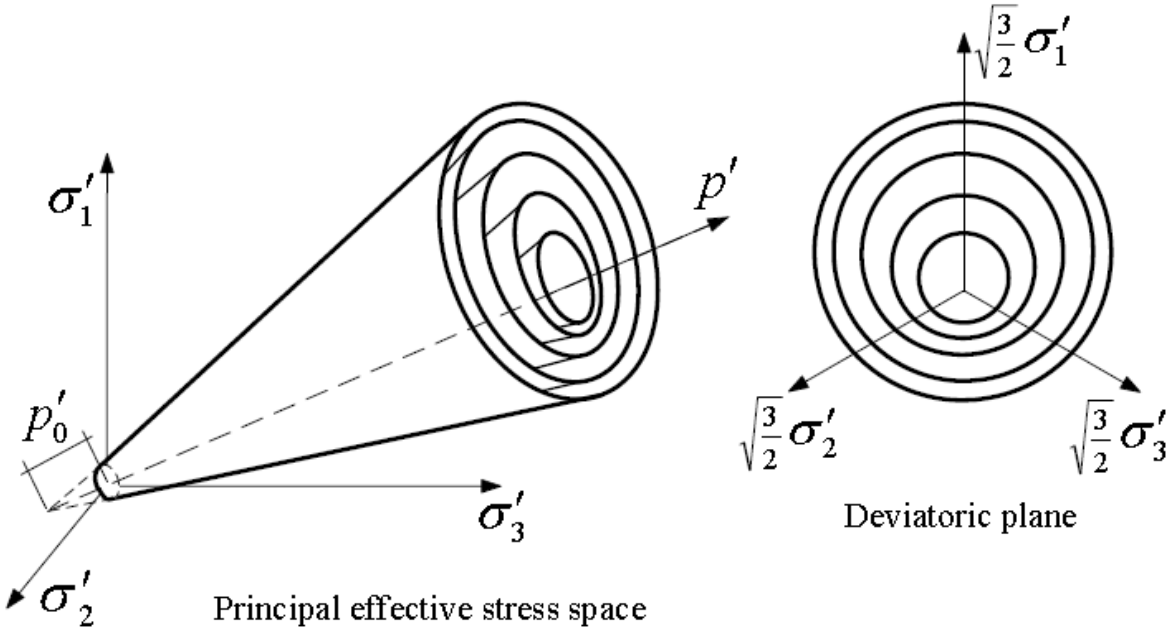

Figure A.3. Multi-yield surfaces in principal effective stress space and deviatoric plane (after Prevost 1985, Parra 1996, and Yang 2000).

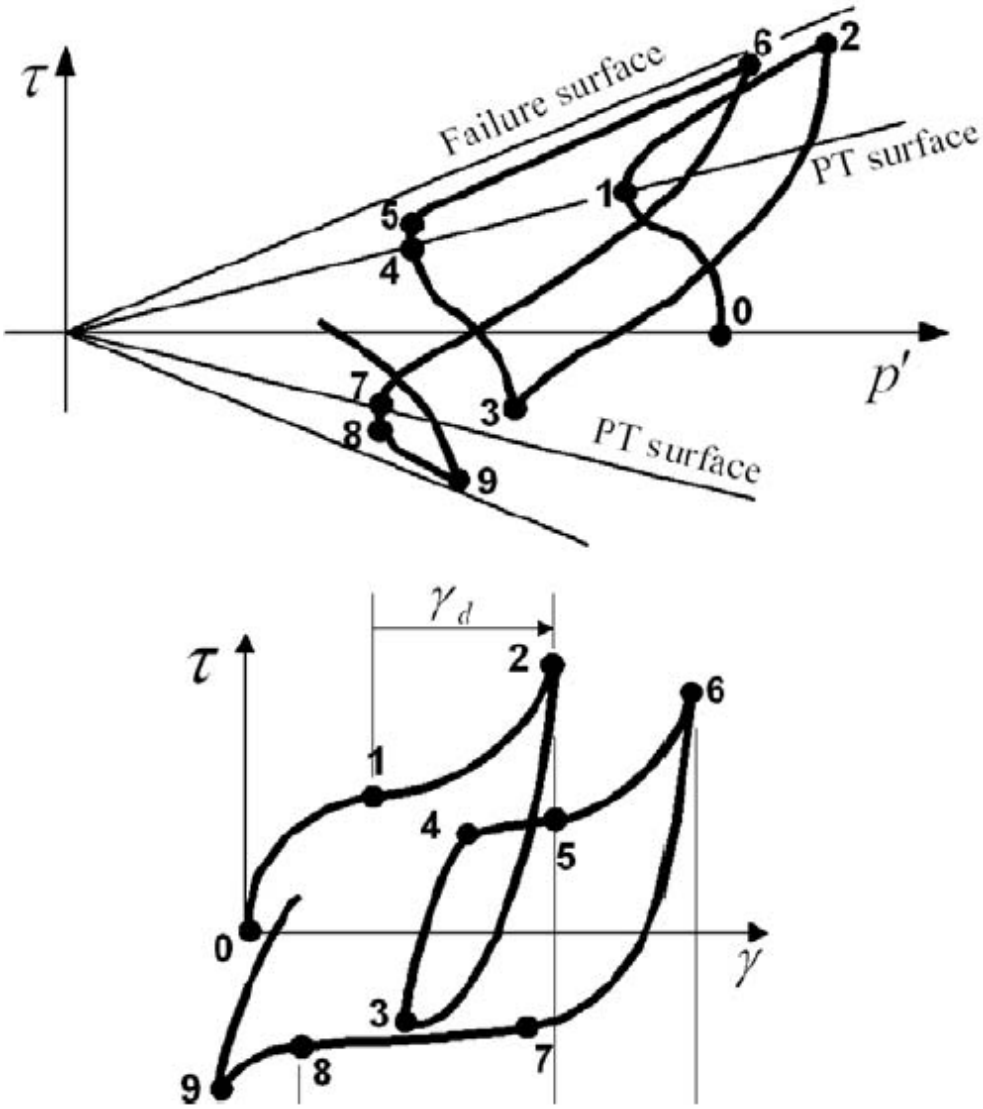

Figure A.4. Shear effective confinement and shear stress-strain response (Yang and Elgamal 2002, Yang et al. 2003).

Table A.1. Soil Model Parameters

Parameters	Layer 1	Layer 2	Layer 3
Tag	1	2	3
nd	2	2	2
Packing type	Dense	Loose	Medium-dense
Rho, ρ (ton/m^3)	2.3	1.85	2.06
Ref Pressure, p'r (kPa)	100	100	100
Permeability Coeff (m/s)	1.0E-02	6.6E-05	1.0E-02
Shear Wave Vel, Vs (m/s)	240	156	232
Ref Shear Modul, Gr (kPa)	1.32E+05	44.8E+03	1.12 E+05
Ref Bulk Modul, Br (kPa)	3.98E+05	1.34E+05	2.98E+05
Friction Ang, Φ (Deg)	37.2	25	45
Peak Shear Strain, γ_{max}	0.1	0.1	0.1
Pressure Depend Coeff, d	0.5	0.5	0.5
PT Angle, Φ_{PT}	32.2	20	32.2
Contraction1	0.001	0.06	0.001
Contraction2	0.5	5.0	0.5
Contraction3	0.0	0.2	0.05
Dilation1	0.4	0.15	0.4
Dilation2	3.0	3.0	3.0
Dilation3	0.0	0.0	0.0
No Yield Surfaces	20	20	20
Liquefaction1	1.0	1.0	1.0
Liquefaction2	0.0	0.0	0.0
Void Ratio, e	0.55	0.76	0.58

A.3 SOIL MODEL PARAMETERS

This section describes the soil model parameters that are used for PDMY02. This constitutive model includes more than fifteen parameters (OpenSees 2014), as listed below:

- Tag – unique positive integer tag to identify the material
- nd – number of dimensions
- rho – saturated soil mass density
- refPress (p'_r) – reference mean effective confining pressure at which G_r, B_r, and γ_{max} are defined

- refShearModul (G_r) – reference low strain shear modulus at refPress (p'_r)
- refBulkModul (G_r) – reference bulk modulus at refPress (p'_r)
- frictionAng (Φ) – friction angle at peak strength, in degrees
- peakShearStra (γ_{max}) – octahedral shear strain at which shear strength is reached, specified at refPress (p'_r)

$$\gamma_{oct} = \frac{2}{3}\left[\left(\varepsilon_{xx} - \varepsilon_{yy}\right)^2 + \left(\varepsilon_{yy} - \varepsilon_{zz}\right)^2 + (\varepsilon_{xx} - \varepsilon_{zz})^2 + 6\varepsilon_{xx}^2 + 6\varepsilon_{yy}^2 + 6\varepsilon_{zz}^2\right]^{1/2} \qquad [A.1]$$

- pressDependCoe (d) – positive constant that defines variations of *G* and *B* as a function of instantaneous effective confinement p'

$$G = G_r\left(\frac{p'}{p'_r}\right)^d \qquad [A.2]$$

$$B = B_r\left(\frac{p'}{p'_r}\right)^d \qquad [A.3]$$

- PTAng (Φ_{PT}) – phase transformation angle, in degrees
- contrac1 – non-negative constant that defines the rate of shear-induced volume decrease (contraction) or pore pressure buildup. A larger value corresponds to a faster contraction rate.
- contrac2 – non-negative constant that reflects the dilation history of the contraction tendency (accounts for fabric damage)
- contrac3 – non-negative constant that reflects the K_σ effect (overburden stress effect)
- dilat1 – non-negative constant that defines the rate of shear-induced volume increase (dilation). Larger values correspond to a faster dilation rate.
- dilat2 – non-negative constant that defines the rate of shear-induced volume increase (dilation). A larger value corresponds to a faster dilation rate (accounts for fabric damage)
- dilat3 – non-negative constant that reflects the K_σ effect (overburden stress effect)

- liquefac1 – parameter that controls the mechanism of liquefaction-induced perfectly plastic shear strain accumulation, i.e., cyclic mobility. liquefac1 defines the effective confining pressure below which the mechanism is in effect. Smaller values should be assigned to denser sands.
- liquefac2 – parameter that defines the maximum amount of perfectly plastic shear strain developed at zero effective confinement during each loading phase. Smaller values should be assigned to denser sands.
- liquefac3 – parameter that defines the maximum amount of biased perfectly plastic shear strain γ_b that accumulates at each loading phase under biased shear loading conditions, as γ_b=liquefac2*liquefac3. Typically, liquefac3 takes a value between 0.0 and 3.0. Smaller values should be assigned to denser sands.
- noYieldSurf – number of yield surfaces
- cs1, cs2, cs3 – parameters that define a straight critical-state line, e_c in e-p' space

$$e_c = cs1 - cs2 \log\left(\frac{p'}{p_a}\right) \qquad \text{if } cs3 = 0 \qquad [A.4]$$

$$e_c = cs1 - cs2 \left(\frac{p'}{p_a}\right)^{cs3} \qquad \text{if } cs3 \neq 0 \qquad [A.5]$$

where p_a is the atmospheric pressure for normalization.

- e – initial void ratio
- c – cohesion

A.3 GROUND MOTIONS

Ground motions were recorded at two locations in the city of Concepcion in Chile. One ground motion was located at Colegio Inmaculada Concepcion (36.8281˚S, 73.0483˚W), and the other was located at Colegio San Pedro de la Paz (36.8442˚S, 73.1087˚W). The station at Colegio San Pedro de la Paz was closer to the Juan Pablo II Bridge than the other location and had

representative strong records based on epicentral distance (d_e) 109.1 km, hypocentral distance (d_h) 114.6 km, distance to the surface projection of the fault (d_{sp}) 0.0 km, and distance to the rupture plane (d_{rup}) 36.4 km. Acceleration history values were recorded in two horizontal directions, north-south (NS) and east-west (EW), and in one vertical direction. The peak ground acceleration recorded was about 0.65 g in the NS direction (Boroschek et al. 2012). Figure A.5 shows the recorded horizontal acceleration component and its corresponding velocity and displacement profile in the NS direction.

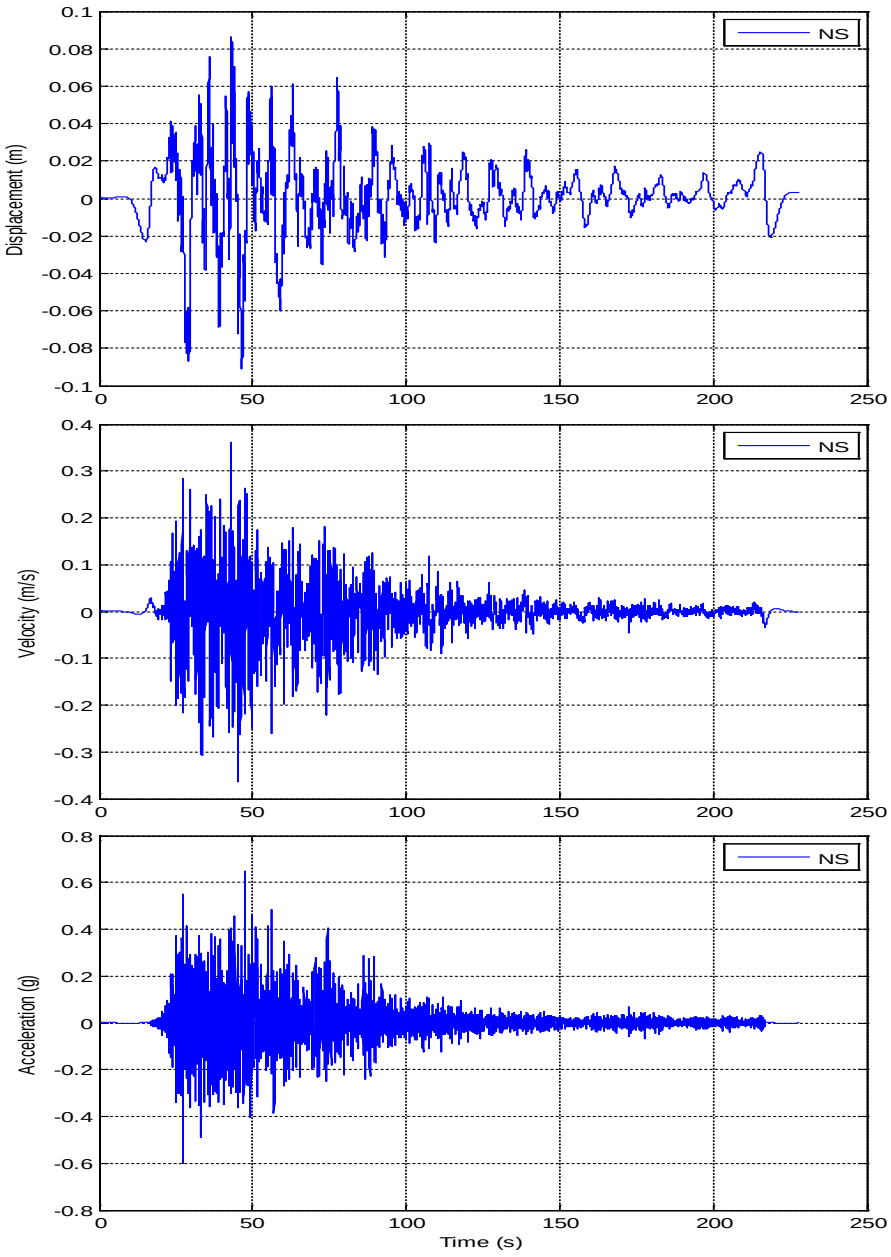

Figure A.5. Time history values of acceleration, velocity, and displacement for the recorded ground motion at the station at Colegio San Pedro de la Paz.

A.4 LOAD AND BOUNDARY CONDITIONS

In the finite element model, the bottom nodes are fixed against the vertical translation. The *equalDOF* command is employed for the nodes that have the same vertical location in order to have equal translational DOFs. The pore pressure DOFs of the corner nodes do not use *equalDOF*, as it was found to cause problems in the analysis (OpenSees 2014). The finite rigidity of the

bedrock is taken into account through a Lysmer-Kuhlemeyer dashpot (1969) and modeled through a *zeroLength* element and the viscous uniaxial material (OpenSees 2014).

The dashpot coefficient is the product of the mass density and shear wave velocity of the bedrock. The dashpot material is defined using the dashpot coefficient and the base area of the soil column. A horizontal force time history, which is proportional to the known velocity time history of the ground motion, is applied at the base of the soil column (corner node). The horizontal force time history is applied as a *Path TimeSeries* object (OpenSees 2014). The force history is a function of the velocity time history, base area of the soil column, and dashpot coefficient. The area of the soil column is included to ensure proportional loading for any desired horizontal element size.

Rayleigh damping parameters were considered in this analysis. Load magnitudes equal to gravity components (vertical, horizontal, inclined) were used to account for gravity. The analysis was implemented in two stages: first by gravity analysis to ensure equilibrium and then by post-gravity analysis (application of earthquake excitation). The permeability of the elements was adjusted in between the analysis stages to maintain hydrostatic conditions after the application of the gravity loads. Each stage of the analysis consisted of separate recorders. The analysis also included penalty constraints, a norm displacement increment test to check for convergence at the end of the iteration steps, and a Krylov-Newton algorithm to solve nonlinear equations (OpenSees 2014). The following section presents the outputs of the soil column analysis.

A.5 RESULTS AND ANALYSIS

Figures A.6 and A.7 present the time history values of acceleration for the recorded ground motions for the site and within the liquefied layer and at the ground surface, respectively. Compared with the base motion (Figure A.5), the observed amplitudes of each of the parameters changed the effect of the soil.

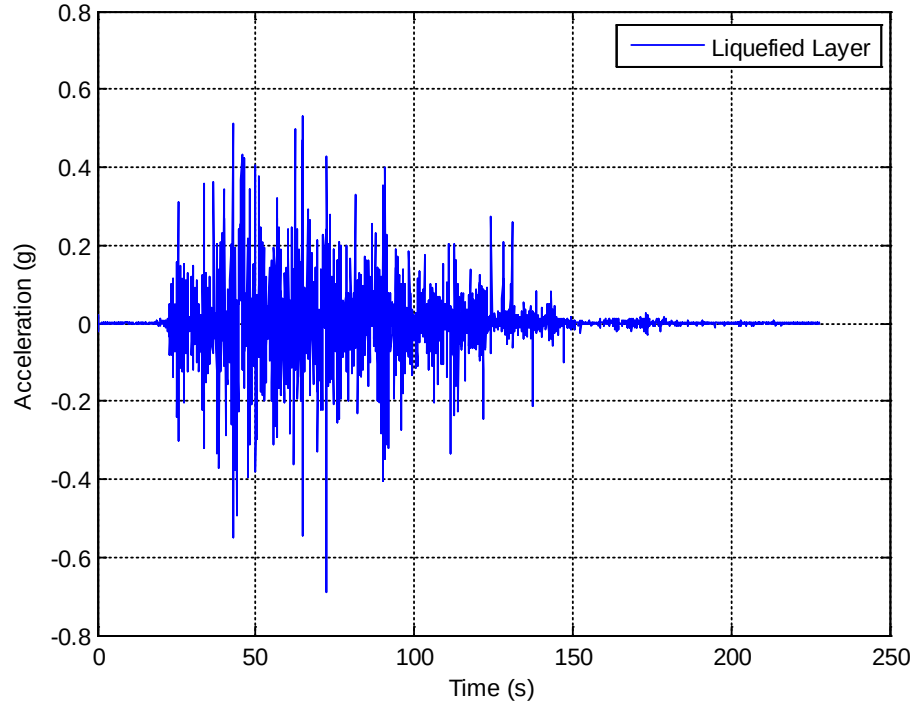

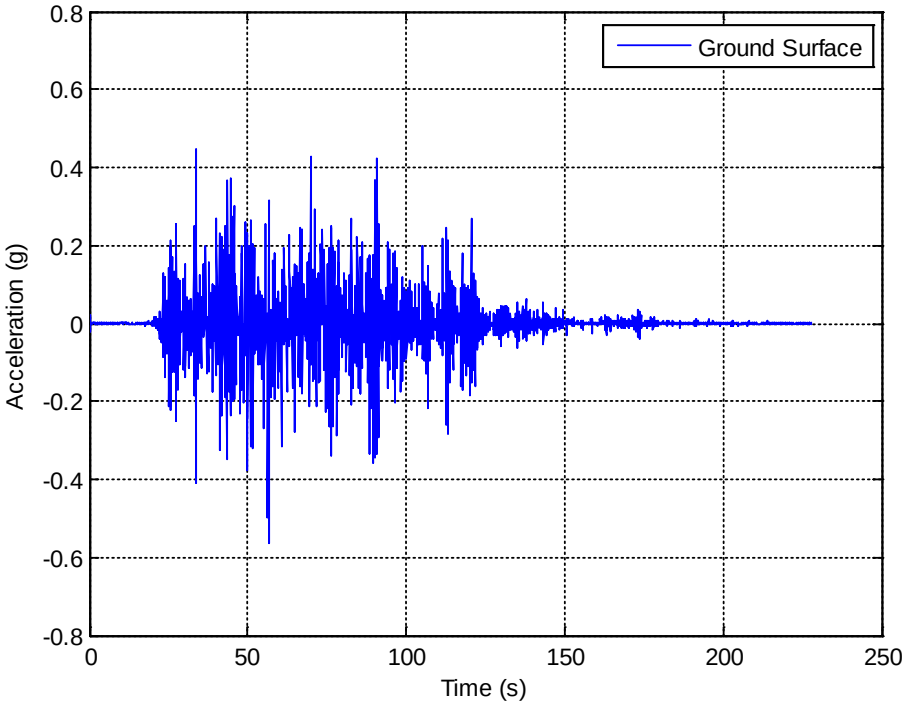

Figure A.6. Acceleration history at ground surface.

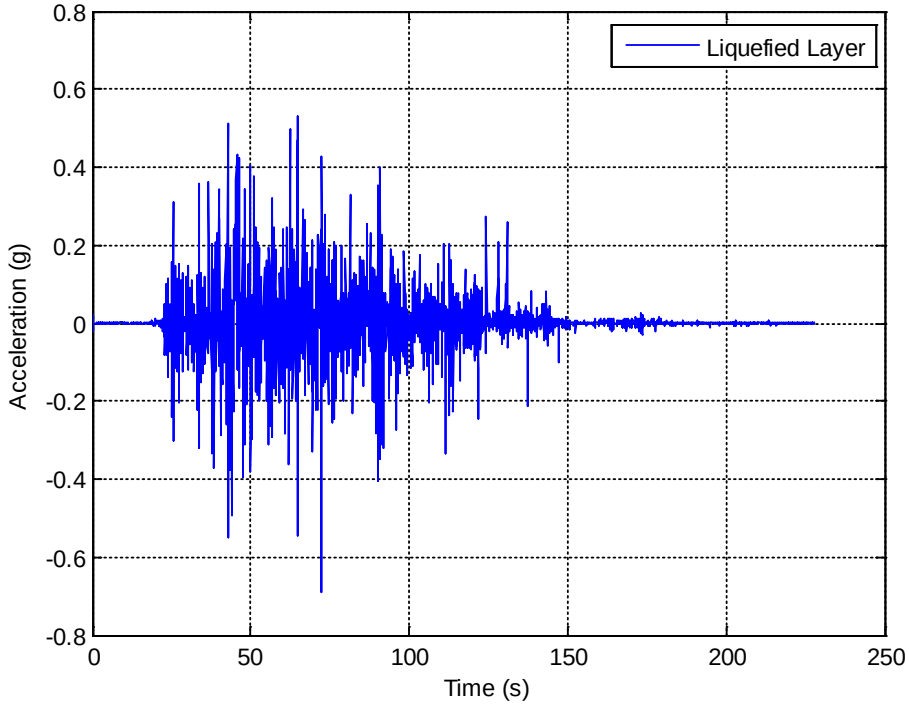

Figure A.7. Acceleration history in the middle of the liquefied layer.

Figure A.8 illustrates the development of the pore pressure ratio (r_u) in terms of the applied time history within the liquefied layer at a depth of 14.5 meters. A layer is considered to be in a liquefied state when the pore pressure ratio reaches unity. Figure A.8 shows that the layer remained liquefied for about 80 s, beginning at about 40 s and ending at 120 seconds. Similar plots of pore pressure ratio with time can be plotted for other depths as well.

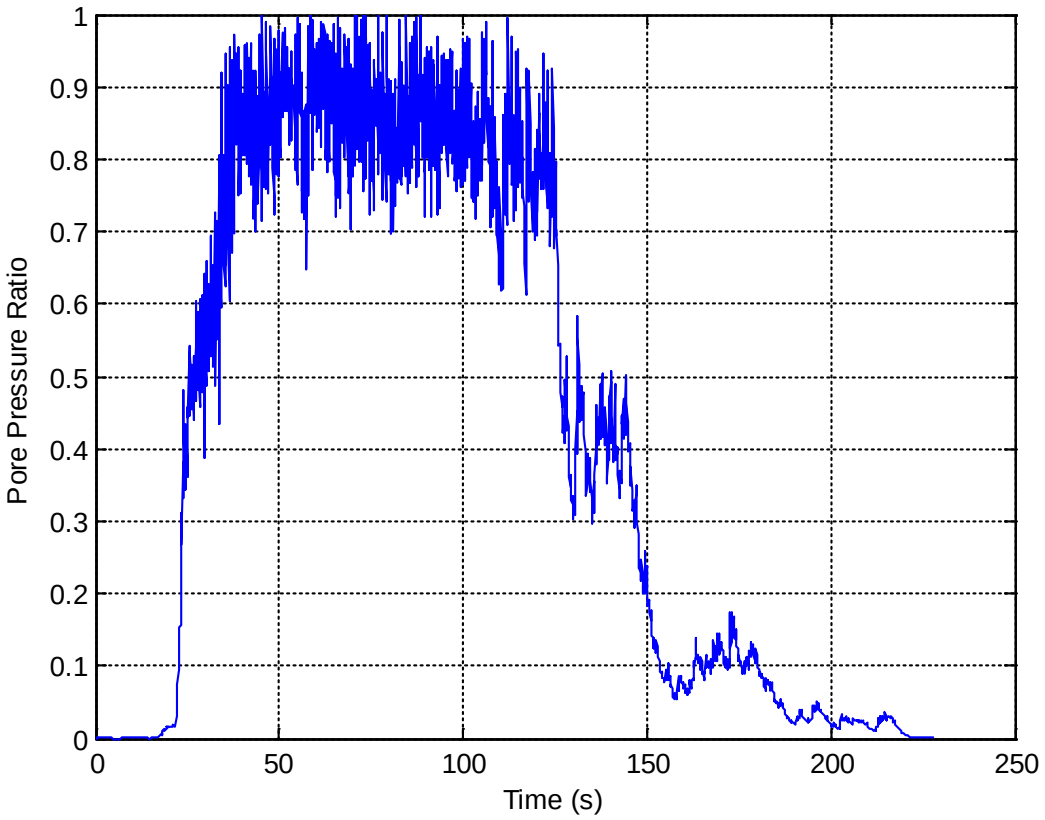

Figure A.8. Pore pressure ratio development within liquefied layer (at depth of 14.5 m) with time.

Figure A.9 presents the variation in pore pressure ratios with depth for different times (44 s, 52 s, 62 s, 65 s). The loose layer that is prone to liquefaction can be identified clearly in this plot. On the other hand, the top layer, which consists of medium-dense sand, does not develop much pore pressure whereas the upper portion of the bottom layer (dense sand) has developed a certain level of pore pressure, perhaps due to the strong shaking at its base.

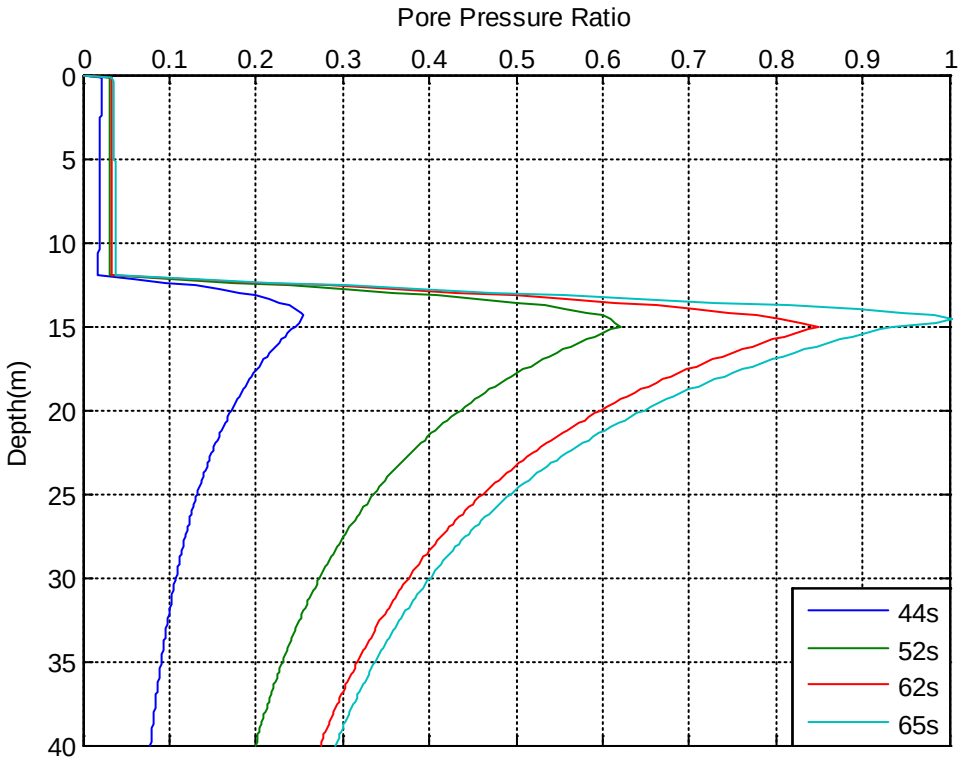

Figure A.9. Pore pressure ratio distribution with depth.

Figure A.10 presents the variations in effective stress with depth for the various times (1 s, 44 s, 52 s, 62 s, 65 s). The effective stress profile at 1 second corresponds closely to the initation of earthquake shaking. The effective stress is seen to decrease progressively with the development of excess pore pressure and nearly reaches zero within the liquefied layer. Figure A.10 also shows that the load transfer during liquefaction is almost zero. This pattern is similar to that observed in the field tests conducted by Rollins and Strand (2008).

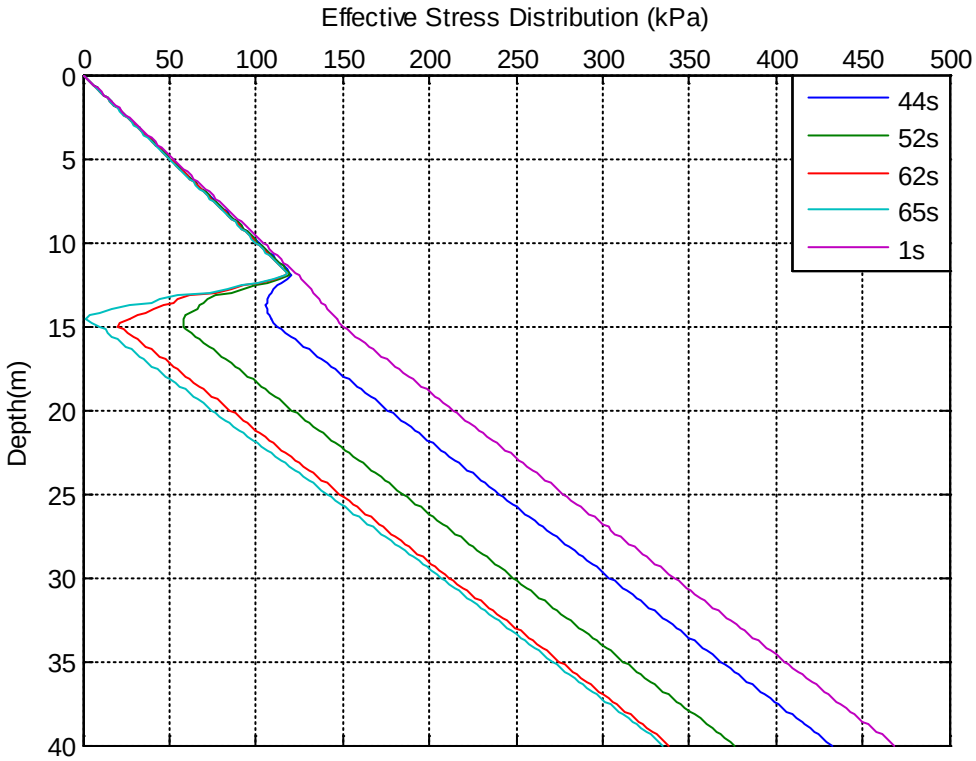

Figure A.10. Effective stress pattern within the soil deposit during shaking.

Figure A.11 presents the variations in the soil settlement pattern with depth at different times (44 s, 52 s, 62 s, 65 s, 227 s). The first four times represent the settlement progress during liquefaction and the final time (227 s) gives the final soil settlement (post-liquefaction) at the end of shaking. The soil settlement is relatively small near the base layers and then increases upwards to the lower side of the liquefied layer. The settlement is then seen to increase substantially within the liquefied layer due to the loss of stiffness and softening. This settlement is transferred to the surface settlement, as seen from the vertical profile. The soil settlement and effective stress distributions within the pile embedment length were used to estimate the axial load distribution and downdrag of the pile.

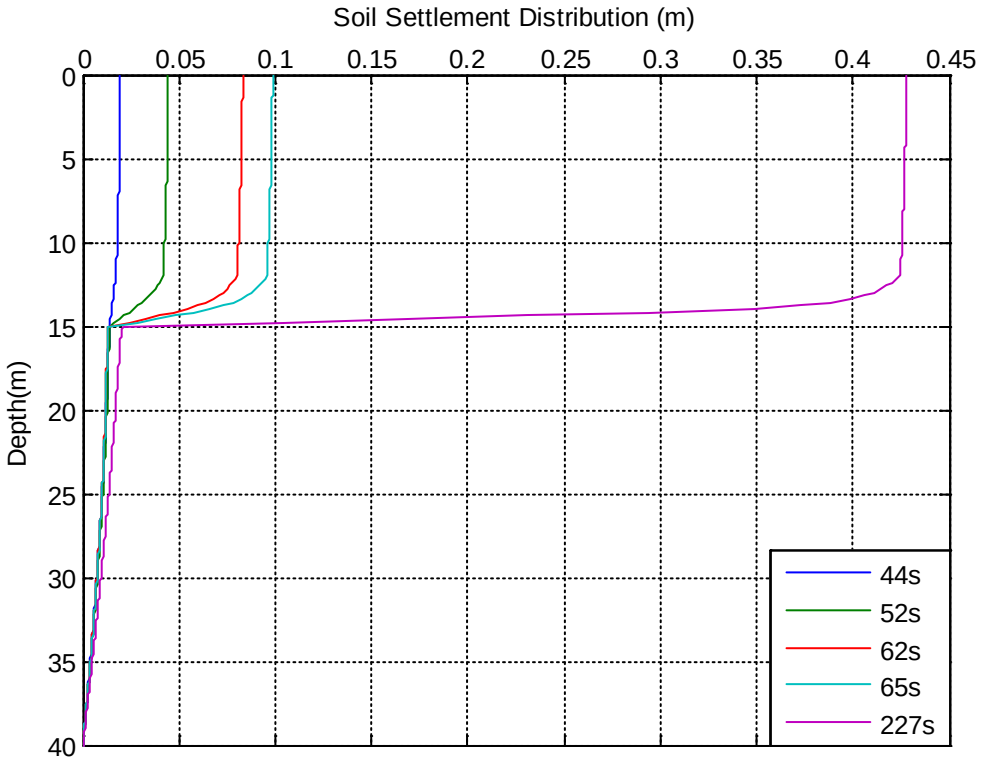

Figure A.11. Soil settlement pattern within the soil deposit during shaking.

A.6 PILE MODELING

A finite element model based on the so-called 'beam on a nonlinear Winkler foundation' was developed for the OpenSees finite element platform (OpenSees 2014). Figure A.12 presents a schematic diagram of the model. A pile, 2.5 m in diameter and 16 m in length, was modeled using elastic beam column elements. The model is defined in two dimensions with three DOFs. The pile was discretized into 80 elements and its Young's modulus was 35 GPa. Pile nodes were constrained against lateral movement and rotation. The other ends of the spring nodes were fixed in all DOFs during the gravity analysis and updated to free the vertical translational DOFs during the transient stage. Nonlinear interface spring elements, t-z and q-z, were chosen to represent the vertical soil response and toe response, respectively. *zeroLength* elements were used to generate

the soil springs. *TzSimple1* and *TzLiq1* are the material models for non-liquefaction conditions and liquefaction conditions, respectively. The input parameters for *TzSimple1* are (1) ultimate capacity (t_{ult}) of the t-z material, (2) displacement (z_{50}) at which 50 percent of the t_{ult} is mobilized during monotonic loading, (3) a viscous damping term (c_{dash}), and (4) two types of backbone relationships for soil types as derived by Reese and O'Neill (1987) and Mosher (1984), respectively. *TzLiq1* inherits *TzSimple1* and modifies its responses based on excess pore pressure during seismic loading (Boulanger et al. 2003).

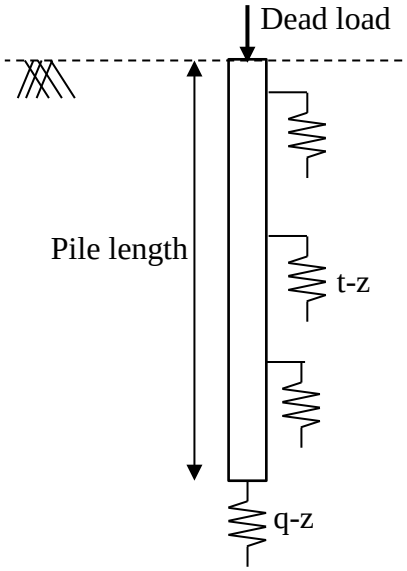

Figure A.12. Schematic diagram of finite element model.

The q-z material for the non-liquefaction condition is *QzSimple1*. The input parameters for the q-z material are (1) ultimate capacity (q_{ult}) of the q-z material in compression loading, (2) displacement (z_{50}) at which 50 percent of the t_{ult} is mobilized during monotonic loading, (3) a viscous damping term (c_{dash}), (4) Vijayvergiya's (1977) backbone relationship for piles in sand and Reese and O'Neill's (1987) relationship for drilled shafts in clay, and (5) an argument for pile toe uplift resistance (Boulanger et al. 2003).

A.7 DRAG LOAD CALCULATIONS

The soil deposit used here consists of three sandy soil layers: medium-dense sand (12 m), loose sand (3 m), and dense sand (25 m). The interface friction angles for the loose, medium, and dense sand were chosen to be 29˚, 30˚, and 31˚, respectively. Soil settlement and effective stress were applied at the free end of the spring elements. A dead load of 12,500 kN was applied at the pile head using a plain load pattern (OpenSees 2014). This analysis also was implemented in two stages as in the previous case of soil column analysis. It also included penalty constraints, a norm displacement increment test to check for convergence at the end of the iteration steps, and the Newton algorithm to solve the nonlinear equations (OpenSees 2014).

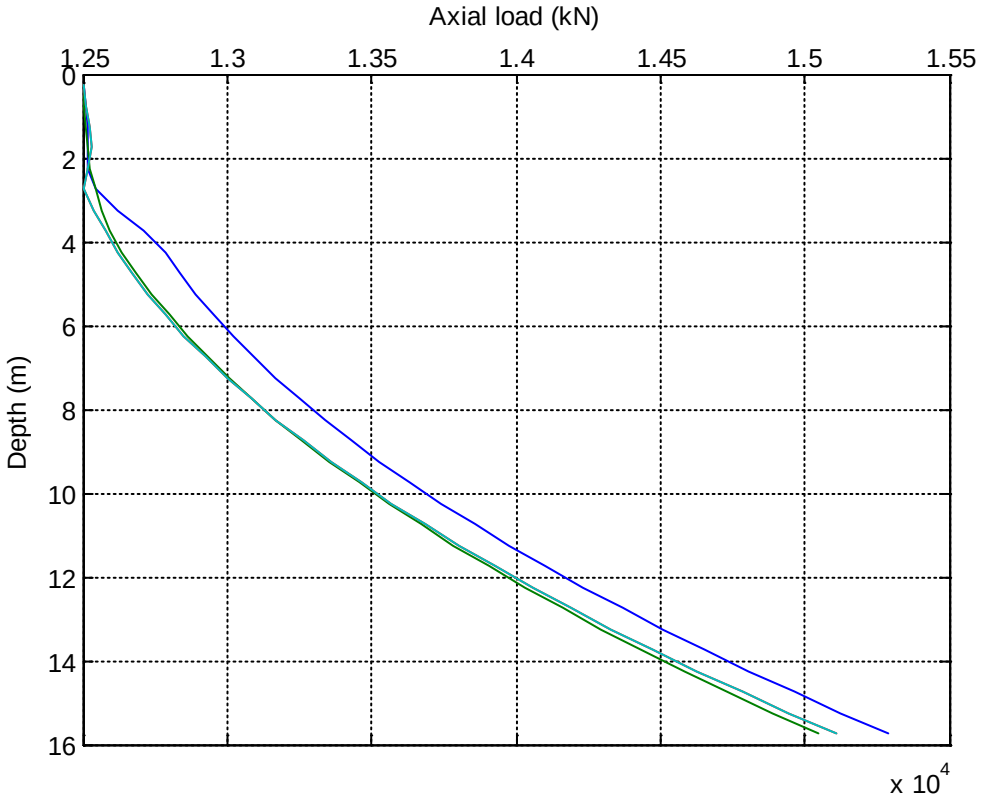

Figure A.13. Axial load distribution due to liquefaction-induced downdrag.

APPENDIX B: DOWNDRAG ANALYSIS FOR WSDOT CASE STUDIES

This Appendix B summarizes the liquefaction-induced downdrag analyses for the case studies in Chapters 3, and 4. Figures B-1 to B-4 show the analysis results for Pier 1 and 2 at the I-5/SR 432 Talley Way interchange. These analyses were performed for the two Cases introduced in Section 3.3.1:

- Case I: No negative side resistance develops prior to liquefaction.
- Case II: Negative side resistance develops along the shaft based on 0.4-inch downdrag settlement before liquefaction.

The load and resistance curves before and immediately after liquefaction are shown at the top left of Figures B-1 to B-4. The load distributions for the short-term and long-term conditions are shown at the top right of the figures. The load and settlement curves for tip resistance and tip penetration are shown at the bottom right of each figure. Once the load distribution and load and settlement curves are obtained, the downdrag settlements for the short-term, long-term before and after liquefaction, and ultimate downdrag (negative side resistance all along the shaft) conditions can be calculated; Figures B-1 to B-4 present these values.

Figures B-5 and B-6 show two sections of the bridge profile with the location of the piers and the available in situ test results for the NE 139th Street near the I-5/I-205 interchange. Tables B-1 through B-10 summarize the soil profiles under each pier. Figures B-7 through B-23 present the analysis results for the drilled shafts for Piers 1 through 10 in this case study. Figures B-24 through B-31 serve to summarize the analyses for Juan Pablo II Bridge Piers 1-2, 5-6, 117-118, and 119-120.

Project name and location: I5 / SR 432- Talley Way interchange, Pier 1
8-feet drilled shaft, L = 160 ft

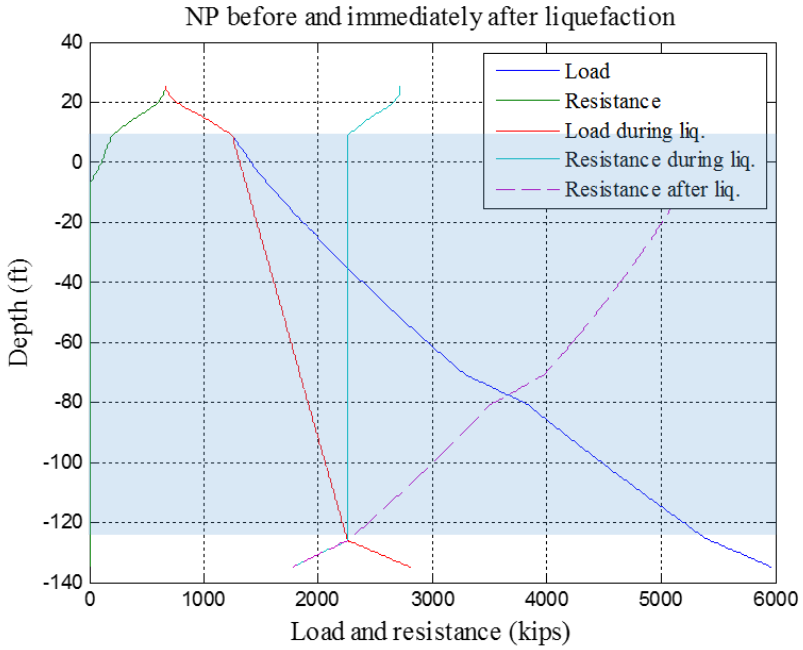

Max drag load before liquefaction (% of ultimate drag load)	0.0 kips (0 %)
Max drag load after liquefaction (% of ultimate drag load)	2223 kips (54 %)
Ultimate drag load	4107 kips
NP location before liquefaction (ft)	25.0
NP location after liquefaction (ft)	-77.7

*Drag load based on WSDOT approach (Average of nominal and residual side resistance) equals 2528 kips.

δ (long-term after liq.) = 4.1764 inch , R (long-term after liq.) = 1777.8498 kips
δ (Ultimate) = 21.948 inch , R (Ultimate) = 5969.3202 kips

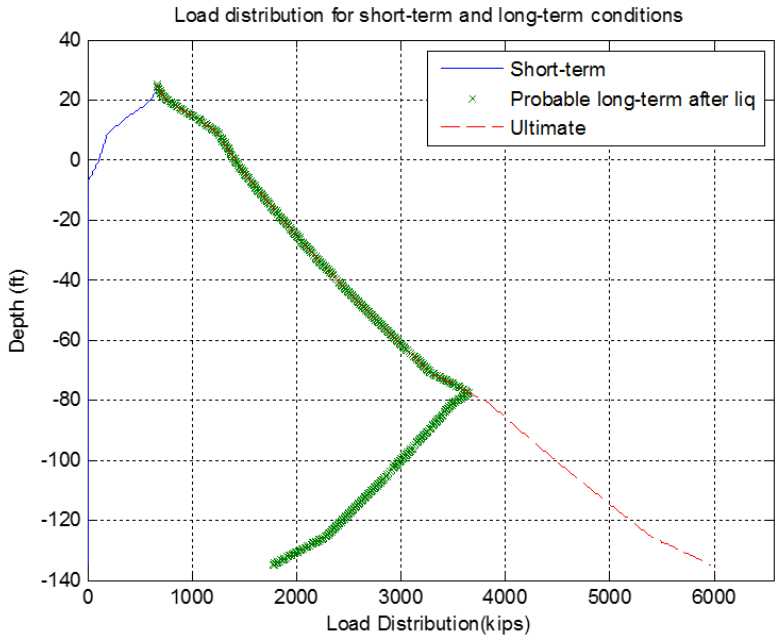

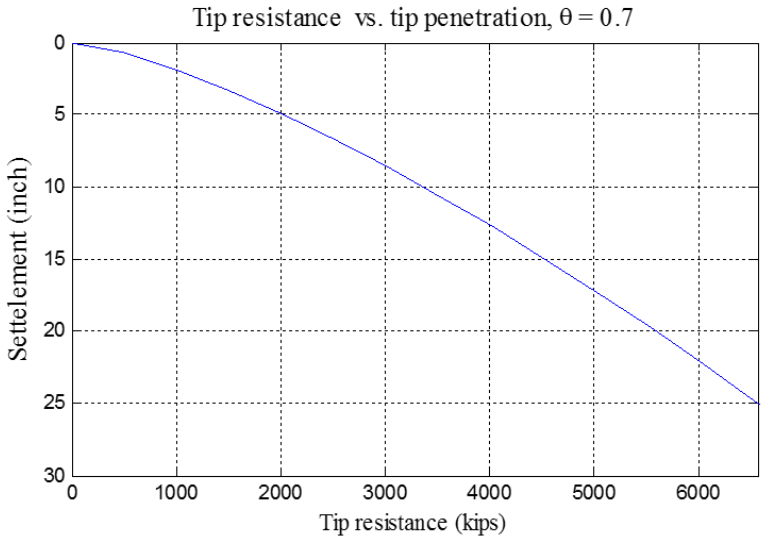

Figure B-1. I-5/SR 432 Talley Way interchange Pier 1: Case I.

Project name and location: I5 / SR 432- Talley Way interchange, Pier 1
8-feet drilled shaft, L = 160 ft

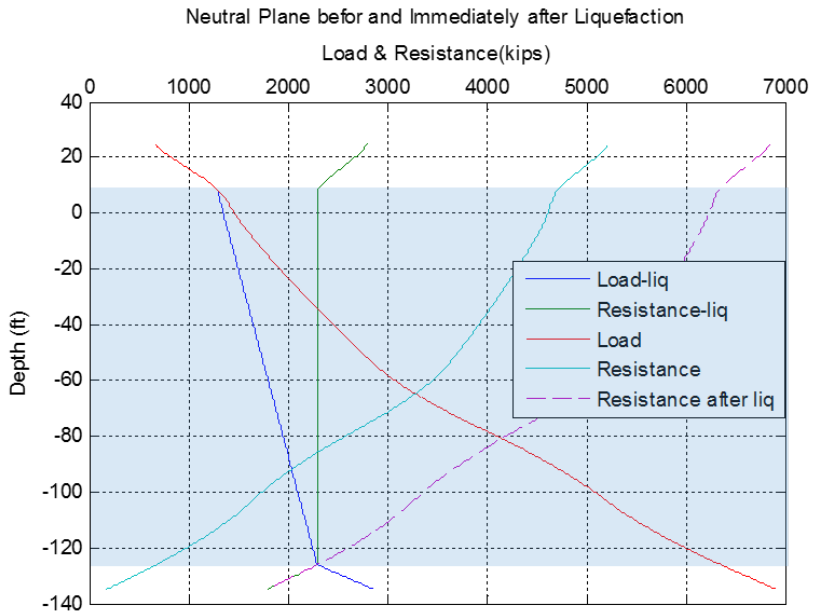

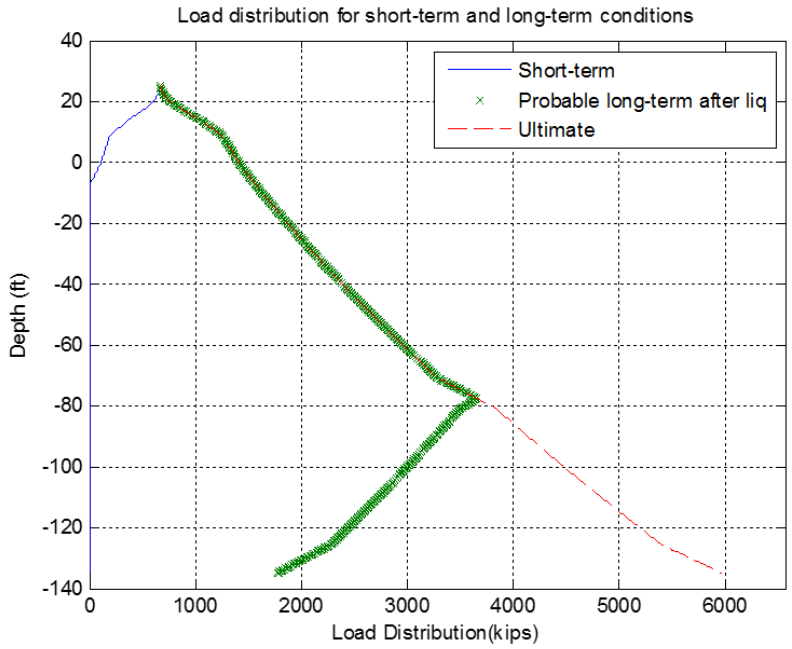

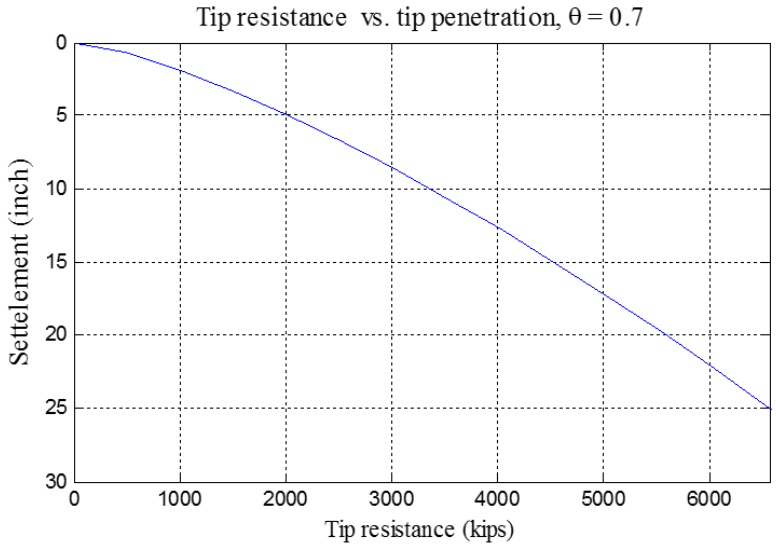

Max drag load before liquefaction (% of ultimate drag load)	0.0 kips (0 %)
Max drag load after liquefaction (% of ultimate drag load)	2223 kips (54 %)
Ultimate drag load	4107 kips
NP location before liquefaction (ft)	25.0
NP location after liquefaction (ft)	-77.7

*Drag load based on WSDOT approach (Average of nominal and residual side resistance) equals 2528 kips.

δ (long-term after liq.) = 4.1764 inch , R (long-term after liq.) = 1777.8498 kips
δ (Ultimate) = 21.948 inch , R (Ultimate) = 5969.3202 kips

Figure B-2. I-5/SR 432 Talley Way I-5 interchange Pier 1: Case II.

Project name and location: I5 / SR 432- Talley Way interchange, Pier 2
8-feet drilled shaft, L = 150 ft

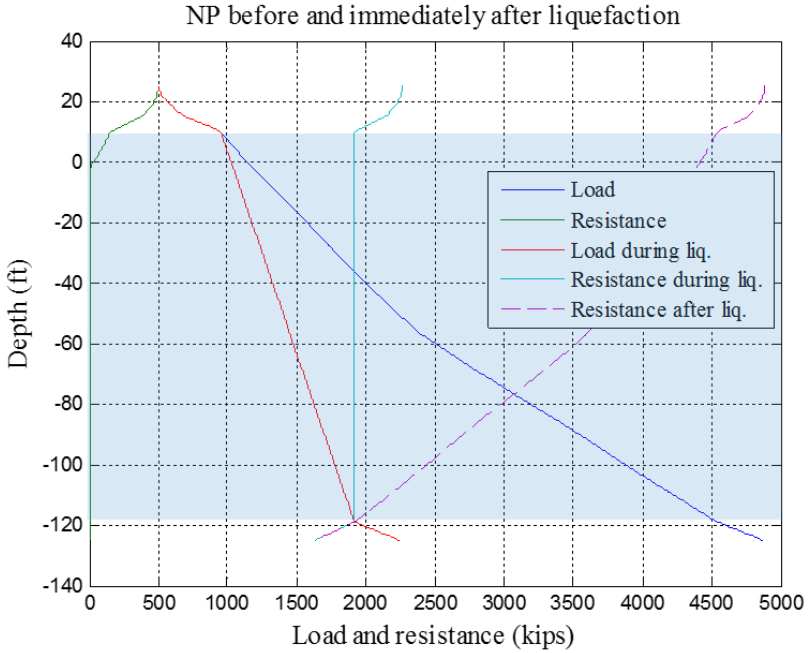

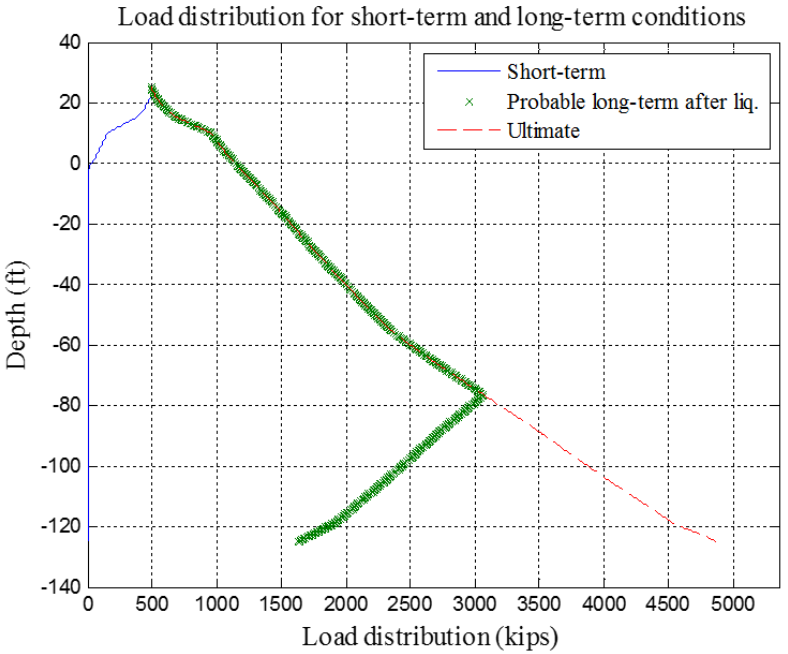

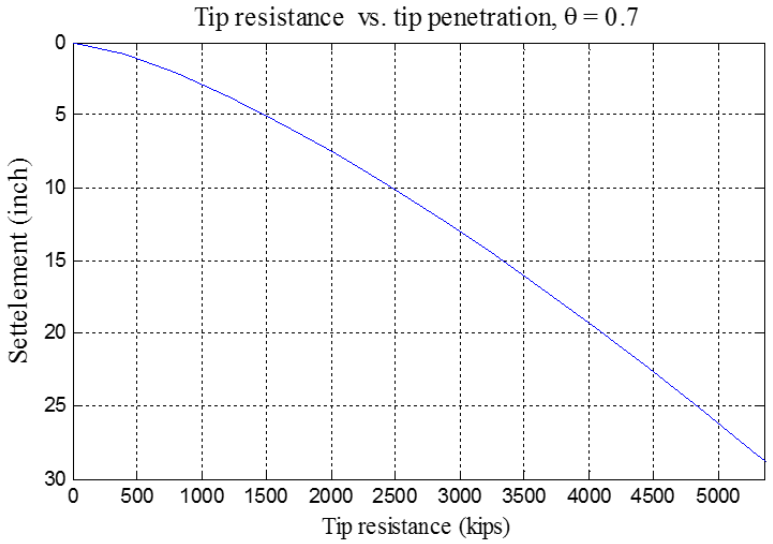

Max drag load before liquefaction (% of ultimate drag load)	0 kips (0 %)
Max drag load after liquefaction (% of ultimate drag load)	1811 kips (56 %)
Ultimate drag load	3252 kips
NP location before liquefaction (ft)	25.0
NP location after liquefaction (ft)	-76.6

*Drag load based on WSDOT approach (Average of nominal and residual side resistance) equals 1942 kips.

δ (long-term after liq.) = 5.658 inch , R (long-term after liq.) = 1633.5098 kips
δ (Ultimate) = 25.2698 inch , R (Ultimate) = 4870.5223 kips

Figure B-3. I-5/SR 432 Talley Way interchange Pier 2: Case I.

Project name and location: I5 / SR 432- Talley Way interchange, Pier 2
8-feet drilled shaft, L = 150 ft

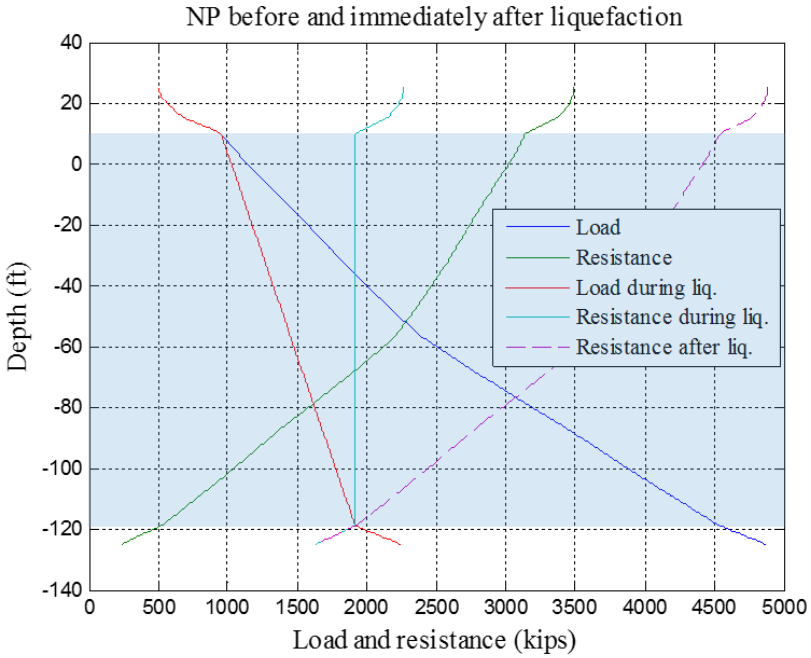

Max drag load before liquefaction (% of ultimate drag load)	1168 kips (36 %)
Max drag load after liquefaction (% of ultimate drag load)	1812 kips (56 %)
Ultimate drag load	3252 kips
NP location before liquefaction (ft)	-49.5
NP location after liquefaction (ft)	-76.6

*Drag load based on WSDOT approach (Average of nominal and residual side resistance) equals 1942 kips.

δ (short-term) = 0 inch, R (short-term) = 0 kips
δ (long-term before liq.) = 0.3937 inch , R (long-term before liq.) = 233.4254 kips
δ (long-term after liq.) = 5.6488 inch , R (long-term after liq.) = 1631.5576 kips
δ (Ultimate) = 25.2698 inch , R (Ultimate) = 4870.5223 kips

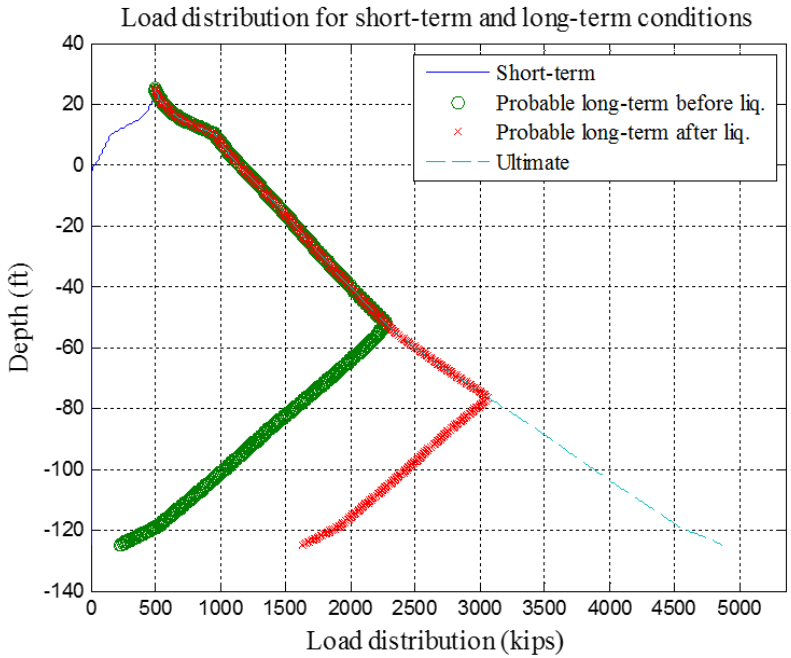

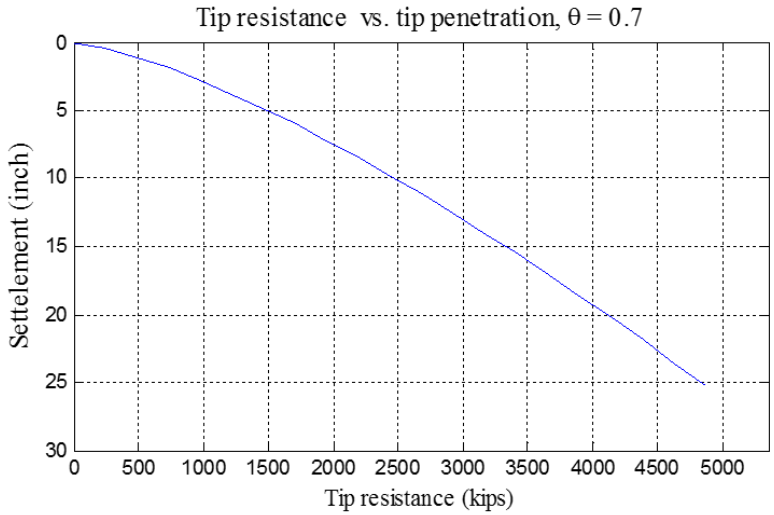

Figure B-4. I-5/SR 432 Talley Way interchange Pier 2: Case II.

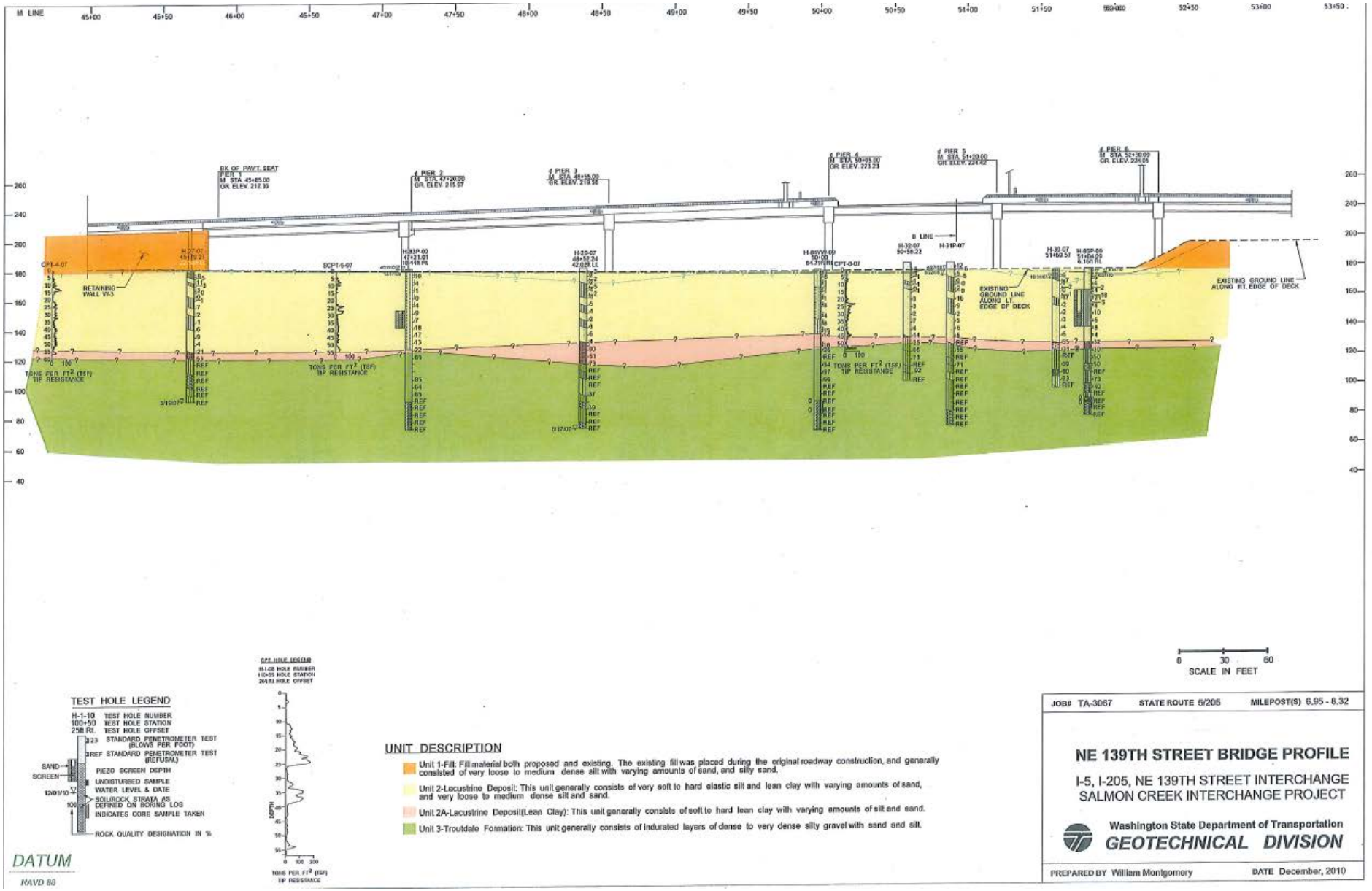

Figure B-5. Bridge profile of the NE 139th Street near the I-5/I-205 interchange

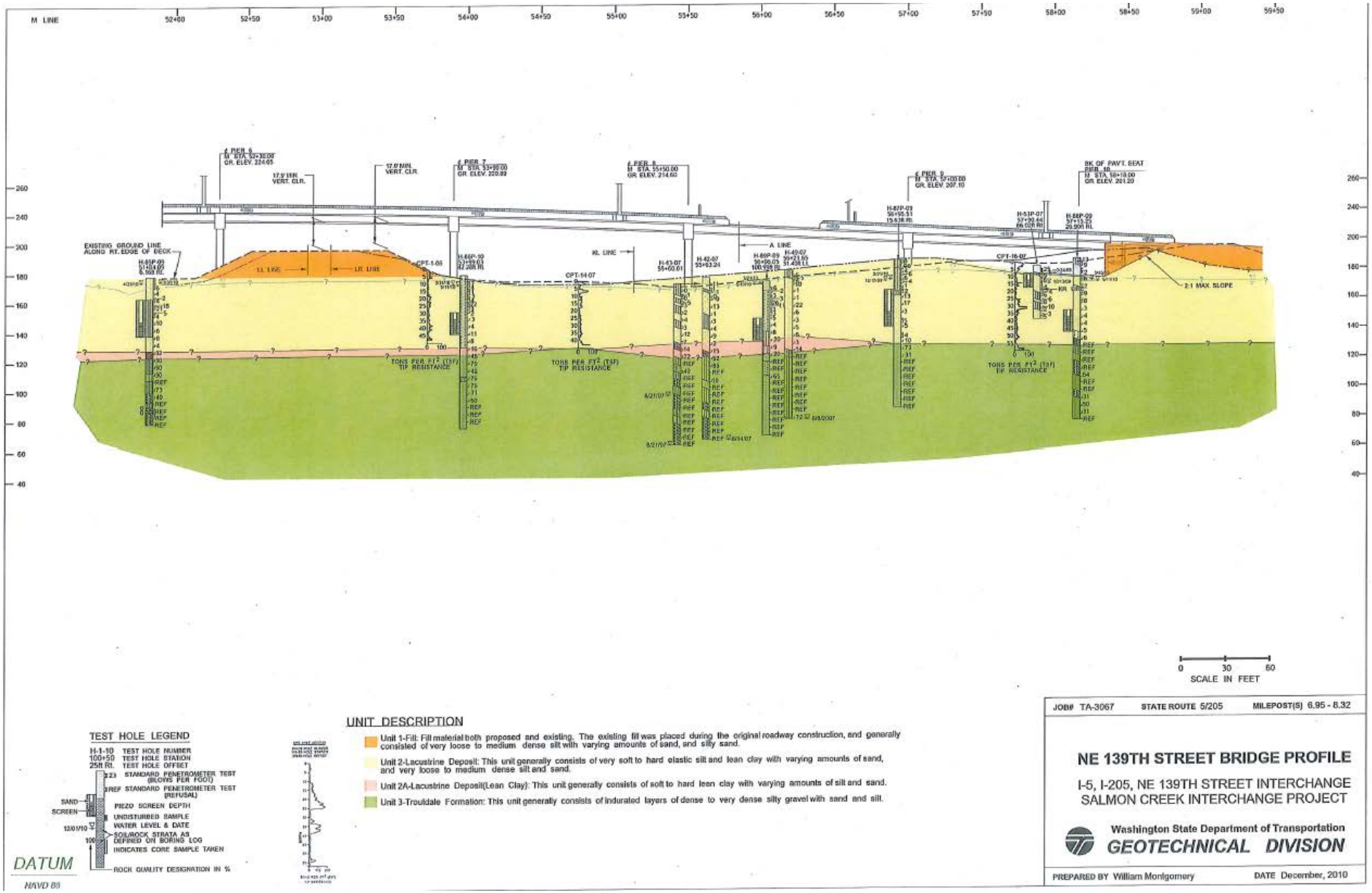

Figure B-6. Bridge profile of the NE 139th Street near the I-5/I-205 interchange

Table B-1. Soil profile under pier 1

Layer	Soil Type	Layer Thickness (ft)	$(N_1)_{60}$	Liquefiable?	Eff. Unit Weight (pcf)
1	Clay	4	19	No	56
2	Sand	5	17	Yes	56
3	Sand	5	6	Yes	56
4	Sand	10	1	Yes	56
5	Sand	5	10	Yes	56
6	Sand	10	2	Yes	56
7	Sand	10	10	Yes	56
8	Sand	5	5	Yes	56
9	Clay	5	26	No	56
10	Sand	71	50	No	78

Table B-2. Soil profile under pier 2

Layer	Soil Type	Layer Thickness (ft)	$(N_1)_{60}$	Liquefiable?	Eff. Unit Weight (pcf)
1	Sand	7	23	No	56
2	Sand	7	7	Yes	56
3	Clay	3	1	No	56
4	Sand	12	4	Yes	56
5	Sand	10	11	Yes	56
6	Sand	15	20	Yes	56
7	Sand	5	27	No	56
8	Sand	71	50	No	78

Table B-3. Soil profile under pier 3

Layer	Soil Type	Layer Thickness (ft)	$(N_1)_{60}$	Liquefiable?	Eff. Unit Weight (pcf)
1	Sand	12	6	Yes	56
2	Sand	5	9	Yes	56
3	Sand	2	4	Yes	56
4	Sand	15	6	Yes	56
5	Sand	10	4	Yes	56
6	Clay	10	7	No	56
7	Clay	10	49	No	78
8	Sand	66	50	No	78

Table B-4. Soil profile under pier 4

Layer	Soil Type	Layer Thickness (ft)	$(N_1)_{60}$	Liquefiable?	Eff. Unit Weight (pcf)
1	Sand	8	20	Yes	56
2	Sand	16	1	Yes	56
3	Sand	17	10	Yes	56
4	Sand	10	20	Yes	56
5	Clay	3	24	No	56
6	Sand	5	32	No	78
7	Sand	71	50	No	78

Table B-5. Soil profile under pier 5

Layer	Soil Type	Layer Thickness (ft)	$(N_1)_{60}$	Liquefiable?	Eff. Unit Weight (pcf)
1	Sand	4	32	No	56
2	Sand	8	12	Yes	56
3	Sand	12	2	No	56
4	Sand	5	24	Yes	56
5	Sand	5	13	Yes	56
6	Sand	5	3	Yes	56
7	Sand	15	7	No	56
8	Sand	76	50	No	78

Table B-6. Soil profile under pier 6

Layer	Soil Type	Layer Thickness (ft)	$(N_1)_{60}$	Liquefiable?	Eff. Unit Weight (pcf)
1	Sand	9	18	Yes	56
2	Sand	10	6	Yes	56
3	Sand	2	38	No	56
4	Sand	18	5	Yes	56
5	Sand	5	14	Yes	56
6	Clay	5	11	No	56
7	Sand	5	23	Yes	78
8	Sand	76	50	No	78

Table B-7. Soil profile under pier 7

Layer	Soil Type	Layer Thickness (ft)	$(N_1)_{60}$	Liquefiable?	Eff. Unit Weight (pcf)
1	Sand	13	12	Yes	56
2	Sand	5	6	Yes	56
3	Sand	5	34	No	56
4	Sand	7	8	Yes	56
5	Sand	20	10	Yes	56
6	Clay	5	42	No	78
7	Sand	5	37	No	78
8	Sand	70	50	No	78

Table B-8. Soil profile under pier 8

Layer	Soil Type	Layer Thickness (ft)	$(N_1)_{60}$	Liquefiable?	Eff. Unit Weight (pcf)
1	Sand	12	2	Yes	56
2	Sand	2	13	Yes	56
3	Sand	20	6	Yes	56
4	Sand	5	18	Yes	56
5	Clay	5	11	No	56
6	Sand	5	20	Yes	78
7	Sand	15	50	No	78
8	Sand	66	50	No	78

Table B-9. Soil profile under pier 9

Layer	Soil Type	Layer Thickness (ft)	$(N_1)_{60}$	Liquefiable?	Eff. Unit Weight (pcf)
1	Sand	4	22	No	56
2	Sand	3	50	No	56
3	Sand	10	8	Yes	56
4	Sand	7	2	Yes	56
5	Sand	10	20	Yes	56
6	Sand	20	5	Yes	56
7	Sand	5	12	Yes	56
8	Sand	71	50	No	76

Table B-10. Soil profile under pier 10

Layer	Soil Type	Layer Thickness (ft)	$(N_1)_{60}$	Liquefiable?	Eff. Unit Weight (pcf)
1	Sand	8	24	No	56
2	Sand	6	4	Yes	56
3	Sand	5	9	Yes	56
4	Sand	5	3	Yes	56
5	Sand	10	12	Yes	56
6	Sand	20	5	Yes	56
7	Clay	5	7	No	56
8	Sand	71	50	No	78

Project name and location: SR 5 139th St NE Bridge, Pier 1
6-feet drilled shaft, L = 75 ft

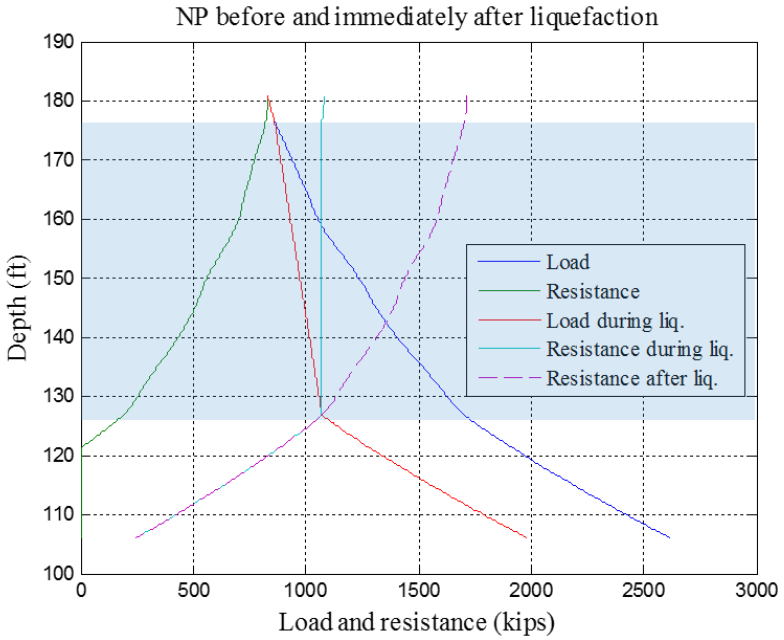

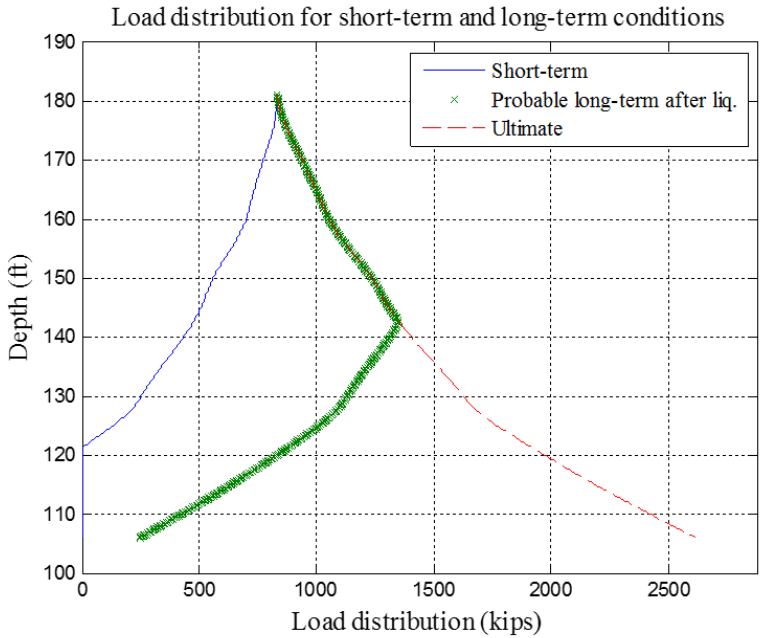

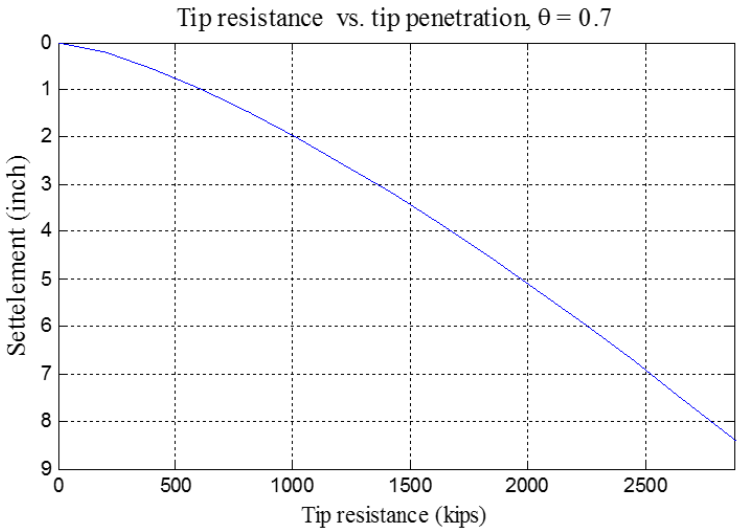

Max drag load before liquefaction (% of ultimate drag load)	0.0 kips (0 %)
Max drag load after liquefaction (% of ultimate drag load)	325 kips (20 %)
Ultimate drag load	1598 kips
NP location before liquefaction (ft)	181.0
NP location after liquefaction (ft)	141.0

*Drag load based on WSDOT approach (Average of nominal and residual side resistance) equals 1309 kips.

δ (long-term after liq.) = 0.28963 inch , R (long-term after liq.) = 246.6121 kips
δ (Ultimate) = 7.3594 inch , R (Ultimate) = 2616.1931 kips

Figure B-7. SR 5 139th St NE Bridge Pier 1: Case I.

Project name and location: SR 5 139th St NE Bridge, Pier 1
6-feet drilled shaft, L = 75 ft

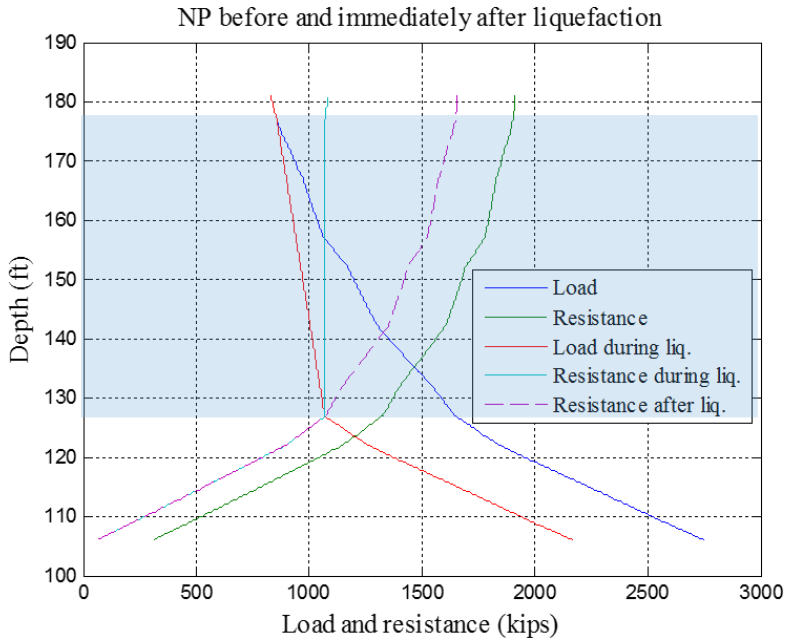

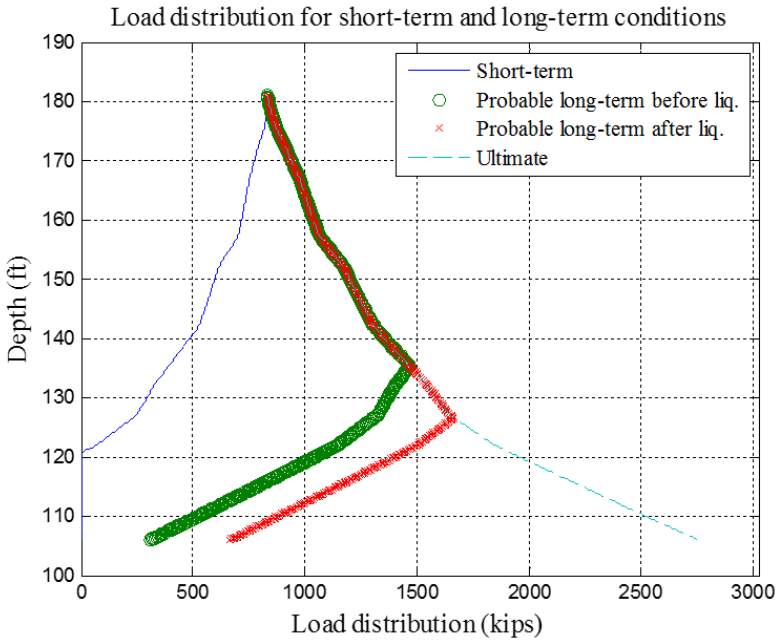

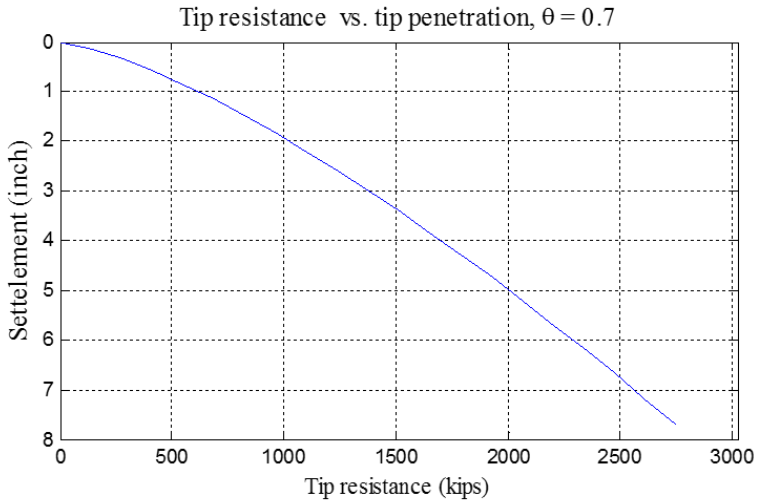

Max drag load before liquefaction (% of ultimate drag load)	444 kips (27 %)
Max drag load after liquefaction (% of ultimate drag load)	325 kips (20 %)
Ultimate drag load	1598 kips
NP location before liquefaction (ft)	135.3
NP location after liquefaction (ft)	141.1

*Drag load based on WSDOT approach (Average of nominal and residual side resistance) equals 1309 kips.

δ (short-term) = 0 inch, R (short-term) = 0 kips
δ (long-term before liq.) = 0.3937 inch , R (long-term before liq.) = 313.0499 kips
δ (long-term after liq.) = 0.041029 inch , R (long-term after liq.) = 60.0762 kips
δ (Ultimate) = 7.7166 inch , R (Ultimate) = 2747.666 kips

Figure B-8. SR 5 139th St NE Bridge Pier 1: Case II.

Project name and location: SR 5 139th St NE Bridge, Pier 2
9-feet drilled shaft, L = 90 ft

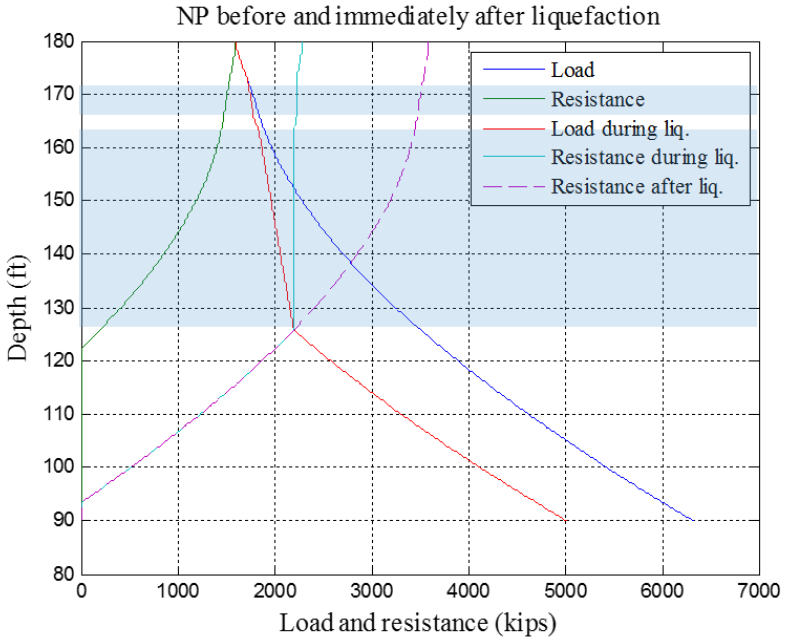

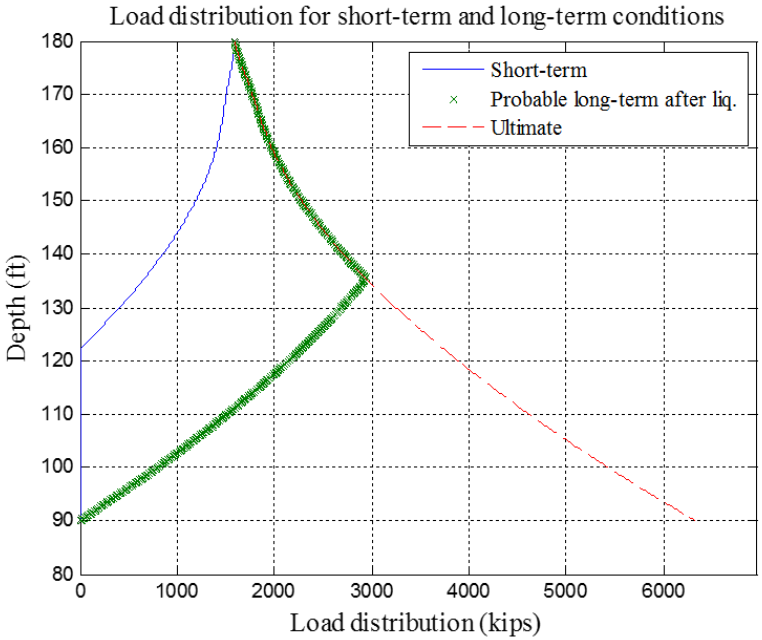

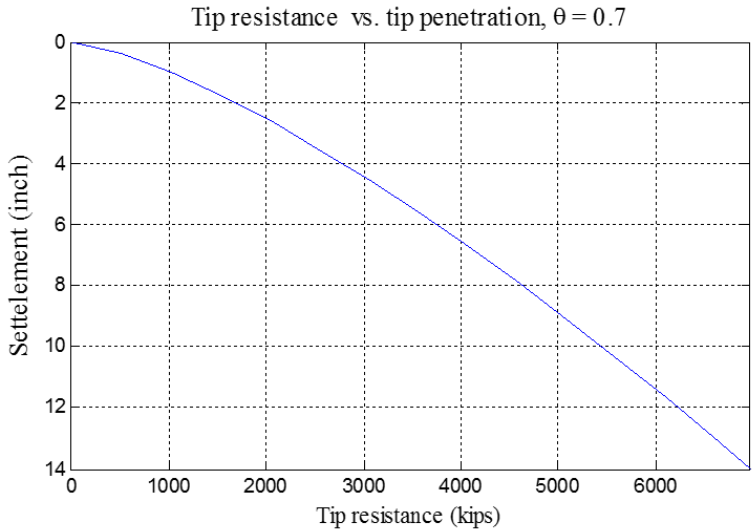

Max drag load before liquefaction (% of ultimate drag load)	0.0 kips (0 %)
Max drag load after liquefaction (% of ultimate drag load)	778 kips (19 %)
Ultimate drag load	4108 kips
NP location before liquefaction (ft)	180.0
NP location after liquefaction (ft)	138.6

*Drag load based on WSDOT approach (Average of nominal and residual side resistance) equals 3490 kips.

δ (long-term after liq.) = 0 inch , R (long-term after liq.) = 0 kips
δ (Ultimate) = 12.2495 inch , R (Ultimate) = 6326.2463 kips

Figure B-9. SR 5 139th St NE Bridge Pier 2: Case I.

Project name and location: SR 5 139th St NE Bridge, Pier 2
9-feet drilled shaft, L = 90 ft

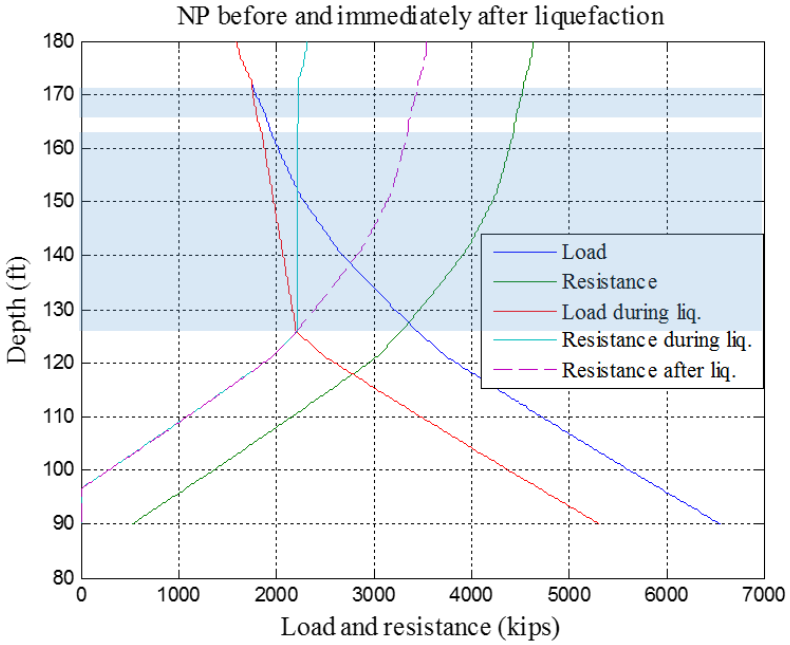

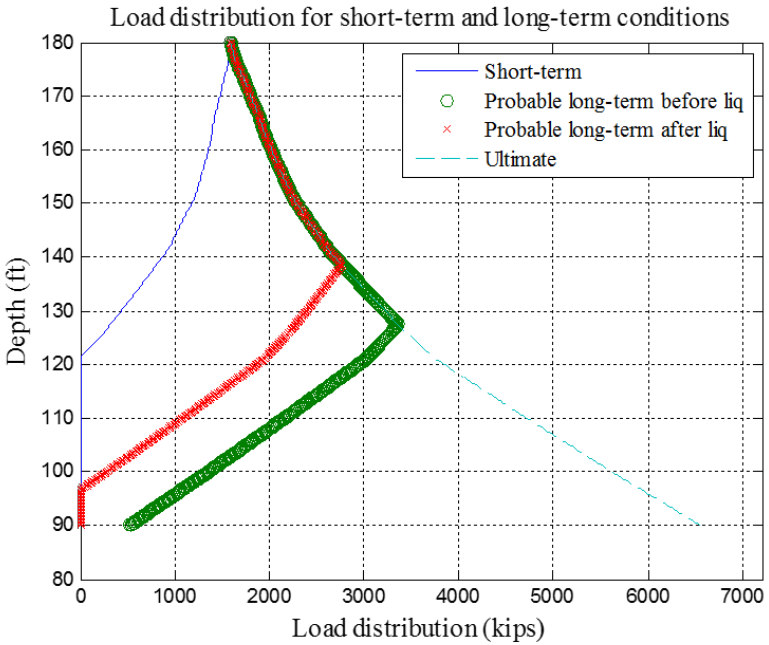

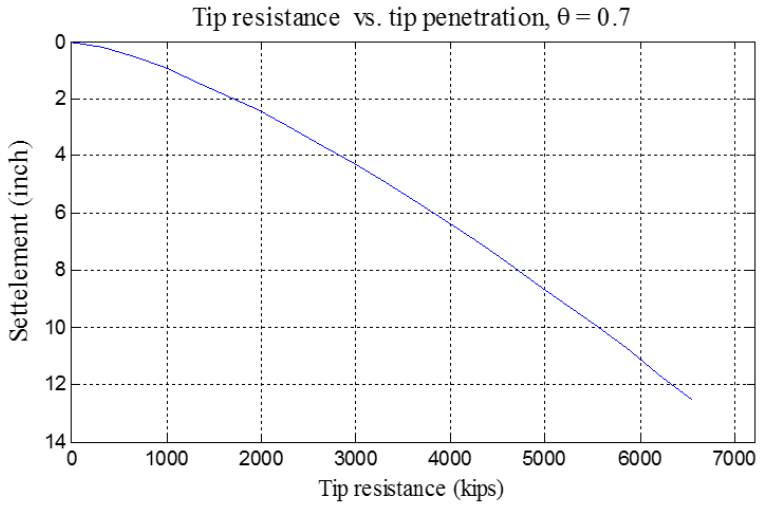

Max drag load before liquefaction (% of ultimate drag load)	1272 kips (31 %)
Max drag load after liquefaction (% of ultimate drag load)	778 kips (19 %)
Ultimate drag load	4108 kips
NP location before liquefaction (ft)	127.5
NP location after liquefaction (ft)	138.6

*Drag load based on WSDOT approach (Average of nominal and residual side resistance) equals 3490 kips.

δ (short-term) = 0 inch, R (short-term) = 0 kips
δ (long-term before liq.) = 0.3937 inch , R (long-term before liq.) = 523.9013 kips
δ (long-term after liq.) = 0 inch , R (long-term after liq.) = 0 kips
δ (Ultimate) = 12.5474 inch , R (Ultimate) = 6557.2583 kips

Figure B-10. SR 5 139th St NE Bridge Pier 2: Case II.

Project name and location: SR 5 139th St NE Bridge, Pier 3
9-feet drilled shaft, L = 100 ft

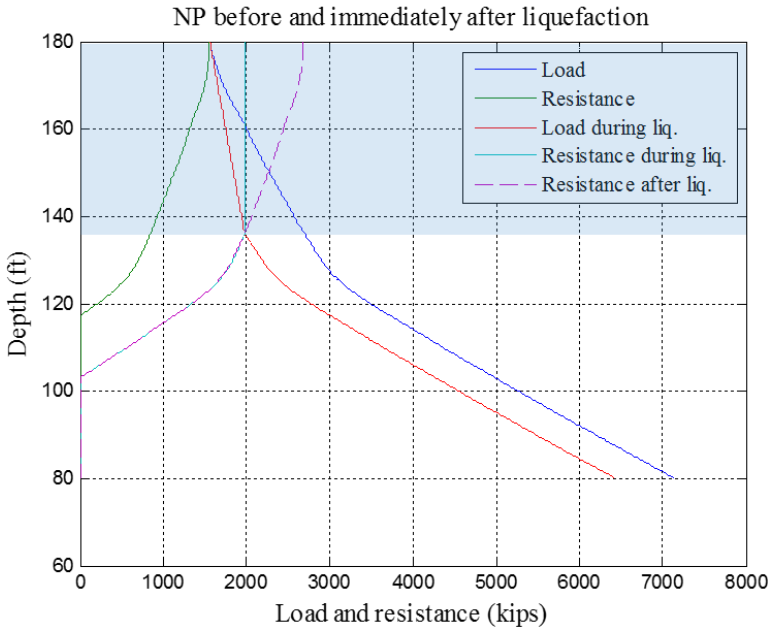

Max drag load before liquefaction (% of ultimate drag load)	0 kips (0 %)
Max drag load after liquefaction (% of ultimate drag load)	427 kips (9 %)
Ultimate drag load	4733 kips
NP location before liquefaction (ft)	180.0
NP location after liquefaction (ft)	150.4

*Drag load based on WSDOT approach (Average of nominal and residual side resistance) equals 4374 kips.

δ (long-term after liq.) = 0 inch , R (long-term after liq.) = 0 kips
δ (Ultimate) = 14.1071 inch , R (Ultimate) = 7142.8045 kips

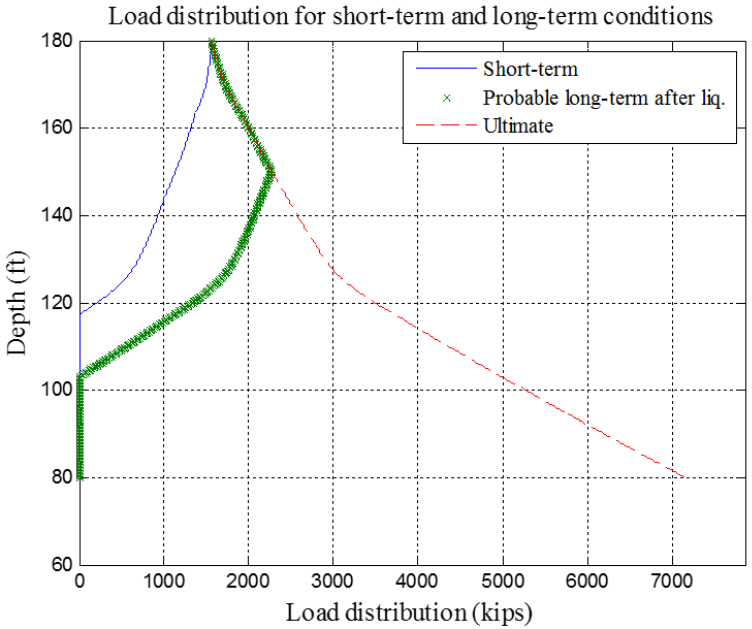

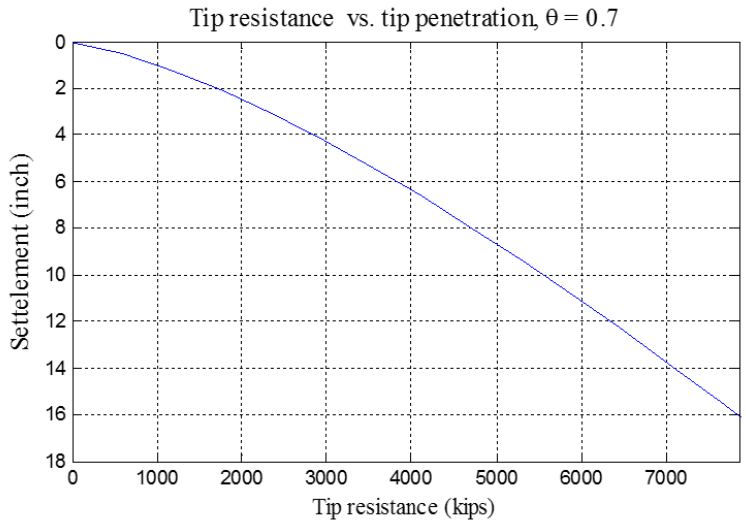

Figure B-11. SR 5 139th St NE Bridge Pier 3: Case I.

Project name and location: SR 5 139th St NE Bridge, Pier 3
9-feet drilled shaft, L = 100 ft

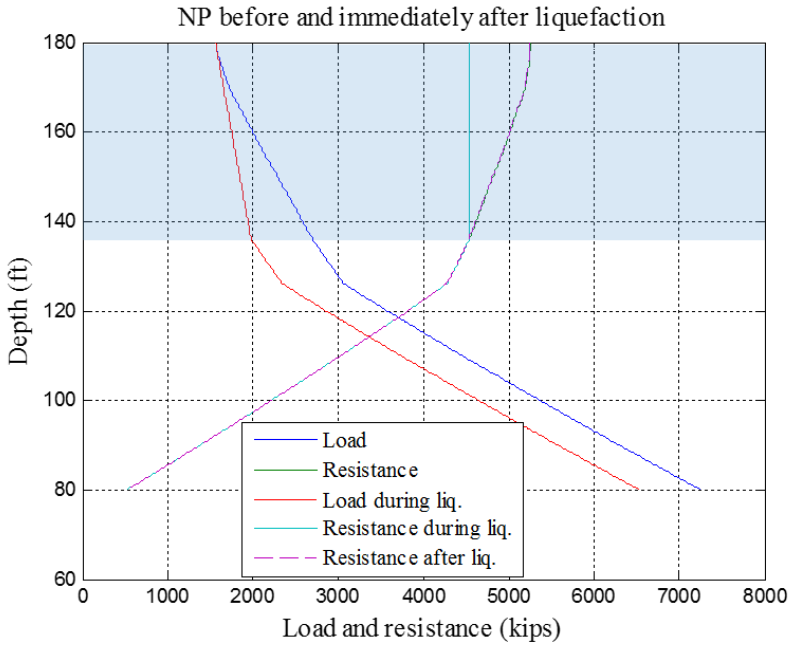

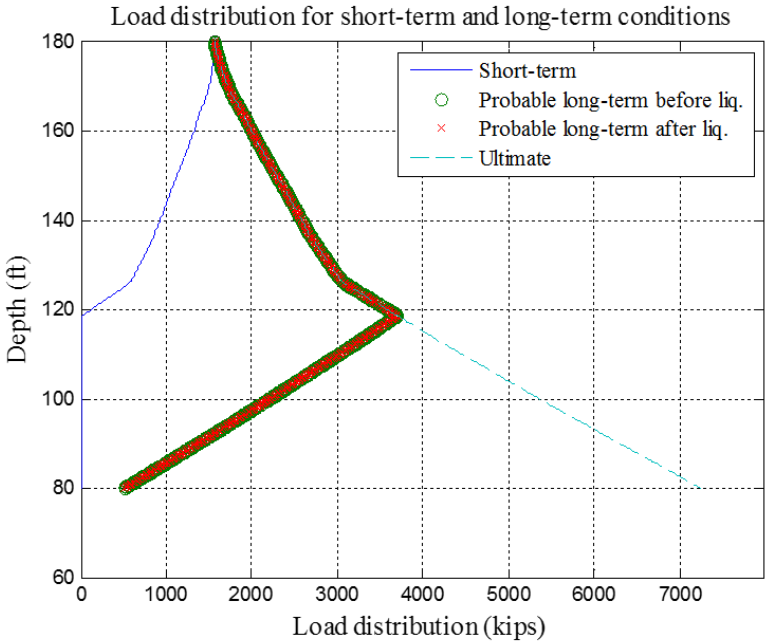

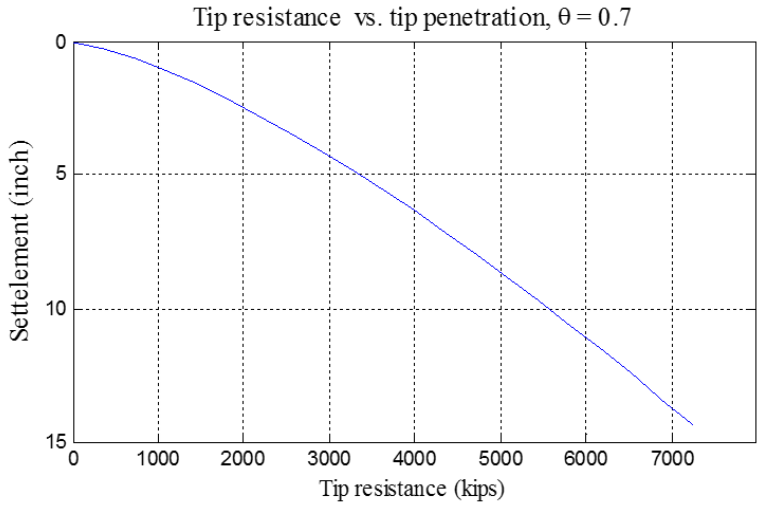

Max drag load before liquefaction (% of ultimate drag load)	1551 kips (33 %)
Max drag load after liquefaction (% of ultimate drag load)	1551 kips (33 %)
Ultimate drag load	4732 kips
NP location before liquefaction (ft)	118.6
NP location after liquefaction (ft)	118.6

*Drag load based on WSDOT approach (Average of nominal and residual side resistance) equals 4374 kips.

δ (short-term) = 0 inch, R (short-term) = 0 kips
δ (long-term before liq.) = 0.3937 inch , R (long-term before liq.) = 523.9013 kips
δ (long-term after liq.) = 0.38316 inch , R (long-term after liq.) = 513.6217 kips
δ (Ultimate) = 14.39 inch , R (Ultimate) = 7247.0788 kips

Figure B-12. SR 5 139th St NE Bridge Pier 3: Case II.

Project name and location: SR 5 139th St NE Bridge, Pier 4
9-feet drilled shaft, L = 95 ft

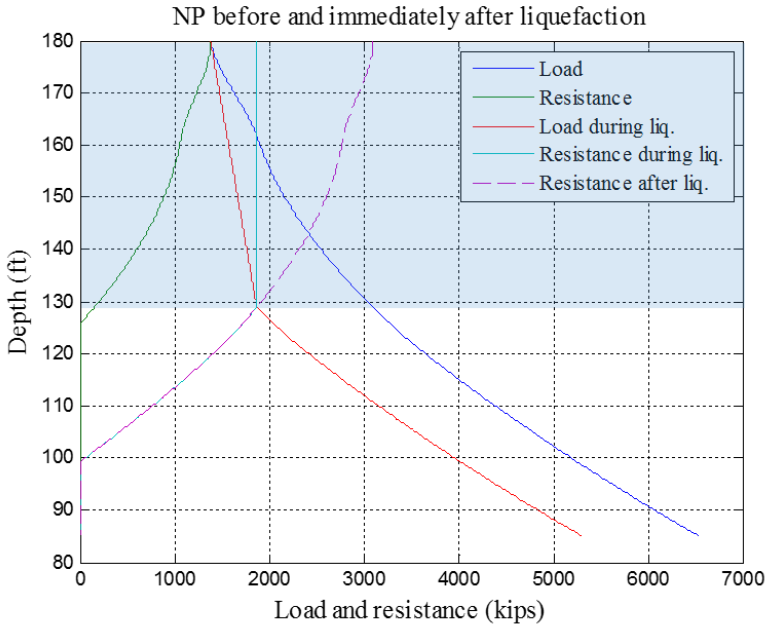

Max drag load before liquefaction (% of ultimate drag load)	0.0 kips (0 %)
Max drag load after liquefaction (% of ultimate drag load)	631 kips (14 %)
Ultimate drag load	4521 kips
NP location before liquefaction (ft)	180.0
NP location after liquefaction (ft)	141.2

*Drag load based on WSDOT approach (Average of nominal and residual side resistance) equals *3951* kips.

δ (long-term after liq.) = 0 inch , R (long-term after liq.) = 0 kips
δ (Ultimate) = 12.9117 inch , R (Ultimate) = 6537.1207 kips

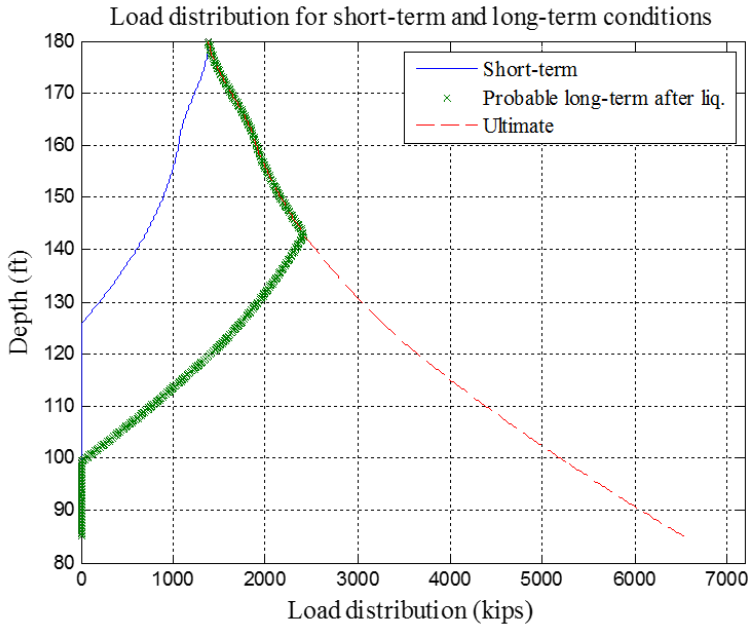

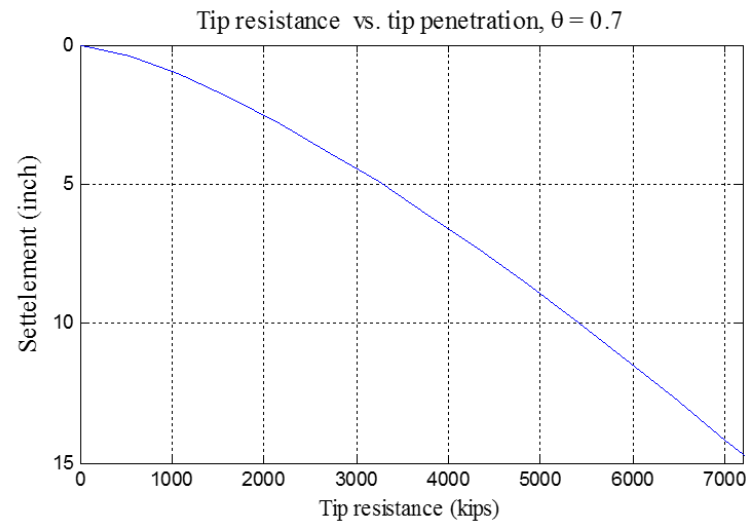

Figure B-13. SR 5 139th St NE Bridge Pier 4: Case I.

Project name and location: SR 5 139th St NE Bridge, Pier 4
9-feet drilled shaft, L = 95 ft

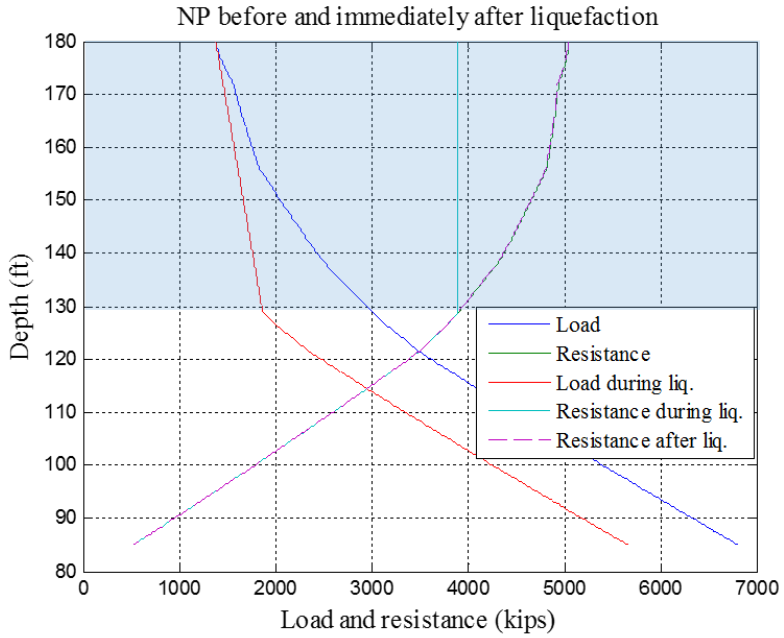

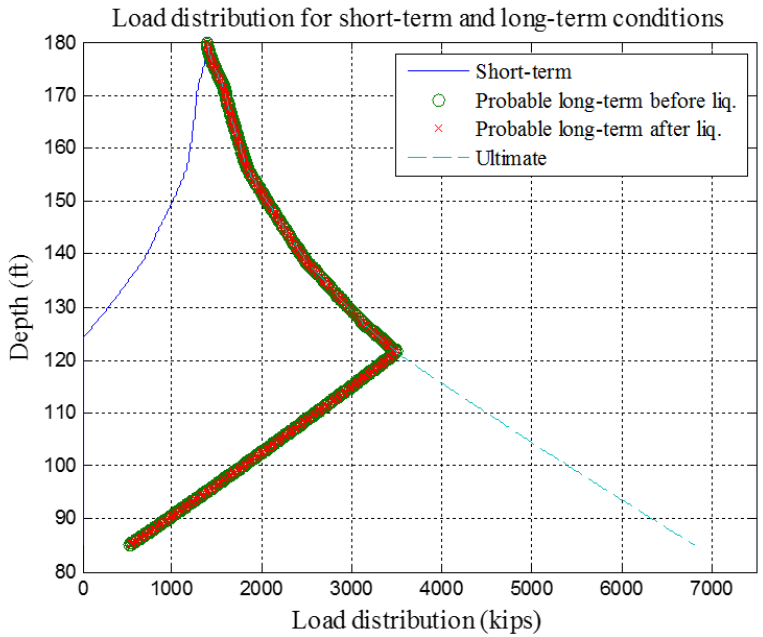

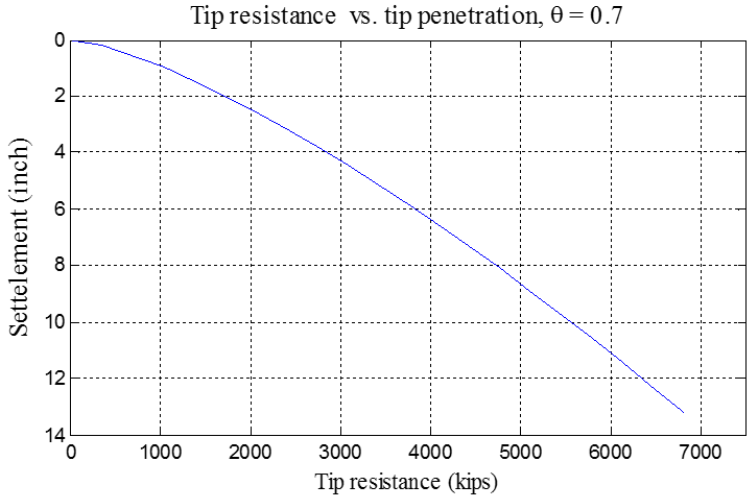

Max drag load before liquefaction (% of ultimate drag load)	1546 kips (34 %)
Max drag load after liquefaction (% of ultimate drag load)	1546 kips (34 %)
Ultimate drag load	4521 kips
NP location before liquefaction (ft)	121.6
NP location after liquefaction (ft)	121.6

*Drag load based on WSDOT approach (Average of nominal and residual side resistance) equals *3951* kips.

δ (short-term) = 0 inch, R (short-term) = 0 kips
δ (long-term before liq.) = 0.3937 inch , R (long-term before liq.) = 523.9013 kips
δ (long-term after liq.) = 0.39283 inch , R (long-term after liq.) = 523.0567 kips
δ (Ultimate) = 13.2108 inch , R (Ultimate) = 6808.5832 kips

Figure B-14. SR 5 139th St NE Bridge Pier 4: Case II.

Project name and location: SR 5 139th St NE Bridge, Pier 5
9-feet drilled shaft, L = 95 ft

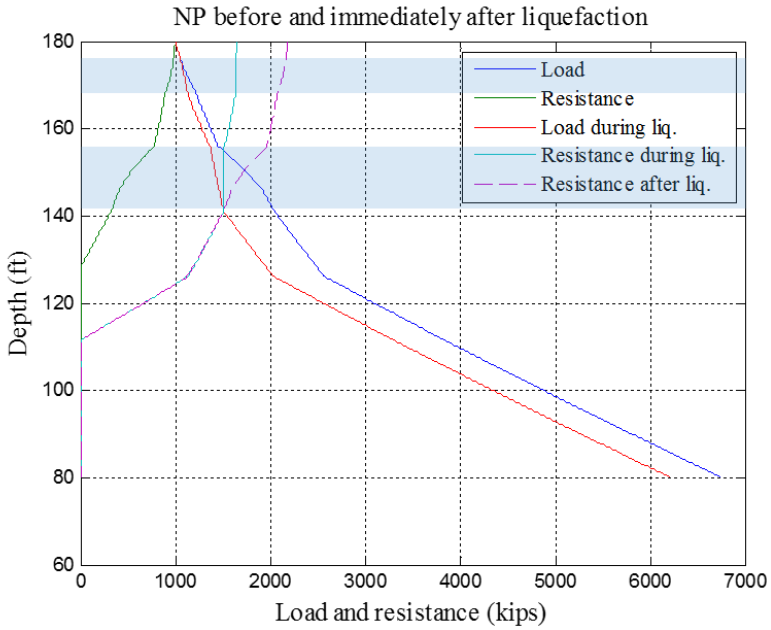

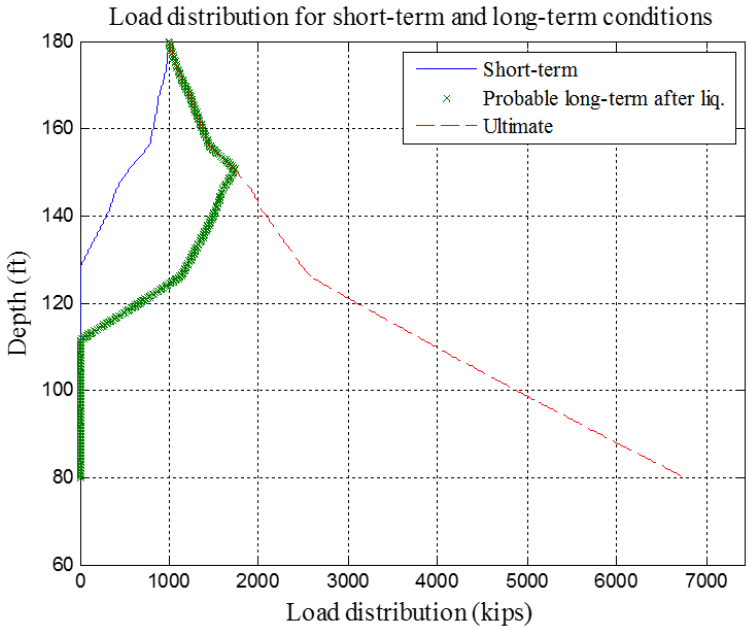

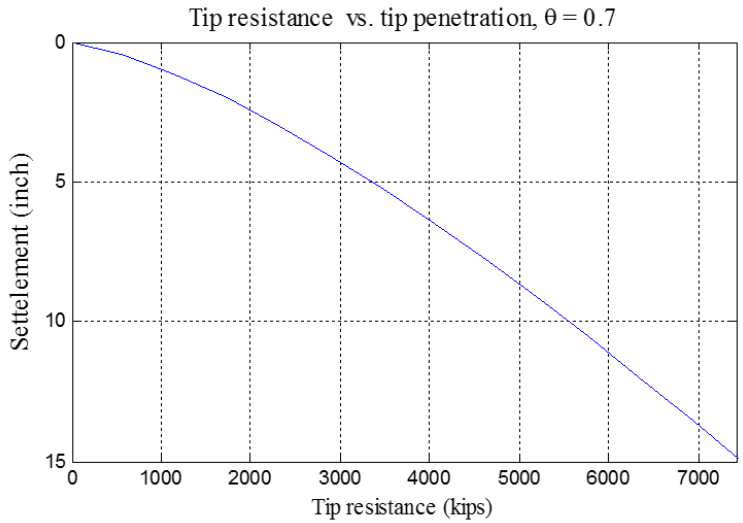

Max drag load before liquefaction (% of ultimate drag load)	0 kips (0 %)
Max drag load after liquefaction (% of ultimate drag load)	448 kips (9 %)
Ultimate drag load	4799 kips
NP location before liquefaction (ft)	180.0
NP location after liquefaction (ft)	150.5

*Drag load based on WSDOT approach (Average of nominal and residual side resistance) equals 4530 kips.

δ (long-term after liq.) = 0 inch , R (long-term after liq.) = 0 kips
δ (Ultimate) = 13.0572 inch , R (Ultimate) = 6750.6805 kips

Figure B-15. SR 5 139th St NE Bridge Pier 5: Case I.

Project name and location: SR 5 139th St NE Bridge, Pier 5
9-feet drilled shaft, L = 95 ft

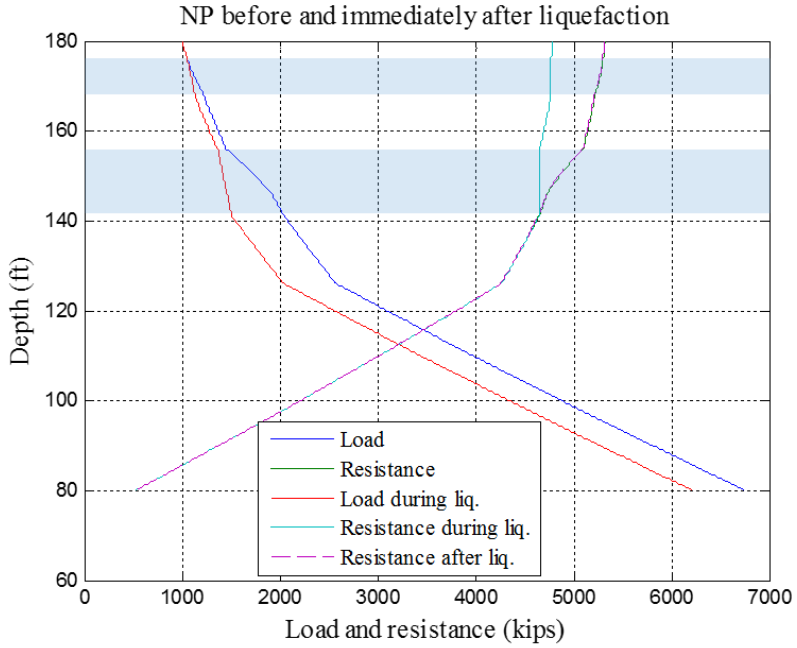

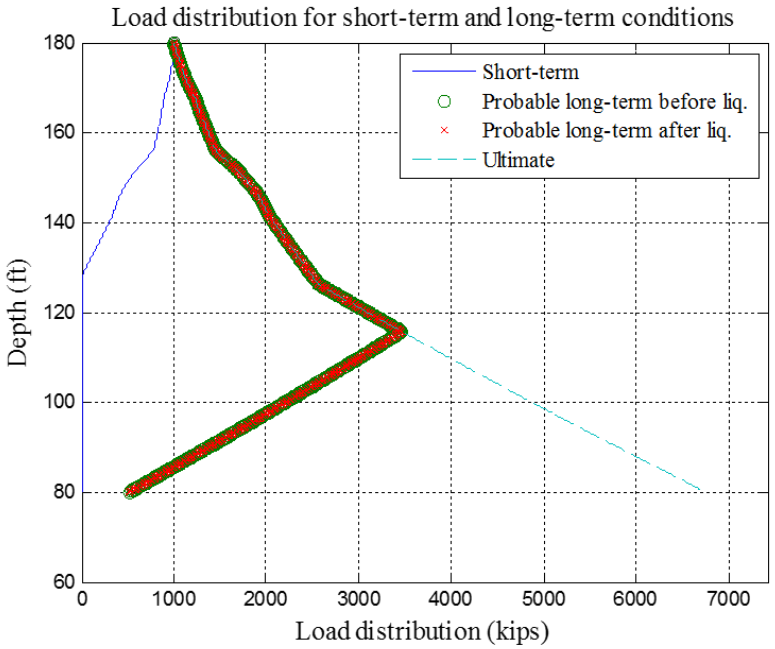

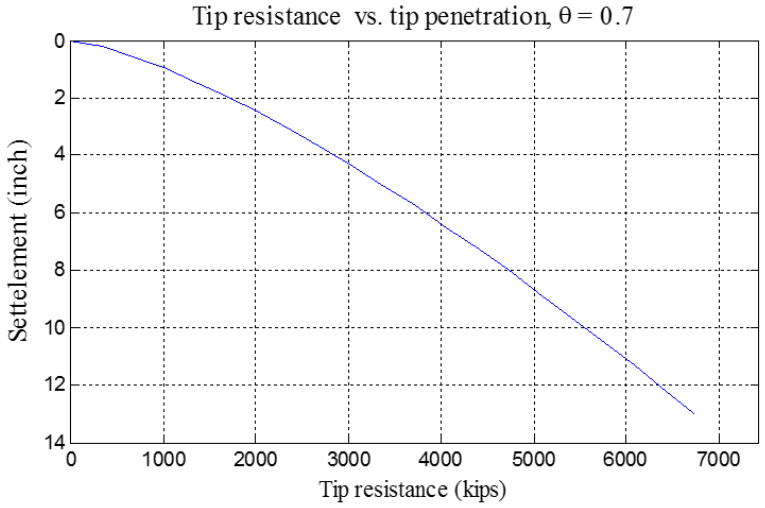

Max drag load before liquefaction (% of ultimate drag load)	1857 kips (39 %)
Max drag load after liquefaction (% of ultimate drag load)	1857 kips (39 %)
Ultimate drag load	4799 kips
NP location before liquefaction (ft)	115.7
NP location after liquefaction (ft)	115.7

*Drag load based on WSDOT approach (Average of nominal and residual side resistance) equals 4530 kips.

δ (short-term) = 0 inch, R (short-term) = 0 kips
δ (long-term before liq.) = 0.3937 inch , R (long-term before liq.) = 523.9013 kips
δ (long-term after liq.) = 0.39114 inch , R (long-term after liq.) = 521.4128 kips
δ (Ultimate) = 13.0572 inch , R (Ultimate) = 6750.6805 kips

Figure B-16. SR 5 139th St NE Bridge Pier 5: Case II.

Project name and location: SR 5 139th St NE Bridge, Pier 6
9-feet drilled shaft, L = 114 ft

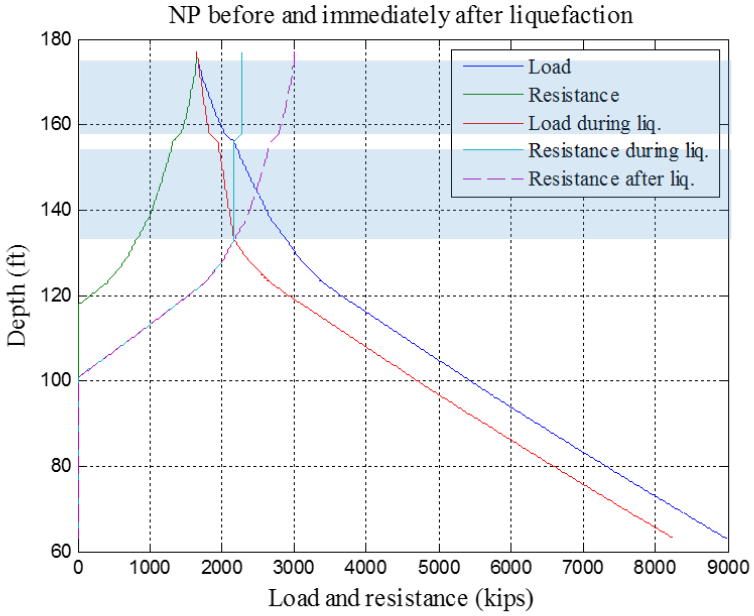

Max drag load before liquefaction (% of ultimate drag load)	0.0 (0 %)
Max drag load after liquefaction (% of ultimate drag load)	521.0 (11 %)
Ultimate drag load	6257 kips
NP location before liquefaction (ft)	177.0
NP location after liquefaction (ft)	144.6

*Drag load based on WSDOT approach (Average of nominal and residual side resistance) equals 5827 kips.

δ (long-term after liq.) = 0 inch , R (long-term after liq.) = 0 kips
δ (Ultimate) = 19.302 inch , R (Ultimate) = 8979.8279 kips

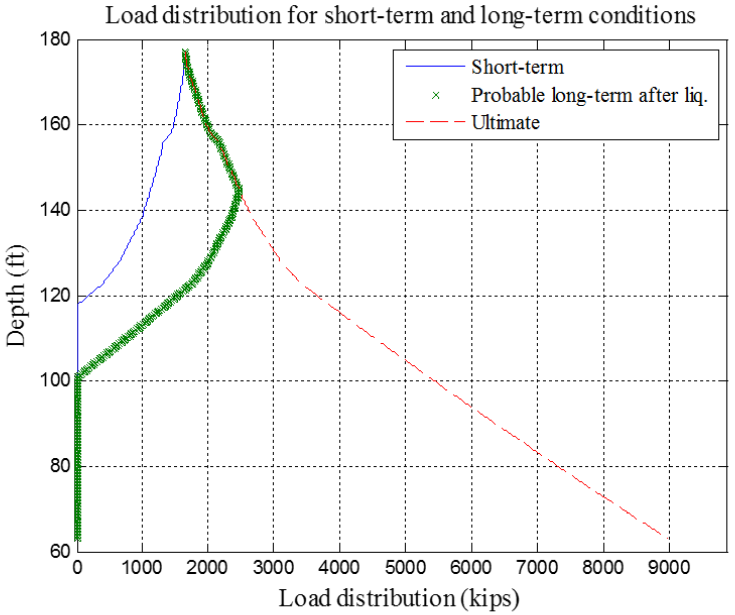

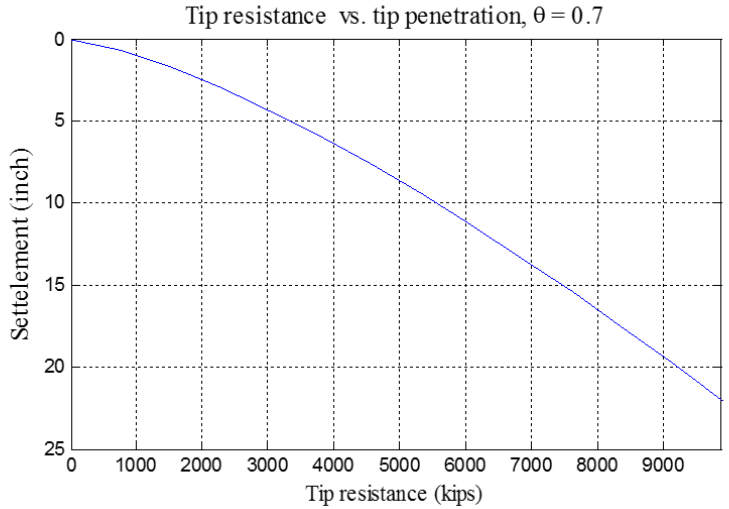

Figure B-17. SR 5 139th St NE Bridge Pier 6: Case I.

Project name and location: SR 5 139th St NE Bridge, Pier 6
9-feet drilled shaft, L = 114 ft

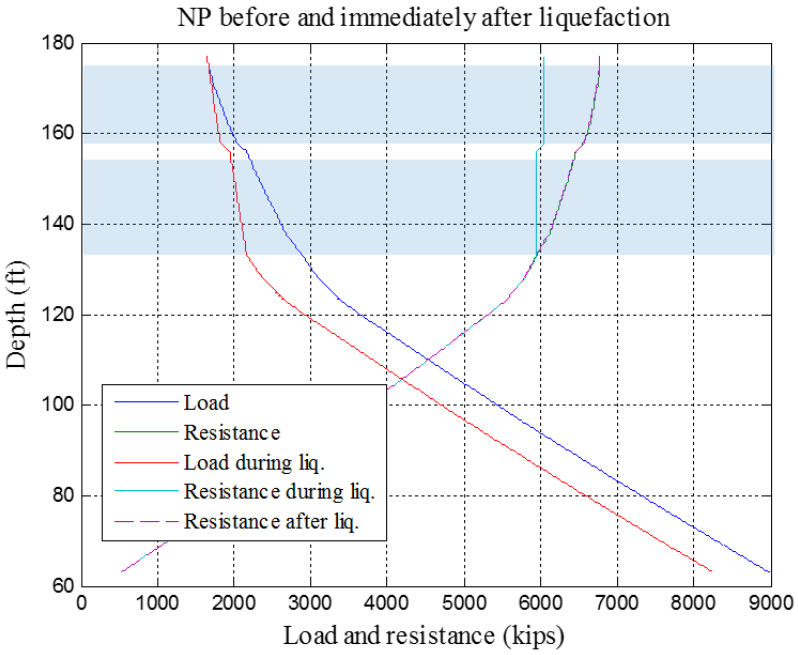

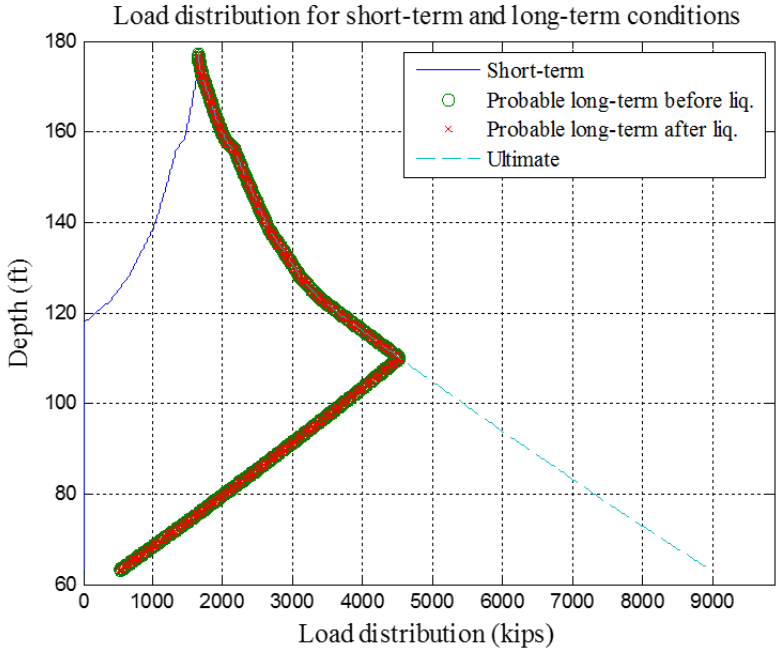

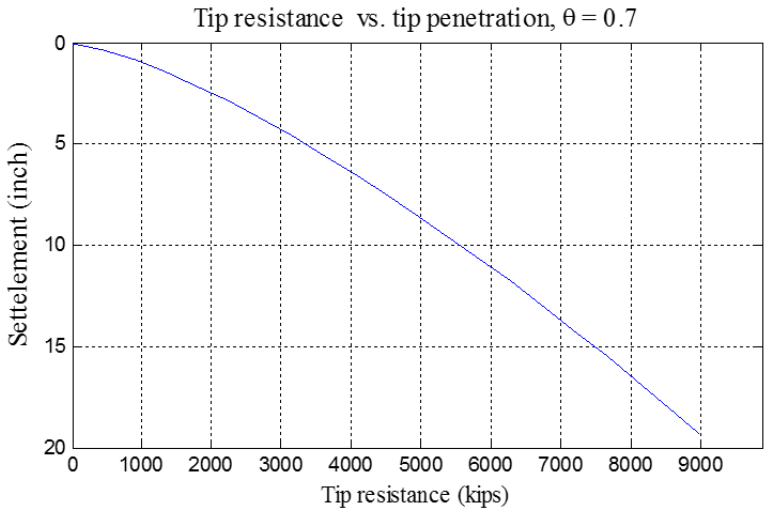

Max drag load before liquefaction (% of ultimate drag load)	2514 kips (36 %)
Max drag load after liquefaction (% of ultimate drag load)	2514 kips (36 %)
Ultimate drag load	6257 kips
NP location before liquefaction (ft)	111.0
NP location after liquefaction (ft)	111.0

*Drag load based on WSDOT approach (Average of nominal and residual side resistance) equals 5827 kips.

δ (short-term) = 0 inch, R (short-term) = 0 kips
δ (long-term before liq.) = 0.3937 inch , R (long-term before liq.) = 523.9013 kips
δ (long-term after liq.) = 0.38796 inch , R (long-term after liq.) = 518.3102 kips
δ (Ultimate) = 19.302 inch , R (Ultimate) = 8979.8279 kips

Figure B-15. SR 5 139th St NE Bridge Pier 6: Case II.

Project name and location: SR 5 139th St NE Bridge, Pier 7
9-feet drilled shaft, L = 117 ft

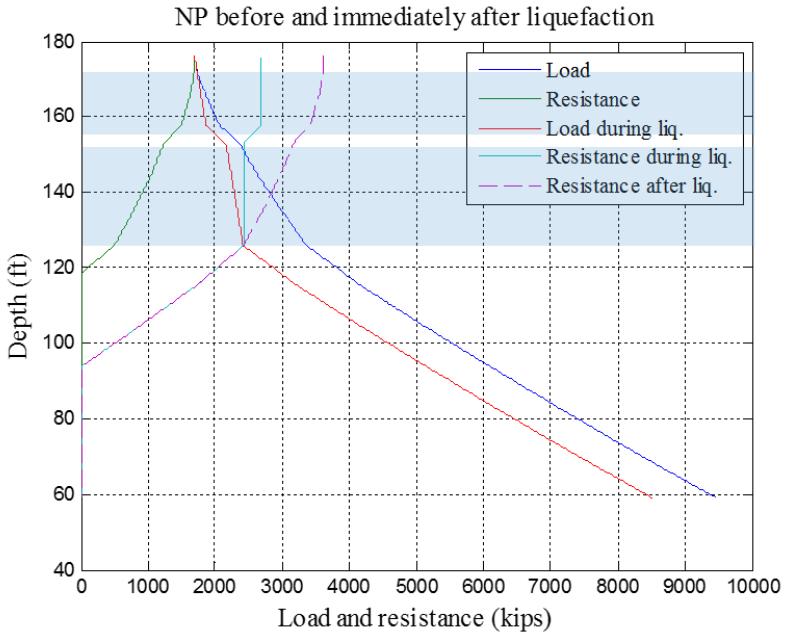

Max drag load before liquefaction (% of ultimate drag load)	0 kips (0 %)
Max drag load after liquefaction (% of ultimate drag load)	741 kips (11 %)
Ultimate drag load	6663 kips
NP location before liquefaction (ft)	176.0
NP location after liquefaction (ft)	140.0

*Drag load based on WSDOT approach (Average of nominal and residual side resistance) equals 6103 kips.

δ (long-term after liq.) = 0 inch , R (long-term after liq.) = 0 kips
δ (Ultimate) = 20.7544 inch , R (Ultimate) = 9468.2115 kips

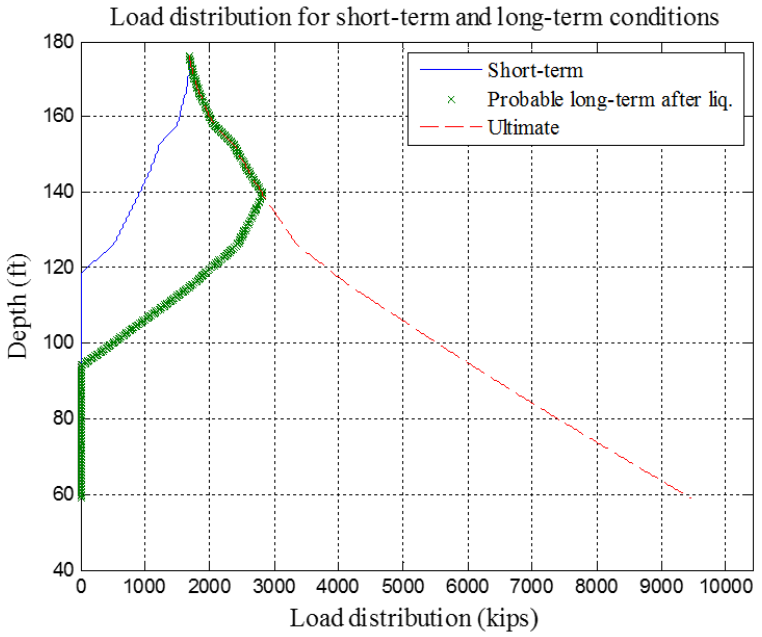

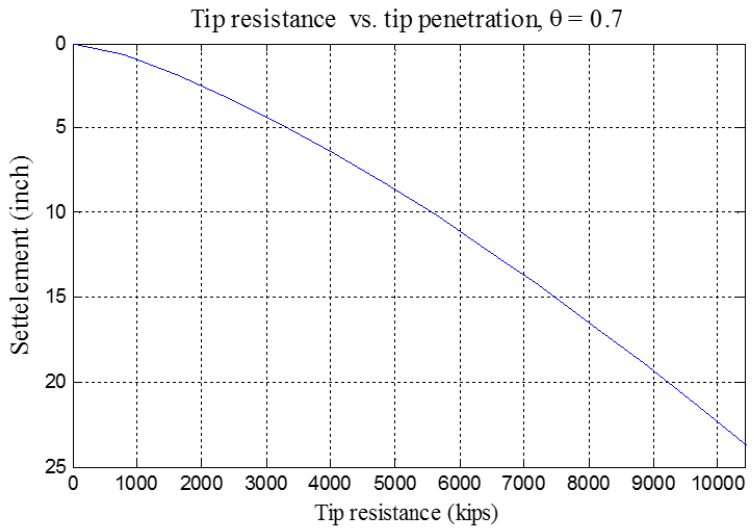

Figure B-16. SR 5 139th St NE Bridge Pier 7: Case I.

Project name and location: SR 5 139th St NE Bridge, Pier 7
9-feet drilled shaft, L = 117 ft

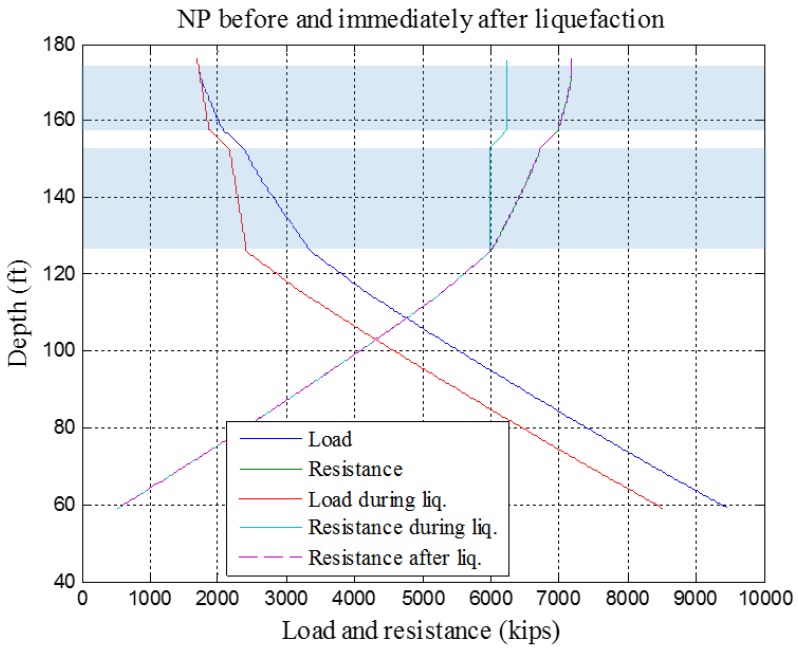

Max drag load before liquefaction (% of ultimate drag load)	2428 kips (37 %)
Max drag load after liquefaction (% of ultimate drag load)	2428 kips (37 %)
Ultimate drag load	6663 kips
NP location before liquefaction (ft)	109.0
NP location after liquefaction (ft)	109.0

*Drag load based on WSDOT approach (Average of nominal and residual side resistance) equals 6103 kips.

δ (short-term) = 0 inch, R (short-term) = 0 kips
δ (long-term before liq.) = 0.3937 inch , R (long-term before liq.) = 523.9013 kips
δ (long-term after liq.) = 0.39154 inch , R (long-term after liq.) = 521.8054 kips
δ (Ultimate) = 20.7544 inch , R (Ultimate) = 9468.2115 kips

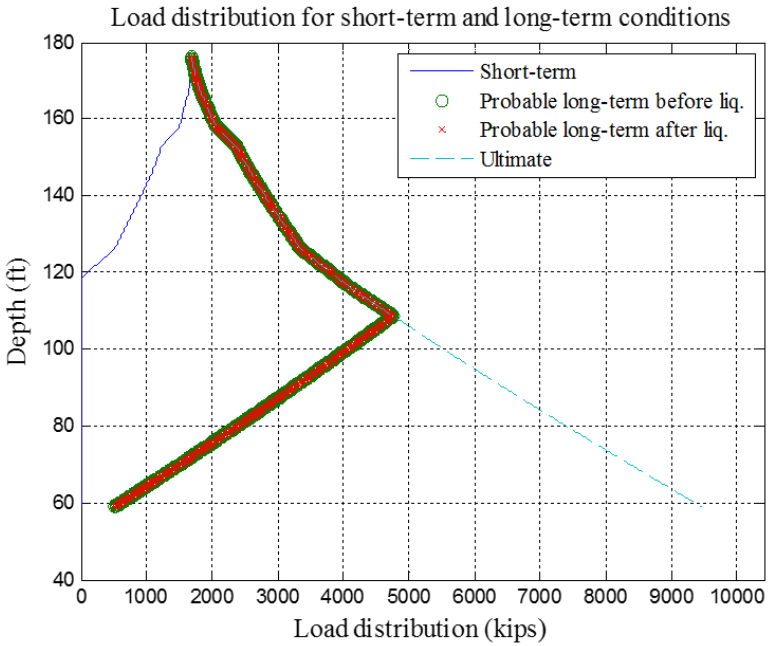

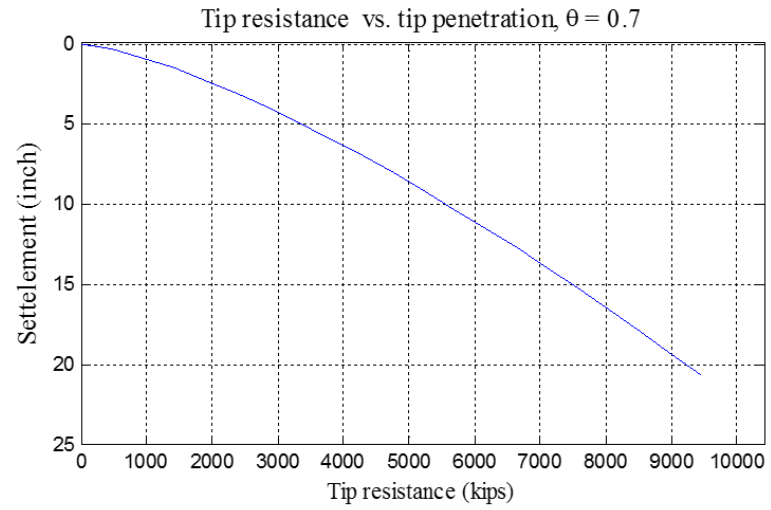

Figure B-17. SR 5 139th St NE Bridge Pier 7: Case II.

Project name and location: SR 5 139th St NE Bridge, Pier 8
9-feet drilled shaft, L = 105 ft

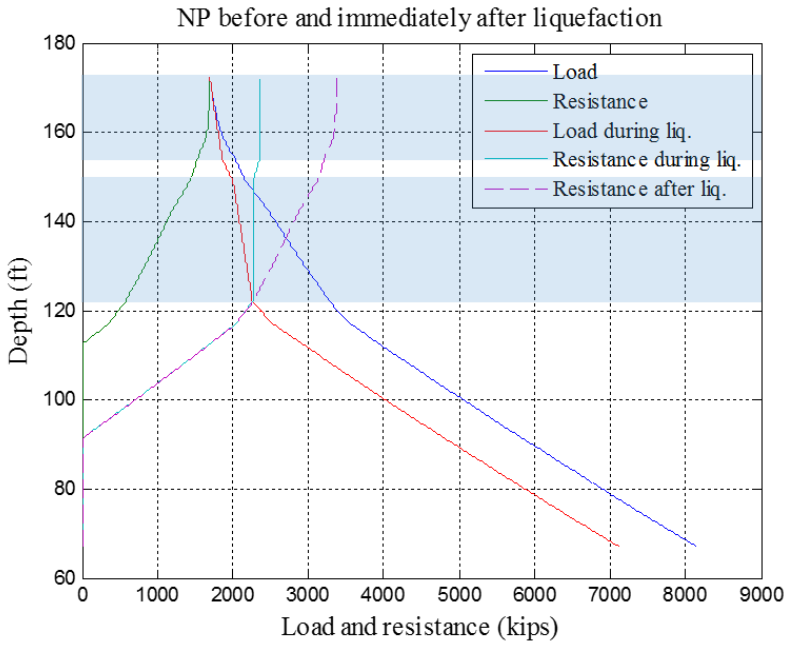

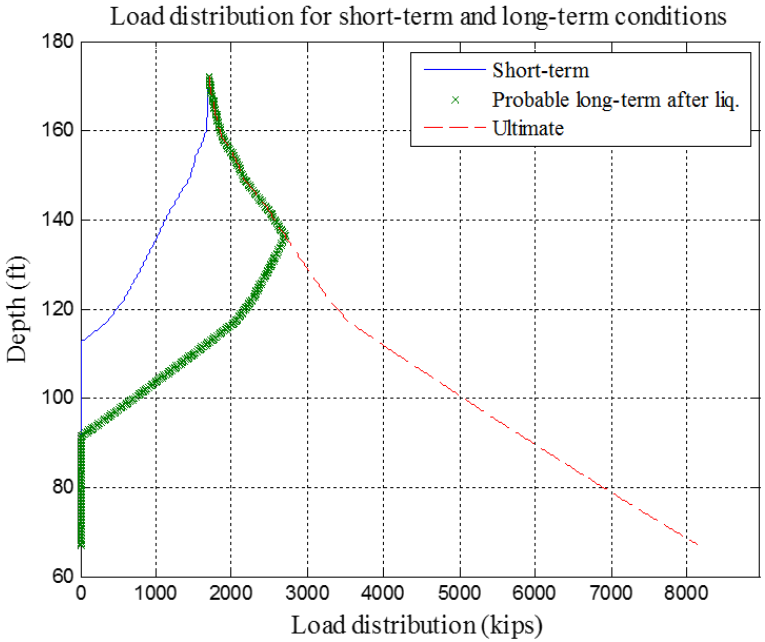

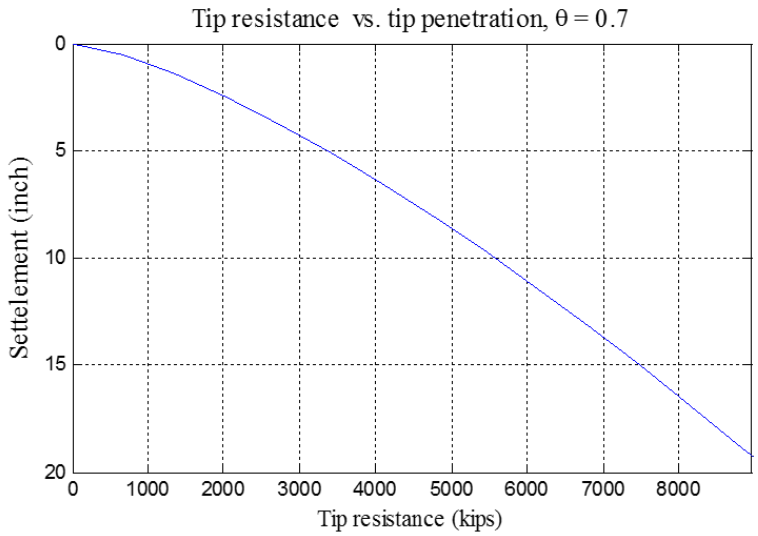

Max drag load before liquefaction (% of ultimate drag load)	0.0 kips (0 %)
Max drag load after liquefaction (% of ultimate drag load)	670 kips (12 %)
Ultimate drag load	5452kips
NP location before liquefaction (ft)	172.0
NP location after liquefaction (ft)	136.1

*Drag load based on WSDOT approach (Average of nominal and residual side resistance) equals 4940 kips.

δ (long-term after liq.) = 0 inch , R (long-term after liq.) = 0 kips
δ (Ultimate) = 16.8834 inch , R (Ultimate) = 8143.7241 kips

Figure B-18. SR 5 139th St NE Bridge Pier 8: Case I.

Project name and location: SR 5 139th St NE Bridge, Pier 8
9-feet drilled shaft, L = 105 ft

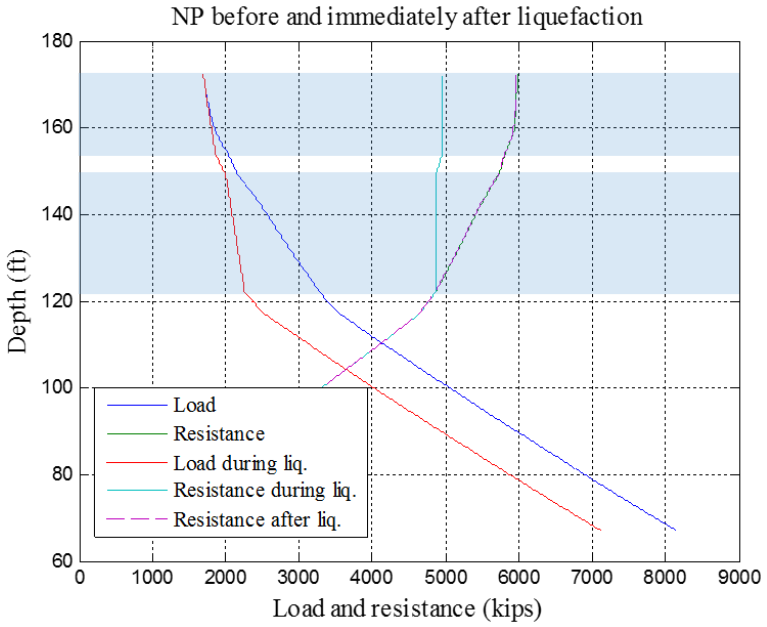

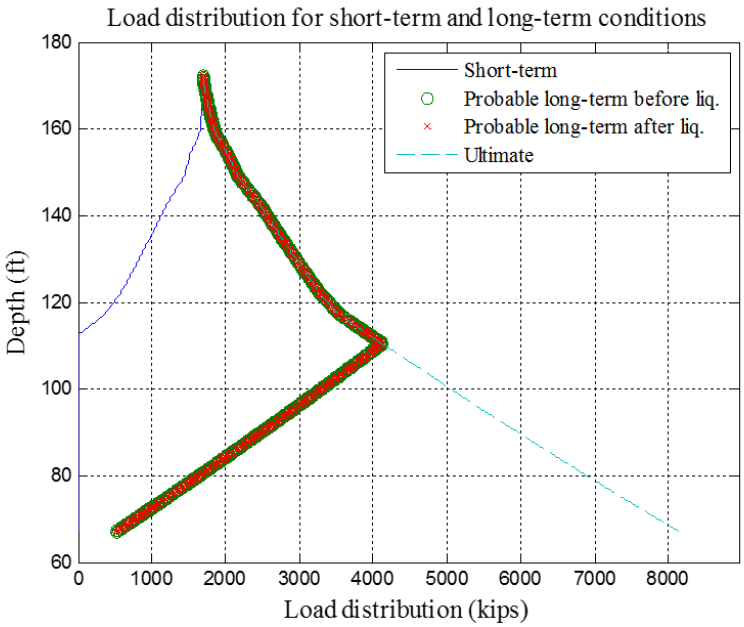

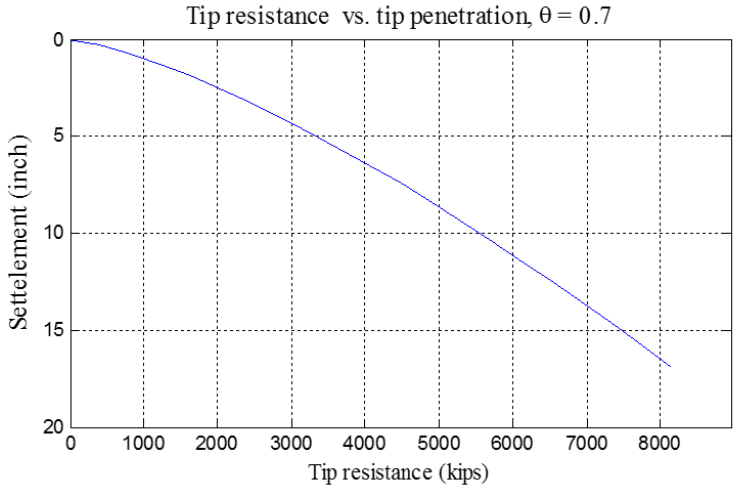

Max drag load before liquefaction (% of ultimate drag load)	1850 kips (34 %)
Max drag load after liquefaction (% of ultimate drag load)	1850 kips (34 %)
Ultimate drag load	5452 kips
NP location before liquefaction (ft)	110.4
NP location after liquefaction (ft)	110.4

*Drag load based on WSDOT approach (Average of nominal and residual side resistance) equals 4940 kips.

δ (short-term) = 0 inch, R (short-term) = 0 kips
δ (long-term before liq.) = 0.3937 inch , R (long-term before liq.) = 523.9013 kips
δ (long-term after liq.) = 0.39192 inch , R (long-term after liq.) = 522.1734 kips
δ (Ultimate) = 16.8834 inch , R (Ultimate) = 8143.7241 kips

Figure B-19. SR 5 139th St NE Bridge Pier 8: Case II.

Project name and location: SR 5 139th St NE Bridge, Pier 9
9-feet drilled shaft, L = 105 ft

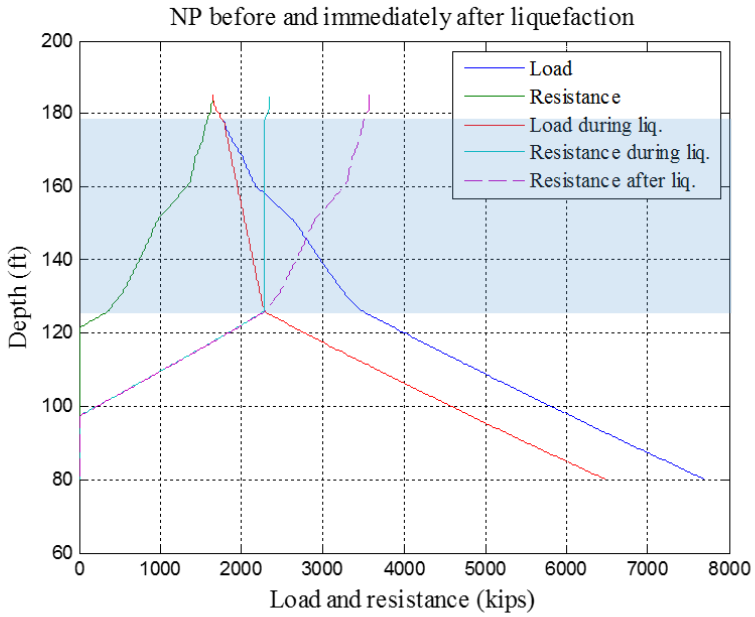

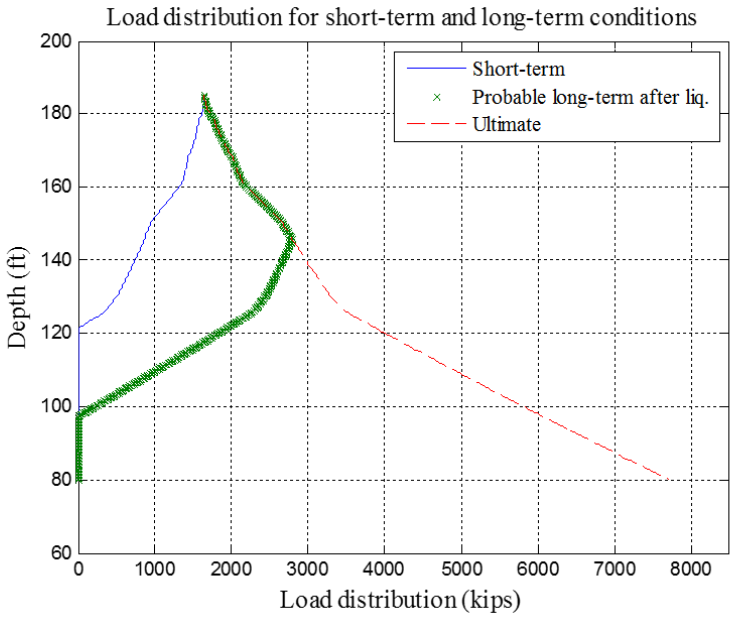

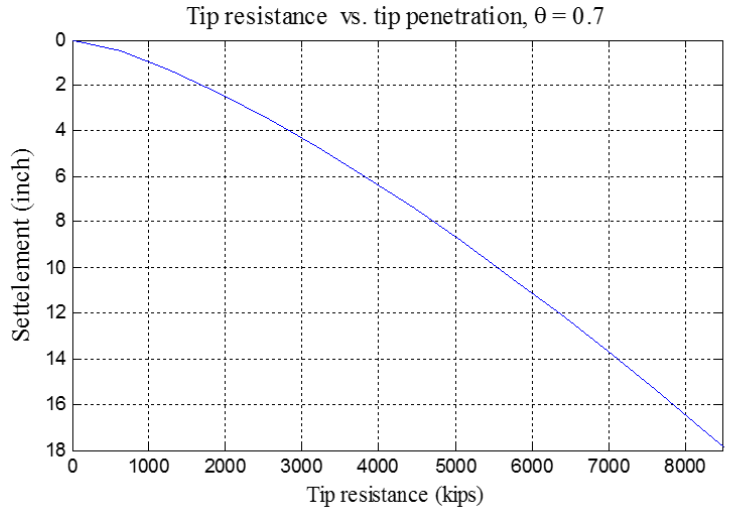

Max drag load before liquefaction (% of ultimate drag load)	0 kips (0 %)
Max drag load after liquefaction (% of ultimate drag load)	778 kips (15 %)
Ultimate drag load	5059 kips
NP location before liquefaction (ft)	185.0
NP location after liquefaction (ft)	146.0

*Drag load based on WSDOT approach (Average of nominal and residual side resistance) equals 4451 kips.

δ (long-term after liq.) = 0 inch , R (long-term after liq.) = 0 kips
δ (Ultimate) = 15.6386 inch , R (Ultimate) = 7700.9199 kips

Figure B-20. SR 5 139th St NE Bridge Pier 9: Case I.

Project name and location: SR 5 139th St NE Bridge, Pier 9
9-feet drilled shaft, L = 105 ft

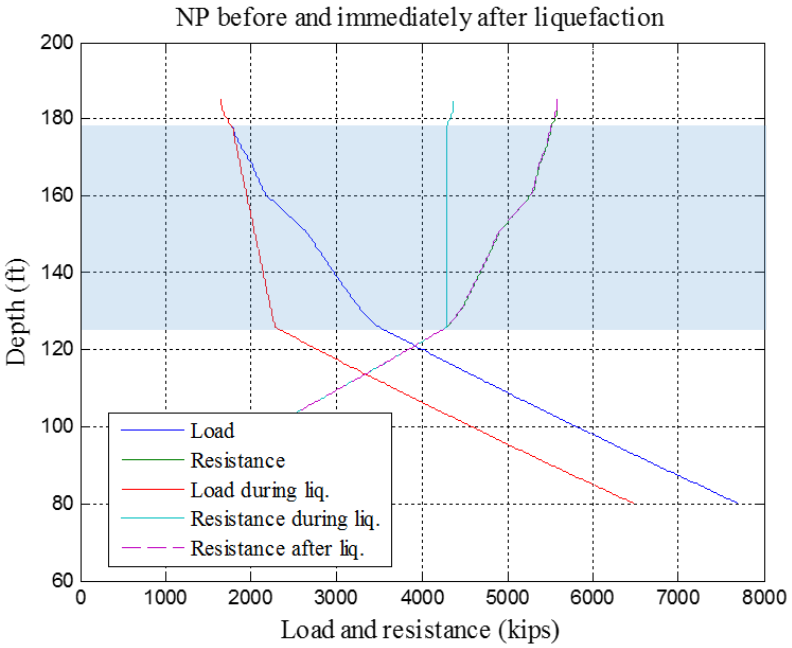

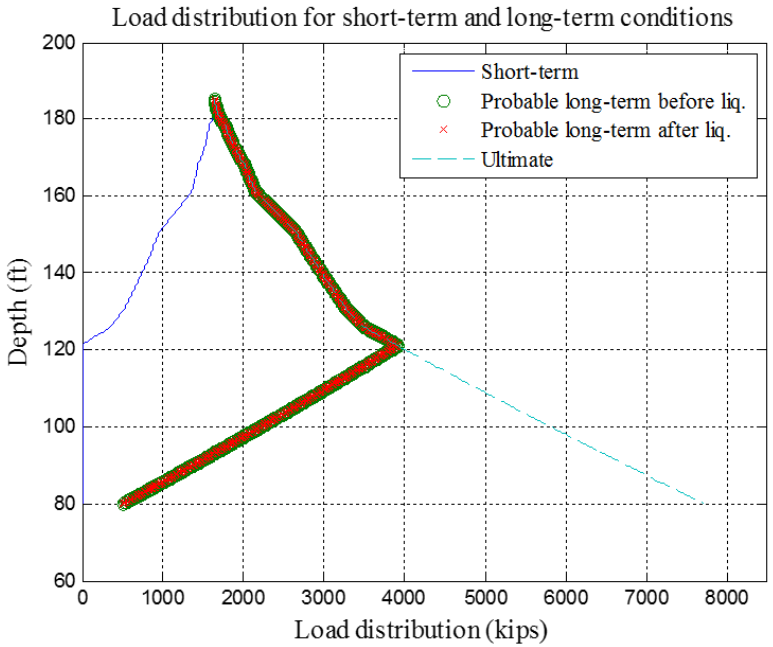

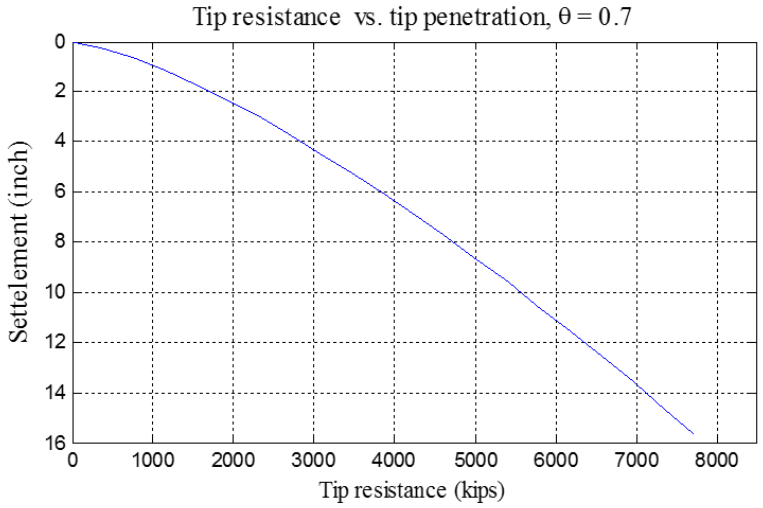

Max drag load before liquefaction (% of ultimate drag load)	1666 kips (33 %)
Max drag load after liquefaction (% of ultimate drag load)	1666 kips (33 %)
Ultimate drag load	5059 kips
NP location before liquefaction (ft)	121.1
NP location after liquefaction (ft)	121.1

*Drag load based on WSDOT approach (Average of nominal and residual side resistance) equals 4451 kips.

δ (short-term) = 0 inch, R (short-term) = 0 kips
δ (long-term before liq.) = 0.3937 inch , R (long-term before liq.) = 523.9013 kips
δ (long-term after liq.) = 0.37778 inch , R (long-term after liq.) = 508.3531 kips
δ (Ultimate) = 15.6386 inch , R (Ultimate) = 7700.9199 kips

Figure B-21. SR 5 139th St NE Bridge Pier 9: Case II.

Project name and location: SR 5 139th St NE Bridge, Pier 10
6-feet drilled shaft, L = 75 ft

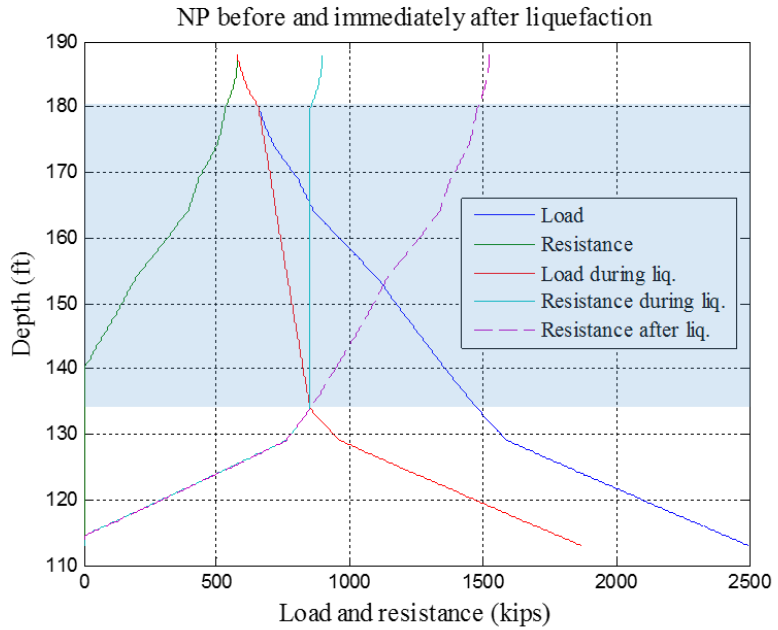

Max drag load before liquefaction (% of ultimate drag load)	0 kips (0 %)
Max drag load after liquefaction (% of ultimate drag load)	397 kips (51 %)
Ultimate drag load	1603 kips
NP location before liquefaction (ft)	188.0
NP location after liquefaction (ft)	152.7

*Drag load based on WSDOT approach (Average of nominal and residual side resistance) equals 1289 kips.

δ (long-term after liq.) = 0 inch , R (long-term after liq.) = 0 kips
δ (Ultimate) = 6.7695 inch , R (Ultimate) = 2497.1675 kips

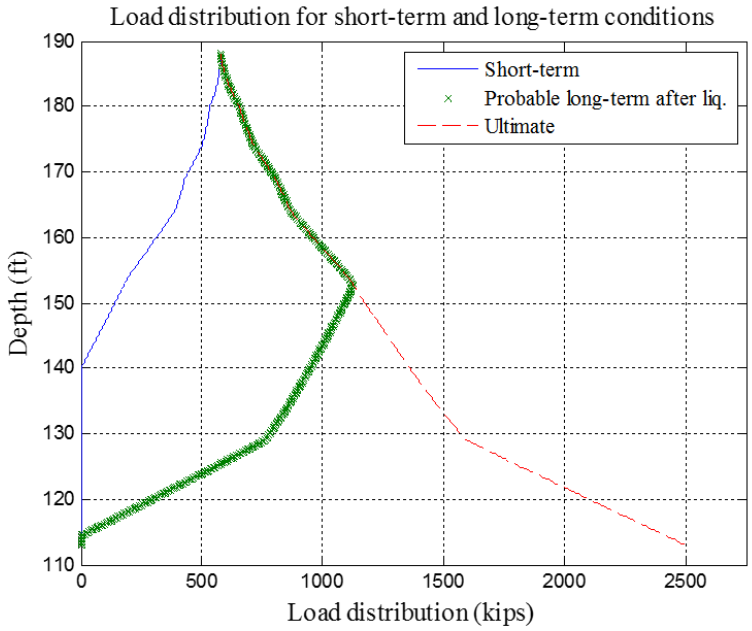

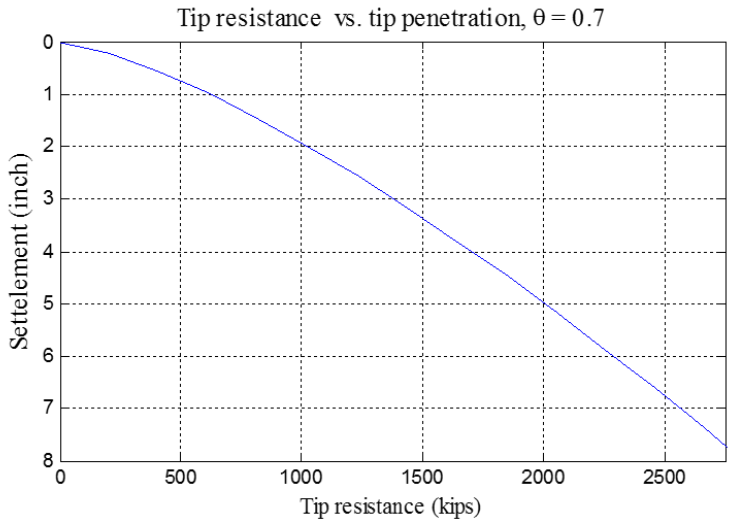

Figure B-22. SR 5 139th St NE Bridge Pier 10: Case I.

Project name and location: SR 5 139th St NE Bridge, Pier 10
6-feet drilled shaft, L = 75 ft

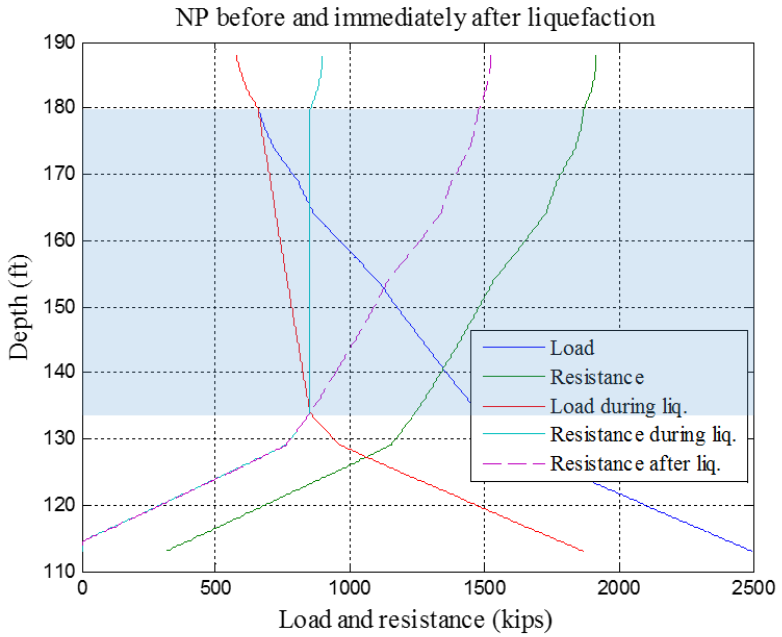

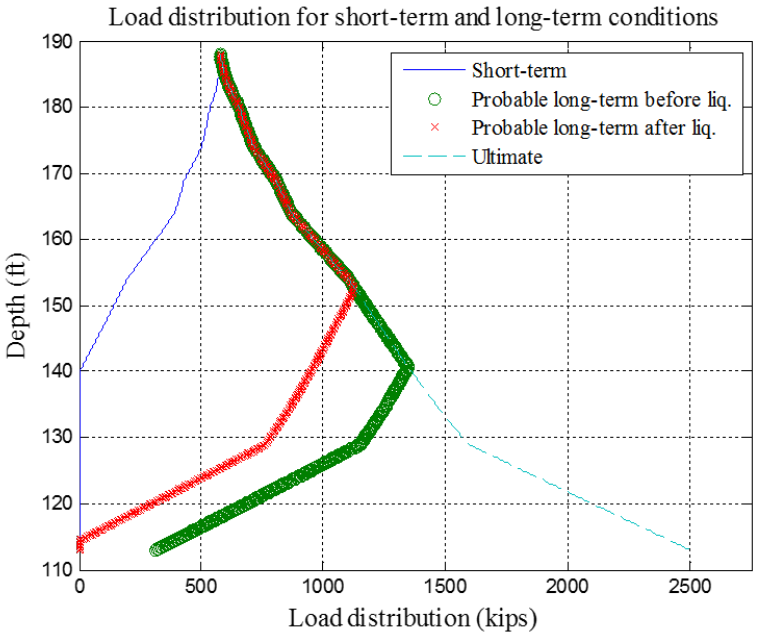

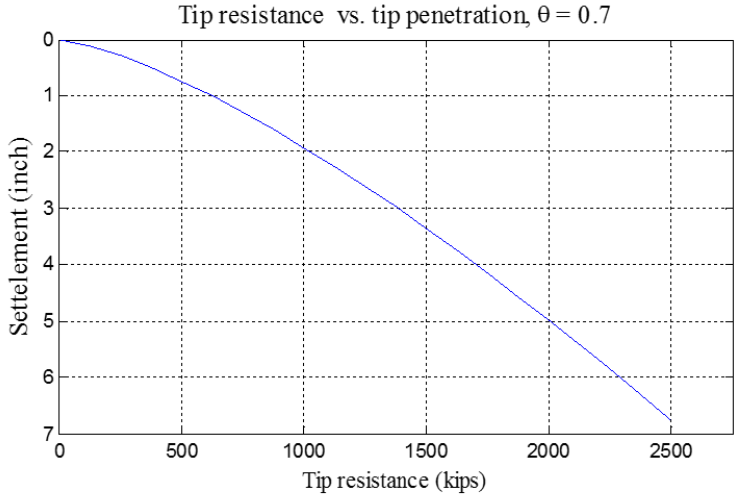

Max drag load before liquefaction (% of ultimate drag load)	571 kips (36 %)
Max drag load after liquefaction (% of ultimate drag load)	397 kips (25 %)
Ultimate drag load	1603 kips
NP location before liquefaction (ft)	141.0
NP location after liquefaction (ft)	152.7

*Drag load based on WSDOT approach (Average of nominal and residual side resistance) equals 1289 kips.

δ (short-term) = 0 inch, R (short-term) = 0 kips
δ (long-term before liq.) = 0.3937 inch , R (long-term before liq.) = 313.0499 kips
δ (long-term after liq.) = 0 inch , R (long-term after liq.) = 0 kips
δ (Ultimate) = 6.7695 inch , R (Ultimate) = 2497.1675 kips

Figure B-23. SR 5 139th St NE Bridge Pier 10: Case II.

Project name and location: Juan Pablo II Bridge, Piers 1 and 2 close to BH 16
8-feet drilled shaft, L = 52.5 ft

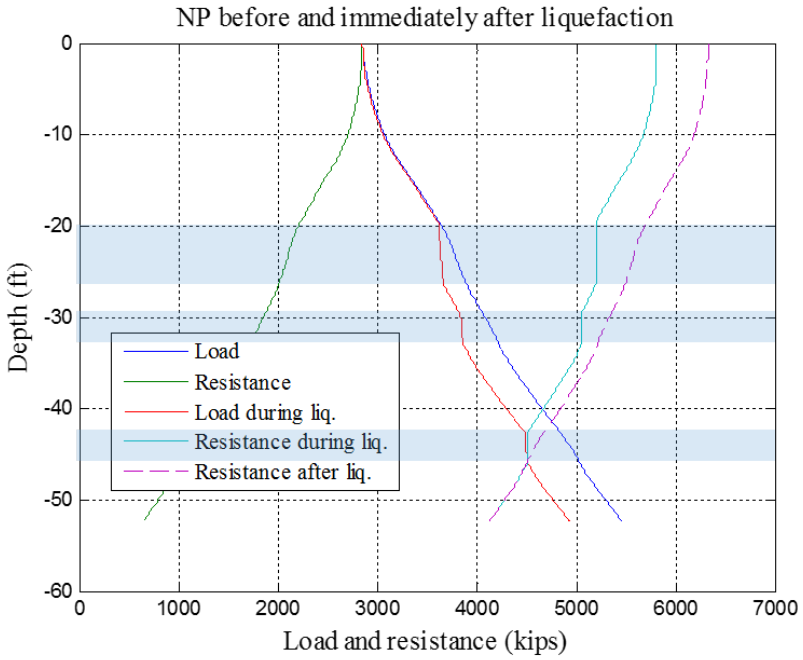

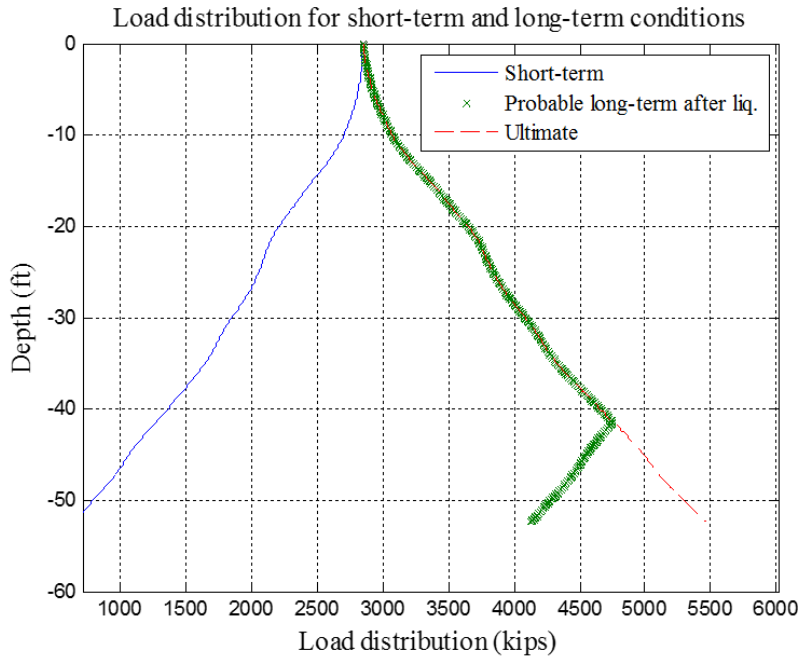

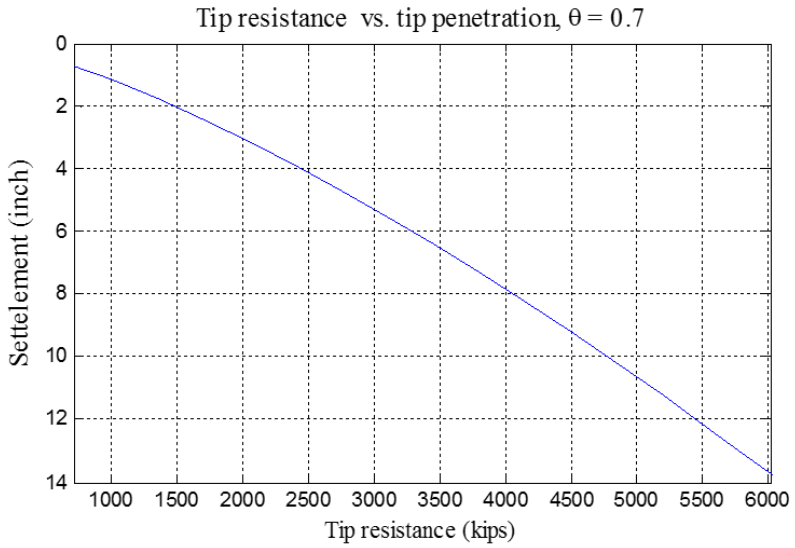

Max drag load before liquefaction (% of ultimate drag load)	0.0 kips (0 %)
Max drag load after liquefaction (% of ultimate drag load)	1572 kips (71 %)
Ultimate drag load	2203 kips
NP location before liquefaction (ft)	0.0
NP location after liquefaction (ft)	-41.5

*Drag load based on WSDOT approach (Average of nominal and residual side resistance) equals 1936 kips.

δ (long-term after liq.) = 8.2005 inch , R (long-term after liq.) = 4130.047 kips
δ (Ultimate) = 12.0423 inch , R (Ultimate) = 5467.2433 kips

Figure B-24. Juan Pablo II Bridge Piers 1 and 2: Case I.

Project name and location: Juan Pablo II Bridge, Piers 1 and 2 close to BH 16
8-feet drilled shaft, L = 52.5 ft

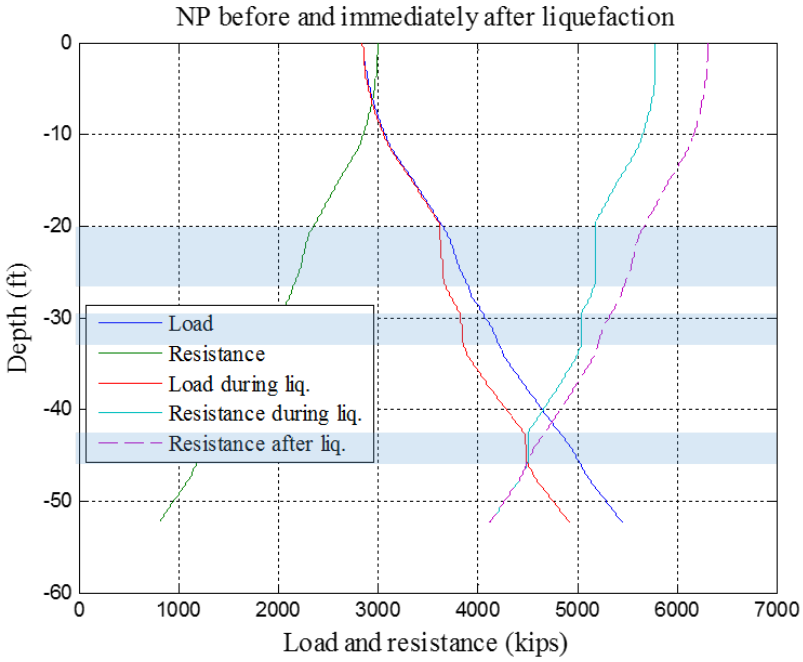

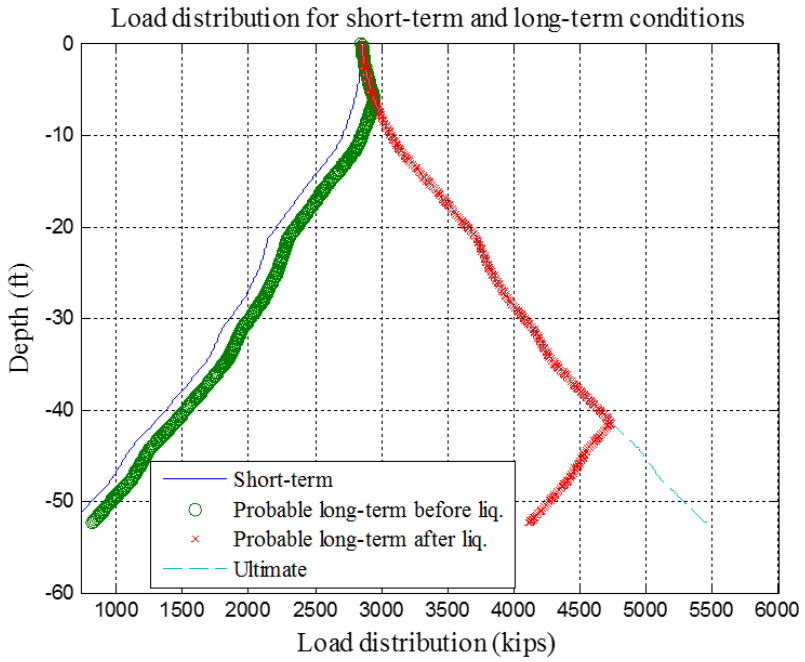

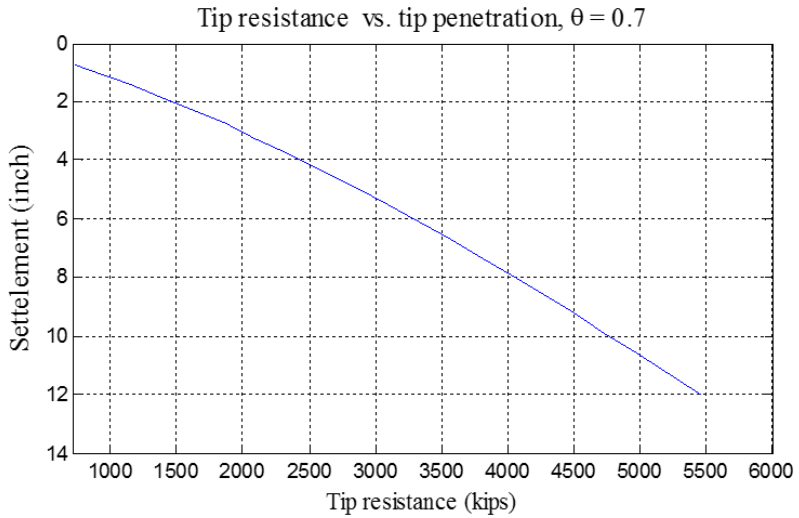

Max drag load before liquefaction (% of ultimate drag load)	55 kips (2.5 %)
Max drag load after liquefaction (% of ultimate drag load)	1572 kips (71 %)
Ultimate drag load	2203 kips
NP location before liquefaction (ft)	-6.1
NP location after liquefaction (ft)	-41.5

*Drag load based on WSDOT approach (Average of nominal and residual side resistance) equals 1936 kips.

δ (short-term) = 0.66041 inch, R (short-term) = 656.6203 kips
δ (long-term before liq.) = 1.0541 inch , R (long-term before liq.) = 808.5952 kips
δ (long-term after liq.) = 8.1624 inch , R (long-term after liq.) = 4116.0157 kips
δ (Ultimate) = 12.0148 inch , R (Ultimate) = 5458.1285 kips

Figure B-25. Juan Pablo II Bridge Piers 1 and 2: Case II.

Project name and location: Juan Pablo II Bridge, Piers 5 and 6 close to BH 10
8-feet drilled shaft, L = 52.5 ft

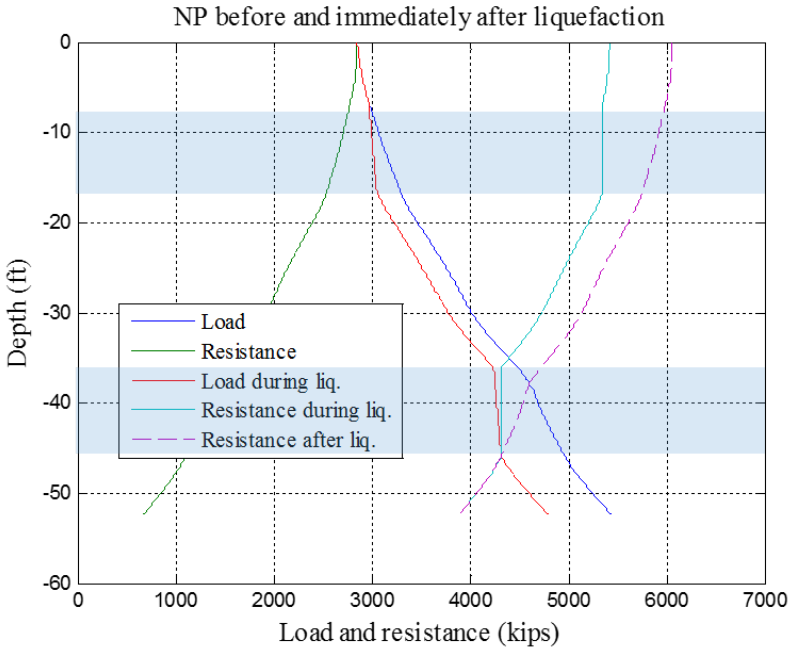

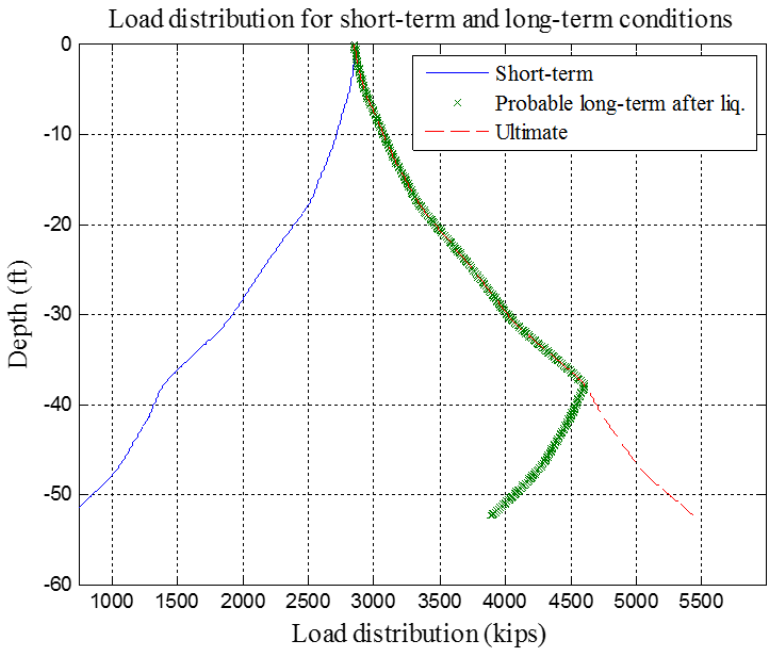

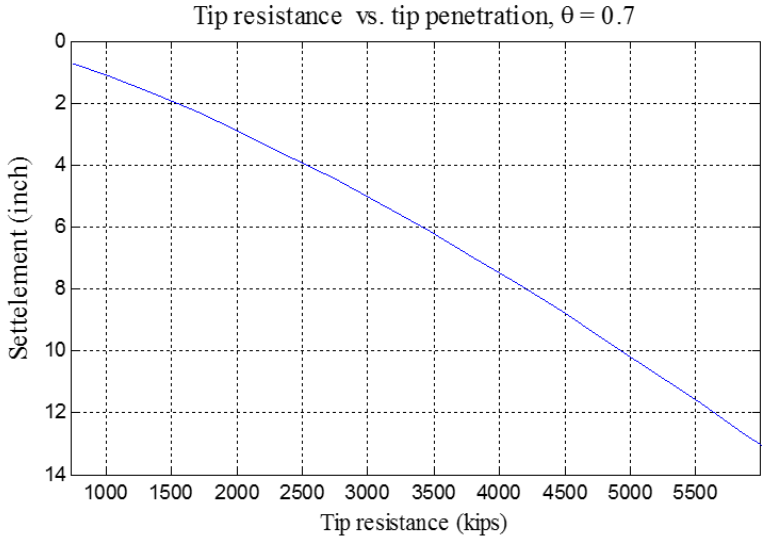

Max drag load before liquefaction (% of ultimate drag load)	0.0 kips (0 %)
Max drag load after liquefaction (% of ultimate drag load)	1453 kips (67 %)
Ultimate drag load	2176 kips
NP location before liquefaction (ft)	0.0
NP location after liquefaction (ft)	-38.0

*Drag load based on WSDOT approach (Average of nominal and residual side resistance) equals 1852 kips.

δ (long-term after liq.) = 7.2134 inch , R (long-term after liq.) = 3890.62 kips
δ (Ultimate) = 11.4203 inch , R (Ultimate) = 5441.0203 kips

Figure B-26. Juan Pablo II Bridge Piers 5 and 6: Case I.

Project name and location: Juan Pablo II Bridge, Piers 5 and 6 close to BH 10
8-feet drilled shaft, L = 52.5 ft

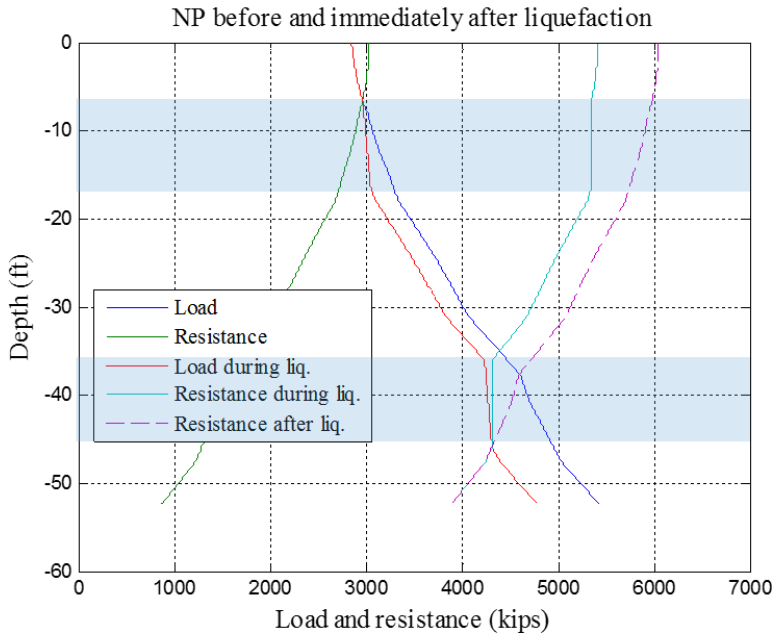

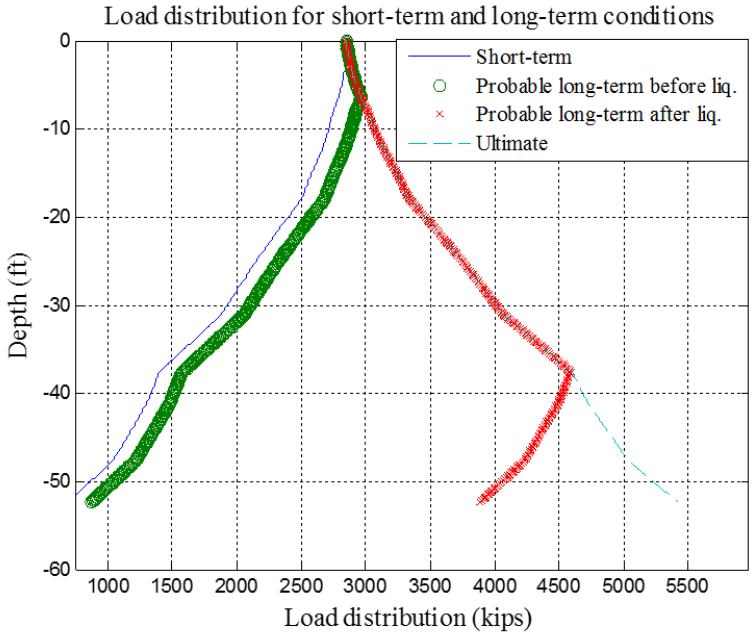

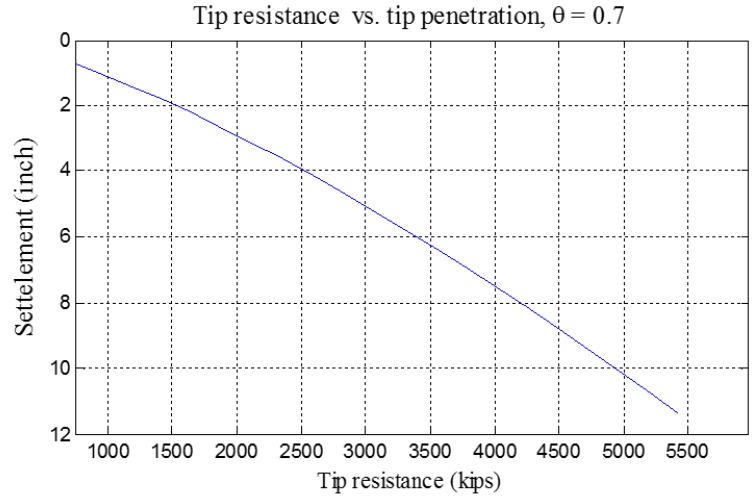

Max drag load before liquefaction (% of ultimate drag load)	68 kips (3 %)
Max drag load after liquefaction (% of ultimate drag load)	1453 kips (67 %)
Ultimate drag load	2176 kips
NP location before liquefaction (ft)	-6.4
NP location after liquefaction (ft)	-38.0

*Drag load based on WSDOT approach (Average of nominal and residual side resistance) equals 1852 kips.

δ (short-term) = 0.67099 inch, R (short-term) = 687.1898 kips
δ (long-term before liq.) = 1.0647 inch , R (long-term before liq.) = 867.4942 kips
δ (long-term after liq.) = 7.1896 inch , R (long-term after liq.) = 3881.2258 kips
δ (Ultimate) = 11.3816 inch , R (Ultimate) = 5427.559 kips

Figure B-27. Juan Pablo II Bridge Piers 5 and 6: Case II.

Project name and location: Juan Pablo II Bridge. Piers 117, and 118 close to BH 3
8-feet drilled shaft, L = 52.5 ft

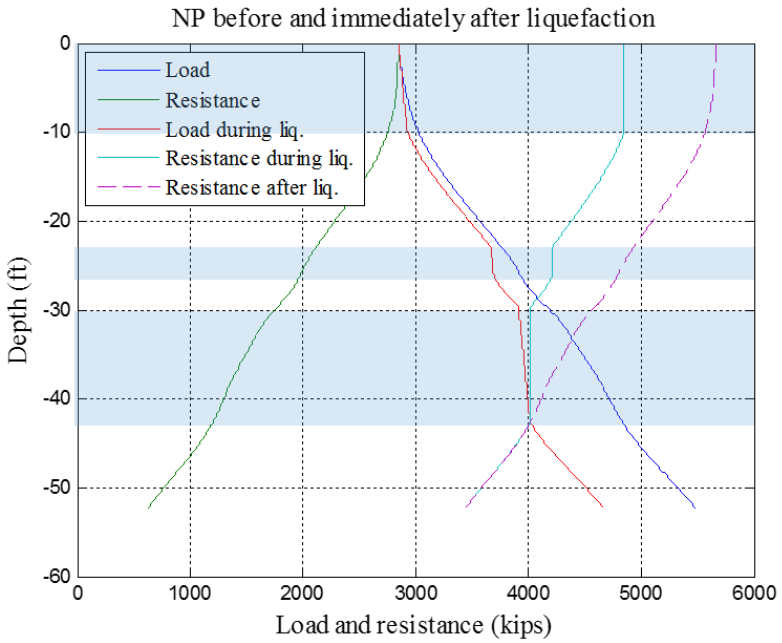

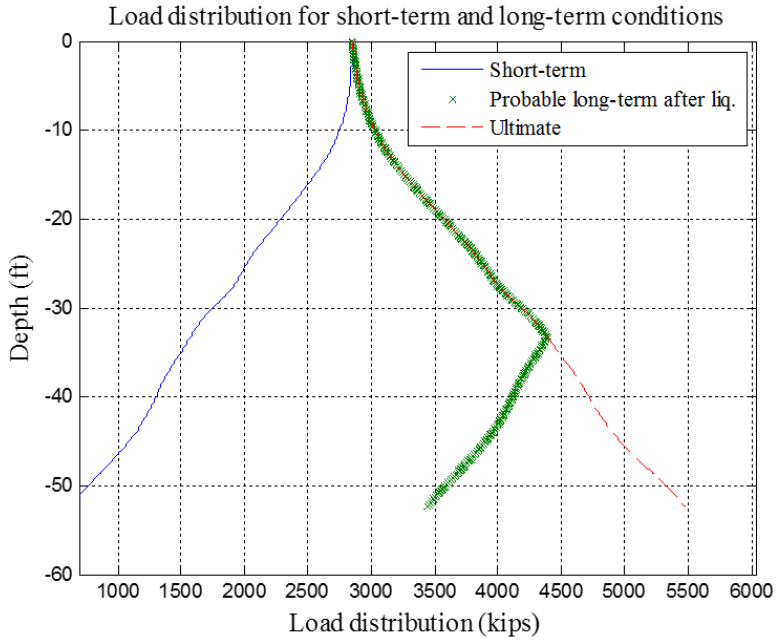

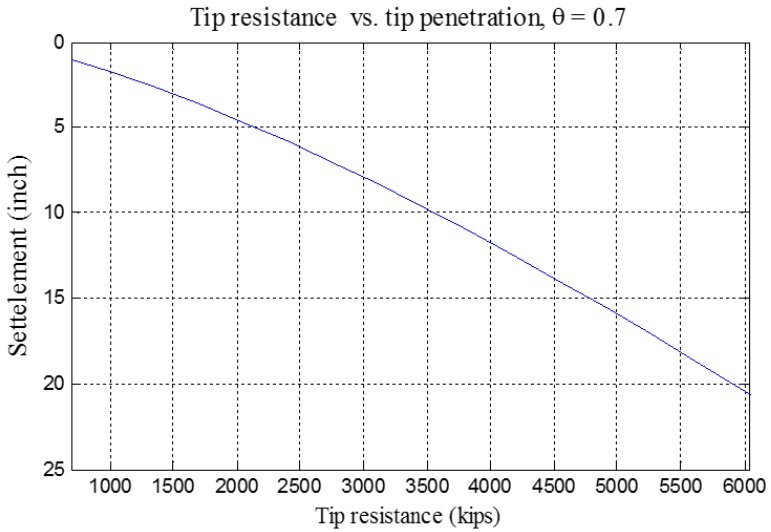

Max drag load before liquefaction (% of ultimate drag load)	0.0 kips (0 %)
Max drag load after liquefaction (% of ultimate drag load)	1271 kips (57 %)
Ultimate drag load	2221 kips
NP location before liquefaction (ft)	0.0
NP location after liquefaction (ft)	-33.4

*Drag load based on WSDOT approach (Average of nominal and residual side resistance) equals 1812 kips.

δ (long-term after liq.) = 9.5615 inch , R (long-term after liq.) = 3442.6361 kips
δ (Ultimate) = 18.1014 inch , R (Ultimate) = 5485.7824 kips

Figure B-28. Juan Pablo II Bridge Piers 117 and 118: Case I.

Project name and location: Juan Pablo II Bridge, Piers117 and 118 close to BH 3
8-feet drilled shaft, L = 52.5 ft

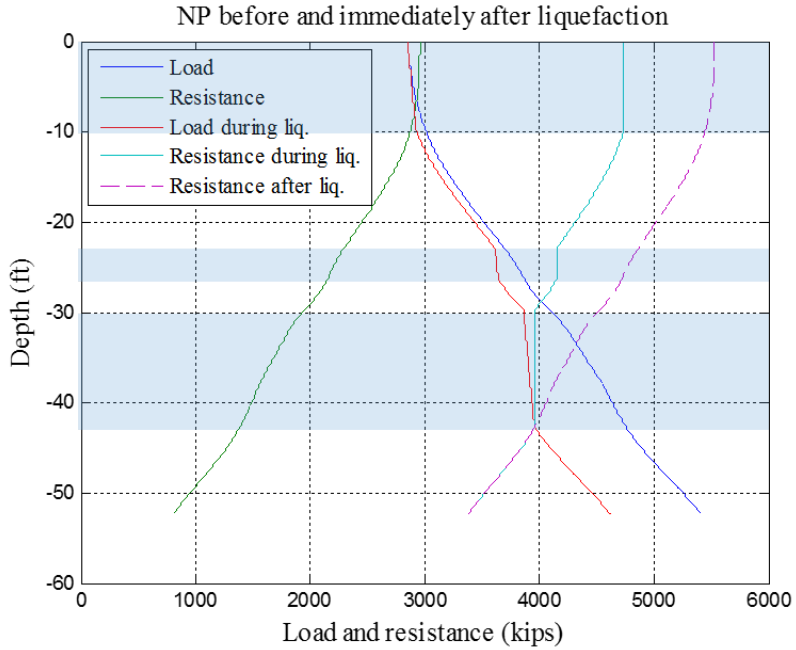

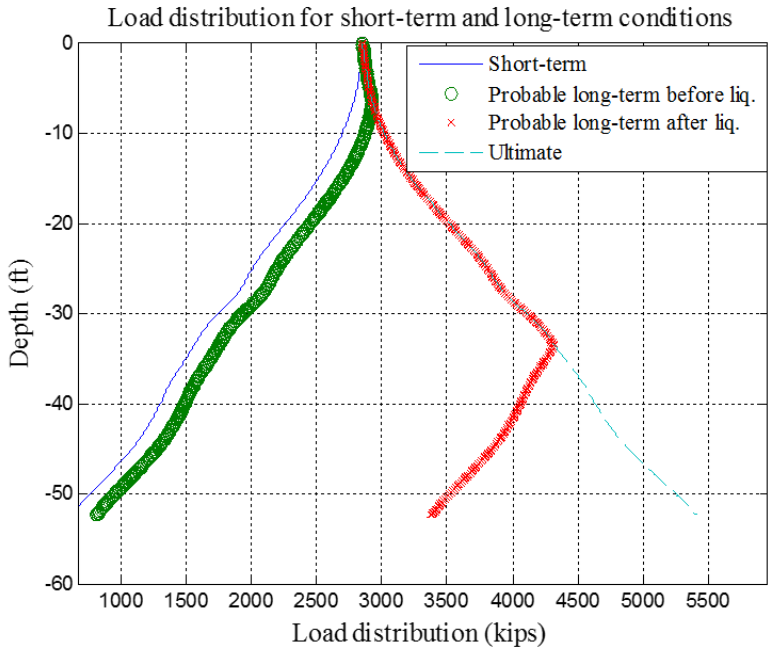

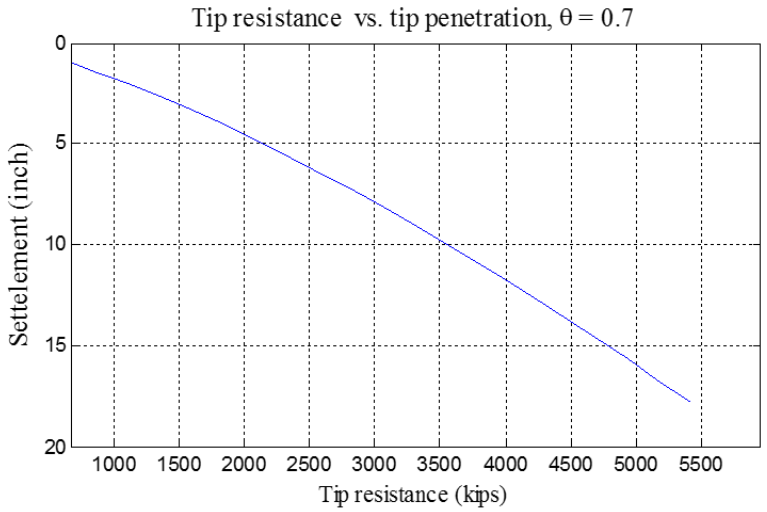

Max drag load before liquefaction (% of ultimate drag load)	24 kips (1 %)
Max drag load after liquefaction (% of ultimate drag load)	1271 kips (57 %)
Ultimate drag load	2221 kips
NP location before liquefaction (ft)	-5.4
NP location after liquefaction (ft)	-33.4

*Drag load based on WSDOT approach (Average of nominal and residual side resistance) equals 1812 kips.

δ (long-term after liq.) = 9.5615 inch , R (long-term after liq.) = 3442.6361 kips
δ (Ultimate) = 18.1014 inch , R (Ultimate) = 5485.7824 kips

Figure B-29. Juan Pablo II Bridge Piers 117 and 118: Case II.

Project name and location: Juan Pablo II Bridge, Piers 119 and 120 close to BH 7
8-feet drilled shaft, L = 52.5 ft

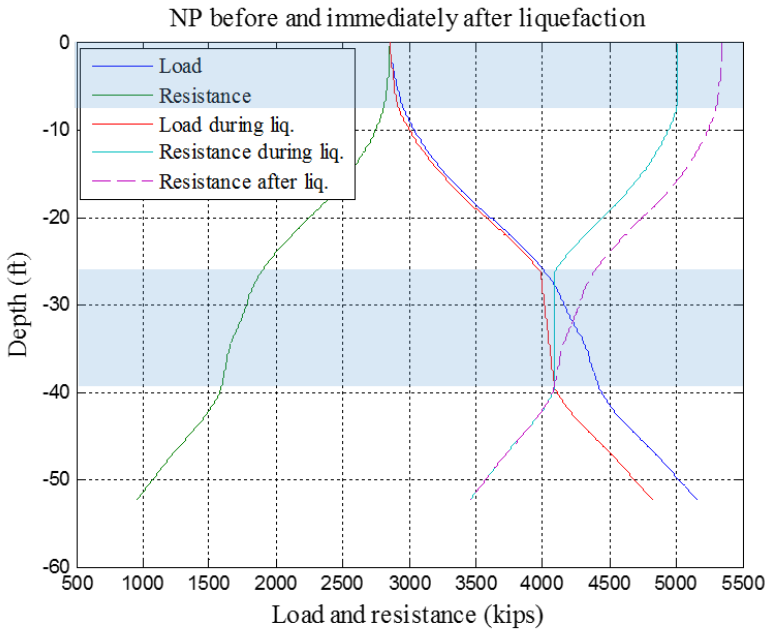

Max drag load before liquefaction (% of ultimate drag load)	0.0 kips (0 %)
Max drag load after liquefaction (% of ultimate drag load)	1116 kips (59 %)
Ultimate drag load	1897 kips
NP location before liquefaction (ft)	0.0
NP location after liquefaction (ft)	-32.1

*Drag load based on WSDOT approach (Average of nominal and residual side resistance) equals 1730 kips.

δ (long-term after liq.) = 9.987 inch , R (long-term after liq.) = 3449.3992 kips
δ (Ultimate) = 17.3496 inch , R (Ultimate) = 5162.2172 kips

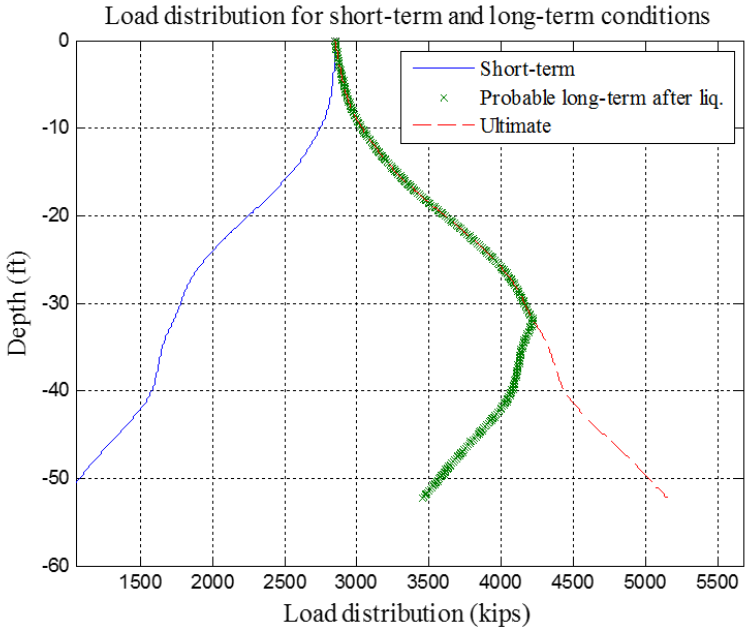

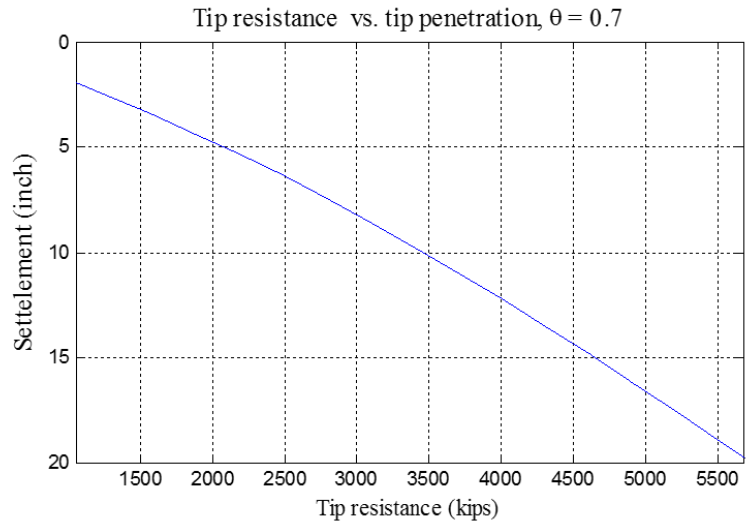

Figure B-30. Juan Pablo II Bridge Piers 119 and 120: Case I.

Project name and location: Juan Pablo II Bridge, Piers 119 and 120 close to BH 7
8-feet drilled shaft, L = 52.5 ft

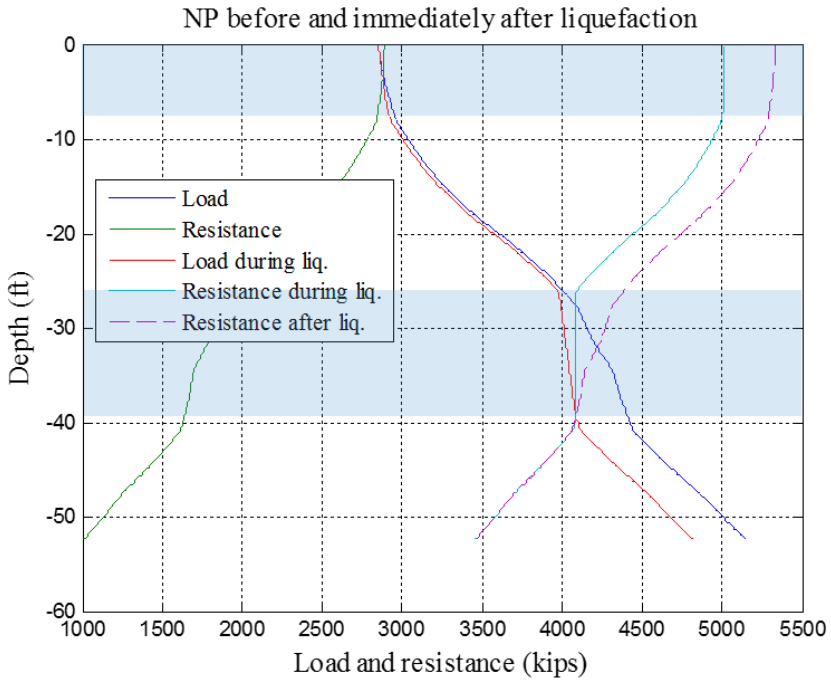

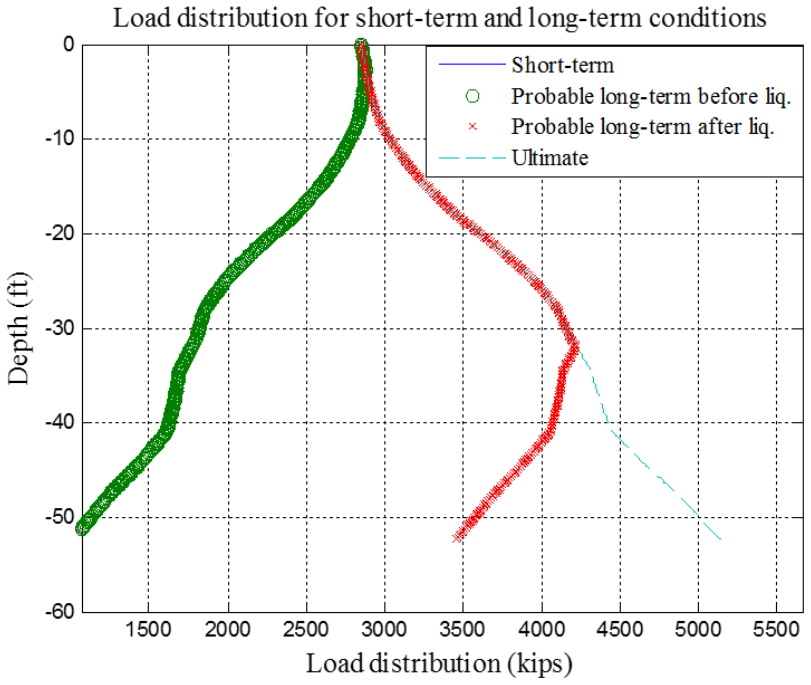

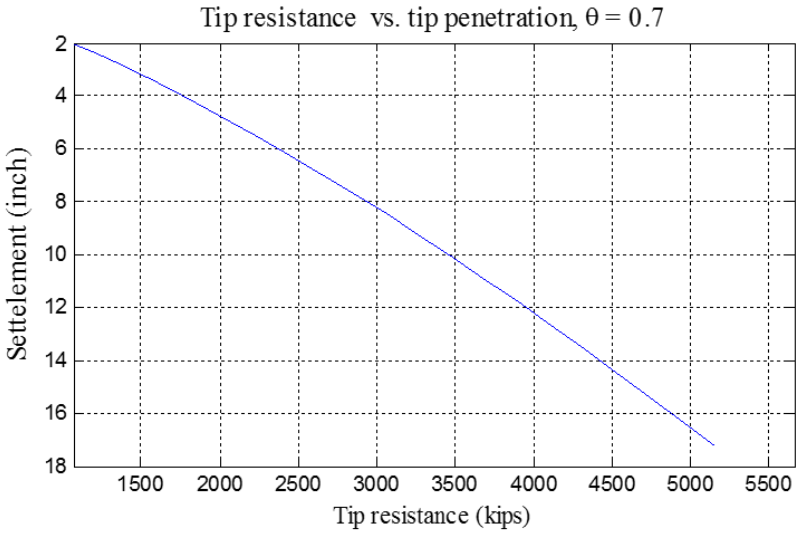

Max drag load before liquefaction (% of ultimate drag load)	24 kips (1 %)
Max drag load after liquefaction (% of ultimate drag load)	1116 kips (59 %)
Ultimate drag load	1897 kips
NP location before liquefaction (ft)	-5.4
NP location after liquefaction (ft)	-32.1

*Drag load based on WSDOT approach (Average of nominal and residual side resistance) equals 1730 kips.

δ (short-term) = 1.7528 inch, R (short-term) = 969.6104 kips
δ (long-term before liq.) = 2.1465 inch , R (long-term before liq.) = 1006.4778 kips
δ (long-term after liq.) = 9.9685 inch , R (long-term after liq.) = 3448.8254 kips
δ (Ultimate) = 17.2428 inch , R (Ultimate) = 5145.1384 kips

Figure B-31. Juan Pablo II Bridge Piers 119 and 120: Case II.

APPENDIX C: NEUTRAL PLANE METHOD AND THE POSSIBLE NEED TO USE RESIDUAL STRENGTH IN LIQUEFIED LAYERS

The American Association of State Highway and Transportation Officials (AASHTO) (2014) recommends the use of residual strength in liquefiable layers for the explicit method of design, as discussed in Chapter 2. Here we discusses the possible need for implications regarding the use of residual strength on neutral plane (NP) method.

The side resistance of a drilled shaft is a function of the excess pore water pressure ratio, r_u, as shown in $f_s = \sigma'_{vo} K_o \tan(\delta)(1 - r_u)$ (Boulanger and Brandenberg 2004). At the moment of initial liquefaction r_u equals 1; this value will gradually decrease to zero as the excess pore water pressure dissipates. The corresponding effect on the shaft will be dependent on the location of the liquefiable layer with respect to the NP.

Figure C.1 presents the variations in the load and resistance curves for the case when $r_u = 1$ (Line 1), during pore pressure dissipation (Line 2), and after complete dissipation (Line 3) for the case when the liquefiable layer is above the NP. Note that the dashed lines represent the load and the solid lines represent resistance. Because tip resistance will not be affected when the liquefiable layer is above the NP, no change in settlement will occur at any time. However, the drag load would decrease during seismic action and as the excess pore pressure increases to $r_u = 1$. Also, the drag load would revert to the static condition, as shown schematically in Figure C1 (a). So, the maximum drag load would remain the same as it is in the static condition.

Figure C.2 presents the variations in the load and resistance curves for the case when $r_u = 1$ (Line 1), during pore pressure dissipation (Line 2), and after complete dissipation (Line 3) for the case when the liquefiable layer is below the NP. As in Figure C1, the dashed lines represent the load and the solid lines represent resistance. The tip resistance for this case will increase during seismic action until $r_u = 1$, but will remain constant at this value during excess pore pressure dissipation and even after complete dissipation. The downdrag settlement would correspond to the increased tip resistance. For this case, the drag load would increase and reach its maximum value when $r_u = 0$.

Clearly, this discussion suggests that the need for residual strength does not arise when the pore pressure is not fully dissipated when using NP analysis. The most critical condition for liquefaction-induced drag load and downdrag settlement on deep foundations is when the excess pore pressure has fully dissipated.

The same discussion holds if the side resistance of shaft decrease because of the liquefaction-induced effects and changes the soil properties after fully dissipation of pore water pressure. In the NP method, the liquefaction-induced effects are reflected in both of load and resistance curves and considering the residual strength would not lead to a more conservative analysis.

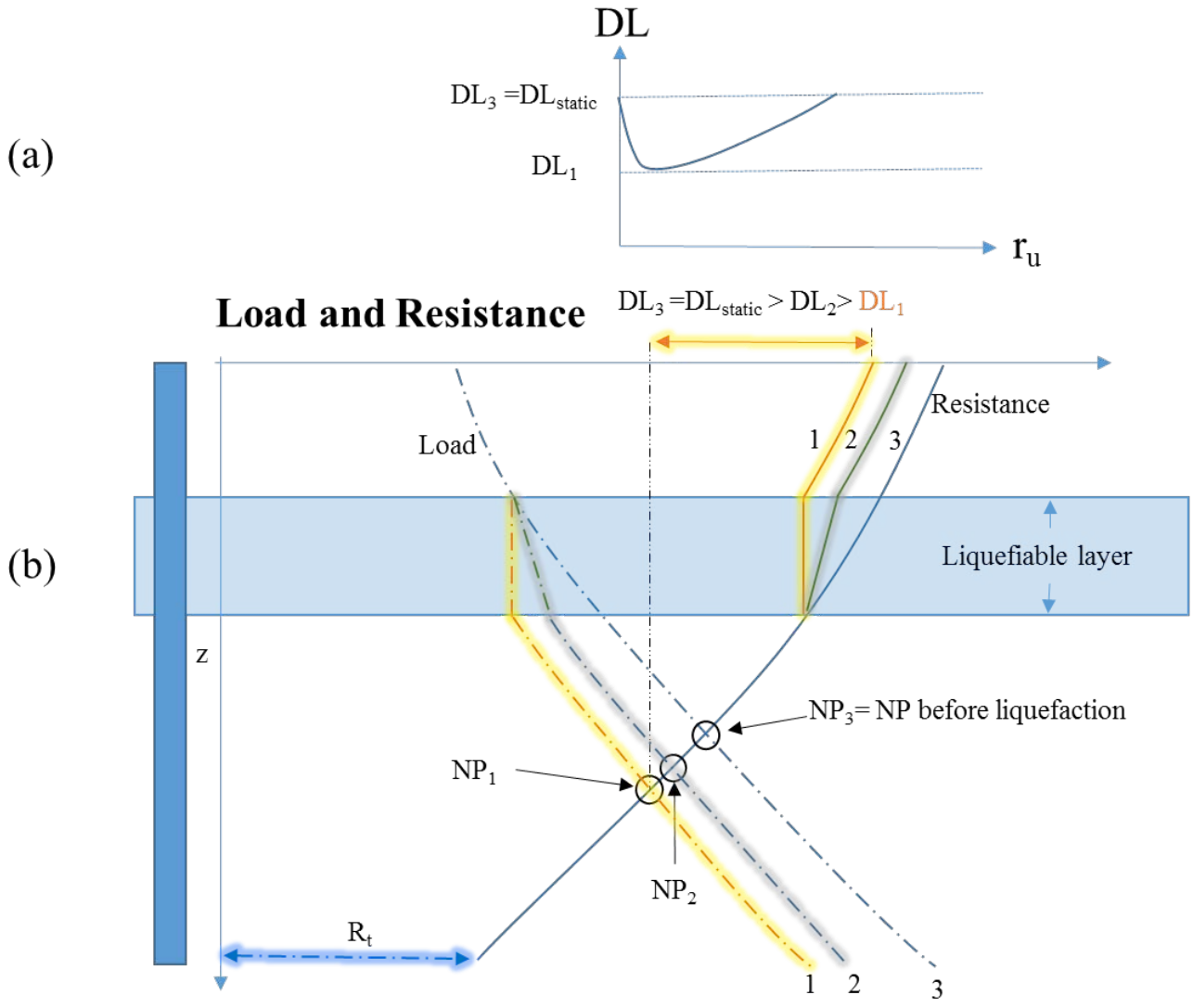

Figure C.1. Comparison of drag loads (DLs) during and after liquefaction when the liquefiable layer is above the neutral plane (NP).

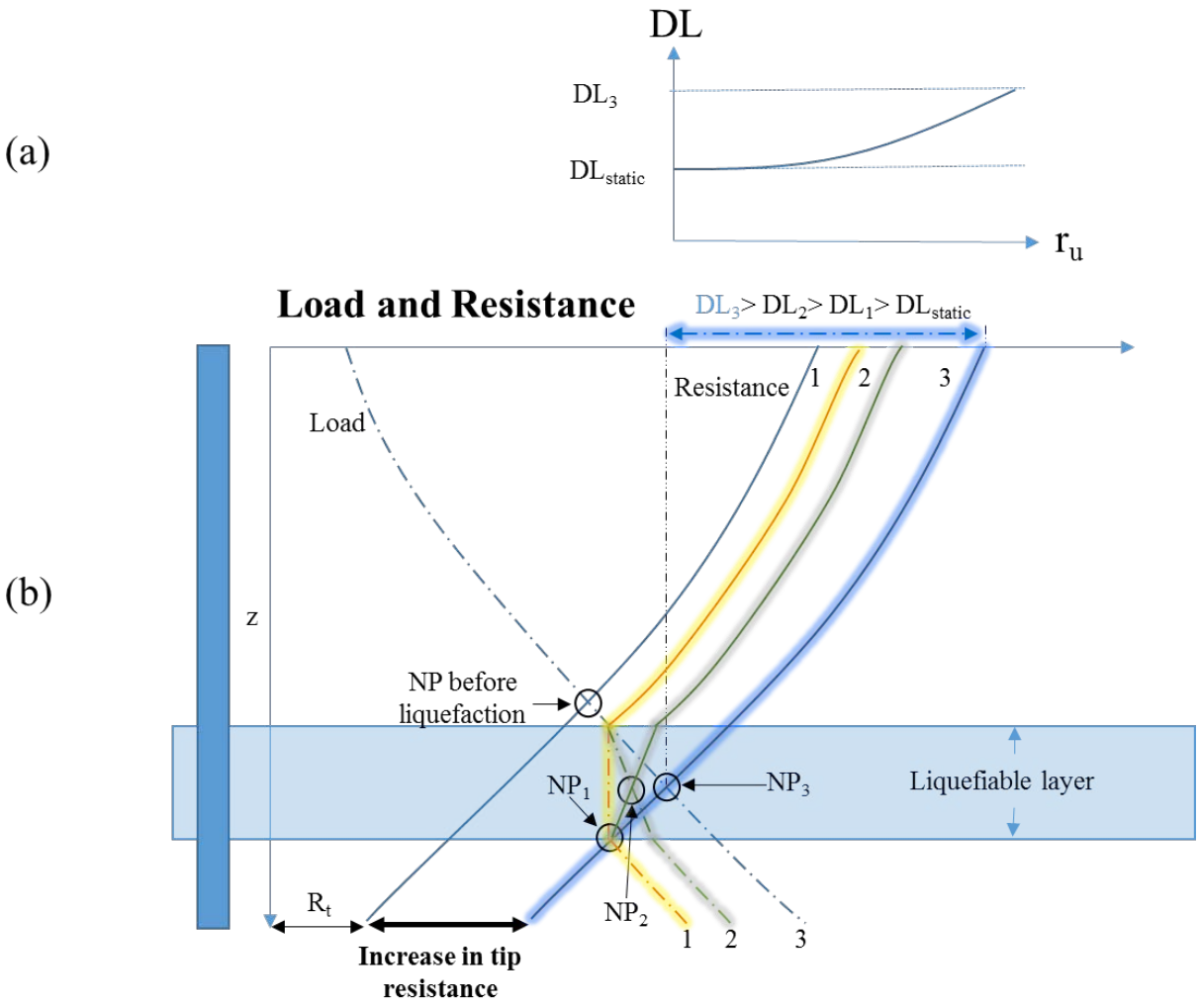

Figure C.2. Comparison of drag loads (DLs) during and after liquefaction when the liquefiable layer is below the neutral plane (NP).

Americans with Disabilities Act (ADA) Information:
This material can be made available in an alternate format by emailing the Office of Equal Opportunity at wsdotada@wsdot.wa.gov or by calling toll free, 855-362-4ADA(4232). Persons who are deaf or hard of hearing may make a request by calling the Washington State Relay at 711.

Title VI Statement to Public:
It is the Washington State Department of Transportation's (WSDOT) policy to assure that no person shall, on the grounds of race, color, national origin or sex, as provided by Title VI of the Civil Rights Act of 1964, be excluded from participation in, be denied the benefits of, or be otherwise discriminated against under any of its federally funded programs and activities. Any person who believes his/her Title VI protection has been violated, may file a complaint with WSDOT's Office of Equal Opportunity (OEO). For additional information regarding Title VI complaint procedures and/or information regarding our non-discrimination obligations, please contact OEO's Title VI Coordinator at (360) 705-7082.